GFZ Helmholtz Centre POTSDAM

METAL-AID From invention to injection

Green rust formation and reactivity with arsenic species

Dissertation

to obtain the academic degree of

Doktor der Naturwissenschaften (Dr. rer. nat.)

submitted to the Department of Earth Sciences

of Freie Universität Berlin

Freie Universität Berlin

by

Jeffrey Paulo H. Perez

Berlin, October 2019

This work was carried out from October 2016 to October 2019 at GFZ German Research Centre for Geosciences under the supervision of Prof. Dr. Liane G. Benning, within the framework of the Metal-Aid Innovative Training Network supported by a grant from the European Commission's Marie Skłowdowska-Curie Actions program (project no. 675219).

First reviewer (Erstgutachterin):

Prof. Dr. Liane G. Benning
Department of Earth Sciences, Freie Universität Berlin
Interface Geochemistry Section, GFZ German Research Centre of Geosciences

Second reviewer (Zweitgutachter):

Prof. Dr. Thomas Neumann
Department of Applied Geochemistry, Technische Universität Berlin

Doctoral Committee (Promotionsausschuss):

Prof. Dr. Esther Martina Schwarzenbach (Vorsitzes)
Department of Earth Sciences, Freie Universität Berlin

Prof. Dr. Christiane Stephan-Scherb (Stellv. Vorsitzes)
Department of Earth Sciences, Freie Universität Berlin
Materials Engineering, BAM Federal Institute for Materials Research and Testing

Prof. Dr. Liane G. Benning
Department of Earth Sciences, Freie Universität Berlin
Interface Geochemistry, GFZ German Research Centre of Geosciences

Prof. Dr. Friedhelm von Blanckenberg
Department of Earth Sciences, Freie Universität Berlin
Earth Surface Geochemistry, GFZ German Research Centre of Geosciences

Dr. Jörg Elis Hoffmann
Department of Earth Sciences, Freie Universität Berlin

Day of defense (Disputationsdatum):

17th of January 2020

Erklärung der Eigenständigkeit

Hiermit versichere ich, dass ich die vorliegende Arbeit selbstständig verfasst und keine anderen als die angegebenen Quellen und Hilfsmittel benutzt habe; alle Ausführungen, die anderen Schriften wörtlich oder sinngemäß entnommen wurden, kenntlich gemacht sind und die Arbeit in gleicher oder ähnlicher Fassung noch nicht Bestandteil einer Studien- oder Prüfungsleistung war.

Berlin, October 2019

_____

Jeffrey Paulo H. Perez

Declaration

This dissertation is a cumulative work of peer-reviewed scientific papers, either published, submitted for publication or in the final stages of preparation for submission. The candidate confirms that the work submitted is his own, except where work which has formed part of jointly-authored publications has been included. The contribution of the candidate and the other authors to this work have been explicitly indicated below. The candidate confirms that appropriate credit has been given within the thesis where reference has been made to the work of others. This dissertation is based on the following papers:

Chapter 2 reproduces a manuscript published in *Micron*

Freeman, H.M.; **Perez, J.P.H.**; Hondow, N.; Benning, L.G.B.; Brown, A.P. (2019). Beam-induced oxidation of mixed-valent Fe (oxyhydr)oxides (green rust) monitored by STEM-EELS. *Micron*, 122, 46-52.
DOI: https://doi.org/10.1016/j.micron.2019.02.002

HMF and JPHP conceived and designed the study with the help of LGB and APB. HMF, JPHP and APB collected the STEM-EEL spectra. NH performed the cryogenic TEM sample preparation. HMF, JPHP and APB interpreted the results and prepared the manuscript with contribution from all authors.

Chapter 3 reproduces a manuscript published in *Science of the Total Environment*

Perez, J.P.H.; Freeman, H.M.; Schuessler, J.A.; Benning, L.G.B. (2019). The interfacial reactivity of arsenic species with green rust sulfate (GR_{SO4}). *Science of the Total Environment*, 648, 1161-1170.
DOI: https://doi.org/10.1016/j.scitotenv.2018.08.163

JPHP conceived and designed the study with the help of LGB. HMF helped in the collection of TEM images and spectra. JAS provided training on trace metal analysis by ICP-OES. JPHP performed the batch adsorption experiments, ICP-OES analyses and material characterization. JPHP processed the data, interpreted the results and prepared the manuscript with contribution from all authors.

Chapter 4 reproduces a published in *Environmental Science and Technology*

Perez, J.P.H.; Freeman, H.M.; Brown, A.P.; Van Genuchten, C.M.; Dideriksen, K.; S'ari, M.; Tobler, D.J.; Benning, L.G. (2020). Direct visualization of arsenic binding on green rust sulfate. *Environmental Science & Technology*.
DOI: https://doi.org/10.1021/acs.est.9b07092

JPHP conceived and designed the study with the help of LGB. JPHP performed the batch experiments and aqueous geochemical analyses. The material characterization data were collected with the help of the following people: HMF and APB for the STEM-EDX images and spectra; CMvG, LGB, DJT and KD for the As K-edge EXAFS; DJT and KD for the high energy X-ray total scattering data. MS did the NMF analysis. JPHP processed the data, interpreted the results and prepared the manuscript with contribution from all authors.

Chapter 5 reproduces a manuscript published in *ACS Earth and Space Chemistry*

Perez, J.P.H.; Tobler, D.J.; Thomas A.N.; Freeman, H.M.; Dideriksen, K.; Radnik, J.; Benning, L.G.B. (2019). Adsorption and reduction of arsenate during the Fe^{2+}-induced transformation of ferrihydrite. *ACS Earth & Space Chemistry*, 3, 884-894. DOI: https://doi.org/10.1021/acsearthspacechem.9b00031

JPHP conceived and designed the study with the help of LGB. JPHP performed the batch experiments and aqueous geochemical analyses. The material characterization data were collected with the help of the following people: HMF for the TEM images; DJT and KD for the high energy X-ray total scattering data; ANT for the Fe K-edge EXAFS; LGB, DJT and KD for the As K-edge XANES; and JR for the XPS data. JPHP processed the data, interpreted the results and prepared the manuscript with contribution from all authors.

Chapter 6 reproduces a manuscript in the final stages of preparation for submission in *Journal of Hazardous Materials*

Perez, J.P.H.; Schiefler, A.A; Navaz Rubio, S.; Reischer, M.; Overheu, N.D.; Benning, L.G.; Tobler, D.J. Arsenic removal from natural groundwater using 'green rust' and its implication on contaminant mobility.

JPHP conceived and designed the study with the help of DJT and LGB. JPHP and MR collected the groundwater samples. JPHP carried out all geochemical analyses of the collected groundwater and set-up the long-term batch experiments. JPHP and AAS carried out sampling of liquid phases for ICP-OES, performed the XRD measurements and collected the SEM images. SNR performed Rietveld refinements on the collected XRD patterns. JPHP processed the data, interpreted the results and prepared the manuscript with contribution from all authors.

In addition to scientific papers included in this dissertation, the candidate also wrote and contributed to the following manuscripts:

Perez, J.P.H.*; Mangayayam, M.C.*; Navaz Rubio, S.; Freeman, H.M.; Tobler, D.J.; Benning, L.G.B. (2018). Intercalation of aromatic sulfonates in 'green rust' via ion exchange. *Energy Procedia*, 146, 179-187.
DOI: https://doi.org/10.1016/j.egypro.2018.07.023
*Both authors contributed equally

JPHP and MCM conceived and designed the study with the help of LGB. JPHP performed the batch experiments and performed the XRD analyses. The material characterization data were collected with the help of the following people: HMF for the TEM images and analysis and DJT for the high energy X-ray total scattering data. JPHP processed and analyzed the XRD and TEM data. SNR performed the Rietveld refinements on the collected XRD patterns. MCM performed the pair distribution function analysis. JPHP interpreted the results and prepared the manuscript with contribution from all authors.

Mangayayam, M.C., **Perez, J.P.H.**, Dideriksen, K., Freeman, H.M., Bovet, N., Benning, L.G., Tobler, D.J. (2019). Structural transformation of sulfidized zero valent iron and its impact on long-term reactivity. *Environmental Science: Nano*, 6, 3422-3430.
DOI: https://doi.org/10.1039/C9EN00876D

JPHP collected and analyzed the high resolution TEM images, electron diffraction patterns, STEM-EDX spectra and elemental maps, interpreted all the S/TEM data and helped with the preparation of the manuscript.

Hövelmann, J.; Stawski, T.M.; Freeman, H.M.; Besselink, R.B.; Mayanna, S.; **Perez, J.P.H.**; Hondow, N.S.; Benning, L.G. (2019). Struvite crystallization and the effect of Co^{2+} ions. *Minerals*, 9(9), 503.
DOI: https://doi.org/10.3390/min9090503

JPHP collected and interpreted the high resolution TEM images and helped with the preparation of the manuscript.

Wang, H.Y., Byrne, J.M., Benning, L.G.B., Thomas, A.N., Göttlicher, J., Höfer H.E., Mayanna, S., **Perez, J.P.H.**, Kontny, A., Kappler, A., Guo, H.M., Norra, S. Sequestration of As in greigite and pyrite in lacustrine buried peat: A case study from the Hetao Basin. Submitted to *Geochimica et Cosmochimica Acta*.

JPHP helped in the collection and interpretation of As and Fe K-edge EXAFS data, and in the preparation of the manuscript.

Acknowledgements

This work would not be possible without the help of the following people:

First and foremost, I would like to express my deepest and heartfelt gratitude to my PhD supervisor, Prof. Dr. Liane G. Benning, for her constant guidance and support throughout this entire PhD journey. I really appreciate your encouragement, especially at times when experiments were not going smoothly as planned, and for always making time for scientific discussions. I would not be the researcher that I am now without your help and for that I will be forever grateful.

My co-supervisors, Dr. Dominique J. Tobler and Dr. Helen M. Freeman, thank you for always being there to provide valuable feedback and for helping me navigate through this academic journey. I could not have wished for better scientific mentors.

My wonderful colleagues at the Interface Geochemistry research group at GFZ, thank you for all your support throughout my PhD and for the countless scientific discussions about my research work.

My fellow PhD students from Metal-Aid Innovative Training Network (ITN), especially to my closest friends Marco, Flavia, Virginia and Adrian, thank you for everything that we've shared these past three years. This whole journey has been wonderful, and all of you will always have a special place in my heart.

All the professors and industrial partners from Metal-Aid ITN for all the constructive comments on progress report presentations and for all the advice and inspiring stories that you've shared during networking sessions.

All my scientific collaborators for patiently teaching and training me on all the state-of-the-art characterization techniques I've used during my PhD: Dr. Andy P. Brown, Dr. Case van Genuchten, Dr. Knud Dideriksen, Dr. Jörg Radnik, Dr. Nicole Hondow, Dr. Peter Adler, Dr. Sathish Mayanna, Dr. Jan A. Schüssler. It has been a huge pleasure working with all of you.

The European Commission's Marie Skłodowska-Curie Actions program for funding the Metal-Aid ITN (project no. 675219) which gave me a great opportunity to do the best possible research during my PhD and allowed me to travel to amazing places for our network meetings.

The Royal Society of Chemistry and the Geo.X Research Network for funding my research visits to use the state-of-the-art S/TEM facilities at the University of Leeds (UK). The Geo.X Research Network and To.Sca Lab for the travel grants. The European Synchrotron Radiation Facility for the XAS beamtime, especially to Dr. Sakura Pascarelli of the BM23 beamline. The Advance Photon Source at Argonne National Laboratory for the PDF

beamtime, especially to Dr. Olaf Borkiewicz and Dr. Kevin A. Beyer of the 11 ID-B beamline.

Sandy Herrmann, our secretary of the Interface Geochemistry research group, for always being there to help me deal with all the administrative and bureaucratic parts of my PhD. More importantly, thank you for being supportive when I was writing my PhD thesis.

Clare Desplats, the project manager of Metal-Aid ITN, for organizing all the network meetings and being patient with all of us ESRs during the entire project.

My Filipino friends in Potsdam, Lovely, Irene, Weng, Tin, Gerome, Val, Mizzi, Karla, Kath, Pat, Rey, Donnie, Kirk, and around Europe, Jay-el, Joey, Nina, Angelica, Ryo, you have all been the closest thing to a family I have here. *Maraming salamat at mahal ko kayo*!

Leon, for being my strength throughout this whole endeavor and for unconditionally loving me throughout these years. To more years to come! *Ik hou van jou*!

Lastly, to my beloved parents, my earnest thanks for their loving support during my PhD. I dedicate this work to them.

Abstract

Elevated levels of arsenic (As) in soils and groundwaters remain a pressing global challenge due to its widespread occurrence and distribution, high toxicity and mobility. In oxygen-limited subsurface conditions, redox-active mineral phases can be important substrates in controlling the fate and mobility of As in the environment. Among these redox-active minerals, green rust (GR) phases, an Fe(II)-Fe(III)-bearing layered double hydroxide, have been shown to be able to sequester a wide range of toxic metals and metalloids, including As. However, prior to my PhD work, very little was known regarding how GR phases interact with As species and what is the fate of the immobilized As under dynamic geochemical conditions. GR phases are suggested to form through the transformation of metastable iron mineral phases in non-sulfidic, reducing environments. However, the exact mechanism and pathway of this transformation, as well as the fate of mineral-associated As (i.e. whether it is re-released back into the groundwater by desorption, dissolution or redox transformation) is not yet known but critically needed for modelling As cycling in contaminated environments.

To address these knowledge gaps, I conducted a series of experimental geochemical studies and combined them with various laboratory- and synchrotron-based solid and liquid phase characterization methods to examine the interaction between GR sulfate (GR_{SO4}) and As species [As(III) and As(V)]. Specifically, I performed several batch experiments under anoxic and near-neutral pH conditions to determine As-GR interaction mechanisms during GR formation and transformation. Moreover, I also quantified how these transformation reactions affect the toxicity and mobility of As species in contaminated environments.

From the batch adsorption experiments, I showed that synthetic GR_{SO4} can adsorb up to 160 and 105 mg of As(III) and As(V) per g of solid, respectively. These adsorption capacities are among the highest reported for iron (oxyhydr)oxides that form in soils and groundwaters. Results from this study also show that As removal by GR_{SO4} can be inhibited by several geochemical parameters such as pH, high ionic strength, presence of co-existing inorganic ions (e.g., Mg^{2+}, PO_4^{3-}, Si) and low temperature.

I also employed an integrated nano-scale solid-state characterization approach to elucidate As-GR_{SO4} interactions. Specifically, I combined scanning transmission electron microscopy (STEM) coupled with energy dispersive X-ray (EDX) spectroscopy together with bulk synchrotron-based X-ray techniques including high energy X-ray total scattering, pair distribution function (PDF) analysis and X-ray absorption spectroscopy (XAS). With these, I was able to directly visualize and pinpoint As binding sites at the GR surface sites and to identify the binding mechanism for both As(III) and As(V). In the case of As(III)-reacted GR, STEM-EDX maps showed that As(III) were preferentially adsorbed at the GR crystal edges, primarily as bidentate binuclear (^2C) inner-sphere surface complexes based from the differential PDF and As K-edge XAS data. For the As(V)-reacted GR, As(V) was sequestered as a newly-formed As-bearing mineral phase parasymplesite and as adsorbed As(V) species at the GR edges (in ^2C geometry).

To assess the fate of As in subsurface environments, I studied As during GR formation and transformation to quantify As uptake and/or its potential release back into solution and the stability of GR and other Fe (oxhydr)oxide phases in this process. During the Fe^{2+}-induced transformation of As(V)-bearing ferrihydrite, I followed the changes in aqueous behavior and speciation of As, as well as the changes in composition of the Fe mineral phases, as a function of varying $Fe^{2+}_{(aq)}/Fe(III)_{solid}$ ratios (0.5, 1 ,2). In all the ratios tested, GR_{SO4}, goethite and lepidocrocite formed in the early stages of transformation ($\leq$ 2h). However, at low ratios (<2), the initially formed GR_{So4} and/or lepidocrocite disappeared as the reaction progressed, leaving goethite and unreacted ferrihydrite after 24 h. At an $Fe^{2+}_{(aq)}/Fe(III)_{solid}$ ratio of 2, GR_{SO4} was formed and remained in the solids until the end of the 24-h transformation, with goethite and unreacted ferrihydrite. The initial As(V) was partially reduced to As(III) by the surface-associated Fe^{2+}-GT redox couple, and extent of reduction increased from 34 to 44% as $Fe^{2+}_{(aq)}/Fe(III)_{solid}$ ratios increased. Despite this reduction to the more mobile and more toxic As(III) species, no significant As release was observed during the mineral transformation reactions.

Finally, I tested the long-term stability and reactivity of GR by aging synthetic GR_{SO4} in pristine and As-spiked natural groundwater at ambient (25 °C) and low (4 °C) temperatures. The spiked As in the groundwater was completely removed after 120 days at 25 °C while the removal rate was ~2 times slower at 4 °C with only ~66% As removal after 120 days. On the other hand, the stability of synthetic GR_{SO4} in groundwater was strongly affected by the presence of adsorbed As species and temperature. At ambient temperature, the initial GR_{SO4} aged in As-free groundwater was converted to GR_{CO3} by ion exchange within a few days and both GR phases eventually transformed to magnetite after 120 days. Remarkably, both the addition of As species in groundwater and lowering the temperature increased long-term GR_{SO4} stability through the inhibition of (a) ion exchange in the GR_{SO4} interlayer (i.e., slower conversion to GR_{CO3}) and (b) transformation of GR to magnetite. Moreover, a synergistic stabilization effect was observed with both As addition and low temperature, significantly enhancing GR stability up to a year.

Overall, the work presented in this thesis clearly emphasizes the potential role of GR phases in controlling the mobility and toxicity of As species in subsurface environments. Specifically, I contributed to the fundamental understanding of the reactions involving As(III) and As(V) at GR surfaces, elucidating the relevant binding mechanisms and visualizing specific binding sites of immobilized As species. This work also identified critical geochemical factors that affect As removal and GR formation and transformation under anoxic and circum-neutral pH conditions. More importantly, I was able to show the enhanced long-term stability of GR in natural groundwaters and its prolonged reactivity for As sequestration.

Zusammenfassung

Erhöhte Arsengehalte in Böden und Grundwässern bleiben aufgrund ihres weitverbreiteten Auftretens, ihrer hohen Toxizität und ihrer hohen Mobilität eine dringende globale Herausforderung. Unter sauerstoffbegrenzten Untergrundbedingungen können redoxaktive Mineralphasen wichtige Substrate für die Kontrolle des Verbleibs und der Mobilität von Arsen (As) in der Umwelt sein. Unter diesen redoxaktiven Mineralien wurde gezeigt, dass Grüner Rost (GR) –Phasen – ein Fe(II)-Fe(III) -beinhaltendes doppelschichtiges Hydroxid - ein breites Spektrum von toxischen Metallen und Metalloiden, einschließlich As, binden können. Bevor ich mit deiesem Projekt für meine Doktorarbeit begann, war nur sehr wenig darüber bekannt, wie GR-Phasen mit As-Spezies interagieren und wie sich das immobilisierte As unter dynamischen geochemischen Bedingungen verhält. Es wurde angenommen, dass sich durch die Umwandlung metastabiler Eisenmineralphasen in nicht sulfidischen, reduzierenden Umgebungen oft GR-Phasen bilden. Der genaue Mechanismus und Weg dieser Umwandlung sowie der Verbleib des mit Mineralien assoziierten As (z.B. ob es durch Desorption, Auflösung oder Redox-Umwandlung wieder in das Grundwasser freigesetzt wird) sind jedoch noch nicht bekannt, werden aber dringend für die Modellierung des As-Kreislaufs in kontaminierten Umwelten benötigt .

Mit dem Ziel diese Wissenslücken zu schließen, führte ich eine Reihe experimenteller geochemischer Studien durch und kombinierte diese mit verschiedenen Methoden zur Fest- und Flüssigphasencharakterisierung auf Labor- und Synchrotronbasis, um die Wechselwirkung zwischen GR-Sulfat (GR_{SO4}) und As-Spezies [As(III) und As(V)] im Detail zu untersuchen. Insbesondere führte ich mehrere Batch-Experimente unter suboxischen/anoxischen und zirkumneutralen pH-Bedingungen durch, um die As-GR-Wechselwirkungsmechanismen während der GR-Bildung und -Transformation zu bestimmen. Darüber hinaus quantifizierte ich, wie sich diese Transformationsreaktionen auf die Toxizität und Mobilität von As-Spezies in kontaminierten Umgebungen auswirken.

Durch eine Serie von Adsorptionsexperimenten zeigte ich, dass synthetisches GR_{SO4} bis zu 160 mg As(III) bzw. 105 mg As(V) pro g Feststoff adsorbieren kann. Diese Adsorptionskapazitäten gehören zu den höchsten berichteten Werten für Eisen(oxyhydr)oxide in Böden und Grundwässern. Meine Ergebnisse zeigen auch, dass die Entfernung des As durch GR_{SO4} durch die Einwirkung verschiedener geochemischer Parameter wie den pH-Wert, die hohe Ionenstärke, das Vorhandensein von koexistierenden anorganischen Ionen (z. B., Mg^{2+}, PO_4^{3-}, Si) sowie die niedrige Temperatur gehemmt werden kann.

Ich habe auch einen integrierten Nano-Charakterisierungsansatz für Festkörper angewendet, um die As-GR_{SO4}-Wechselwirkungen zu erläutern. Insbesondere kombinierte ich Raster-Transmissionselektronenmikroskopie (RTEM) und energiedispersive Röntgenspektroskopie (EDX) mit synchrotronbasierter Hoch-Energie-Röntgen-Totalstreuung und Analyse der Paarverteilungsfunktion (PDF) sowie Röntgenabsorptionsspektroskopie (XAS). Mit diesen kombinierten Ansätzen konnte ich As-Bindungsstellen an den GR-Oberflächenstellen direkt sichtbar machen und lokalisieren sowie den Bindungsmechanismus sowohl für As(III) als auch für As (V) identifizieren. Im

Fall von mit As (III) reagiertem GR zeigten meine STEM-EDX-Karten, dass As (III) bevorzugt an den GR-Kristallrändern adsorbiert wurde, hauptsächlich als zweizähnige zweikernige (^{2}C) Innenkugel-Oberflächenkomplexe. Für das mit As(V) umgesetzte GR wurden 83% des As(V) als eine neugebildete As-tragende Parasymplesit-Mineralphase sequestriert und nur ein kleinerer Teil der As(V) -Spezies wurden an den GR-Rändern (in ^2C-Geometrie) adsorbiert.

Um den Verbleib von As in natürlichen unterirdischen Umgebungen abzuschätzen, untersuchte ich das Verhalten von As während der GR-Bildung und –Umwandlung. Somit konnte ich die As-Aufnahme und/oder die mögliche Freisetzung in die Lösung sowie die Stabilität von GR und anderen Fe Oxhydroxid/Oxid-Phasen in diesen wichtigen Untergrundprozessen quantifizieren. Während der Fe^{2+}-induzierten Umwandlung von As (V)-tragendem Ferrihydrit, verfolgte ich die Änderungen des wässrigen Verhaltens und der Speziation von As sowie die Änderungen der Zusammensetzung der Fe-Mineralphasen, als eine Funktion der Änderung von $Fe^{2+}_{(aq)}/Fe(III)_{Feststoff}$ Verhältnissen (0,5, 1, 2) . Unter allen getesteten Verhältnissen bildeten sich GR_{SO4}, Goethit und Lepidocrocit in den frühen Stadien der Transformation ($\leq$ 2h). Bei niedrigen $Fe^{2+}_{(aq)}/Fe(III)_{Feststoff}$ Verhältnissen ($<$2) verschwand das anfänglich gebildete GR_{SO4} und/oder Lepidocrocit jedoch mit fortschreitender Reaktion. Nach 24 h blieben nur Goethit und das nicht umgesetzte Ferrihydrit zurück. Bei einem $Fe^{2+}_{(aq)}/Fe(III)_{Feststoff}$ von 2 wurde GR_{SO4} gebildet und blieb stabil bis zum Ende der 24-stündigen Umwandlung zusammen mit Goethit und nicht umgesetztem Ferrihydrit. Das anfängliche As(V) wurde durch das oberflächenassoziierte Fe^{2+}-GT-Redoxpaar teilweise zu As(III) reduziert, und das Ausmaß der Reduktion stieg von 34 auf 44%, wenn das $Fe^{2+}_{(aq)}/Fe(III)_{Feststoff}$ Verhältnis zunahm. Trotz dieser Reduktion in die mobileren und toxischeren As(III)-Spezies wurde während der Mineralumwandlungsreaktionen keine signifikante As-Freisetzung beobachtet.

Schließlich testete ich die Langzeitstabilität und Reaktivität von GR durch das Altern von synthetischem GR_{SO4} in As-freiem und mit As-Spikes versetztem natürlichen Grundwasser bei Umgebungstemperaturen (25 °C) und niedrigen Temperaturen (4 °C). Das zugesetzte As wurde nach 120 Tagen bei 25 °C vollständig entfernt, während die Entfernungsrate bei 4 °C mit nur ~66% As Entfernung nach 120 Tagen ~2-mal langsamer war. Gleichzeitig wurde die Stabilität von synthetischem GR_{SO4} stark durch das Vorhandensein adsorbierter As-Spezies und die Temperatur beeinflusst. Bei Umgebungstemperatur wurde das anfänglich in As-freiem Grundwasser gealterte GR_{SO4} innerhalb weniger Tage durch Ionenaustausch in GR_{CO3} umgewandelt, und beide GR-Phasen wandelten sich schließlich nach 120 Tagen in Magnetit um. Bemerkenswerterweise erhöhten sowohl die Zugabe von As-Spezies im Grundwasser als auch die Absenkung der Temperatur die langfristige GR_{SO4}-Stabilität. Dies passierte durch die Hemmung von (a) Ionenaustausch in der GR_{SO4}-Zwischenschicht (d.h. langsamere Umwandlung in GR_{CO3}) und (b) Umwandlung von GR zu Magnetit. Darüber hinaus wurde ein synergistischer Stabilisierungseffekt sowohl bei As-Zugabe als auch bei niedriger Temperatur beobachtet, wodurch die GR-Stabilität bis zu einem Jahr signifikant verbessert wurde.

Die Ergebnisse meiner Doktorarbeit zeigen deutlich die wichtige Rolle von GR-Phasen bei der Kontrolle der Mobilität und Toxizität von As-Arten in unterirdischen Umgebungen. Insbesonders habe ich zum grundlegenden Verständnis der Reaktionen von As(III) und

As(V) an GR-Oberflächen beigetragen, die relevanten Bindungsmechanismen aufgeklärt und spezifische Bindungsstellen von immobilisierten As-Spezies sichtbar gemacht. Mit dieser Arbeit identifizierte ich auch kritische geochemische Faktoren, die die As-Entfernung sowie die GR-Bildung und -Transformation unter anoxischen und zirkumneutralen pH-Bedingungen beeinflussen. Noch wichtiger ist, dass ich die verbesserte Langzeitstabilität von GR in natürlichen Grundwässern und seine verlängerte Reaktivität für die As-Sequestrierung nachweisen konnte.

This work is dedicated to my beloved mother, ***Blanca****, who passed away last year. I love you and I miss you every single day!*

Table of Contents

Chapter 1

Introduction

1.1 Mineral Surfaces and their Influence on Pollutant Dynamics

The Earth's surface and (near-)subsurface environments are dominated by reactions at the interface between solids, fluids and gases, encompassing a wide range of temporal and spatial scales. Specifically, interfacial reactions between solids (i.e., rocks, minerals) and water greatly influence several key (bio)geochemical processes, including weathering, soil genesis, biomineralization, nutrient and trace element cycling and contaminant dynamics.

Naturally occurring metal (oxyhydr)oxide phases, as well as clay minerals, formed from the weathering of primary rock-forming minerals, are important substrates in controlling the fate and mobility of pollutants. Interfacial reactions at mineral surfaces (e.g., mineral dissolution-precipitation, sorption-desorption, etc.) govern the sequestration and/or re-release of pollutants in soils and groundwater. Redox-active mineral phases are, in particular, important within the context of pollutant dynamics because they often act as reductants/oxidants (e.g., Fe^{2+}/Fe^{3+} in Fe (oxyhydr)oxides or clays) for inorganic and organic contaminants, including natural (i.e., geogenic) and anthropogenic toxic metal(oid)s (e.g., arsenic, chromium, selenium, uranium) and organic pollutants (e.g., chlorinated solvents).

1.2 'Green Rust': A Brief Overview

Green rust (GR) is a redox-active mixed-valent Fe(II)-Fe(III) layered double hydroxide (LDH) which has been documented to form during the corrosion of steel under near-neutral to alkaline conditions. Although first observed as a corrosion product, its presence in natural environments has long been suggested by the greenish blue shade of hydromorphic soils which turn ochre upon exposure to air (Taylor, 1980). Recently, fougérite (IMA 2003-057), a naturally occurring GR mineral phase belonging to the hydrotalcite group, has been identified in gley soils in the forest of Fougères, Brittany, France (Trolard et al., 2007). Since then, GR phases have been identified in several other anoxic to suboxic natural and engineered systems such as groundwater (Christiansen et al., 2009a), ferruginous lakes (Koeksoy et al., 2019; Vuillemin et al., 2019; Zegeye et al., 2012), mofette sites (Rennert et al., 2012) or mine drainage effluent waters (Bearcock et al., 2006; Johnson et al., 2014).

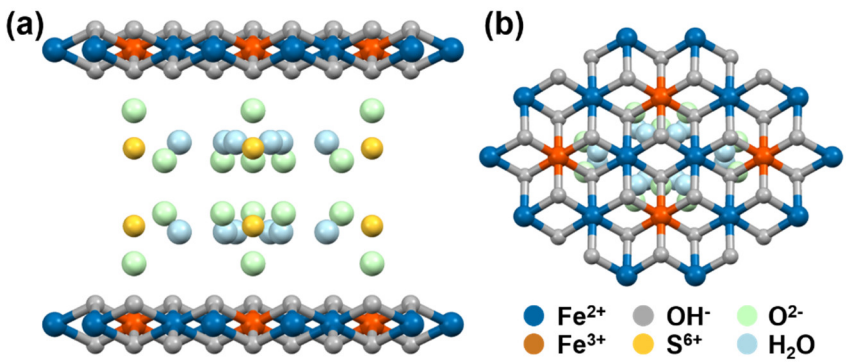

Figure 1.1 (a) Crystal structure of GR_{SO4} along the [001] zone axis showing the Fe(II)-Fe(III) hydroxide sheets and the interlayer region containing a double sheet of hydrated SO_4^{2-} ions. (b) Projection of the structure on the (001) plane illustrating the octahedrally-coordinated Fe(II) and Fe(III) hydroxides.

The structure of GR (Figure 1.1) is similar to LDHs, and is composed of positively charged brucite-like layers of octahedrally coordinated Fe(II)-Fe(III) hydroxide that alternate with negatively charged interlayers of hydrated anions (Géhin et al., 2002), and occasional monovalent cations (Christiansen et al., 2009b; Christiansen et al., 2014). These brucite-like layers and interlayer regions are held together by hydrogen bonding and electrostatic forces (Simon et al., 2003). GR is usually represented by the general formula, $[Fe^{II}_{(1-x)}Fe^{III}_{x}(OH)_2]^{x+}[(x/n)\ A^{n-}{\cdot}mH_2O]^{x-}$, where A^{n-} is the intercalated anion, x is the molar fraction of Fe(III), $[Fe(III)]/[Fe_{total}]$. Although there is no established nomenclature for naming different phases, GR is usually named based on the anionic species present in the interlayer: GR_z where z is the interlayer anion. An overview of common synthetic GR phases is shown in Table 1.1.

The molar fraction (x) of Fe(III) in the GR structure typically ranges between 0.25 and 0.33 (Murad and Taylor, 1984). The upper limit of x at 0.33 ensures a long range order of the Fe^{III} cations surrounded by six Fe(II) cations in hexagonal arrangement (Génin et al., 2005). Moreover, GRs with $x > 0.33$ are *quasi*-absent due to strong electrostatic cation-cation repulsion in the crystal structure as a result of the high density of Fe(III) octahedra in the hydroxide layer. This leads to a disordered iron hydroxide structural lattice and can act as nuclei for the formation of other mixed-valent iron solid phases such as magnetite (Fe_3O_4) (Génin et al., 2005; Ruby et al., 2003).

The nature of the intercalated anions in between the Fe(II)-Fe(III) hydroxide layers influences the structure and composition of GR. Depending on the intercalated anion, GR can be classified into two major groups: green rust one (GR1) and green rust two (GR2) (Bernal et al., 1959). GR1s have spherical or planar anions such as Cl^- and CO_3^{2-} while GR2s have tetrahedral anions such as SO_4^{2-} and SeO_4^{2-} intercalated in between their respective layered structure. The difference in the molecular geometry of the corresponding intercalated anion in GR results in different characteristic stacking arrangements of the Fe(II)-Fe(III) hydroxide layers. The crystal structure of GR1 is isomorphous to pyroaurite ($Mg^{II}_6Fe^{III}_2(OH)_{16}CO_3{\cdot}4H_2O$) or hydrotalcite ($Mg^{II}_4Fe^{III}_2(OH)_{12}CO_3{\cdot}3H_2O$). Hence, GR_{Cl} and GR_{CO3} both have rhombohedral lattice belonging to the $R\bar{3}m$ space group with a stacking sequence of $AcBiBaCjCbA$... where A, B and C are OH^- hexagonal layers, a, b and c are Fe cation layers and i, j and k are interlayer anions (Génin and Ruby, 2004a; Refait

et al., 1998a). This stacking arrangement induces a three-layer repeat with a single plane of hydrated anions. On the other hand, GR_{SO4}, which belongs to the GR2 group, has a trigonal lattice with a $P\bar{3}m1$ space group and a stacking sequence of *AcBij...*, which has a double-layer repeat with two planes of hydrated anions (Génin and Ruby, 2004a; Simon et al., 2003).

Table 1.1 Overview of synthesized GR phases based on the interlayer anion.

Anion	Formula	Space group	Cell parameters a (nm)	Cell parameters c (nm)	Synthesis route	Reference
Br^-	-	$R\bar{3}m$	0.318	2.280	Oxidation	Bernal et al. (1959)
BzS[a]	-	-	-	-	Ion exchange	Perez et al. (2018)
$C_2O_4^{2-}$	$Fe^{II}_6Fe^{III}_2(OH)_{16}C_2O_4 \cdot 4H_2O$	$R\bar{3}m$	0.320	2.340	Oxidation	Refait et al. (1998b)
$C_3H_5O_3^-$	$Fe^{II}_2Fe^{III}(OH)_{16}C_3H_5O_3 \cdot mH_2O$	$R\bar{3}m$	0.318	4.410	Oxidation	Sabot et al. (2007)
CHO_2^-	$Fe^{II}_5Fe^{III}_2(OH)_{14}(HCO_2)_2 \cdot 3H_2O$	$R\bar{3}m$	-	-	Oxidation	Génin and Ruby (2008) Refait et al. (2007)
Cl^-	$Fe^{II}_3Fe^{III}(OH)_8Cl \cdot mH_2O$	$R\bar{3}m$	0.319	2.386	Oxidation	Refait et al. (1998a)
ClO_4^{2-}	$Fe^{II}_3Fe^{III}_2(OH)_{10}(ClO_4)_2 \cdot mH_2O$	-	-	-	Oxidation	Vinš et al. (1987)
CO_3^{2-}	$Fe^{II}_4Fe^{III}_2(OH)_{12}CO_3 \cdot 3H_2O$	$R\bar{3}m$	0.318	2.271	Co-precipitation	Aissa et al. (2006)
			0.316	2.245	Oxidation	Drissi et al. (1995)
			0.316	2.254	Electrochemical	Legrand et al. (2001)
F^-	$Fe^{II}_3Fe^{III}(OH)_8F \cdot mH_2O$	-	-	-	Oxidation	Choi and Batchelor (2008)
I^-	-		0.319	2.480	Oxidation	Vinš et al. (1987)
LAC[b]	-	-	-	2.68 - 4.44	Ion exchange	Ayala-Luis et al. (2010a) Ayala-Luis et al. (2010b)
LAS[c]	-	-	-	2.85	Ion exchange	Ayala-Luis et al. (2007)
OH^-	$(Fe^{II},Mg)_6Fe^{III}_2(OH)_{18} \cdot 4H_2O$	$R\bar{3}m$	0.313	2.256 - 2.385	Naturally occuring	Trolard et al. (2007)
SeO_4^{2-}	$Fe^{II}_4Fe^{III}_2(OH)_{12}SeO_4 \cdot 8H_2O$	$P\bar{3}m1$	-	-	Oxidation	Refait et al. (2000)
SO_3^{2-}	$Fe^{II}_6Fe^{III}_2(OH)_{16}SO_3 \cdot mH_2O$	$R\bar{3}m$	0.322	2.340	Oxidation	Simon et al. (1998)
SO_4^{2-}	$Fe^{II}_4Fe^{III}_2(OH)_{12}SO_4 \cdot 8H_2O$	$P\bar{3}m1$	0.552	1.101	Oxidation	Simon et al. (2003)
			0.318	1.090	Co-precipitation	Géhin et al. (2002)
SO_4^{2-} (Na^+)	$NaFe^{II}_6Fe^{III}_3(SO_4)_2(OH)_{18} \cdot 12H_2O$	$P\bar{3}$	0.953	1.097	Oxidation	Christiansen et al. (2009b)

Note: [a] benzene sulfonate, [b] linear alkyl carboxylate (C9-C16), [c] linear alkyl sulfonate (C10-C13)

In addition to anions, the presence of occasional monovalent cations has been documented in GR_{SO4}. Christiansen et al. (2009b) argued that sodium (Na^+) can be incorporated in the GR_{SO4} interlayer, and they proposed a chemical composition of $NaFe^{II}_6Fe^{III}_3(SO_4)_2(OH)_{18} \cdot 12H_2O$, a crystal structure similar to that of nikischerite with a rhombohedral lattice belonging to the $P\bar{3}$ space group (Huminicki and Hawthorne, 2003). In addition to Na^+, other monovalent cations such as K^+, Rb^+ and Cs^+ can also be incorporated into the interlayer of GR_{SO4} with varying degrees of occupation based on the sulfate ion pair stability constant (Christiansen et al., 2014).

The intercalated species in the GR structure are not limited to inorganic molecules. Using the same chemical design principle as in LDHs, a subclass of GR called organo-GRs, which have organic molecules in the interlayers, has also been synthesized. Various organic aliphatic and aromatic compounds such as carboxylates and sulfonates (see Table 1.1) have been so far been intercalated (Ayala-Luis et al., 2007; Ayala-Luis et al., 2010a; b; Perez et al., 2018; Refait et al., 2007; Refait et al., 1998b; Sabot et al., 2007).

1.3 Green Rust Synthesis and Formation Mechanism

1.3.1 Oxidation of Fe(II) species

Among the strategies for preparing synthetic GR, the oxidation of an Fe(II) solution at a constant pH, usually around pH 7 to 7.5, is the most commonly used synthesis pathway. Early studies examining the corrosion products of ferrous iron suggested that GR forms through the oxidation of aqueous Fe^{2+} species which form *ad hoc* ferrous-ferric "green complexes", followed by the precipitation of GR (Misawa et al., 1973; 1974). More recent studies using electrochemical deposition of GR thin layers support the formation of GR *via* the "green complexes", which were identified as soluble $[(Fe^{II})_2(Fe^{III})_1]$ species (Antony et al., 2008).

Alternatively, GR can also be formed through the oxidation of ferrous hydroxide ($Fe(OH)_2$) or "white rust". In this approach, GR is prepared by precipitating $Fe(OH)_2$ from an anoxic Fe^{2+} solution at around pH 7, followed by the careful oxidation of the suspension while maintaining the desired pH. GR, in this pathway, is assumed to form through the solid-state oxidation of the structural Fe^{2+} in the brucite-like Fe hydroxide layers of $Fe(OH)_2$ (Cornell and Schwertmann, 2003; Génin et al., 1996; Misawa et al., 1973). This solid-state transformation is accompanied by simultaneous incorporation of anions into the interlayer region to maintain electroneutrality in the crystal structure.

1.3.2 Co-precipitation pathway

GR can also be synthesized by co-precipitating mixed aqueous solutions of Fe(II) and Fe(III), containing the desired interlayer anion. This is usually done by titrating the mixed acidic solution (ca. pH 2 to 3) anoxically with NaOH until pH 7 to 8 was reached. An early proposed mechanism for GR_{SO4} formation (Ruby et al., 2006; Ruby et al., 2003) suggested that schwertmannite, a nanocrystalline ferric hydroxysulfate, forms first around pH ~4 and traps all the Fe^{3+} ions and leaves the Fe^{2+} dissolved in solution. Continuous increase in pH leads to the conversion of schwertmannite to goethite ($Fe^{III}OOH$). The surface of the newly-formed goethite acts as a hydroxylating ligand for the Fe^{2+} ions in the solution. The partially hydroxylated Fe(II) complexes, along with the SO_4^{2-} ions, are then adsorbed onto the goethite surface at pH ~5. Then, these hydroxylated complexes condense by olation to form brucite-like clusters of $[Fe(OH)_2(OH_2)_4]^0$ complexes (Jolivet et al., 2004; Jolivet et al., 2006) (Figure 1.2a). Contrary to the previously proposed mechanism via "green complexes" (Misawa et al., 1973), GR_{SO4}, in this pathway, forms through the surface reactions between goethite and the adsorbed SO_4^{2-} ions and hydroxylated Fe(II) complexes, which is shown in Figure 1.2.

The adsorbed SO_4^{2-} ions get trapped between the $Fe^{III}OOH$ interface and the brucite-like cluster. This leads to electron transfer from the brucite-like cluster to the $Fe^{III}OOH$ interface to form an electrostatically balanced Fe(II)-Fe(III) hydroxide layer. The Fe(II)-Fe(III) hydroxide layer then detaches from the $Fe^{III}OOH$ interface and serves as a GR_{SO4} nucleus (Figure 1.2b). This proposed formation mechanism is based on the *in situ* crystal growth of GR_{SO4} at the expense of the $Fe^{III}OOH$ substrate by electron transfer instead of dissolution-precipitation process (Figure 1.2c-d). However, there was no direct evidence provided in the study to support this proposed formation mechanism.

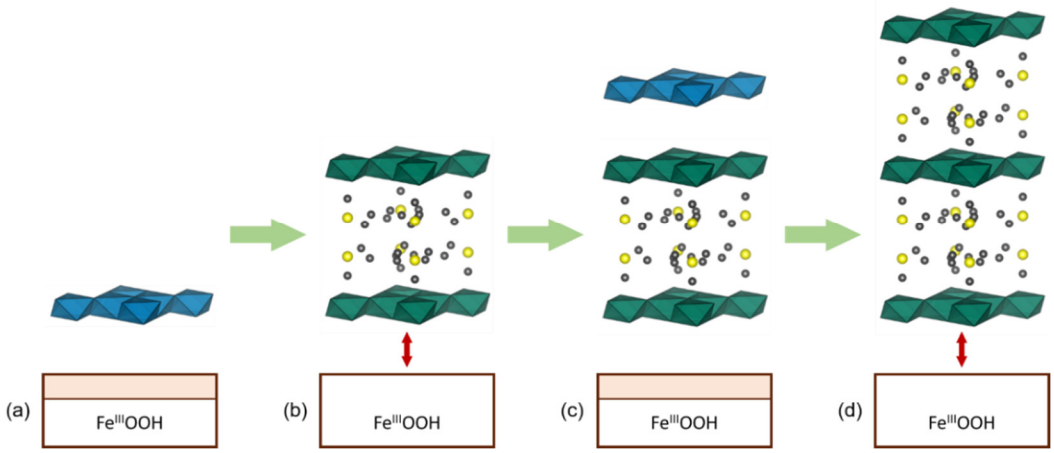

Figure 1.2 Formation of GR_{SO4} from the surface reaction between ferric oxyhydroxides and adsorbed octahedrally connected Fe^{2+} cations and sulfate ions. Light blue coordination octahedra represent brucite-like $[Fe(OH)_2(OH_2)_4]^0$ complexes; dark green octahedra represent Fe(II)-Fe(III) hydroxide sheets of GR_{SO4}; light orange rectangle represents solid-solution interface of $Fe^{III}OOH$.

A detailed mechanism and kinetics of GR_{SO4} formation was reported using *in situ* time-resolved wide-angle X-ray scattering (WAXS) analysis of forming and transforming solid phases in solution under anoxic conditions (Ahmed et al., 2010). The 3D plot of the *in situ* collected time-resolved WAXS data and changes in dissolved iron concentrations are shown in Figure 1.3a and 1.3b, respectively.

As seen in Figure 1.3a, at the beginning of the titration, no diffraction peaks were seen and only a large hump (consequence of scattering from the solution) was observed at pH $<$ 2.8. As pH increased, schwertmannite precipitated and its maximum intensity diffraction peak (212) at ~22.6° grew, accompanied by the decrease in aqueous Fe^{3+} concentration (Figure 1.3b). The aqueous iron speciation analysis revealed that the dominant Fe(III) species at low pH (~3.8) and high concentration of SO_4^{2-} were $FeSO_4^{+}{}_{(aq)}$ and $Fe(SO_4)_2^{-}{}_{(aq)}$. Ahmed et al. (2010) suggested that these Fe(III) species hydrolyzed and polymerized to form aqueous ferric sulfate complexes. Subsequently, these complexes became incorporated into the solid structure forming schwertmannite. With a further increase in pH $<$ 5, the broad diffraction peak of schwertmannite disappeared and the maximum intensity diffraction peak for goethite (101) appeared at ~13.7°. Moreover, a significant decrease in Fe^{2+} concentration was observed and this was interpreted as adsorption onto the schwertmannite nanocrystal surfaces, and this in turn stimulated the Fe^{2+}-induced transformation of schwertmannite to goethite, a reaction that will be

discussed in the next section (Andreeva et al., 1995; Burton et al., 2007; Burton et al., 2008; Hansel et al., 2005; Pedersen et al., 2005; Yee et al., 2006).

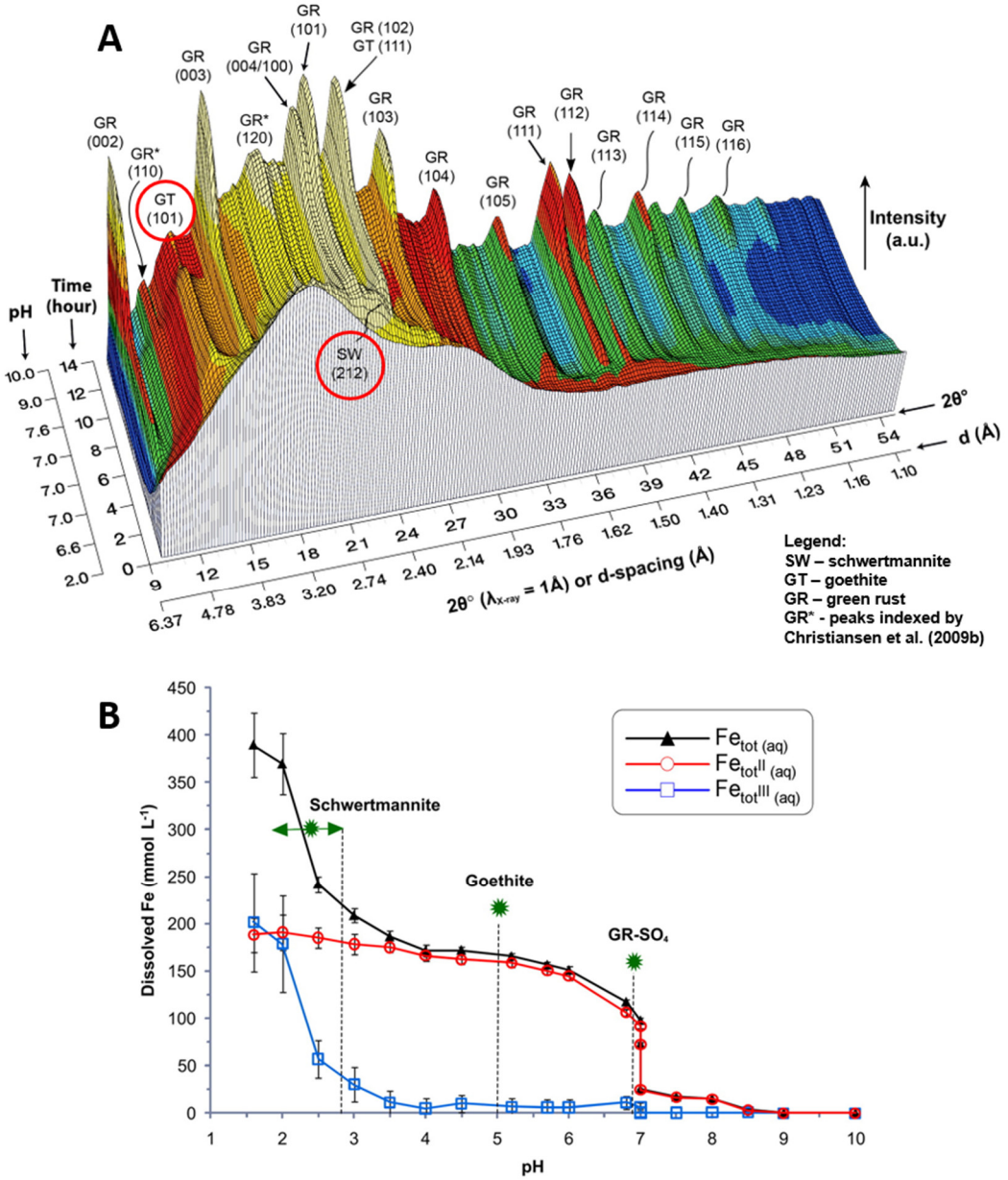

Figure 1.3 (a) 3D plot of time-resolved WAXS patterns collected *in situ* during GR_{SO4} synthesis (Ahmed et al., 2010). GR_{SO4} diffraction peaks match previously indexed peaks (Bernal et al., 1959; Christiansen et al., 2009b; Simon et al., 2003). (b) Changes in dissolved $[Fe(II)_{tot}]$, $[Fe(III)_{tot}]$ and $[Fe_{tot}]$ from an offline experiment, carried out in an equivalent manner to the online WAXS experiment. The pH at which schwertmannite, goethite and GR_{SO4} started to form are marked with a star (*). Reproduced from Ahmed et al. (2010).

As the titration continued to pH values between 6.8 to 7 (Figure 1.3a), the intensity of the goethite (101) peak decreased, concomitant with the appearance of distinct sharp diffraction peaks corresponding to GR_{SO4} (Bernal et al., 1959; Christiansen et al., 2009b; Simon et al., 2003). GR_{SO4} was found to be the sole solid iron phase as the pH increased to 8.5. Analysis of the crystallite size showed that the particle growth of GR_{SO4} from pH 8.5 was predominantly along the *a*-*b* crystallographic plane. Based on these results, it is

unlikely that GR_{SO4} forms through the surface reaction of brucite-like clusters of Fe^{II} complexes and the interface of goethite. Instead, Fe^{2+} ions hydrolyze onto the surface of goethite at pH <7 and initiate electron-transfer reactions with the structural Fe^{3+} in goethite (Handler et al., 2009; Hiemstra and van Riemsdijk, 2007). Further increase in alkalinity (pH >7) will prevent the Fe^{2+} from being released back into the solution. As a result, it is incorporated into the iron oxyhydroxide structure to generate mixed Fe^{II}-Fe^{III} brucite-like octahedral sheets stabilized by adsorbed SO_4^{2-}. As Fe^{2+} continues to hydrolyze, the sheets become the "nuclei" that will grow to form the GR_{SO4} crystal structure.

1.3.3 Fe^{2+}-catalyzed transformation from metastable Fe(III) phases

Another pathway through which GR can be formed under anoxic and circum-neutral pH conditions is through the Fe^{2+}-catalyzed transformation of metastable Fe(III)-bearing nanophases (e.g., ferrihydrite, schwertmannite, jarosite). For example, ferrihydrite, a ubiquitous nanoparticulate ferric oxyhydroxide commonly found in natural environments, is thermodynamically metastable and usually transforms to more crystalline iron (oxyhydr)oxides (Cornell and Schwertmann, 2003). This transformation, however, is very slow under ambient conditions, usually taking several months to years (Das et al., 2011; Schwertmann et al., 2004).

In the presence of dissolved aqueous Fe^{2+}, the ferrihydrite transformation is however sped up and catalyzed, reaching completion in mere minutes to hours (Hansel et al., 2005; Liu et al., 2007; Yang et al., 2010). Under anoxic, circum-neutral pH conditions, ferrihydrite readily transforms to either lepidocrocite or goethite in the presence of aqueous Fe^{2+} (Boland et al., 2014; Hansel et al., 2005), a transformation initiated by the adsorption of Fe^{2+} onto the hydroxide surface. The mineral-bound Fe(II) is then oxidized to surface Fe(III), electrically-conducted through the solid and finally ejected as aqueous Fe^{2+} (Gorski and Scherer, 2011; Handler et al., 2014; Hiemstra and van Riemsdijk, 2007; Zarzycki et al., 2015). This electron conduction process creates a "reactive" surface site where ferrihydrite recrystallizes to goethite or lepidocrocite. If the aqueous Fe(II) is in excess compared to Fe(III) (oxyhydr)oxide (i.e., $[Fe^{2+}]_{aq}/[Fe(III)]_{solid} \geq 2$), goethite or lepidocrocite further transforms to GR (Ahmed et al., 2010; Wang et al., 2014), and the GR formation mechanism is, in that case, the same as discussed in Section 1.3.2. Over longer time periods, GR can in turn transform via dissolution precipitation to magnetite, a more thermodynamically stable mixed-valent Fe oxide (Sumoondur et al., 2008). The proposed GR formation and transformation pathway is shown in Figure 1.4.

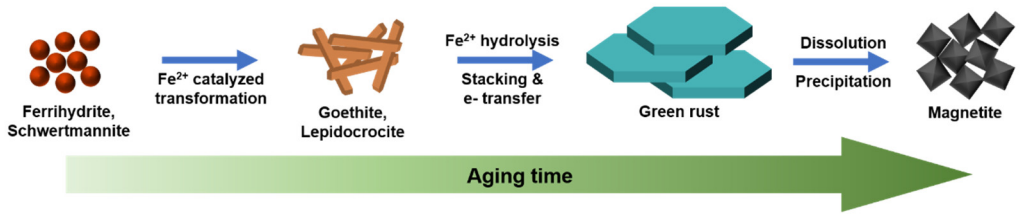

Figure 1.4 Proposed pathway of the formation of GR from metastable Fe phases and its subsequent transformation to magnetite.

1.4 Interaction between GR and Metals and Metalloids

The reactive and redox properties of GR have, over the past 20 years, made GR gain renewed scientific interest because of its importance in biogeochemical cycling of nutrients and contaminants, and its potential for environmental remediation. It can sequester a wide-range of pollutants in contaminated soils and groundwater, including both organic contaminants and metal(loid)s. This is indeed a consequence of its nanoparticulate nature, high redox reactivity, near-neutral PZC and high surface area (Usman et al., 2018). As a redox-active phase, GR can interact with metals and metalloids via the following mechanisms: (i) adsorption, (ii) reduction or (iii) structural incorporation (i.e., intercalation, cationic substitution) (Figure 1.5).

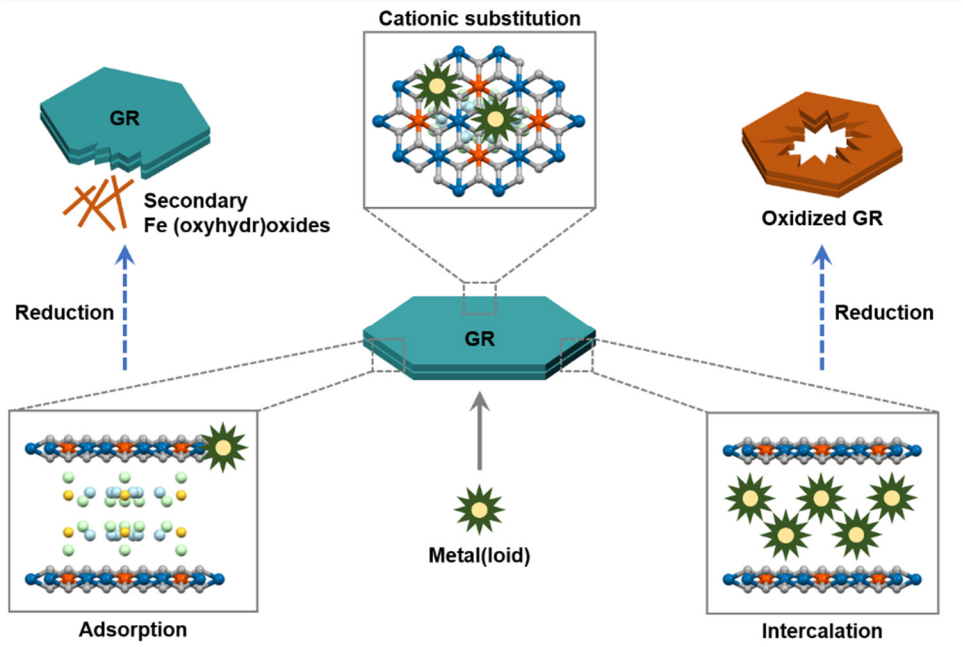

Figure 1.5 Schematic representation of the interaction of GR with metal(loid)s: (i) adsorption; (ii) reduction and (iii) structural incorporation (i.e., intercalation, cationic substitution).

Below, I outlined research related to some of the important studies about GR interactions with specific metals and metalloids. It is not intended to be an exhaustive review of the matter, and I discuss the main issue related to interactions described in Figure 1.5 by using several examples for each interaction type.

1.4.1 Adsorption

Arsenic

Arsenic in groundwater is predominantly found in its inorganic forms, arsenite [As(III)] and arsenate [As(V)], the former being most toxic and more mobile (Vaughan, 2006). Studies on the removal of As(III) and As(V) using GR_{SO4} and GR_{CO3} have shown that both species do not undergo reduction. Instead, As(III) and As(V) species form bidentate binuclear (^2C) inner-sphere surface complexes with the edge of GR layers, as a result of the double corner sharing between the arsenic complexes and the apices of the adjacent FeO_6 octahedra

(Jönsson and Sherman, 2008; Randall et al., 2001). As(V) exhibited higher removal efficiencies ($> 94\%$) compared to As(III) (16%), and remained adsorbed in the solid even after its oxidation to lepidocrocite (Lin and Puls, 2003; Randall et al., 2001).

Wang et al. (2010) further investigated the nature of surface complexation of arsenic species on GR_{Cl} using As K-edge extended X-ray absorption fine structure (EXAFS). In the case of As(V), EXAFS-derived As-Fe distances at 3.35 and 3.49 Å suggested the presence of both bidentate binuclear (^2C) and monodentate mononuclear (^1V) inner-sphere complexes, respectively, on the (110) surface of GR crystals. At lower surface coverages, the number of neighbors measured at 3.34 Å was below 2, which is lower than the expected value for ^2C surface complexes. This was attributed to the possible presence of outer-sphere complexes; however, no significant basal Bragg peak shift was observed to indicate an intercalation of AsO_4^{3-} in the GR interlayer. For As(III), the formation of ^2C and ^1V surface complexes on the GR surface was implied by the EXAFS-derived distances of 3.37 and 3.50 Å. Interestingly, an As-As distance at 3.32 Å was observed, which was attributed to the formation of As(III) dimers on the GR surface. This As-As correlation was also observed during the anaerobic reduction of As(V)-sorbed lepidocrocite by *Shewanella putrefaciens* ATTCC 12099, wherein As(III) was found as oligomeric species on the surface of the biogenic GR_{CO3} (Ona-Nguema et al., 2009). The measured atomic distance for the As-As pairs (3.32 Å) indicated that binding of $As^{III}_2O_5^{4-}$ dimer to the edge of GR_{Cl} layers happened by sharing corners with the FeO_6 octahedra. This limits adsorption of As(III) to the edges since reactive single-coordinated and double-coordinated OH^- species only occur on the (110) surfaces forming the crystal edges.

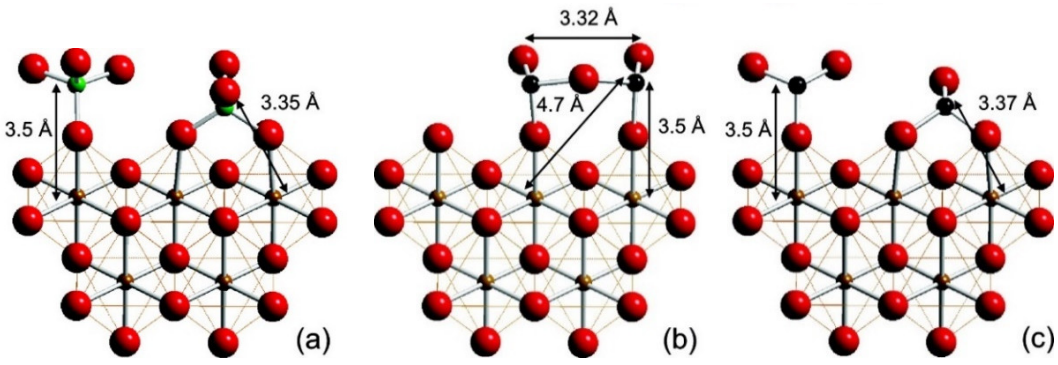

Figure 1.6 Surface complexation of arsenic species on the surface of GR_{Cl} displayed along the (001) plane. (a) The bidentate binuclear (^2C) and monodentate mononuclear (^1V) inner-sphere surface complexation of As^VO_4 tetrahedra on the FeO_6 octahedra at the edges of GR_{SO4}. (b) Proposed $As^{III}_2O_5$ dimer binding to the FeO_6 octahedra *via* monodentate corner-sharing complex. (c) The bidentate binuclear (^{2}C) and monodentate mononuclear (^1V) inner-sphere surface complexation of $As^{III}O_3$ pyramids on the FeO_6 octahedra at the edges of GR_{SO4}. Reproduced from Wang et al. (2010).

Antimony

Often closely associated with As as sulfides or oxides, very little information is known on the geochemical behavior of antimony (Sb) in groundwaters. Antimony is usually found as Sb(III) and Sb(V) in the environment with the former being more toxic, a behavior similar to As (Filella et al., 2002). Mitsunobu et al. (2009) studied the interaction between GR_{SO4} and Sb(V) using a combination of X-ray diffraction and absorption spectroscopic

approaches. Although they did not determine the maximum adsorption capacity, the highest amount of Sb(V) adsorbed on the GR surface was found to be around 6.09 mg g^{-1} which decreased at initial concentrations higher than 1 mM [Sb]. Based on the EXAFS data, the adsorbed Sb(V) was interpreted to form an inner-sphere complex with the $Fe^{III}O_6$ octahedra at the edge of GR layers. In addition, a slight decrease in the d_{00l} spacing was observed at higher concentrations of Sb(V) which suggests interlayer anion exchange. However, the amount of Sb(V) adsorbed as an outer-sphere surface complex was less significant than the adsorbed inner-sphere complexes. Interestingly, they also showed that the adsorption of Sb(V) onto the GR particle edges resulted in the stabilization of GR. This stabilization effect has been previously observed for GR when dissolved phosphate and silica were adsorbed, as their presence inhibited the oxidative transformation of GR (Bocher et al., 2004; Kwon et al., 2007).

1.4.2 Reduction

Chromium

Due to its importance in several metallurgical and chemical industries, hexavalent chromium is one of the most common toxic contaminants in groundwater. As such, several studies on the application of GR for groundwater remediation have focused on the reduction of Cr(VI), and they especially tried to elucidate the kinetics of this reaction. For example, Loyaux-Lawniczak et al. (2000; 1999) examined Cr(VI) reduction using GR_{SO4} and showed that, instead of being reduced into its metal (oxyhydr)oxide, chromium was reduced to Cr(III) and was incorporated into the structure of the mineral end-product. The Cr-substituted mineral end-product was identified as a poorly ordered Cr(III)-Fe(III) oxyhydroxide, similar to 2-line ferrihydrite.

Later on, Williams and Scherer (2001) studied the kinetics of Cr(VI) reduction using GR_{CO3}. At near-neutral pH, GR_{CO3} (0.25 g L^{-1}) exhibited fast reduction rates for chromium (k_{obs} = 3.3 x 10^{-3} s^{-1}) with a half-life of four minutes. This is significantly faster compared to reduction rates for GR observed for chlorinated organic contaminants (Erbs et al., 1999; Hansen et al., 1996). The mineral end-product was also Cr-substituted ferrihydrite and the formation of such poorly-ordered Cr(III)-Fe(III) oxyhydroxide was attributed to the reduction of Cr^{VI} by structural Fe(II) in GR after CrO_4 exchanges with the interlayer CO_3^{2-} or adsorbs onto the GR surface. The so-produced phase is unstable and, subsequently, the Fe hydroxide sheets rearrange leading to the most disordered form of ferric hydroxide. Legrand et al. (2004) also studied the kinetics of Cr(VI) reduction using GR_{CO3}. However, their results indicated a heterogeneous reaction mechanism involving the formation of fully ferric GR where successive Cr(III) monolayers precipitate on the surface. This mechanism was inferred to result in surface passivation and thus a further increased rate limitation. They suggested that this explains the initial rapid reduction rates, followed by decreased removal of Cr(VI) as Cr(III) monolayers accumulate on the surface. The formation of such a monolayer also suggests that the reaction with GR_{CO3} took place via a GR-CrO_4 surface complex intermediate.

Using a combination of atomic force microscopy, X-ray diffraction and transmission electron microscopy (TEM), Skovbjerg et al. (2006) defined the molecular-scale mechanisms

involving Cr(VI) reduction in the presence of GR_{SO4}. Their highly complementary results suggested the following mechanism: CrO_4^- ions diffuse into the GR interlayer and are subsequently reduced to Cr(III) by structural Fe^{2+}. This leads to the blocking of the interlayer region from further ion exchange by the sparingly soluble Cr(III) solid. Meanwhile, Cr(VI) is simultaneously reduced at the GR solid-solution interface. The fast reduction rate at the interface is facilitated by electron transfer from the GR center to its surface. Subsequently, less stable GR zones dissolve and amorphous Cr(III)-Fe(III) solids precipitate, which can transform topotactically to Cr-substituted goethite, instead of ferrihydrite, through the *in situ* deprotonation of GR, followed by a slight rearrangement of crystal structure.

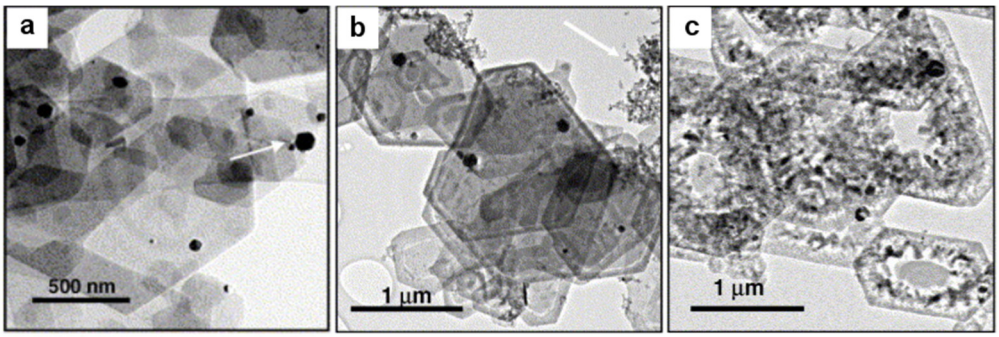

Figure 1.7 Bright-field TEM images of GR_{SO4} before and after reduction of Cr(VI). (a) Typical hexagonal plate-like morphology of GR. Small black crystals of magnetite indicated by the arrow. (b-c) GR_{SO4} after the reduction of Cr(VI). (b) Formation of dark rims indicating the exchange of CrO_4^- ions in the interlayer after 10 minutes. Precipitated amorphous Cr, Fe solid indicated by the arrow. (c) Growth of goethite crystals from the rims of GR crystal which have mostly dissolved. Modified from Skovbjerg et al. (2006).

Uranium

In addition to industrial sources, radioactive metal wastes also contribute to contamination of groundwaters. Such wastes are usually stored in deep underground facilities that are protected with synthetic and natural barriers to prevent leakage. Several studies have investigated the potential of GR for the reduction of radioactive metals such as uranium. O'Loughlin et al. (2003) examined the reduction of U(VI) using GR_{SO4}. Complete reduction (>99.9%) of U(VI) to U(IV) was achieved after 24 hours, accompanied by the partial oxidation of GR to magnetite. The reduction of U(VI) led to the formation of discreet uraninite ($U^{IV}O_2$) nanoparticles (ca. 2-9 nm), which were deposited on the edges of the GR crystals. Latta et al. (2015) investigated the influence of the intercalated anion in the GR structure to its interaction with U(VI) species in a buffered aqueous media. GR_{SO4} and GR_{Cl} demonstrated excellent removal efficiencies of >99% and 92%, respectively. However, only 34% to 63% of U(VI) was reduced to U(IV) using GR_{CO3}. Moreover, UO_2 nanoparticles were not formed after the reduction of U(VI). Instead, U(IV) monomers were observed either as surface complexes or as adsorbed species. This suggested that the use of a highly buffered batch solution may have affected the speciation of U(VI) and the reactivity of GR, which in turn led to the formation of non-uraninite monomeric-type species.

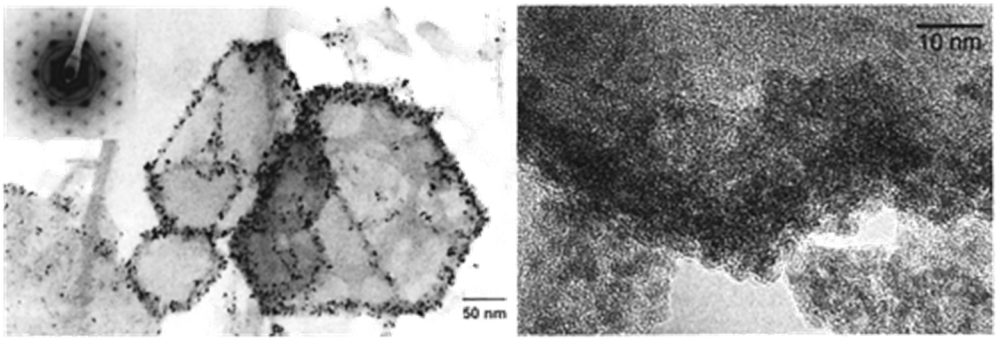

Figure 1.8 TEM images of U(VI)-reacted GR_{SO4}: (Left) Dark-field image of GR particles showing the UO_2 nanoparticles on the edges of the GR_{SO4} crystal. Inset shows the electron diffraction pattern of the hexagonal *c*-axis spot pattern of single crystal GR_{SO4} and the polycrystalline ring pattern of UO_2. (Right) HRTEM image of the highly crystalline UO_2 nanoparticles. Reproduced from O'Loughlin et al. (2003).

1.4.3 Structural incorporation of inorganic ions

Cationic substitution

Cationic substitution in minerals is a common. In iron minerals, a wide variety of cations can be exchanged, particularly with the structural Fe(II) or Fe(III) in iron (oxyhydr)oxides. This process, however, has been less studied with respect to the GR structure. Early studies with GR_{Cl} and GR_{CO3} were done by substituting structural Fe^{2+} with Ni^{2+} (Refait et al., 1990), while later studies focused on the partial substitution of Fe^{2+} with Mg^{2+} and Zn^{2+} in GR_{CO3} (Ahmed et al., 2008; Refait et al., 2002) and the substitution of Fe^{3+} with Al^{3+} in GR_{SO4} (Ruby et al., 2008). Since elements such as Mg^{2+} and Al^{3+} are major elements in soils and groundwater, understanding how metal cation substitution driven changes in GR composition affect its stability and reactivity is crucial to predicting the behavior of both GR and the substituted metals in natural environments. In addition, the ability of GR to immobilize toxic trace metals, such as Zn^{2+} or Ni^{2+} by structural incorporation, highlights the potential of GR for subsurface remediation techniques.

Yet, the mechanisms involving cationic substitution are still poorly understood and it is likely dependent on the nature of the cation and the synthesized pathway for the GR host. For example, the substitution of Ni^{2+} leads to an increase in the GR lattice parameter a value, as Ni^{2+} is preferentially exchanged with structural Fe(II) but also, to a minor extent, with Fe(III). In the case of Al-substituted GRs, Al induces lattice strain which can significantly change the GR properties. Among these, crystallinity seems to decrease with increasing Al(III) content while particle size of Al-GR_{SO4} becomes smaller (Ruby et al., 2008), which in turn can affect their redox activity and surface properties of the GR host.

Interlayer incorporation

The intercalation of selenate [Se(VI)] in the GR interlayer has been reported (Refait et al., 2000), with the resulting GR_{SeO4} being isomorphous to GR_{SO4}, with an interlayer spacing of 10.9 Å characteristic of GR2 types. The above research showed that the interaction between GR and Se(VI) does not just lead to reduction but that intercalation of SeO_4^{2-} occurs prior to reduction, which ultimately facilitates electron transport. Once GR_{SeO4} is formed it itself continues to reducie any remaining Se(VI) in the bulk solution to Se(IV),

which is adsorbed on the GR hydroxide surface. Meanwhile, the intercalated SeO_4^{2-} ions do not undergo reduction due to the stability of the chemical bonds and diffusive barrier in the interlayer. A similar mechanism was observed through analyses of the isotope fractionation of Se during its interaction with GR_{SO4} (Johnson and Bullen, 2003). For GR_{SO4}, the interaction of Se(VI) with GR_{SO4} follows a diffusion and then reduction step. Due to the high amounts of exchangeable anions in GR_{SO4}, majority of the Se(VI) becomes incorporated into the interlayer, at a rate which is mass transfer limited and is relative to its reduction rate. Interestingly, there was an early observed ~10-h lag during reduction of Se(VI) using GR_{SO4}. Since it is unlikely that the lag was caused by diffusion-related phenomena in the interlayer sites, the lag in Se(VI) reduction may have been caused by a change in the resulting GR structure. It was suggested that oxidative damage led to GR crystal defects, which increased the active surface sites for reduction afterwards.

1.5 Background and Scope of the Study

There are still many open questions related to the interactions between the various GR phases and toxic metals and metalloids. Although GR phases have been investigated for the reduction of toxic metals (e.g., Cr, U), the adsorptive properties of GR (Section 1.4.1) and their importance in the treatment of contaminated groundwaters are far less studied.

Among the toxic metals and metalloids discussed in Section 1.4, elevated levels of arsenic (As) in soils and groundwater remain to be a significant threat globally due to its widespread occurrence and distribution, toxicity and mobility. Groundwater contamination from natural (i.e., geogenic) As sources is prevalent worldwide, especially in Bangladesh, India, Hungary and Argentina (Figure 1.9) where hundreds of millions of people are affected (Smedley and Kinniburgh, 2002). The prime source for this geogenic As is derived from the weathering and/or transformation of As-containing primary mineral phases (Amini et al., 2008; Mukherjee et al., 2006). Meanwhile, major anthropogenic sources of As include metal ore smelting, coal combustion, glass manufacturing, catalyst production, semiconductor manufacturing, and the use of arsenical fungicides, herbicides and insecticides (Bissen and Frimmel, 2003; Mandal and Suzuki, 2002; Matschullat, 2000). Both these sources can enter groundwaters that are used for drinking water or agricultural purposes where they then enter the human food chain (Vaughan, 2006).

In natural aquatic environments, dissolved As is commonly present as inorganic arsenite ($H_3As^{III}O_3$) and arsenate ($H_3As^{V}O_4$), the former being the more toxic and mobile form (Hughes, 2002; Sharma and Sohn, 2009). Based on their acid dissociation constants, they are present as aqueous neutral species $H_3As^{III}O_3$ for As(III) in moderate reducing conditions and $H_2AsO_4^-$ and $HAsO_4^{2-}$ for As(V) in well-oxidized environments (Ferguson and Gavis, 1972; Inskeep et al., 2002). However, the redox transformation kinetics of As(III) and As(V) is relatively slow, leading to the occurrence of both species being present in oxic and anoxic environments (Masscheleyn et al., 1991).

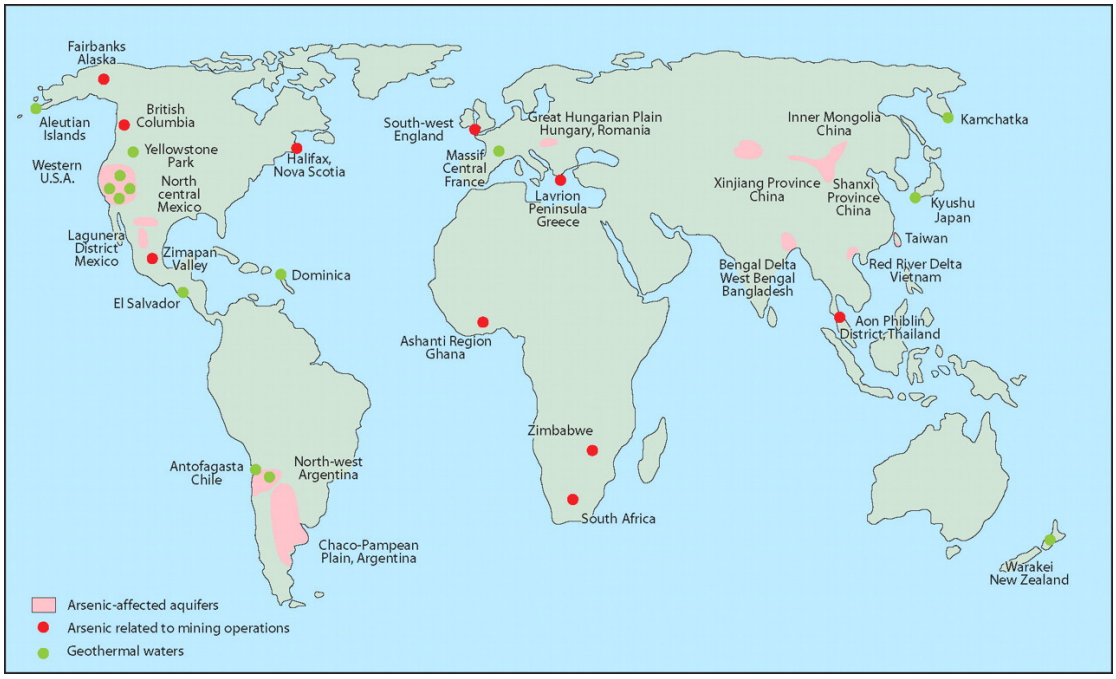

Figure 1.9 World map showing areas of known relatively high concentrations of arsenic, generally associated with hydrothermal areas (hot springs), mining activities or contaminated aquifers. Reproduced from Vaughan (2006) (modified figure from Smedley and Kinniburgh (2002)).

In contaminated soils and groundwaters, the adsorption of As onto redox-active mineral substrates such as GR may be crucial in controlling its fate and mobility. Thus, a fundamental understanding of the interaction between GR and As species is needed in order to determine the critical factors that influence As sequestration and/or release, as well as its transport in subsurface environments. However, due to the oxygen-sensitive nature of GR, there is still a poor understanding on how GR forms in natural environments and there is still a lack of quantitative data on its potential role in the cycling of As. In addition, most of these processes are far too complex to study solely in natural systems because of multiple existing feedback interactions between abiotic and biotic factors. To help alleviate this dearth of understanding of natural processes, reactions at mineral-water interfaces are often examined using experimental studies which are based on simplified analogue model systems wherein key environmental parameters can be constrained under simulated natural conditions. Such an approach allows experimental studies wherein reactions that control As speciation and distribution in natural environments to be investigated using verifiable hypotheses and controlled variables.

Earlier studies on the interaction between GR and As species using batch adsorption experiments reported oxidation of As(III) to the more toxic and mobile As(V) under anoxic conditions (Su and Wilkin, 2005). However, succeeding studies using X-ray absorption spectroscopy (XAS) have shown that GR cannot oxidize As(III) or reduce As(V) (Jönsson and Sherman, 2008; Wang et al., 2010). EXAFS data from these studies have also been essential in determining the local bonding environment of adsorbed As on GR phases (see example above in Section 1.4.1). However, most of these studies so far only focused on bulk XAS analyses, and no complementary techniques that could provide direct and high spatial resolution have been employed yet to validate these molecular-scale interactions inferred

to occur at the GR surfaces and interfaces. More importantly, previous studies examine GR-As interactions primarily in simple analogue systems and no data on more "complex" matrices relevant to natural systems (e.g., varying pH, presence of co-existing ions) are available so far. In addition, while there are prior studies documenting the formation and transformation pathways of pure GR (see examples in Section 1.3.2 and 1.3.3), another aspect of GR-As interactions that is still not understood is the influence of toxic As species on its formation kinetics or transformation. This has not yet been quantified, although this information is critically needed for modeling As cycling in subsurface settings. Thus, there is a clear need to elucidate the mechanism and pathways of GR formation and transformation in the presence of As and under relevant subsurface redox conditions.

1.6 Research Objectives

The objectives of this PhD were therefore designed with the above knowledge gaps in mind. The main aim is to elucidate the interaction between green rust (GR) and arsenic (As) species during GR formation and transformation under anoxic conditions, and to quantify how these transformation reactions affect the toxicity and mobility of As species in contaminated subsurface environments. The research objectives can be divided into five main areas.

1. To quantify the effects of variable geochemical conditions on As removal by GR
2. To gain a better understanding on the binding mechanism of As to GR surfaces
3. To determine the impact of As on GR formation and its transformation to secondary iron (oxyhydr)oxide phases
4. To elucidate the fate of As species during GR formation and its transformation
5. To evaluate the long-term stability and reactivity of As-GR in contaminated subsurface environments and to elucidate its impact on As mobility

1.7 Thesis Overview

This thesis consists of seven chapters, including this introductory chapter. The contents are summarized below.

Chapter 2 reports the effects of (scanning) transmission electron microscopy (S/TEM) analysis on the morphology, structure, chemical composition and oxidation state of GR.

Chapter 3 reports detailed As adsorption properties of GR under relevant subsurface geochemical conditions, revealing critical environmental parameters which control As removal efficiency.

Chapter 4 reports new insights into the interaction between As species and GR using molecular-scale characterization techniques, which allowed both the direct visualization and the quantitative elucidation of As(III) and As(V) binding mechanism on reactive GR surfaces.

Chapter 5 reports the work to evaluate the pathways leading to the formation of GR through the abiotic transformation As(V)-bearing ferrihydrite under circum-neutral pH

conditions; this study focuses on the effect of dissolved Fe^{2+} on the extent of GR formation and the changes in aqueous behavior and oxidation state of immobilized As.

Chapter 6 reports long-term batch experiments on the stability and reactivity of GR when reacted with a natural groundwater collected from an As-impacted site in Copenhagen, Denmark.

Chapter 7 contains the most important conclusions made throughout this work, as well as suggestions for future work.

Chapter 2

Beam-induced oxidation of green rust sulfate monitored by monochromated STEM-EELS

This chapter is adapted from:

Freeman, H.M.; **Perez, J.P.H.**; Hondow, N.; Benning, L.G.B.; Brown, A.P. (2019). Beam-induced oxidation of mixed-valent Fe (oxyhydr)oxides (green rust) monitored by STEM-EELS. *Micron*, 122, 46-52.

Available at: https://doi.org/10.1016/j.micron.2019.02.002

Abstract

Analytical transmission electron microscopy (TEM) is often used to investigate morphologies, crystal structures, chemical compositions and oxidation states of highly reactive mixed-valent mineral phases. Of prime interest, due to its potential role in toxic metal remediation, is green rust sulfate (GR_{SO4}) an Fe^{II}-Fe^{III} layered double hydroxide. In this study, we quantified the effects that TEM analysis has on GR_{SO4} in order to ensure the measured material properties are a result of synthesis and reaction kinetics, and not due to sample preparation and analysis technique. To do this, we compared two sample preparation techniques (anoxic drop-cast with drying, and frozen-hydrated cryogenic) and exposed samples to the electron beam for several minutes, acquiring fluence series between ca. 40 e^- $Å^{-2}$ and 10,000 e^- $Å^{-2}$. TEM imaging and electron diffraction showed that the hexagonal plate-like morphology and crystal structure of GR_{SO4} were largely unaffected by sample preparation and analysis technique. However, quantitative analysis of a series of monochromated Fe $L_{3,2}$-edge electron energy loss spectra (EELS) showed that electron irradiation induces oxidation. We measured an Fe(II)/Fe(III) ratio of 1.94 (as expected for GR_{SO4}) at 50 $e^-Å^{-2}$. However, above this fluence, the ratio logarithmically decreased and dropped to ca. 0.5 after 1000 $e^-Å^{-2}$. This trend was approximately the same for both sample preparation techniques implying that it is the beam alone which causes valence state changes, and not exposure to oxygen during transfer into the TEM or the vacuum of the TEM column. Ultimately this work demonstrates that GR valence can be quantified by EELS provided that the sample is not over exposed to electrons. This also opens the possibility of quantifying the effect of redox-sensitive toxic metals (e.g., As, Cr, Se) on Fe oxidation state in GR phases (relevant to the treatment of contaminated soils and water) with a higher spatial resolution than other techniques (e.g., Mössbauer spectroscopy).

2.1 Introduction

Green rust (GR) materials are redox-active, mixed-valent Fe(II)-Fe(III) layered double hydroxides which exhibit high surfaces area and can intercalate inorganic or organic species into the plate-like structure due to their anion exchange capacity (Goh et al., 2008; Newman and Jones, 1998; Usman et al., 2018). GR phases can be easily engineered for a wide-range of applications such as catalysis, electrochemistry, and environmental remediation (Bhave and Shejwalkar, 2018; Chen et al., 2018; Huang et al., 2019; Zhang et al., 2018). In particular, they are promising reactants for groundwater remediation where they have been shown to remove toxic metal contaminants from water by adsorption (Jönsson and Sherman, 2008; Mitsunobu et al., 2009), reduction (O'Loughlin et al., 2003; Perez et al., 2019a; Skovbjerg et al., 2006; Thomas et al., 2018), interlayer intercalation (Refait et al., 2000) and substitution of structural Fe (Ahmed et al., 2008; Refait et al., 1990).

Green rust sulfate ($[NaFe^{II}_6Fe^{III}_3(OH)_{18}(SO_4)_2{\cdot}12H_2O]$ hereafter referred to as GR_{SO4}) is composed of positively charged brucite-like iron hydroxide layers that alternate with interlayers containing sulfate and water molecules (following Christiansen et al. (2009b)). The structural Fe(II)/Fe(III) ratio of 2 has been determined by Mössbauer spectroscopy, chemical analysis, and X-ray diffraction (Christiansen et al., 2009b; Génin et al., 1996; Hansen et al., 1994; Perez et al., 2019a; Refait et al., 1990; Refait et al., 1999). When using GR for groundwater remediation, it is important the mineral remains stable and does not transform to other iron (oxyhydr)oxides, which can be less effective substrates for the sequestration of toxic metals. For example, partial oxidation or transformation of GR phases to other iron (oxyhydr)oxides can lessen its ability to reduce redox-sensitive metals (e.g. Cr, Se, U) or its adsorption uptake (e.g. As) (Jönsson and Sherman, 2008; O'Loughlin et al., 2003; Perez et al., 2019a; Skovbjerg et al., 2006; Thomas et al., 2018).

One way to check the stability of GR over time is to monitor the Fe(II)/Fe(III) ratio following interaction with metals. As such, it is essential that applied characterization techniques can quantitatively evaluate any changes in oxidation state resulting from environmental reactions and are not a result of the characterization technique itself. Analytical transmission electron microscopy (TEM) provides information at high spatial resolution regarding the morphology, crystal structure, chemical composition and oxidation state of a specimen. To date, many TEM studies of GR have used conventional sample preparation techniques (drop-cast and dried) under anoxic conditions (Ahmed et al., 2010; Bach et al., 2014; Géhin et al., 2002; Mann et al., 1989; Perez et al., 2019a; Skovbjerg et al., 2006; Thomas et al., 2018). Such methods involve aqueous sample dilution, drop-casting onto a TEM grid and drying with alcohol in an anaerobic chamber to minimize the risk of oxidation. The dried grid thus contains a well dispersed sample that is subsequently exposed to air for rapid transfer into the TEM. Much of the literature regarding TEM of GR has so far assumed that both sample preparation and the TEM environment do not significantly affect the specimen. In some studies (particularly Johnson et al. (2015)), these factors are taken into account, such as the short term air exposure during sample transfer to the TEM and electron beam-induced "nanoscale restructuring", where low dose operating conditions were used (Johnson et al., 2015). Here, we further explore these factors in relation to the stability of the oxidation state by measuring electron energy loss spectra (EELS) at the

valence sensitive Fe $L_{3,2}$-edge following both conventional (anoxic drop-cast and dried) and cryogenic (cryo; frozen hydrated suspension) sample preparation for a range of controlled electron fluences.

Avoiding exposure of GR to oxygen prior to TEM analysis and to vacuum dehydration during TEM analysis can be achieved by retaining the mineral in a thin layer of vitreous ice; the suspension must be wetted, blotted and plunge frozen into liquid ethane for cryo transfer into the TEM. This method results in the GR plates being dispersed in a thin layer of electron transparent, vitreous ice. Cryo-TEM has been successfully used to investigate the formation of magnetite (Fe_3O_4) from a ferrihydrite precursor, which can often proceed via GR as a transient phase, a process that had previously only been quantified by time resolved X-ray diffraction (Dey et al., 2015; Michel et al., 2010; Sumoondur et al., 2008). The cryo-TEM sample preparation used by Dey et al. (2015) was required to capture and monitor the morphological changes of the gel-like ferrihydrite precursor phase at various points during the transformation reaction.

Assessing a specimen's sensitivity to electron irradiation can be achieved by collecting an electron fluence series whereby data are repeatedly acquired over the same area, starting at the lowest achievable fluence (this may be images, diffraction patterns or spectra). A critical fluence can then be determined when the property being measured changes by a characteristic value (e.g., $1/e^-$). Previous TEM studies of Fe-bearing minerals have used EELS to show that electron irradiation can induce changes in the oxidation state of structural Fe (Garvie et al., 2004; Pan et al., 2010). In the work of Garvie et al. (2004), a threshold fluence of 10^4 $e^-Å^{-2}$ (for a 100 kV beam) was determined for the iron silicate mineral cronstedtite ($Fe^{II}_2Fe^{III}(SiFe^{III}O_5)(OH)_4$). It was found that beyond this fluence, the electron beam-induced loss of structural H in the specimen was likely to be significant enough to cause oxidation, as measured by an increasing Fe(III) contribution to the EELS Fe $L_{3,2}$-edge. It was also demonstrated that thinner specimens (<400 Å) were more susceptible to beam-induced alterations. Conversely, 200 kV EELS analysis at the Fe L_3-edge by Pan et al. (2010) showed a reduction in Fe(III) content following electron irradiation of various Fe-bearing phases (e.g., iron phosphate dihydrate, ferrihydrite, hemosiderin and ferritin). They proposed that the dominant damage mechanism was radiolysis induced loss of structural O, OH and H_2O, resulting in both Fe coordination and oxidation state changes. In addition, the hydrated samples were found to be more beam sensitive than cronstedtite (reported by Garvie et al. (2004)), potentially due to increased levels of H_2O associated with these minerals increasing the efficiency of radiolysis.

The work reported here used analytical (S)TEM including imaging, selected area electron diffraction (SAED) and monochromated EELS to monitor changes in morphology, crystal structure and Fe(II)/Fe(III) ratio of GR_{SO4} plates that were prepared through two different TEM sample preparation techniques: (i) drop-cast onto TEM grids and dried (in anoxic atmosphere, with rapid air transfer to the TEM) and (ii) frozen hydrated suspensions cryo-transferred and cryo-analyzed. This allowed us to isolate the factors which we hypothesized might contribute to a change in oxidation state: (i) exposure to oxygen during TEM transfer of anoxic drop-cast and dried samples (potentially sufficient to oxidize the sample); (ii) exposure to the vacuum in the microscope column (potentially sufficient to cause loss of interlayer water molecules and associated sulfate groups in the A,

B planes which may lead to a change in the interlayer charge balance, increasing Fe(III) content (Simon et al., 2003)); and (iii) exposure to electron irradiation (potentially sufficient to either induce a loss of structural H and oxidize the specimen (Garvie et al., 2004), or induce radiolysis and reduce the specimen (Pan et al., 2010)).

In this work, we revisit similar Fe $L_{3,2}$-edge analysis methods to those used by Pan et al. (2010), but with the improved energy resolution of a monochromated electron source and additional, absolute edge energy measurement by dual EELS acquisition (Gubbens et al., 2010). In addition, we demonstrate the need for low fluence EELS in order to measure representative Fe(II)/Fe(III) ratios for GR_{SO4} at a higher spatial and energy resolution than previously reported techniques (Génin et al., 1996; Hansen et al., 1994; Perez et al., 2019a; Refait et al., 1990; Refait et al., 1999).

2.2 Experimental Section

GR with interlayer sulfate was synthesized in aqueous suspension in an anaerobic chamber (97% N_2, 3% H_2, Coy Laboratory Products, Inc.) at room temperature using a modified co-precipitation method (Géhin et al., 2002; Perez et al., 2019a). We ensured the supernatant used in the sample preparation steps did not contain excess Fe^{2+} from the initial synthesis, as this would have added to the EELS signal. To achieve this, the fresh GR_{SO4} slurry was rinsed inside the anaerobic chamber with de-oxygenated deionized water by centrifugation and re-dispersion until the Fe^{2+} concentration in the supernatant was below 2 mM (as measured by inductively coupled plasma optical emission spectrometry (ICP-OES)). All drop-cast TEM sample preparation was performed in the anaerobic chamber using diluted suspensions in de-oxygenated water. These diluted suspensions were drop cast onto holey amorphous carbon Cu grids (Agar Scientific Ltd.), dehydrated with a drop of ethanol, and allowed to dry within the anaerobic chamber. Samples were transferred to the TEM in a grid box wrapped in parafilm, loaded into a double tilt FEI TEM holder and inserted into the TEM; the grid was exposed to air for approximately 60 s. In all cases, data was collected from clean GR plates; those that were considered free of contamination and/or visible stray iron (oxyhydr)oxide minerals of different valence ratios.

Cryo-TEM sample preparation used non-diluted suspensions. Approximately 3.5 µL was dispensed by micro pipette onto a lacey amorphous carbon-coated Cu grid which was blotted and plunge frozen into liquid ethane by an FEI Vitrobot© markIV (at blot force 6). The undiluted suspension was exposed to air at 100% humidity for less than 5 s before plunge freezing. The frozen sample was then cryo-transferred into the TEM using a Gatan 914 holder with the temperature maintained below -165 °C.

For both sample preparation techniques, an FEI Titan^3 Themis G2 S/TEM operating at 300 kV was used with an FEI Super-X energy dispersive X-ray (EDX) system, a monochromator with an energy spread of ca. 0.35 eV, a Gatan Quantum 965 ER energy filter for dual EELS (which allows for core-loss edges to be calibrated against the simultaneously acquired low loss spectrum) and a Gatan OneView CCD. A ca. 1.4 Å probe was formed for STEM with an estimated convergence semi-angle of ca. 10 mrad (limited by the second smallest C3 aperture) and a probe current of up to 300 pA when the monochromator is excited (as measured by the dose metre on the flu cam, calibrated using

a Faraday cup). Fluence was controlled in STEM by limiting the dwell time (to as low as 0.8 µs) and pixel size and collecting EEL spectra while scanning (i.e. by continuously scanning at a magnification that approximately matches the GR plate size to the field of view). In STEM-EELS mode, a 2.5 mm entrance aperture provided a collection semi-angle of 21 mrad. Spectra were collected for 30 s and then background subtracted (power law) in 'Gatan Microscopy Suite' software (version 3.0.1), with t/λ values generally < 0.35 for anoxic drop-cast specimens. SAED patterns were obtained using an aperture with an effective diameter of 200 nm at the imaging plane. The electron fluence per frame (F) was calculated using the equation below:

$$\boldsymbol{F\left(e^{-}\text{Å}^{-2}\right) = \frac{I \times t}{e^{-} \times d_s^2}}$$

where t is the dwell time, I is the probe current, e^- is the charge of an electron (1.602×10^{-19} C) and d_s is the pixel size.

2.3 Results and Discussion

TEM images showed hexagonal GR_{SO4} plates between 0.1-1 µm in width, and ca. 20-50 nm thick (as measured from the low loss EEL spectrum) (Figure 2.1). The general morphology of the GR plates did not vary between sample preparation technique, and the SAED patterns provide evidence that the hexagonal crystal structure was maintained. EDX spectroscopy (not shown) confirmed the presence of Fe, S and O as expected. Diffraction patterns from both sample preparation techniques show reflections for the (300) and (330) family of spots which are at 2.77 Å and 1.60 Å respectively and close in value to those reported by powder XRD (2.75 Å and 1.59 Å) (Christiansen et al., 2009b). Diffraction patterns collected at higher fluences (>10,000 e^-Å^{-2}) showed slightly lower in-plane atomic spacing values for the same type of pattern, of 2.59 Å (300) and 1.51 Å (330), a reduction of 6% for both planes.

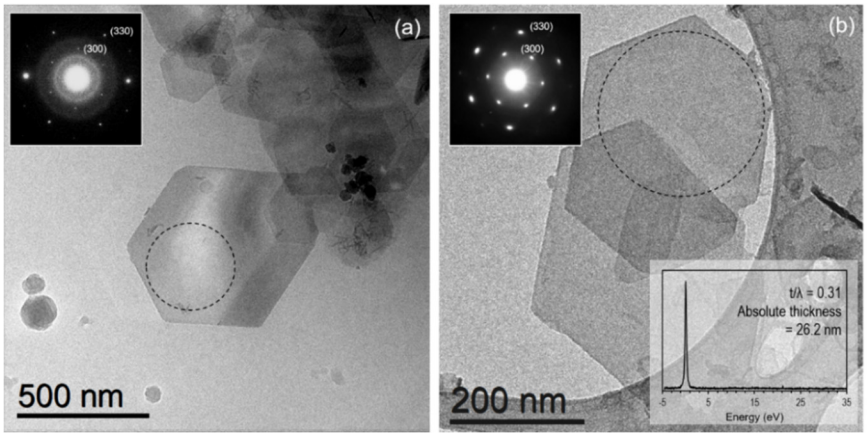

Figure 2.1 TEM images and SAED pattern (inset) of GR_{SO4} (a) cryo frozen-hydrated sample preparation (b) anoxic drop-cast dry sample preparation. Note the additional amorphous ring in (a) from the scattering of electrons by ice. Dashed lines represent areas associated with the SAED pattern, and the low loss EELS spectrum for calculating specimen thickness is shown in (b).

To measure the effect of electron irradiation on oxidation state, EELS Fe $L_{3,2}$-edges were collected at known fluences and compared to reference spectra; Figure 2.2a shows

representative low fluence spectra from both sample preparation techniques and the reference materials. To date, techniques to quantify the Fe(II)/Fe(III) ratio in Fe bearing materials via EELS have used $L_{3,2}$-edges for the white line intensity ratio method (Cavé et al., 2006; van Aken and Liebscher, 2002), have included the O-K edge (Brown et al., 2001), or used reference spectra for non-linear least-squares (NLLS) fitting (Pan et al., 2009; Pan et al., 2010; Pan et al., 2006). With recent advances in EELS energy resolution via the addition of a monochromator or the use of a cold FEG (Paterson and Krivanek, 1990), it is now possible to clearly resolve two sub-peaks within the Fe L_3 edge; the lower energy sub-peak at ca. 709.0 eV can be attributed to a predominant Fe^{2+} contribution and the higher energy sub-peak at ca. 710.8 eV to a Fe^{3+} contribution (Brown et al., 2017). Being able to resolve these two sub-peaks enables a more accurate multiple linear least-square (MLLS) fitting, and a ratio of Fe(II)/Fe(III) to be calculated. In this work, we fitted the acquired Fe $L_{3,2}$-edges against reference spectra of hedenbergite (100% octahedral Fe^{2+}) and hematite (100% octahedral Fe^{3+}) using the 'Gatan Microscopy Suite' software (Figure 2.2b). The higher energy sub-peak of the core loss spectra were energy calibrated to 710.8 eV, background subtracted and area normalized in the energy range 702-730 eV before being fitted. The spectra of the reference material were collected with the same TEM and the same monochromator excitation but under the TEM collection conditions described in Brown et al. (2017).

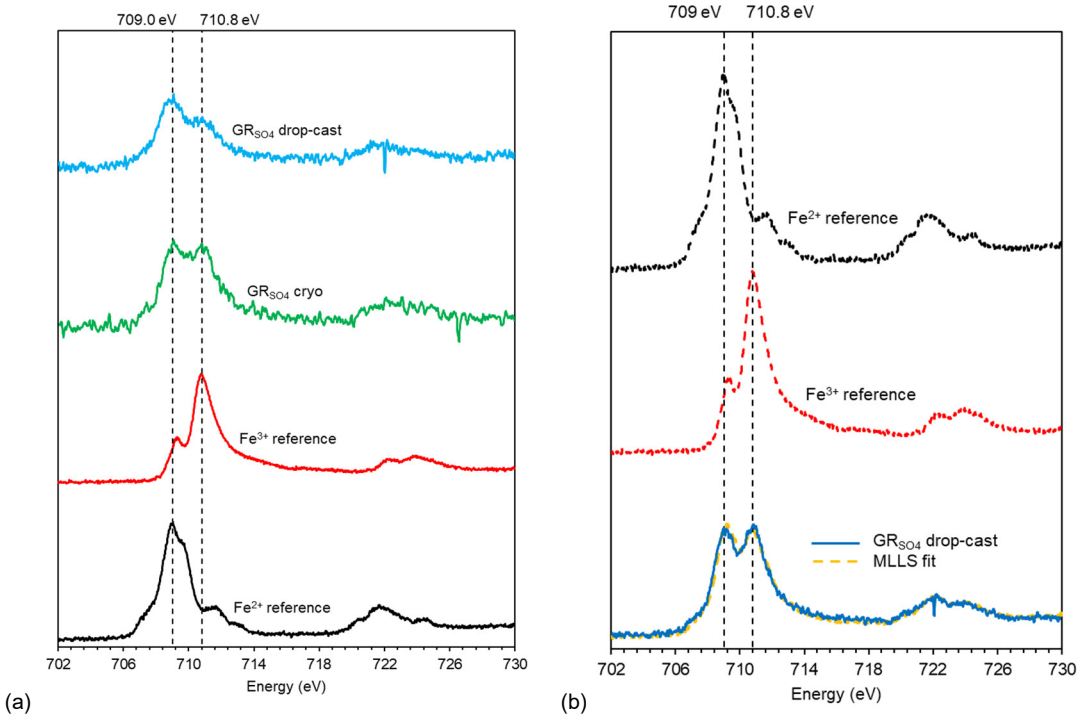

Figure 2.2 (a) Background subtracted Fe $L_{3,2}$-edge spectra for Fe^{2+} (black) and Fe^{3+} (red), plus lowest fluence GR_{SO4} Fe $L_{3,2}$-edge spectra from cryo (frozen hydrated suspension) sample preparation (green) at 255 $e^{-}Å^{-2}$ and GR_{SO4} from anoxic drop-cast sample preparation (blue) at 50 $e^{-}Å^{-2}$. Due to a low signal to noise ratio in the cryo spectrum (due to high levels of scattering in ice), a 5-point moving average has been applied to the data. (b) Example MLLS fitting of a background subtracted and area normalised Fe $L_{3,2}$-edge spectrum of anoxic drop-cast and dried GR_{SO4} (blue) fitted against a reference spectrum MLLS fit (yellow) from haematite (Fe^{3+}) (red) and hedenbergite (Fe^{2+}) (black). The estimated Fe(II)/Fe(III) ratio is 0.89 $\pm$ 0.09. Received fluence for GR_{SO4} spectrum is 730 $e^{-}Å^{-2}$.

Applying this fitting procedure to spectral series from both sample preparation techniques provides quantitative evidence for the *in-situ* oxidation of GR_{SO4} during exposure to the electron beam. Stacked spectral series (along with the MLLS fits) for both the cryo-frozen hydrated GR_{SO4} and the anoxic drop-cast sample preparation methods are shown in Figure 2.3, and the measured change in Fe(II)/Fe(III) ratio with electron fluence is plotted in Figure 2.4 (for both sample preparation techniques). Figure 2.3 shows how the relative intensities of the two sub-peaks in the Fe-L_3 edge change with electron fluence; the intensity of the 709.0 eV peak quickly diminishes for both datasets. By ca. 1000 $e^{-}Å^{-2}$ the relative intensities of the two peaks tend not to change further for the cryo data whereas the 709.0 eV peak continues to reduce for the drop-cast data. Following quantification of these peaks with the MLLS fitting procedure, it is possible to calculate that for the cryo data the Fe(II)/Fe(III) ratio stabilizes at around 0.5 after ca. 1000 $e^{-}Å^{-2}$, and for the drop-cast data it stabilizes at 0.15 after 6000 $e^{-}Å^{-2}$ (Figure 2.4). The initial Fe(II)/Fe(III) ratio was higher for drop-cast samples (ca. 1.93) as it was possible to collect spectra with sufficient signal to noise ratios at a lower fluence due to the lack of vitreous-ice.

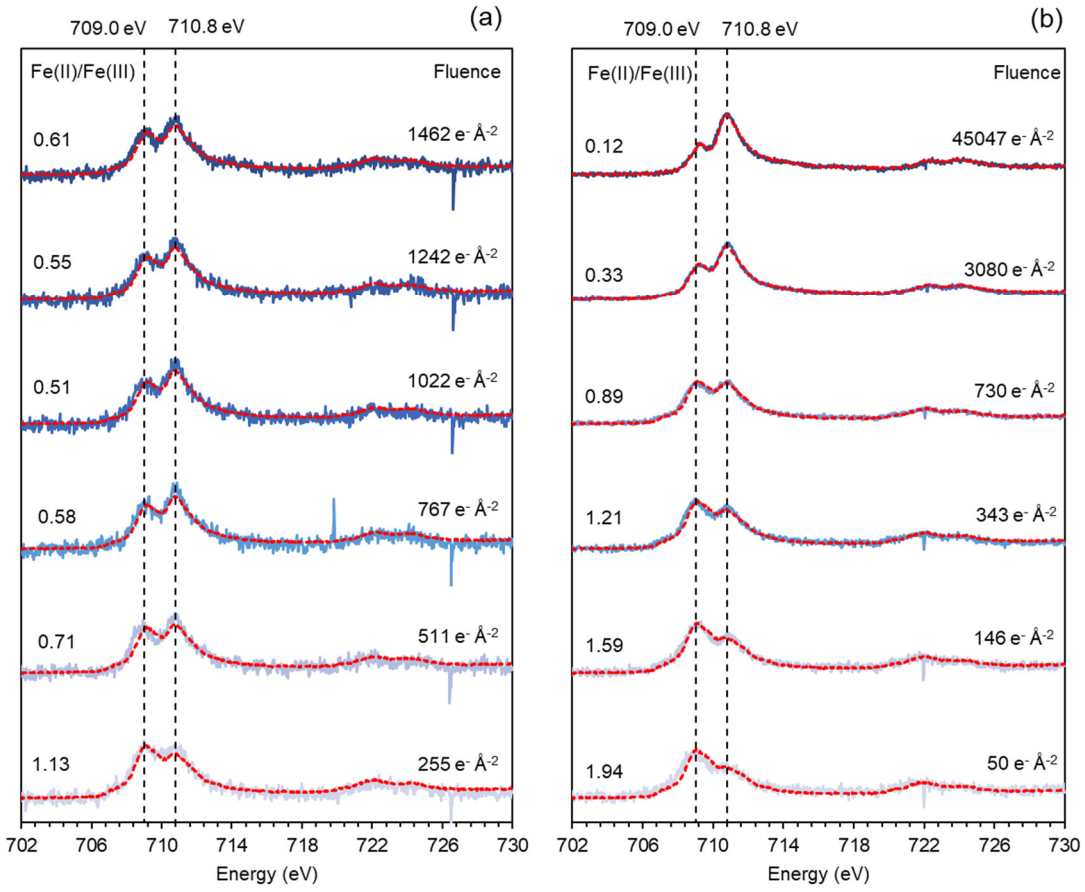

Figure 2.3 Stacked core loss EEL spectra (blue) showing changing shape of the Fe L_3 edge during electron irradiation in cryo-TEM (a) and anoxic drop-cast (b) sample preparation methods. The MLLS fits are shown in red. The corresponding Fe(II)/Fe(III) ratios are shown on the left hand side, and the associated electron fluence shown on the right hand side.

Trendlines have been added to the data series in Figure 2.4 to measure the gradient (i.e., the rate of oxidation with electron fluence) and to extrapolate the data to the theoretical Fe(II)/Fe(III) ratio (2 for GR_{SO4}). These extrapolated trendlines for both sample preparation techniques essentially meet at Fe(II)/Fe(III) = 2 as might be expected. This allowed us to determine a threshold fluence of 40 ± 5 $e^{-}Å^{-2}$, beyond which electron beam-induced oxidation occurred with either preparation method.

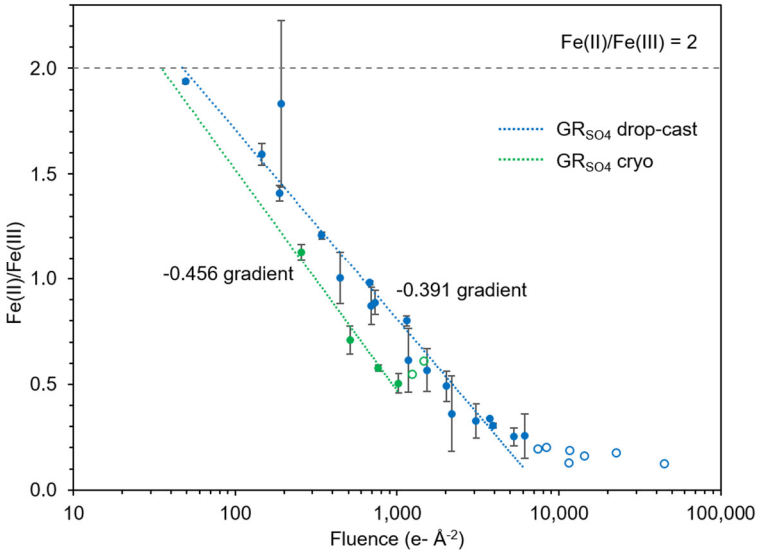

Figure 2.4 Change in Fe(II)/Fe(III) content with electron fluence for conventional (anoxic drop-cast) sample preparation (blue) and cryo (frozen-hydrated) sample preparation (green). Logarithmic (dashed) trendlines have been extrapolated to Fe(II)/Fe(III)=2, terminating where data points begin to plateau at higher fluences (non-filled data points). The error in fluence is not shown here however we estimated a maximum variation of 12% due to a change in probe current during in-situ measurements. The error in Fe(II)/Fe(III) ratio was based on deviation from the least–squares trendline. Note that the cryo data is from a single GR plate whereas the plotted anoxic drop-cast data is from three different GR plates; this is due to the fact that in cryo-TEM it is more challenging to find a suitable sample area (i.e. enough specimen in a thin region of vitreous ice).

We can now address the key factors which we initially hypothesized might contribute to a change in oxidation state of GR when measured by (S)TEM-EELS. We have demonstrated that exposure to oxygen during TEM transfer of the anoxic drop-cast and dried samples was not sufficient to cause discernible oxidation because the measured Fe(II)/Fe(III) ratio (as high as 1.93 ± 0.09) was retained at low fluences. In addition, we can exclude the hypothesis that exposure to the vacuum in the electron column was sufficient to cause loss of interlayer water molecules and associated sulphate groups which may have led to a charge imbalance, as we have observed similar trends from both anoxic drop-cast samples and cryo-frozen-hydrated samples, the latter of which is not directly exposed to the vacuum. The third hypothesis regarding electron irradiation induced valence changes has also been addressed and we showed that there is a threshold fluence of 40 ± 5 $e^{-}Å^{-2}$ for the onset of GR oxidation for either specimen preparation route. Unfortunately, collecting EELS spectra at such a low fluence is challenging and we have compromised spatial resolution to approximately the size of an individual GR plate in order to approach these values. Above this fluence threshold, we saw progressive oxidation of the GR for anoxic drop-cast samples, where exposure to electron irradiation was sufficient to induce

the deprotonation of apical OH^- ions in the Fe octahedra (i.e. loss of structural H as reported by Garvie et al. (2004) for mixed-valent Fe-bearing silicates). This charge imbalance within the Fe hydroxide layer is compensated through the oxidation of structural Fe(II) to Fe(III). The *in situ* oxidation of GR phases through deprotonation of the apical OH^- ions has been previously studied in GR carbonate by Mössbauer spectroscopy and X-ray photoelectron spectroscopy (Génin et al., 2006; Mullet et al., 2008; Ruby et al., 2008; Ruby et al., 2006). For cryo-frozen-hydrated samples, this also seems to be the case for relatively low fluences (i.e. $<$1000 $e^-Å^{-2}$), however beyond this point, the Fe(II)/Fe(III) content apparently stabilizes at ca. 0.5. At fluence values above 1000 $e^-Å^{-2}$ the vitreous ice (encasing the GR plates) has been shown to melt and or sublime (Ilett et al., 2019) and certainly by this stage diffusion limited damage due to the beam-induced radiolysis of the ice will become significant so that H_2O loss and reduction (as reported by Pan et al. (2010)) might operate alongside the ongoing beam-induced oxidation (as reported by Garvie et al. (2004) and documented in this study). The fact that the Fe(II)/Fe(III) ratio plateaus at a value of ca. 0.5 suggests that together, these mechanisms have a balanced effect which does not alter the net oxidation state (Figure 2.4).

The subtle differences between in-plane atomic spacings measured by SAED for low ($<$1000 $e^-Å^{-2}$) and high ($>$10,000 $e^-Å^{-2}$) fluences could also be evidence for beam-induced oxidation. Calculations by Shannon (1976)) showed that the ionic radius of Fe depends on its oxidation state; 0.780 Å in Fe(II) and 0.645 Å in Fe(III), which corresponds to a 17 % reduction in ionic radius following complete oxidation (Shannon, 1976). While dehydration of the sample (in the TEM high vacuum column) would also decrease d-spacing, this reduction would only occur between iron hydroxide layers and not in-plane. The measured fluence dependent reduction of in-plane atomic spacings in this study might therefore be attributed to the partial oxidation of Fe although further investigation, collecting a fluence series of SAED patterns, would be needed to confirm this. If confirmed, this method could be used to monitor GR oxidation on TEMs which do not have the ability to acquire high resolution monochromated EELS.

Ultimately, with this work we have demonstrated that only by using low fluences can one obtain truly representative Fe(II)/Fe(III) ratios in GR when analyzing these redox sensitive materials by STEM-EELS. Spatial resolution has been compromised to achieve this however smart acquisition techniques such as that reported by Sader et al. (2010) may be used to improve spatial resolution and assess valence variation across an individual GR plate (Sader et al., 2010). This technique relies on averaging spectra from the same position within multiple plates to increase EELS signal and improve spatial resolution while minimizing net fluence.

2.4 Conclusion

We have studied GR_{SO4} using analytical TEM, in particular monochromated STEM-EELS, to demonstrate the sensitivity of Fe(II) content under electron irradiation. Using anoxic drop-casting and cryogenic sample preparation techniques allowed us to isolate the cause of oxidation to structural H loss induced by the electron beam, and not exposure to oxygen during sample transfer into the TEM or to the vacuum within the TEM column. MLLS

fitting to reference Fe L_3-edge EEL spectra enabled the Fe(II)/Fe(III) ratio to be determined which was plotted against electron fluence to identify the beam induced oxidation rate. The lowest fluence Fe(II)/Fe(III) ratio was 1.93 ± 0.09 at 40 $e^{-}Å^{-2}$ and compares favorably with the expected value of 2. Beam induced *in situ* oxidation of GR_{SO4} was quantified for both sample preparation techniques allowing us to calculate a threshold fluence at which oxidation begins (40 $e^{-}Å^{-2}$), and at which the Fe(II)/Fe(III) ratio stabilizes at 0.15 for anoxic drop-cast samples (6000 $e^{-}Å^{-2}$) and 0.5 for cryo-samples (at ca. 1000 $e^{-}Å^{-2}$). Based on these results we have developed a robust analytical TEM methodology for the investigation of highly redox sensitive materials like GR. This low fluence approach can be applied to measure the spatial variation in Fe(II) content across a single GR plate and to measure change in Fe(II) content of GR reacted with toxic metals such as As, Cr and Se (relevant to the remediation of polluted water).

Chapter 3

Green rust sulfate as an effective adsorbent for arsenic removal from water

This chapter is adapted from:

Perez, J.P.H.; Freeman, H.M.; Schuessler, J.A.; Benning, L.G. (2019). The interfacial reactivity of arsenic species with green rust sulfate (GR_{SO4}). *Science of the Total Environment*, 648, 1161-1170.

Available at: https://doi.org/10.1016/j.scitotenv.2018.08.163

Abstract

Arsenic (As) contamination in groundwater is a significant health and environmental concern worldwide because of its wide distribution and toxicity. The fate and mobility of As is greatly influenced by its interaction with redox-active mineral phases, among which green rust (GR), an Fe^{II}-Fe^{III} layered double hydroxide mineral, plays a crucial role. However, the controlling parameters of As uptake by GR are not yet fully understood. To fill this gap, we determined the interfacial reactions between GR sulfate (GR_{SO4}) and aqueous inorganic As(III) and As(V) through batch adsorption experiments, under environmentally-relevant groundwater conditions. Our data showed that, under anoxic conditions, GR_{SO4} is a stable and effective mineral adsorbent for the removal of As(III) and As(V). At an initial concentration of 10 mg L^{-1}, As(III) removal was higher at alkaline pH conditions (~ 95% removal at pH 9) while As(V) was more efficiently removed at near-neutral conditions (> 99% at pH 7). The calculated maximum As adsorption capacities on GR_{SO4} were 160 mg g^{-1} (pH 8-9) for As(III) and 105 mg g^{-1} (pH 7) for As(V). The presence of other common groundwater ions such as Mg^{2+} and PO_4^{3-} reduces the efficiency of As removal, especially at high ionic strengths. Long-term batch adsorption experiments (up to 90 days) revealed that As-interacted GR_{SO4} remained stable, with no mineral transformation or release of adsorbed As species. Overall, our work shows that GR_{SO4} is one of the most effective As adsorbents among iron (oxyhydr)oxide phases.

3.1 Introduction

Elevated levels of dissolved arsenic (As) in ground- and drinking waters remain a significant global environmental and public health concern because of the wide-spread occurrence and distribution, as well as toxicity and mobility of As in the environment (Vaughan, 2006). In groundwaters, As is commonly present as inorganic oxyanions arsenite ($H_3As^{III}O_3$) and arsenate ($H_3As^{V}O_4$), with the former being the more toxic form (Hughes, 2002; Sharma and Sohn, 2009). Based on their acid dissociation constants, As(III) forms the neutral species $H_3As^{III}O_3$ at moderately reducing conditions ($pK_{a1,2,3}$ = 9.23, 12.13, 13.40) while As(V) is present as $H_2As^{V}O_4^-$ and $HAs^{V}O_4^{2-}$ ($pK_{a1,2,3}$ = 2.20, 6.97, 11.53) in oxidized environments (Ferguson and Gavis, 1972; Inskeep et al., 2002). However, it is important to note that the relatively slow redox transformation kinetics allows both As(III) and As(V) to persist under both anoxic and oxic conditions (Masscheleyn et al., 1991).

Green rust (GR) minerals are redox-active phases, which belong to the family of Fe^{II}-Fe^{III} layered-double hydroxides (LDHs). Their ability to treat or remove toxic metals from groundwater has been investigated (Usman et al., 2018), yet the fundamental adsorption properties or uptake capacities of metals on GR phases have still not been quantified. The high potential of GR as a material for groundwater remediation stems from its structural and redox properties. GR is composed of positively charged brucite-like layers of octahedrally coordinated Fe^{II}-Fe^{III} hydroxides that alternate with negatively charged interlayers of anions and water molecules, as well as monovalent cations (Christiansen et al., 2009b). These brucite-like layers and interlayer regions are held together by hydrogen bonding and electrostatic forces. GR is typically represented by the general formula, $[Fe^{II}_{(1-x)}Fe^{III}_x(OH)_2]^{x+}[(x/n)\ A^{n-}\cdot mH_2O]^{x-}$, where A^{n-} is the intercalated anion such as Cl^-, CO_3^{2-} and SO_4^{2-}, and x is the molar fraction of Fe^{III}, $[Fe^{III}]/[Fe_{total}]$ (Géhin et al., 2002). These properties allow GR to remove toxic metal contaminants by adsorption (Jönsson and Sherman, 2008; Mitsunobu et al., 2009), reduction (Christiansen et al., 2011; O'Loughlin et al., 2003; Skovbjerg et al., 2006), interlayer intercalation (Refait et al., 2000), and substitution of structural Fe in the octahedral sheets (Ahmed et al., 2008; Refait et al., 1990).

Considering the worldwide health implications of As-contaminated ground- and drinking waters (World Health Organization, 2017), it is paramount that we understand the removal efficiency of As through interactions with various mineral substrates. There is an imminent challenge regarding the development, testing and validating the usefulness of adequate mineral phases that have high metal-specific uptake capacities, strong binding affinities and excellent stabilities. Adsorption-based technologies are promising groundwater clean-up strategies because of their facile implementation, relative cost-effectiveness and high removal efficiency (Leus et al., 2017). However, to optimize the efficiency of subsurface remediation strategies, the interactions between inorganic As species and the surfaces of redox-active minerals such as GR must be quantified in detail.

Su and Wilkin (2005) examined the interaction of As(III) and As(V) with synthetic green rust carbonate (GR_{CO3}) and monitored the changes in the aqueous phase. Their results showed that As(V) removal rates using GR_{CO3} were higher compared to As(III) due to the higher affinity of iron (oxyhydr)oxides for As(V) than the more toxic As(III). The

mechanism of adsorption of As species onto GR mineral phases (e.g., GR_{Cl}, GR_{CO3}, GR_{SO4}) has also been investigated previously using X-ray absorption spectroscopy (XAS) (Jönsson and Sherman, 2008; Randall et al., 2001; Wang et al., 2010). In these studies, As(III) and As(V) were found to both form bidentate binuclear (^2C) and monodentate mononuclear (^1V) inner-sphere complexes on the FeO_6 octahedra at the edges of the GR crystal. However, the fundamental adsorption parameters (e.g., effects of pH, adsorbent loading, ionic strength, potentially competing ions), as well as the maximum uptake capacity and critical adsorption kinetics, necessary for understanding interactions between GR and As in groundwaters have never been evaluated in detail.

Herein, we aimed to close this gap through an in-depth investigation on the interfacial interactions between freshly-precipitated green rust sulfate (GR_{SO4}) and aqueous inorganic As species. We evaluated the performance of GR_{SO4} as an effective adsorbent for the removal of arsenite [As(III)] and arsenate [As(V)] by examining adsorption reactions as a function of pH, adsorbent loading, ionic strength, varying initial As concentrations, time and the presence of potentially interfering ions in groundwater. Our results revealed that GR_{SO4} is a highly effective adsorbent for the removal of As species from groundwater.

3.2 Experimental Section

3.2.1 Mineral synthesis and characterization

GR with interlayer sulfate (GR_{SO4}) was synthesized in an anaerobic chamber (97% N_2, 3% H_2, Coy Laboratory Products, Inc.) at room temperature using the co-precipitation method (Géhin et al., 2002). In brief, separate Fe(II) (0.3 M) and Fe(III) (0.1 M) solutions were prepared from reagent grade $(NH_4)_2Fe(SO_4)_2{\cdot}6H_2O$ and $Fe_2(SO_4)_3$ salts (VWR) and deoxygenated Milli-Q water (ca. 18.2 MΩ cm^{-1}). GR synthesis was initiated by mixing the Fe(III) and Fe(II) solutions (ca. pH 2) under constant stirring at 350 rpm. Subsequently, a 0.3 M NaOH solution was slowly titrated into the mixed Fe^{II}-Fe^{III} solution until the pH reached 8. Base addition resulted in the precipitation of a dark blue-green suspension, which was stirred and aged further for one hour. The suspension was then washed with O_2-free Milli-Q water to remove excess solutes. The yield of the washed GR_{SO4} slurry was determined based on the difference between the total Fe concentration of an aliquot of the suspension dissolved in 0.3 M HNO_3 and the dissolved Fe concentration in the supernatant after filtration through a 0.2-µm syringe filter. The Fe ion concentration was analyzed by inductively coupled plasma optical emission spectrometry (ICP-OES). Each batch of GR_{SO4} slurry (ca. 8.2 g L^{-1}) was prepared fresh and kept in the anaerobic chamber adsorption experiments for a maximum of 24 h.

The solid GR_{SO4} samples were analyzed by X-ray powder diffraction (XRD), nitrogen sorption, transmission electron microscopy (TEM), selected area electron diffraction (SAED), energy dispersive X-ray spectroscopy (EDX), electron energy-loss spectroscopy (EELS), high angle annular dark field scanning transmission electron microscopy (HAADF-STEM), X-ray photoelectron spectroscopy (XPS) and Mössbauer spectroscopy to determine their structure, particle sizes, morphologies, surface properties, as well as redox and full chemical composition. Detailed information on all phase characterizations can be found in the Supporting Information (see Section 3.5.1).

3.2.2 Adsorption experiments

All batch adsorption experiments were carried out in triplicate at room temperature inside the anaerobic chamber using headspace crimp vials with the washed GR_{SO4} suspensions (S/L = 4 g L^{-1}) reacted with 10 mg L^{-1} aqueous As(III) or As(V) solutions. The mixed samples were shaken at 250 rpm for 24 h followed by the separation of solids and supernatants by filtration through 0.22-µm syringe filters. The obtained liquid phases were acidified (ca. pH 2 with Merck Suprapur® grade HNO_3) and stored at 4°C until analysis. The elemental composition of the liquid phases was determined following the method described in Schuessler et al. (2016) using an axial ICP-OES Varian 720ES. Full details of all tested parameters [e.g., varying pH (7 to 9), adsorbent loading (solid to solution ratio, S/L 2 to 6 g L^{-1}), ionic strength (IS* 0.5 to 0.005 M), competing ions (Ca^{2+}, Mg^{2+}, PO_4^{3-}) and time (5 min to 90 days)] for the batch adsorption experiments and analytical methods can be found in the Supporting Information (Table S3.1).

3.2.3 Adsorption kinetics and isotherms

Kinetic rates of As adsorption were determined at pH 8 using an initial As concentration of 10 mg L^{-1} and an adsorbent loading of 4 g L^{-1}. The mixtures were shaken for 5 min, 10 min, 15 min, 30 min, 1 h, 2 h, 4 h, 8 h, 16 h and 24 h after which the solids were separated from the supernatant and analysed as described above. Adsorption isotherms were obtained at room temperature at pH 7 and 8-9 using an adsorbent loading of 4 g L^{-1}, initial As concentrations up to 1,000 mg L^{-1} and contact time of 24 h. The obtained equilibrium adsorption data were fitted to the Langmuir and Freundlich isotherm models (Limousin et al., 2007).

3.3 Results and Discussion

3.3.1 Synthesis and characterization of GR_{SO4}

The morphology, size and chemical composition of the synthesized GR_{SO4} particles were characterized by TEM imaging and analytical spectroscopy. The micrographs (Figure 3.1a) of the synthesized material revealed a well-defined hexagonal plate-like morphology typical of GR_{SO4} (Géhin et al., 2002). The diameter of particles varied between 50 and 500 nm while the estimated thickness of the particles calculated by the log-ratio (relative) method (Malis et al., 1988) from the low loss EEL spectra was around 16 to 20 nm. The SAED pattern (Figure 3.1a inset) shows the distinctive hexagonal *c*-axis spot pattern of a single crystal GR_{SO4} (Ahmed et al., 2010). The elemental composition (Table S3.2), which was calculated from the EDX spectra, is comparable to the theoretical values based on the chemical formula, $Fe^{II}_4Fe^{III}_2(OH)_{12}SO_4 \cdot 8H_2O$ (Simon et al., 2003). The mineralogy of the freshly-precipitated material was confirmed through XRD patterns (Figure S3.1) to be pure GR_{SO4} as evidenced through the typical sharp and symmetric basal (00*l*) reflections corresponding to the interlayer distances between the Fe^{II}-Fe^{III} octahedral hydroxide sheets (Simon et al., 2003). No other iron (oxyhydr)oxide phases were identified in the freshly-precipitated GR_{SO4} samples.

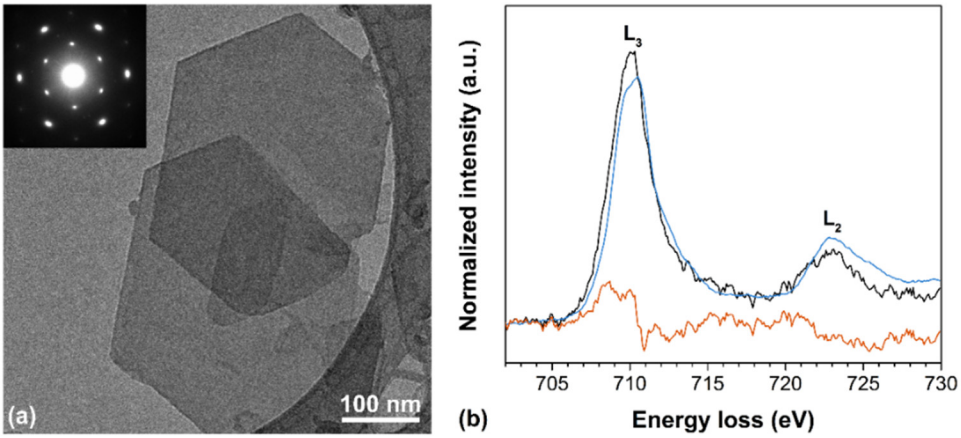

Figure 3.1 (a) TEM image of GR_{SO4} with SAED pattern of a single particle in inset. (b) Fe $L_{2,3}$-edge EEL spectrum of GR_{SO4} sample (black) with a received electron fluence of 50 $e^{-}Å^{-2}$, fitted against a reference spectrum MLLS fit (orange) from hedenbergite (Fe^{2+}, blue) and hematite (Fe^{3+}, red).

The oxidation state of Fe can be determined by the EELS Fe L_3-edge position and shape, where octahedrally-coordinated Fe(III) has a peak energy ca. 1.8 eV higher than octahedrally-coordinated Fe(II) (Brown et al., 2017). Separate peaks attributed to Fe^{2+} (709 eV) and Fe^{3+} (710.8 eV) within the primary L_3 peak are resolvable when EEL spectra are acquired at higher resolution EELS ($<$ 0.3 eV). Using the EELS resolution of the microscope used for this work (0.8 eV), the Fe(II)/Fe(III) ratio was estimated by comparing our experimental spectra to reference spectra collected under the same conditions. Theoretical spectra were calculated by stoichiometrically combining the intensity-normalized spectra of the Fe standards for hedenbergite (octahedrally coordinated Fe^{2+}) and hematite (octahedrally coordinated Fe^{3+}). This resulted in a theoretical spectrum for GR_{SO4} (where Fe(II)/Fe(III) = 2) which allowed for the direct comparison between the Fe L_3 peak shape and position in our sample and the theoretical spectrum (blue line in Figure 3.1b; Figure S3.2). This revealed that the shape of the Fe L_3-edge for the GR_{SO4} sample matched the linear reference fit for a Fe(II)/Fe(III) ratio of 2, with minor differences. This is evidenced by the changes in shape and position of the L_3 peak in the theoretical spectrum as the GR composition becomes more Fe(III)-rich. This is also clearly shown in Figure S3.2, where the theoretical spectra for Fe(II)/Fe(III) ratios from 1 to 0.2, and the residual of each fit are shown. These results suggest that our sample had an Fe(II)/Fe(III) ratio corresponding to 2.

The surface chemistry of the synthesized GR_{SO4} was analyzed by XPS and the wide scan spectrum (Figure S3.3) revealed photoelectron peaks of Fe *2p*, O *1s* and S *2p* at binding energies of 710.7, 531.9 and 168.8 eV, respectively. The Fe $2p_{1/2}$ and $2p_{2/3}$ photoelectron peaks (Figure 3.2a) were observed at 724.0 and 710.7 eV, respectively. The value of the Fe $2p_{2/3}$ peak maxima was shifted to slightly higher binding energy compared to a GR with interlayer carbonate (GR_{CO3}, 709.4 eV), which also has an Fe(II)/Fe(III) ratio of 2.0 (Mullet et al., 2008). This indicates a slightly higher Fe(III) content in our synthesized GR_{SO4}. However, the presence of a characteristic Fe(II) satellite peak at 726.7 eV and a Fe(III) satellite peak at 731.0 eV confirmed the presence of both Fe(II) and Fe(III) in our sample at the desired ratio of 2. The peak shape and positions of the Fe $2p_{1/2}$ and $2p_{2/3}$

photoelectron peaks were also similar to previously reported XPS spectra for GR_{SO4} (Nedel et al., 2010). Furthermore, the relative contributions of the deconvoluted O *1s* peaks at 530.2, 531.8 and 532.6 eV (Figure 3.2b) that were assigned to Fe-O, O-H and adsorbed water (Table S3.3), respectively, were in agreement with values obtained by Mullet et al. (2008). The S *2p* doublet (Figure 3.2c) at 168.8 eV confirmed the presence of SO_4^{2-} in the interlayer region.

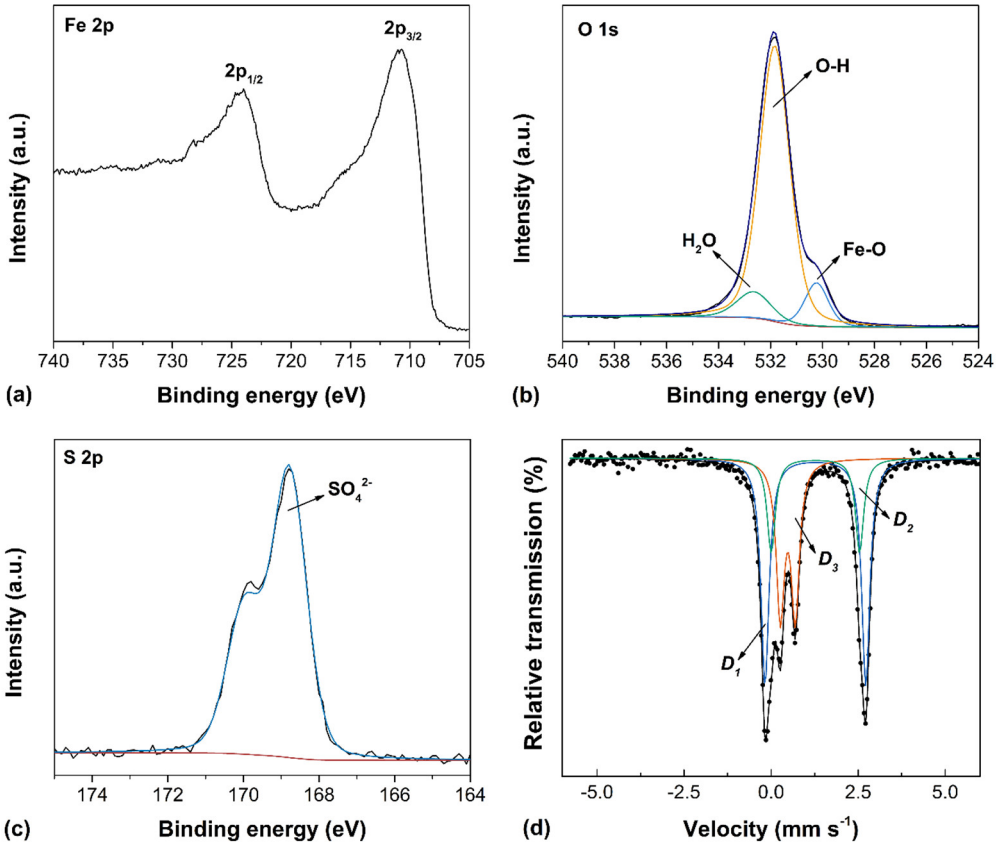

Figure 3.2 (a-c) High resolution XPS spectra of GR_{SO4}: (a) Fe *2p*, (b) O *1s* and (c) S *2p* spectra. (d) ^{57}Fe Mössbauer spectrum of GR_{SO4} recorded at 20 K and fitted with three doublets.

The iron chemistry of the synthesized GR_{SO4} was characterized by Mössbauer spectroscopy which revealed two apparent doublets (Figure S3.4), but with a certain line broadening of the outer doublet and a slight asymmetry of its line shape. An improved fit shown in Figure 3.2d was obtained by using three doublets D_1, D_2 and D_3 (hyperfine parameters, see Table S3.4). In this fit, doublets D_1 and D_2 correspond to high spin Fe(II) cations in the brucite-like octahedral sheets while doublet D_3 corresponds to high spin Fe(III) cations (Géhin et al., 2002). The relative areas of the doublets in the Mössbauer spectrum allowed us to calculate an Fe(II)/Fe(III) ratio in the GR_{SO4} sample of 2.09, which is in agreement with the ratio of 2 from our EELS data (Figure 3.1b, Figure S3.2), as well as literature data (Géhin et al., 2002; Simon et al., 2003). However, it should be noted that the Mössbauer spectra for GR_{SO4} reported in literature are usually fitted with one Fe(II) doublet (Figure S3.4, Table S3.4) instead of two doublets (Figure 3.2d). It is worth noting nevertheless, that in our GR_{SO4}, the two doublets D_1 and D_2 revealed the same isomer shift, but these differed somewhat in their quadrupole splittings (ΔE_Q), thereby suggesting the

presence of two inequivalent Fe(II) sites. The component with the largest ΔE_Q was attributed to Fe(II) ions far away from the anions (Génin and Ruby, 2004b), whereas the presence of a component with smaller ΔE_Q suggested the presence of Fe(II) sites containing anions in their environment. Such components have been previously observed in Mössbauer spectra of GR samples with other interlayer anions like carbonate or chloride but not for sulfate (Génin and Ruby, 2004b).

3.3.2 Influence of environmental parameters on As removal

The effect of pH, adsorbent loading (solid to liquid ratio, S/L), ionic strength (IS*) and the presence of other potentially interfering aqueous groundwater ions were investigated to determine their influence on the adsorption of As species on GR_{SO4}. The removal efficiencies of GR_{SO4} for As(III) and As(V) at an initial concentration of 10 mg L^{-1} and under the above-mentioned varying conditions are shown in Figure 3.3.

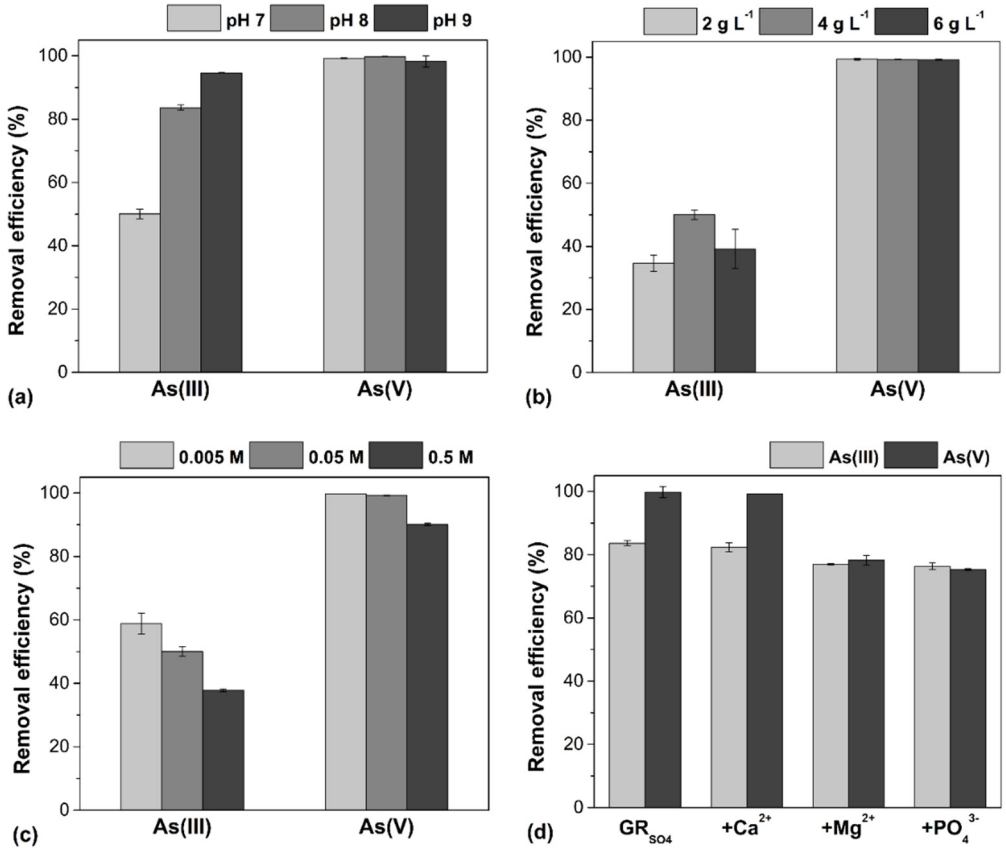

Figure 3.3 Removal of 10 mg L^{-1} As(III) and As(V) upon interaction with GR_{SO4} after 24 h as a function of: (a) pH (S/L = 4 g L^{-1}, IS* = 0.05 M), (b) adsorbent loading, S/L (pH 7, IS* = 0.05 M), (c) ionic strength, IS* (pH 7, S/L = 4 g L^{-1}) and (d) presence of competing groundwater ions (at pH 8 and IS* = 0.05 M): pure GR_{SO4} (no competing ion), Ca^{2+} (100 mg L^{-1}), Mg^{2+} (50 mg L^{-1}) or PO_4^{3-} (10 mg L^{-1}). Error bars represent standard deviations of triplicate experiments (< 5% relative). Note: IS* here is defined as the ionic strength based on a 10x and 100x dilution from the initial 0.5 M IS of the GR_{SO4} suspension (further details, see in Section 3.5.1).

At all pH values tested, the As(V) removal efficiencies (Figure 3.3a) were higher compared to As(III). This is likely because of the higher adsorption affinity of the pentavalent species on iron (oxyhydro)oxide surfaces. No significant differences in As(V)

removal efficiencies between pH 7, 8 and 9 were observed (i.e., within analytical uncertainties < 2%). Although there were no significant differences in removal efficiencies, GR_{SO4} can effectively remove As(V) at a relatively wide range of pH conditions that can be found in contaminated groundwaters (Nickson et al., 2000; Smedley and Kinniburgh, 2002; Zahid et al., 2008). On the contrary, the removal efficiency of As(III) by GR_{SO4} was significantly affected by pH, which is the opposite of what was expected. With pH, As(III) removal efficiency (50.1 ± 1.5% at pH 7) increased by more than 30% at pH 8 (83.7 ± 0.9%) and another 10% increase was measured at pH 9 (94.6 ± 0.1%). Such surface polymerization of As(III) complexes has been previously suggested for GR_{Cl} and GR_{CO3} by XAS analysis (Ona-Nguema et al., 2009; Wang et al., 2010). Usually, the influence of pH on As adsorption by iron (oxy)hydroxides is controlled by two factors: (1) the speciation of the As in solution and (2) the point of zero charge (PZC) of the adsorbent. Over the pH range tested here, As(III) will mostly exist as $H_3AsO_3^0$ and $H_2AsO_3^-$ species while As(V) is present as $H_2AsO_4^-$ and $HAsO_4^{2-}$ species (Jain et al., 1999). For GR_{SO4} with a PZC of 8.3 (Guilbaud et al., 2013), the net surface charges will be negative at pH > 8.3 and positive at pH < 8.3. As a result of electrostatic repulsion caused by similar negative charges, one would expect the removal of both As(III) and As(V) species to decrease as the pH is increased from 8 to 9, which was not observed in our study. Particularly, for As(III), the biggest increase in removal was observed between pH 7 and 8 with a lesser change between 8 and 9 (Figure 3.3a.). Similar trends have been observed for As interacted with GR_{CO3} (Jönsson and Sherman, 2008) and ferrihydrite (Jain et al., 1999; Raven et al., 1998). An increased As(III) adsorption at higher pH can be attributed to the possible formation of multi-nuclear complexes on the surfaces of GR_{SO4}.

With increased adsorbent loading from 2 to 4 g L^{-1}, the removal efficiency of As(III) also increased by ca. 15% from 34.6 ± 2.7 to 50.1 ± 1.5% (Figure 3.3b). This increase was caused by the larger number of active surface sites available for As(III) complexes (Asere et al., 2017). However, with further increase in loading to 6 g L^{-1}, the efficiency decreased to 39.2 ± 6.2%. In the case of As(V), no significant differences (< 0.3% relative) in removal efficiencies were observed among the adsorbent loadings tested (Figure 3.3b).

The removal efficiencies for both As species decreased with increasing ionic strength, IS* (Figure 3.3c). For As(V), this decrease was only about 10% (from > 99.8 to 90.1 ± 0.4%) as ionic strength increased from 0.005 to 0.5 M. On the other hand, this inhibitory effect was more pronounced for As(III) where the removal efficiency decreased from 58.9 ± 3.2% at an ionic strength of 0.005 M to 37.8 ± 0.4% at an ionic strength of 0.5 M, although the overall removal was lower compared to As(V). The decrease in As removal at higher IS* can be caused by the decrease in available surface sites of GR_{SO4}. This results from potential aggregation of GR_{SO4} particles due to disturbances in the electrostatic double layer (Shipley et al., 2009). Although the presence of ionic species in the supernatant can also decrease the removal efficiency, the dissolved solutes in our experiments (e.g., Fe^{2+}, NH_4^+, Na^+, Cl^- and SO_4^{2-} ions) have been shown to have little or no effect on As adsorption (Asere et al., 2017; Guo and Chen, 2005; Gupta et al., 2009).

Common aqueous groundwater ions can compete for the available active surface sites on GR_{SO4} (Folens et al., 2016; Leus et al., 2018). We tested the effect of relevant dissolved potentially interfering ions in the water matrix through competitive adsorption experiments with Ca^{2+} (100 mg L^{-1}), Mg^{2+} (50 mg L^{-1}) or PO_4^{3-} (10 mg L^{-1}) and As (10 mg L^{-1}) to the GR_{SO4} suspension at pH 8. The concentrations of the competing ions were chosen based on the average aqueous ion concentrations in As-contaminated groundwaters in Bangladesh and West Bengal, India (Nickson et al., 2000; Zahid et al., 2008) and mining-contaminated groundwater sites (Smedley and Kinniburgh, 2002; Williams et al., 1996). The comparison (Figure 3.3d) revealed no significant change in the removal of As(III) and As(V) resulting from the presence of Ca^{2+} ions. On the other hand, the presence of Mg^{2+} ions decreased the removal efficiency by 6.7 ± 1.0% for As(III) and 21.5 ± 2.1% for As(V) compared to the Mg^{2+} free system. However, analysis of the liquid phases by ICP-OES revealed that Mg^{2+} was not adsorbed on GR_{SO4}, but remained solvated in the supernatant. This decrease in As removal can be caused by the high ionic potential of Mg^{2+}, allowing it be solvated by water molecules (Lightstone et al., 2001) and resulting in the formation of outer-sphere hydrated Mg^{2+} complexes. Such aqueous complexes could potentially reduce the accessibility of active surface sites of GR_{SO4} for As adsorption. The presence of PO_4^{3-} ions also resulted in the inhibition of As adsorption, where the removal efficiency for As(III) and As(V) decreased by 7.3 ± 1.3 and 24.5 ± 1.8%, respectively. Phosphate, with a tetrahedral molecular geometry analogous to the structure of AsO_4^{3-}, can also form complexes in the same lateral (010) and (100) GR surfaces sites where As complexes bind (Bocher et al., 2004). This can result in a competition between PO_4^{3-} and As species on the available GR_{SO4} binding sites, thereby explaining the reduced As removal efficiency. Remarkably, the phosphate removal efficiency was > 90% for both the As(III) and As(V) competitive adsorption experiments. This likely results from the higher affinity of iron (oxyhydr)oxides for phosphate compared to As, as indicated by its higher adsorption equilibrium constant (Roberts et al., 2004), and the slow exchange of initially adsorbed phosphate on the GR_{SO4} surface sites with the competing As species (Hongshao and Stanforth, 2001).

3.3.3 Adsorption kinetics

The rate of As removal over 24 h was determined at pH 8 by measuring the adsorption kinetics in batch experiments at initial As concentration of 10 mg L^{-1} As(III) or As(V), S/L of 4 g L^{-1} and an ionic strength of 0.05 M. After fitting the kinetic data with various adsorption models, the best fit ($R^2 > 0.9999$) resulted from the pseudo-2nd order kinetic model (Ho, 2006). The linearized plots for the pseudo-2nd order kinetic models are shown in Figure 3.4. The calculated adsorption

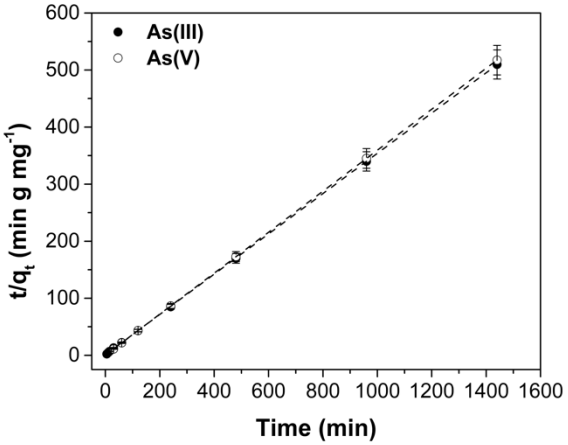

Figure 3.4 Pseudo-2nd order kinetic data and model fits for the adsorption of As species on GR_{SO4}. Initial concentration is 10 mg L^{-1} at pH 8, S/L ratio of 4 g L^{-1} and IS* of 0.05 M. Error bars represent analytical uncertainty (<5% relative).

rate constants (k_2; Table S3.6) revealed that the uptake of both As species was very fast. Full adsorption (>99% removal) of As(V) was achieved within 30 min of contact with GR_{SO4}, while As(III) reached equilibrium after 4 h. The more rapid removal of As(V) was caused by the stronger binding affinity of pentavalent As over the trivalent As species to iron (oxyhydr)oxides (Roberts et al., 2004). These fast adsorption uptake rates show that GR_{SO4} can efficiently remove As(III) and As(V) within a short time.

3.3.4 Long-term batch adsorption experiments

At an initial As concentration of 10 mg L^{-1}, GR_{SO4} remained stable during the course of the 90-day monitoring of batch adsorption experiments. No other iron (oxyhydr)oxide mineral phases were identified in XRD patterns of these long-term equilibrated and As-interacted samples (Figure 3.5a). The TEM images and SAED patterns (Figure 3.5b) also showed that the GR_{SO4} particles in the 90-day long interacted samples maintained their well-defined thin hexagonal plate-like morphology and crystal structure. These observations were also confirmed by the fact that the long-term monitoring of aqueous As in the supernatant (Figure S3.6) revealed that the initial adsorbed As was not released back into the aqueous phase. Previous studies have shown that adsorbed As can slow down or inhibit the transformation of GR minerals to other iron (oxyhydr)oxides such as magnetite (Su and Wilkin, 2005; Wang et al., 2014), which explains the stability of the As-interacted GR_{SO4} even after 90 days in our study. In addition, our results are also consistent with long-term batch experiments of Su and Wilkin (2005), who showed that As-interacted GR_{CO3} remained stable for up to 60 days.

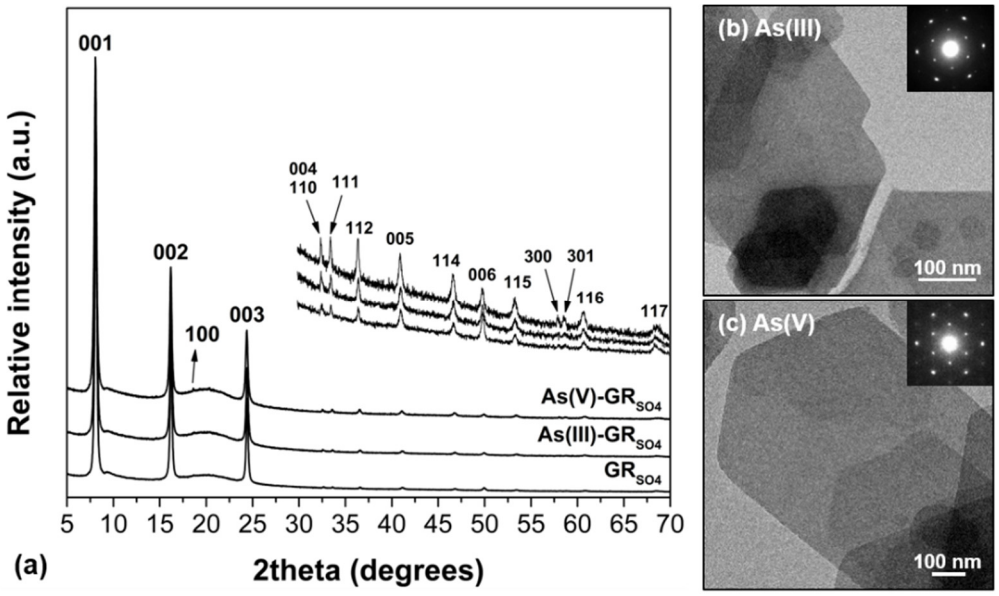

Figure 3.5 (a) XRD patterns and (b-c) TEM images (inset: SAED pattern) GR_{SO4} interacted with 10 mg L^{-1} As(III) and As(V) after 90 days. XRD peaks of GR_{SO4} were assigned based on published diffraction data (Simon et al., 2003). The broad amorphous hump at ~20° 2θ comes from the XRD sample holder.

3.3.5 Adsorption isotherms and mechanism

The As adsorption isotherms at all tested pH values are shown in Figure 3.6. Equilibrium adsorption data were fitted to Langmuir and Freundlich isotherm models and the calculated fitting parameters for both models are shown in Table S3.7. Based on the fitting, the adsorption of As species on GR_{SO4} is best described using the Langmuir model, indicating a homogenous monolayer binding of As surface complexes at the solid/water interface (Leus et al., 2017). Using the Langmuir adsorption model, we determined the maximum As adsorption capacities for both As species onto GR_{SO4} (Table 3.1). At alkaline pH, the maximum adsorption capacity of As(III) was 2.2 times higher than the value at neutral pH, while As(V) had 1.5 times higher maximum adsorption capacity at pH 7 compared to pH 8-9.

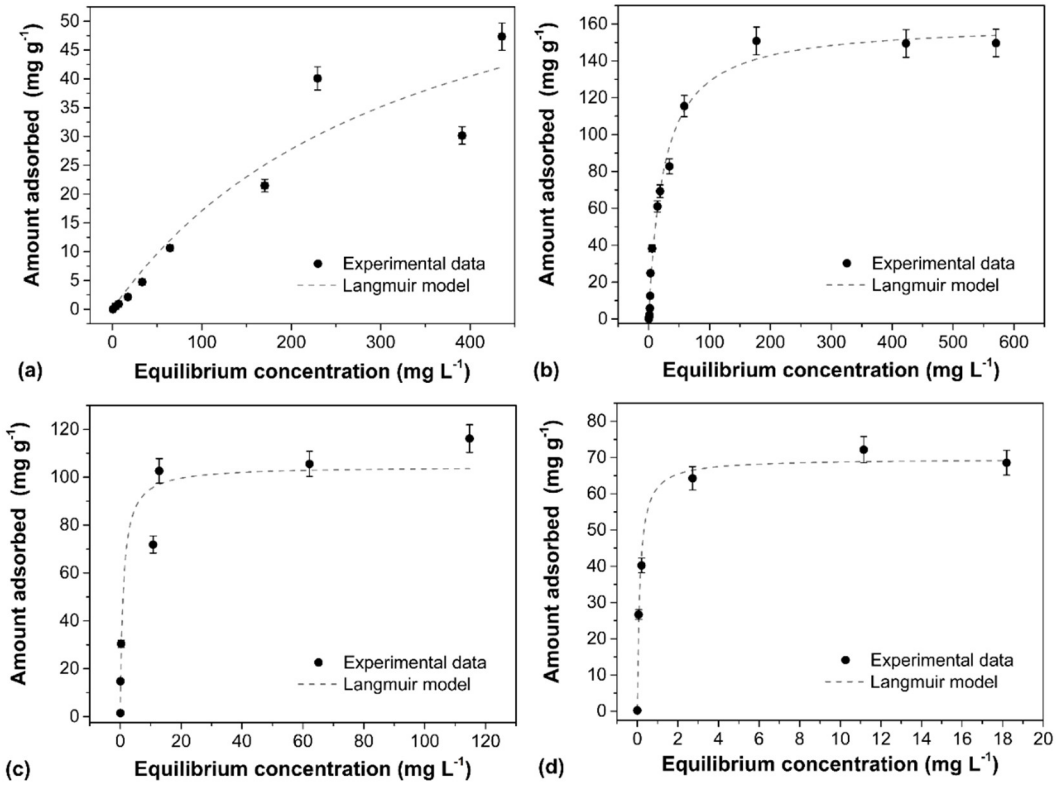

Figure 3.6 Langmuir adsorption isotherms of As species on GR_{SO4}. (a-b) Adsorption of As(III) at pH 7 and 8-9, respectively. (c-d) Adsorption of As(V) at pH 7 and 8-9, respectively. Error bars represent analytical uncertainty (< 5% relative) (see Table S3.1 for details).

The spatial distribution of the adsorbed As(III) on the GR particles, at an initial concentration of 500 mg L^{-1}, was examined using HAADF-STEM imaging coupled with EDX mapping (Figure 3.7). The EDX elemental map (Figure 3.7d) and associated intensity profile (Figure 3.7g) show that higher concentrations of As can be found near the GR particle edges (ca. two times higher than the (001) GR surface). In addition, the HAADF-STEM image (Figure 3.7a) alone shows increased intensity at the GR particle edges which we interpret to be associated with increased As concentration. These results, combined with the adsorption isotherm results, strengthen previous findings that suggested that As(III) and As(V) form monodentate mononuclear (^1V) and bidentate binuclear (^2C) inner-

sphere complexes on the GR particle edges (Jönsson and Sherman, 2008; Wang et al., 2010). However, the maximum adsorption capacity for As(III) determined in the current study could also indicate that surface complexation may not be limited to the GR_{SO4} particle edges but, as mentioned before, may also result from the presence of multi-nuclear arsenite complexes (Ona-Nguema et al., 2009; Wang et al., 2010).

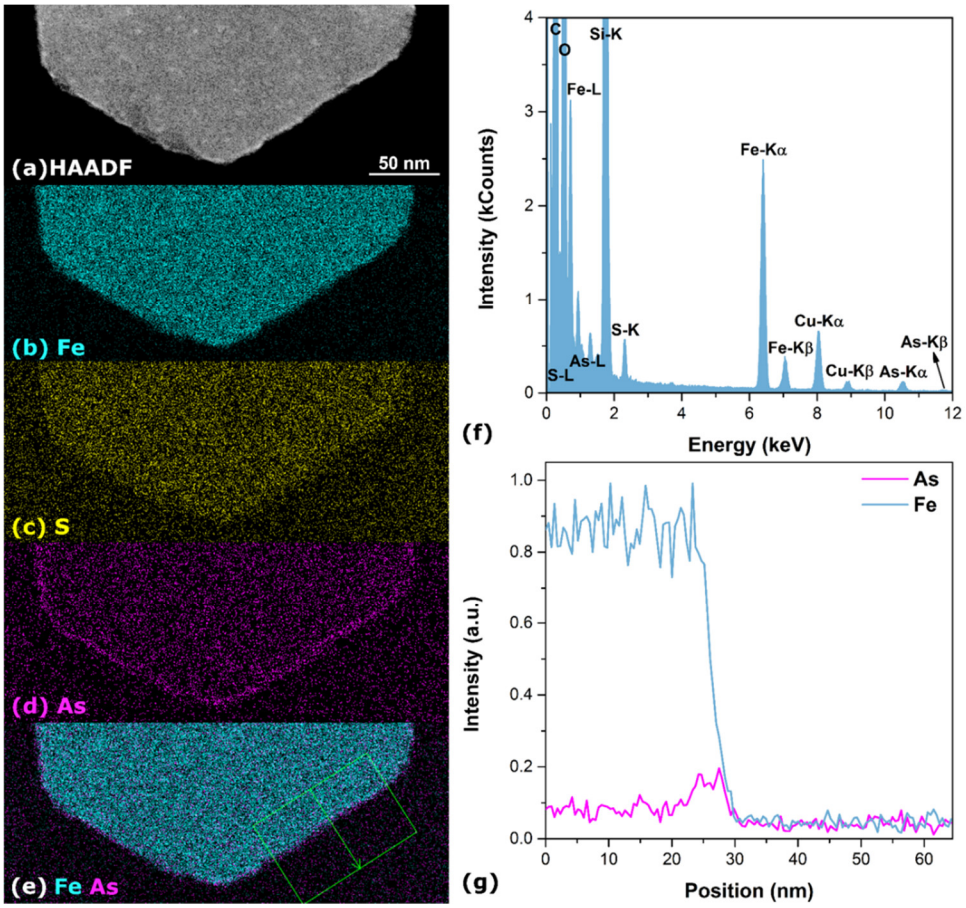

Figure 3.7 (a) HAADF-STEM overview of GR_{SO4} interacted with 500 mg L^{-1} of As(III) and the corresponding (b) EDX elemental maps for (b) Fe (light blue), (c) S (yellow), (d) As (magenta) and (e) combined Fe and As. (f) The EDX spectrum of (a). The Si signal comes from the use of headspace crimp vials while C and Cu peaks come from the TEM grid. (g) The EDX signal intensity profile shows the change in concentration of Fe and As along the line drawn across the marked area in green (e).

In addition to surface complexation, previous studies with selenate have shown that tetrahedral oxyanions (e.g., SeO_4^{2-}) can also be removed by GR phases by interlayer intercalation (Refait et al., 2000). In our study intercalation of As(III) and As(V) in the interlayer region of GR would have resulted in changes in the basal spacing since the ionic radius of AsO_3^{3-} (2.11 Å) and AsO_4^{3-} (2.48 Å) are different to that of SO_4^{2-} (2.30 Å) (Goh et al., 2008). However, XRD patterns of GR_{SO4} interacted with As(III) and As(V) at 10 mg L^{-1} (Figure 3.5a) and 500 mg L^{-1} (Figure S3.7) do not exhibit shifts in the basal (001) reflections (ca. 10.9 Å) to accommodate such intercalations. The intercalation of As(III) and As(V) in our study, might have been inhibited because SO_4^{2-} cannot be readily exchanged in layered double hydroxides (de Roy et al., 2001; Miyata, 1983).

3.3.6 Environmental significance of GR in contaminated environments

Using the adsorption isotherm modelling data, we compared the calculated adsorption capacities for As species on GR_{SO4} and with literature data for all described iron (oxyhydr)oxides, oxyhydroxysulfates and sulfides, which have also been evaluated for their efficiency as mineral substrate for the treatment of As contaminated groundwater resources (Table 3.1).

Table 3.1 Comparison of As adsorption capacities of GR_{SO4} with common iron (oxyhydr)oxides, oxyhydroxy sulfates and sulfides.

Entry No.	Adsorbent	Particle size (nm)	Surface area (m^2 g^{-1})[a]	Tested pH	Adsorption capacity (mg g^{-1}) As(III)	As(V)	Reference
1	Goethite	-	39	9	22.0	4.0	Lenoble et al. (2002)
2	Hematite	5	162	7	95.0	47.0	Tang et al. (2011)
3	Maghemite	7-12	169	-	67.0	95.4	Lin et al. (2012)
4	Magnetite	12	99	8	134.9	172.3	Yean et al. (2005))
5	Ferrihydrite	-	202	5	552.9	222.1	Raven et al. (1998)
6	Schwertmannite	-	280[b]	9	280.4	166.5	Burton et al. (2009)
7	Mackinawite	2	350	7	9.7	32.2	Wolthers et al. (2005)
8	Troilite	-	3	7	17.3	-	Bostick and Fendorf (2003)
9	Pyrite	-	41	7	1.0	-	Bostick and Fendorf (2003)
10	GR_{CO3}	100-300	-	7.5	123.0	-	Su & Wilkin (2005)
			-	10.5	43.8	6.91	Su & Wilkin (2005)
11	GR_{SO4}	50-500	25[c]	7	74.0	104.5	This work
				8-9	160.3	69.6	This work

[a] Specific surface area determined by the Brunauer–Emmett–Teller (BET) model. [b] Estimated from Davidson et al. (2008) [c] Measured nitrogen sorption isotherm can be found in Figure A2.5.

Our data show clearly that GR_{SO4} is among the most effective adsorbents among all the phases listed in Table 3.1. This finding has important implications for the fate and mobility of As in anoxic groundwaters where GR_{SO4} exists. To the best of our knowledge, this is the first study to report the adsorption isotherms of As(III) and As(V) for GR_{SO4}, as well as the in-depth examination of critical adsorption parameters for As removal. We have shown that at circum-neutral and slightly alkaline pH conditions, GR_{SO4} can efficiently adsorb large amounts of As(III) and As(V), making GR_{SO4} one of the best performing iron-bearing mineral phases in terms of As adsorption. For As(III) at slightly alkaline pH, GR_{SO4} is only outperformed by ferrihydrite (Table 3.1, entry 5) and schwertmannite (Table 3.1, entry 6) (Davidson et al., 2008). Ferrihydrite and schwertmannite are poorly ordered, highly reactive and thermodynamically metastable iron-bearing mineral phases which can transform at ambient conditions to more thermodynamically stable crystalline iron (oxyhydr)oxides such as goethite and hematite,

fast at alkaline conditions but slow at near-neutral pH values (Brinza et al., 2015; Burton et al., 2008; Davidson et al., 2008; Vu et al., 2013; Yee et al., 2006). Moreover, comparing our data with other Fe-bearing phases (Table 3.1) shows that among mixed-valent and redox-active iron (oxyhydr)oxides and sulphides, GR_{SO4} exhibits an unprecedented As(III) uptake and also remains stable for long time periods. Even compared to magnetite (Table 3.1, entry 4) and iron sulfides (e.g., troilite, pyrite; Table 3.1, entries 7-9) that are crystalline and highly stable in reduced environments, our GR_{SO4} showed higher adsorption capacities. This exceptional As adsorption capacity makes GR_{SO4} a novel and potentially highly environmentally-relevant mineral substrate for As sequestration in near-neutral pH and reduced to slightly oxidized groundwater systems.

Previous studies have shown that GR phases can oxidize As(III) to As(V) (Su and Puls, 2004; Su and Wilkin, 2005). Although not investigated in this study, possible redox transformation can heavily impact the toxicity and mobility of As in soils and groundwaters. As(III) oxidation by GR mineral phases would be a favorable process as it would result in a less toxic and less mobile As(V) species (Vaughan, 2006). On the other hand, reduction of As(V) to the far more toxic As(III) and the potential re-release into groundwaters because of the lower affinity of As(III) for ferric iron (oxyhydr)oxides would be far more damaging (Roberts et al., 2004). Further studies are needed to confirm the potential of As(III) oxidation in the presence of GR and to determine the geochemical and thermodynamic driving forces in this reaction.

As for redox-active mineral adsorbents, arsenic can still be released from GR_{SO4} since its sequestration is highly dependent on pH conditions and redox environment. Sudden changes in pH or Eh of the system may cause potential release of surface immobilized As species back into the groundwater either by dissolution or redox-change driven transformation of GR phases (Cundy et al., 2008). Iron mineral phases such as goethite and magnetite, which are common transformation end-products of GR, are, however, far less reactive and effective mineral substrates for As sequestration (Table 3.1), which can lead to remobilization of As in groundwaters.

3.4 Conclusion

In this work, we investigated the interfacial reactivity between GR_{SO4} and As species. An extensive batch adsorption study was performed to examine the influence of various critical environmental parameters such as initial concentration, pH, adsorbent loading, ionic strength and presence of potentially interfering ions on As removal. We have successfully demonstrated that GR_{SO4} is an effective and stable As(III) and As(V) mineral adsorbent compared to other iron (oxyhydr)oxide phases. GR_{SO4} demonstrated remarkable maximum adsorption capacities for As(III) and As(V) of up to 160 and 105 mg g^{-1}, respectively. This exceptional As adsorption reactivity makes GR a potentially novel and environmentally-relevant mineral substrate for the sequestration of As in reduced groundwater systems. The removal of As is also highly pH dependent – high As(III) removal was obtained at higher pH while As(V) removal was found to be more favourable at circum-neutral conditions. GR_{SO4} exhibited fast As uptake rates at alkaline conditions. Common groundwater species such as Mg^{2+} and PO_4^{3-} were found to affect the efficiency of As adsorption onto GR_{SO4}.

Overall, our results clearly highlight importance of redox-active GR mineral phases in removing As species from aqueous solutions and their potential crucial role in the remediation of contaminated groundwaters.

3.5 Supporting information

3.5.1 Experimental and analytical methods

Mineral characterization

Ambient temperature X-ray diffraction (XRD) patterns were recorded on a Bruker D8 powder diffractometer equipped with a BSI Si(Li) solid detector operating at 40 kV and 40 mA using Cu Kα radiation (λ = 1.5406 Å) with a 0.017° step in the range of Bragg angles 2ϑ of 5° to 70°. Samples for XRD analysis were loaded on a silicon wafer and the sample holder was sealed using an X-ray transparent cap (Bruker Dome, Polytron) with a low oxygen diffusion rate to minimize oxidation/transformation. The surface area of the synthesized materials was determined by nitrogen sorption on a Micromeritics Gemini VII 2390 Surface Area Analyzer at 77 K. Samples were dried inside a desiccator in the anaerobic chamber for a week, and dried further under vacuum at room temperature for 24 h prior to surface area analysis to ensure removal of adsorbed water.

Samples for transmission electron microscopy (TEM) were prepared in an anaerobic chamber (95% N_2, 5% H_2, Coy Laboratory Products, Inc.) and just prior to TEM analyses were suspended in isopropyl alcohol and dropcast onto a holey amorphous carbon copper grid. The grid was loaded into a single tilt TEM holder and sealed for rapid transfer (< 30 s) into the TEM. Micrographs (TEM) and electron energy-loss spectra (EELS) were recorded using an FEI Tecnai G2 F20 X-Twin FEG TEM operated at 200 kV and equipped with a Gatan Imaging Filter (GIF) Tridiem™. Energy dispersive X-ray (EDX) spectra and maps were collected with an FEI Titan Themis3 FEG TEM operated at 300 kV and equipped with a Super-X EDX detector system. The energy resolution for EEL spectra was 0.8 eV, as measured from the full width at half maximum (FWHM) of the zero loss peak and the convergence semi-angle was 1.3 mrad. Selected area electron diffraction (SAED) patterns were obtained using an aperture with an effective diameter of 250 nm at the image plane. We tested if the specimens remained stable under the electron beam dose to optimize analyses and worked at conditions where no significant changes in the specimens' morphology or crystal structure were observed during data acquisition (10 min per region of interest).

X-ray photoelectron spectroscopy (XPS) analysis was performed using a KRATOS Axis Ultra X-ray photoelectron spectrophotometer with a monochromated Al Kα X-ray (1486.6 eV) operated at 150 W with a charge neutralizer. Analytical chamber base pressure was maintained at *ca.* 10^{-9} mbar throughout data collection. Survey and high-resolution scans were recorded with pass energies of 80 and 20 eV, respectively. Accurate binding energies were calibrated with respect to the adventitious C *1s* peak at 285 eV. The spectra were fitted by a least-squares fitting routine using Unifit software after subtraction with a Shirley background.

^{57}Fe Mössbauer spectra were recorded at 20 K using a standard WissEl spectrometer equipped with a ^{57}Co(Rh) radioactive source and operating in the constant acceleration mode. Samples were loaded in an acrylic glass sample holder in the anaerobic chamber (about 10 mg Fe cm^{-2}) and placed into a Janis SHI 850-5 closed cycle refrigerator. The spectra were evaluated using the MossWinn 4.0 Software (Klencsár et al., 1996) within the thin absorber approximation. All isomer shifts refer to ∝-Fe.

Influence of adsorption parameters, potentially interfering species and long-term monitoring

The effect of pH on the interaction of As species with GR_{SO4} was examined at pH 7, 8 and 9. Both the washed GR_{SO4} suspension and the As solutions were adjusted to the desired pH before the adsorption experiments. The pH adjustment was done using 1 M HCl or 0.3 M NaOH to avoid possible buffer interactions. The GR_{SO4} adsorbent was mixed with As solution (10 mg L^{-1}) using an adsorbent loading of 4 g L^{-1}. The mixture was shaken at 250 rpm for 24 h at room temperature. In order to prevent any change due to GR dissolution, pH below the arsenate dissociation i.e. pKa ~6.7 was not tested. Buffers were also not used to exclude potential effects on GR reactivity (Yin et al., 2017). Separate experiments, where pH was monitored were done and pH drifts of only < 0.5 pH units were observed.

The effect of the adsorbent loading (solid to solution ratio S/L) on the adsorption of As was also investigated using loadings of 2, 4 and 6 g L^{-1}. In this case, the As solution (10 mg L^{-1}, pH 7) was added to various GR_{SO4} suspensions (also pH 7), and batch adsorption experiments were done as described previously.

The effect of the total ion concentration (ionic strength, IS*) of the mixture was also studied by diluting the supernatant from an initial ionic strength of 0.5 M to 0.05 and 0.005 M using O_2-free Milli-Q water. Afterwards, the As solution (10 mg L^{-1}, pH 7) was added to the GR_{SO4} suspension (pH 7) at an adsorbent loading of 4 g L^{-1}. Batch adsorption experiments were conducted as described above. It must be noted that this ionic strength (IS*) is different than IS usually used in previously published adsorption experiments where ionic salts (e.g., NaCl, KNO_3) are added to achieve a particular total ion concentration (e.g., Burton et al. (2009), Shipley et al. (2009)).

The effect of potentially interfering ions on the performance of GR_{SO4} and its selectivity were studied by performing competitive adsorption between As and the three most common groundwater ions. Maintaining an adsorbent loading of 4 g L^{-1}, a pH 8 and using an As concentration of 10 mg L^{-1}, we used either Ca^{2+} (100 mg L^{-1}), Mg^{2+} (50 mg L^{-1}) or PO_4^{3-} (10 mg L^{-1}) as competing ions. These were prepared from of $CaCl_2{\cdot}2H_2O$, $MgSO_4{\cdot}7H_2O$ and $Na_3PO_4{\cdot}12H_2O$, respectively, and these were co-added to the GR_{SO4} suspension with the As maintaining as solid to solution ratio at 4 g L^{-1}. The concentrations of the competing species were chosen based on the groundwater chemistry of common As contaminated sites (Nickson et al., 2000; Zahid et al., 2008). Batch adsorption experiments were done as previously stated.

Long-term monitoring experiments were done in 100-mL serum bottles. Similar to the previous set-up, the As solution (10 mg L^{-1}, pH 8) was added to the GR_{SO4} suspension (pH 8) at an adsorbent loading of 4 g L^{-1} and a total suspension volume of 100 mL. Batch adsorption experiments were conducted as described above but with suspension in contact with the As solution for up to 90 days.

Elemental ion concentration analysis [adapted from Schuessler et al. (2016))]

Prior to ICP-OES analysis, acidified liquid samples (pH ~2) were diluted gravimetrically in acid-cleaned polypropylene (PP) tubes. Sample dilutions were done using 0.3 M HNO_3 (Merck Suprapure grade) containing 1 mg g^{-1} Cs as an ionization buffer to achieve matrix

matching with calibration standards prepared from a mixture of single ICP element standards (Merck certipur, traceable to NIST reference materials). Scandium (1 µg g^{-1}) was added as an internal standard. Dilution factors ranging from 1.33 to 200 were adapted to ensure that the analyte solutions were within the concentration range of the matrix-matched calibration standards (linearity criteria $R^2 > 0.9990$) and with final HNO_3 and Cs concentrations of 0.3 M and 1 mg g^{-1}, respectively. For each analytical session, instrumental stability and drift were monitored using Ar, Cs and Sc at emission wavelengths of 459.311, 420.067 and 335.372 nm for each sample analysis, respectively, as well as regular measurements of a quality control (QC) solution, similar to sample compositions. Instrumental statistical limits of detection (LoD = 3SD above background) or limits of quantification (LoQ = 10SD above background) were determined in each analytical session based on nine repeat analysis of 0.3 M HNO_3 (+ 1 mg g^{-1} Cs) used for sample dilution.

Concentrations of As, Ca, Fe, Mg, Na and S in the samples were evaluated using the emission wavelengths of 193.696, 318.127, 261.382, 285.213, 330.237 and 180.669 nm, respectively. The determined LoD and LoQ for As were 0.020 and 0.052 µg g^{-1}, respectively. Detection limits translate to maximum detectable removal efficiency of > 99.8%. Analytical uncertainties at a 95% confidence level for concentrations quantified (above LoQ) during this study are ~5% relative, verified by repeat analyses of a QC solution, which was similar to the sample compositions (Table S3.1).

Ion chromatography (IC)

The concentration of dissolved phosphate remaining in the supernatant after the competitive adsorption experiments was analyzed by ion chromatography (IC) using conductivity detection (ICS 3000, Dionex, Corp.) with an ASRS Ultra II 2 mm suppressor and a Dionex conductivity detector. Chromatographic separation was achieved using the analytical column AS 11 HC (Dionex Corp.) at 35 °C. The liquid samples were eluted using KOH solution of varying concentrations over time. The LoD was 1 mg L^{-1}, which translates to maximum detectable removal efficiency of > 90%. The initial KOH concentration was 1.4 mM, maintained for 6 min. After 12 min, 10 mM KOH solution was reached and 15 mM solution was in use after 22 min. After 32 min analysis time, 60 mM KOH concentration was reached, followed by a rapid decrease to 1.4 mM after 33.1 min. This initial level of 1.4 mM was kept for additional 17 min to equilibrate the system. Calibration standards having different concentrations were measured every day. Standard deviation of sample and standard quantification is below 10% (determined by at least two measurements).

Table S3.1 ICP-OES analytical results of quality control solutions (QC) analyzed during this study prepared from single elements standard solutions (Merck, CertiPur) to achieve chemical compositions similar to experimental sample solutions. The mean results of n replicate analyses are given together with the standard deviation (SD) and the relative standard deviation (RSD) (SD represents 68% of the population, 2SD represents 95 % of the population). The measured deviation from reference value is a quantitative estimation of accuracy.

	As (µg g^{-1})	Fe (µg g^{-1})	Na (µg g^{-1})	S (µg g^{-1})	Ca (µg g^{-1})	Mg (µg g^{-1})
QC verify (n = 8)	0.54	7.38	7.66	5.60		
SD	0.01	0.04	0.06	0.15		
RSD	1%	0%	1%	3%		
2RSD	2%	1%	2%	5%		
Reference value	*0.510*	*7.09*	*8.09*	*5.04*		
Uncertainty of reference value	*0.003*	*0.07*	*0.08*	*0.05*		
Measured deviation from reference value	**5%**	**4%**	**-5%**	**11%**		
QC verify (n = 4)	1.99	6.30	16.19	26.29		
SD	0.01	0.03	0.10	0.25		
RSD	0.3%	0.4%	0.6%	0.9%		
2RSD	1%	1%	1%	2%		
Reference value	*1.97*	*6.31*	*15.49*	*25.77*		
Uncertainty of reference value	*0.01*	*0.06*	*0.16*	*0.26*		
Measured deviation from reference value	**1%**	**-0.2%**	**5%**	**2%**		
QC verify (n = 4)	0.65	6.24	5.74	6.47		
SD	0.02	0.12	0.10	0.11		
RSD	2%	2%	2%	2%		
2RSD	5%	4%	3%	3%		
Reference value	*0.66*	*6.40*	*6.39*	*6.45*		
Uncertainty of reference value	*0.002*	*0.41*	*0.41*	*0.05*		
Measured deviation from reference value	**-1%**	**-3%**	**-10%**	**0.3%**		
QC verify (n = 4)		1.72	1.55	1.79	0.842	0.504
SD		0.01	0.04	0.03	0.004	0.003
RSD		1%	2%	2%	0.5%	1%
2RSD		2%	5%	3%	1%	198%
Reference value		*1.71*	*1.69*	*1.710*	*0.840*	*0.510*
Uncertainty of reference value		*0.02*	*0.02*	*0.002*	*0.004*	*0.003*
Measured deviation from reference value		**0.3%**	**-9%**	**4%**	**-0.3%**	**1%**

3.5.2 Characterization data of GR_{SO4}

Table S3.2 Elemental composition of GR_{SO4} based on EDX analysis.

Element	Theoretical (atomic %)	Measured (atomic %)
Fe	19.4	21.3 ± 1.3
O	77.4	75.5 ± 1.7
S	3.2	3.2 ± 1.0

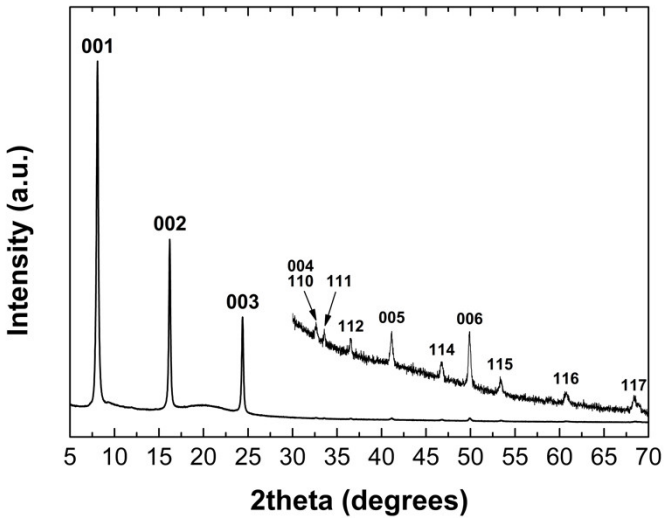

Figure S3.1 XRD pattern of freshly co-precipitated GR_{SO4} at pH 8. XRD peaks were assigned based on published diffraction data (Simon et al., 2003). The broad amorphous hump at ~20° 2θ comes from the XRD sample holder.

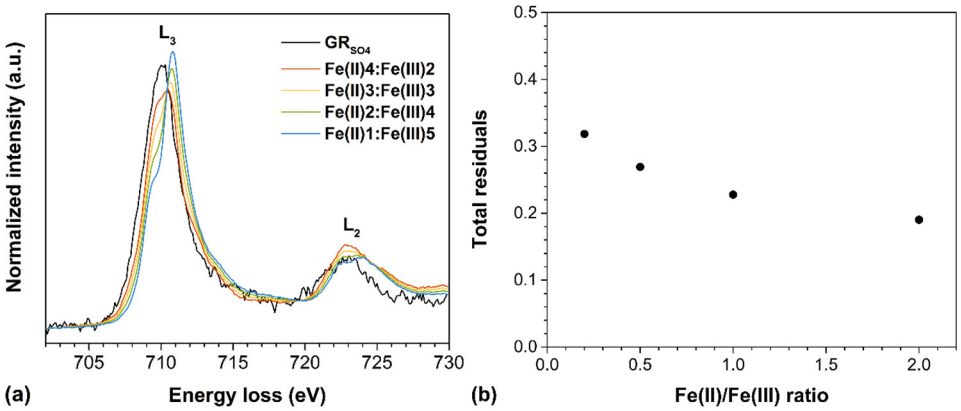

Figure S3.2 (a) Normalized Fe $L_{2,3}$-edge EEL spectrum of GR_{SO4} and normalized calculated reference fits for varying Fe(II):Fe(III) ratios. (b) Total residuals (absolute value) calculated from the difference between the experimental spectrum of GR_{SO4} and the calculated reference fits.

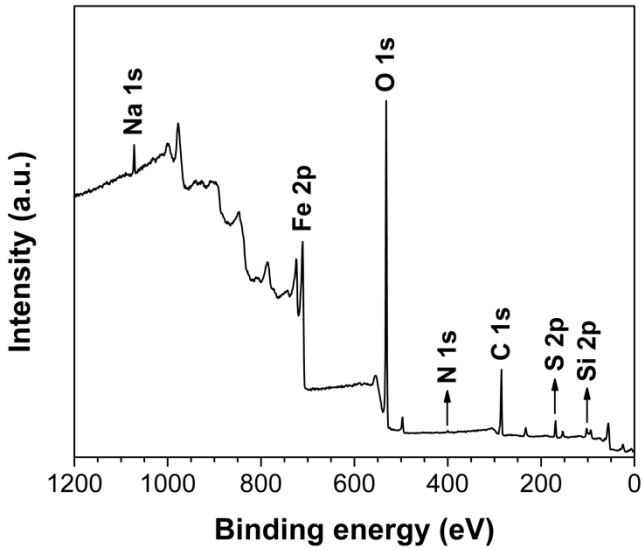

Figure S3.3 Wide scan XPS spectrum of GR_{SO4}. N *1s* peak comes from adsorbed $NH_4^{+}{}_{(aq)}$ from the initial aqueous Fe(II) precursor solution and Si 2p is from the headspace crimp vials.

Table S3.3 Interpretation of deconvoluted high-resolution O *1s* XPS spectra of GR_{SO4}.

Peak assignment	Binding energy (eV)	FHWM (eV)	Relative area (%)
Fe-O	530.2	1.06	10.0
O-H	531.8	1.36	81.2
H_2O	532.6	1.55	8.79

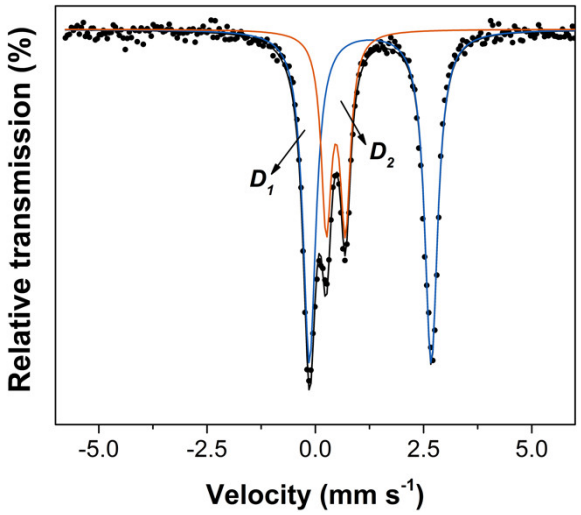

Figure S3.4 ^{57}Fe Mössbauer spectrum of GR_{SO4} recorded at 20 K fitted with one Fe(II) doublet (D_1) similar to those reported by Géhin et al. (2002)).

Table S3.4 Hyperfine parameters of GR_{SO4} at 20 K. Mössbauer spectrum fitted with two Fe(II) doublets (χ^2 = 1.6376).

	Assignment	δ (mm s^{-1})	ΔE_Q (mm s^{-1})	$\Gamma/2$ (mm s^{-1})	Relative area (%)	Fe(II)/Fe(III)
D_1	Fe(II)	1.27	2.89	0.28	47.8	2.09
D_2	Fe(II)	1.27	2.54	0.28	19.9	
D_3	Fe(III)	0.48	0.43	0.28	32.3	

Note: δ - isomer shift (with respect to α-Fe at room temperature); ΔE_Q - quadrupole splitting; $\Gamma/2$ - half width at half maximum

Table S3.5 Hyperfine parameters of GR_{SO4} at 20 K. Mössbauer spectrum fitted with one Fe(II) doublet (χ^2 = 3.2033).

	Assignment	δ (mm s^{-1})	ΔE_Q (mm s^{-1})	$\Gamma/2$ (mm s^{-1})	Relative area (%)	Fe(II)/Fe(III)
D_1	Fe(II)	1.27	2.81	0.36	68.8	2.21
D_2	Fe(III)	0.47	0.44	0.29	31.2	

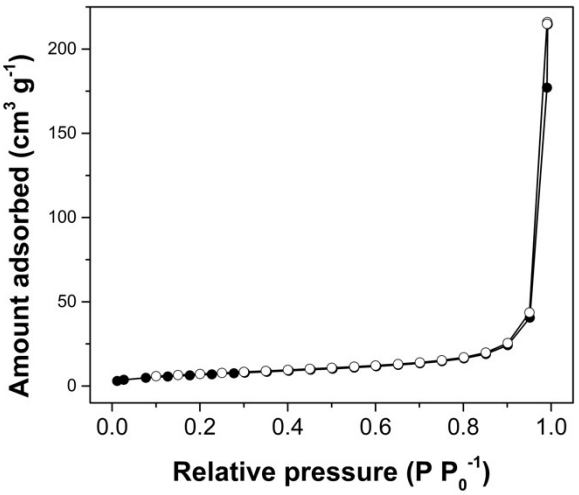

Figure S3.5 Nitrogen adsorption (filled symbols) and desorption (open symbols) of GR_{SO4} at 77K.

3.5.3 Batch adsorption data for As-GR_{SO4} interactions

Table S3.6 Adsorption fitting parameters of As(III) and As(V) for the pseudo-2nd order kinetic model.

As species	q_e (mg g^{-1})	k_2	R^2
As(III)	2.83	0.11	> 0.9999
As(V)	2.78	0.36	> 0.9999

Table S3.7 Adsorption isotherm fitting parameters of As(III) and As(V) on GR_{SO4}.

		Langmuir			Freundlich		
pH	As species	q_{max} (mg g^{-1})	K_L (L mg^{-1})	R^2	K_L	n	R^2
7	As(III)	74.0	0.003	0.9145	0.67	1.45	0.8999
	As(V)	104.5	1.01	0.9354	40.8	4.22	0.9015
8-9	As(III)	160.3	0.041	0.9895	22.7	3.12	0.8887
	As(V)	69.6	7.76	0.9919	45.8	5.61	0.9326

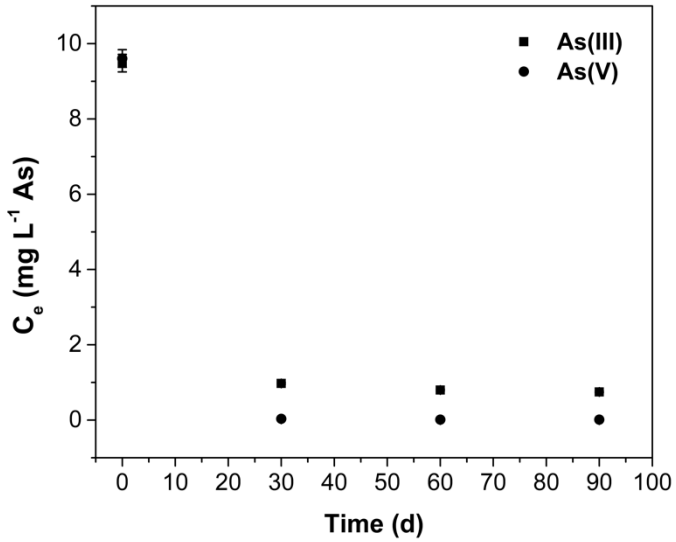

Figure S3.6 Long-term monitoring of the equilibrium concentrations of As species in the aqueous phase of the As-interacted GR_{SO4} suspension that started with an initial concentration of 10 mg L^{-1}. Error bars represent analytical uncertainty (< 5% relative) based of replicate measurements of QC solution analyzed together with the samples (Table S3.1).

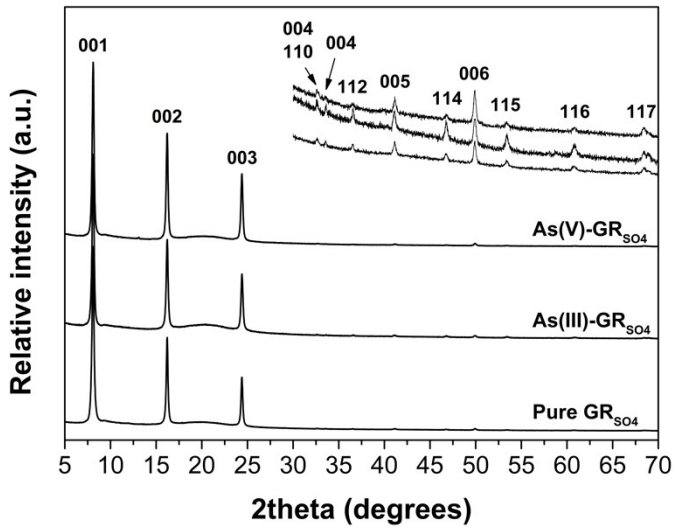

Figure S3.7 XRD patterns of (a) pure GR_{SO4} and sample interacted (b) As(III) and (c) As(V) at an initial concentration of 500 mg L^{-1} at pH 7 for 24 h. XRD peaks of GR_{SO4} were assigned based on published diffraction data (Simon et al., 2003). The broad amorphous hump at ~20° 2θ comes from the XRD sample holder.

Table S3.8 Estimated amount of As(III) and As(V) that can be intercalated into GR_{SO4} interlayer used in this study.

Oxidation state	pH	q_{max} (mg g^{-1})	Chemical speciation	Approx. mole fraction	Max. amount of As that can be intercalated (mg g^{-1})	Relative contribution to q_{max} (%)
As(III)	7	74	$H_3AsO_3^0$	1	-	-
	9	160	$H_3AsO_3^0$	0.6	-	-
			$H_2AsO_3^-$	0.4	3.10	1.93
As(V)	7	105	$H_2AsO_4^-$	0.5	3.87	3.70
			$HAsO_4^{2-}$	0.5	1.94	1.86
	9	70	$HAsO_4^{2-}$	1	3.87	5.56

Chapter 4

Revealing arsenic binding mechanisms on green rust sulfate at the nano-scale

This chapter is adapted from:

Perez, J.P.H.; Freeman, H.M.; Brown, A.P.; Van Genuchten, C.M.; Dideriksen, K.; S'ari, M.; Tobler, D.J.; Benning, L.G. (2020). Direct visualization of arsenic binding on green rust sulfate. *Environmental Science & Technology*.

Available at: https://doi.org/10.1021/acs.est.9b07092

Abstract

'Green rust' (GR), a redox-active Fe(II)-Fe(III) layered double hydroxide, is a potential environmentally-relevant mineral substrate for arsenic (As) sequestration in reduced, subsurface environments. GR phases have high As uptake capacities at circum-neutral pH but the exact mechanisms of interaction between GR and As species are still poorly understood. Here, we document the reaction mechanisms between GR sulfate and As species [As(III), (V)] through scanning transmission electron microscopy (STEM) coupled with energy dispersive X-ray (EDX) spectroscopy, and combined it with synchrotron-based X-ray total scattering, pair distribution function (PDF) analysis and X-ray absorption spectroscopy (XAS). Our data revealed that As(III) and As(V) are preferentially adsorbed at GR crystal edges as bidentate binuclear (^{2}C) inner-sphere surface complexes, although the presence of oligomeric As(III) surface complexes cannot be completely ruled out. Secondary Fe-As phases were not present in As(III)-reacted GR, but a ferrous arsenate (parasymplesite, $Fe^{II}_3(As^{V}O_4)_2{\cdot}8H_2O$) formed in the As(V)-reacted GR sample, acting as an additional immobilization pathway for As(V). These new insights into As-GR interactions highlight the impact of GR on As mobility and toxicity in contaminated subsurface environments.

4.1 Introduction

'Green rust' (GR) phases are redox-active layered double hydroxides (LDHs), consisting of positively-charged Fe(II)-Fe(III) hydroxide layers separated by negatively-charged hydrated interlayers with anions (e.g., Cl^-, SO_4^{2-}, CO_3^{2-}) (Usman et al., 2018), and occasionally monovalent cations (Christiansen et al., 2009b; Christiansen et al., 2014). GR phases have been observed as steel corrosion products (O'Loughlin et al., 2003) but their prevalence in many natural anoxic and suboxic environments, for example in gley soils (Abdelmoula et al., 1998; Trolard et al., 1997), groundwaters (Christiansen et al., 2009a), ferruginous lakes (Koeksoy et al., 2019; Vuillemin et al., 2019; Zegeye et al., 2012), mofette sites (Rennert et al., 2012) and mine drainage sites (Bearcock et al., 2006; Johnson et al., 2014) are increasingly recognized. GR phases are nanoparticulate, and they have a point of zero charge around pH 8 (Guilbaud et al., 2013), and thus can act as essential mineral substrates for the removal of toxic oxyanions.

Among the most toxic oxyanions, arsenic (As) is often found in high concentrations in drinking and groundwaters where it poses a significant global environmental and public health concern (Vaughan, 2006; World Health Organization, 2017). Concentration of As in contaminated natural waters can be as high as 5,000 µg L^{-1}, while mining-influenced environments (e.g., groundwaters affected by mine drainage) can reach concentrations up to 850,000 µg L^{-1} (Smedley and Kinniburgh, 2002). These concentrations are of concern, especially because the World Health Organization limit for As in drinking water is 10 µg L^{-1} (World Health Organization, 2017), or even lower in some countries (e.g., Denmark, 5 µg L^{-1} (Ersbøll et al., 2018); Netherlands, 1 µg L^{-1} (Ahmad and Bhattacharya, 2019; Ahmad et al., 2018))

GR phases are among the most effective Fe (oxyhydr)oxides for As sequestration under anoxic conditions and circum-neutral to slightly alkaline pH (Perez et al., 2019a; Su and Wilkin, 2005), but a clear mechanistic understanding of the As-GR interaction process is still lacking. From extended X-ray absorption fine structure (EXAFS) analyses, it has been proposed that both As(III) and As(V) adsorb to GR edges as bidentate binuclear (^2C) and/or monodentate mononuclear (^1V) inner-sphere surface complexes (Jönsson and Sherman, 2008; Randall et al., 2001; van Genuchten et al., 2019b). Furthermore, As(III) has been reported to be able to form unique multi-nuclear oligomeric surface complexes on GR surfaces, with two As(III) pyramids binding to adjacent FeO_6 octahedra in a ^1V geometry forming an As-As dimer by sharing an oxygen atom (Ona-Nguema et al., 2009; Wang et al., 2010).

Such EXAFS data have indeed helped identify possible local bonding environments for GR surface adsorbed As species, but the lack of independent cross-confirming data to verify the EXAFS results led, not surprisingly, to contrasting interpretations (Jönsson and Sherman, 2008; Wang et al., 2010). Pinpointing the nano-scale interactions between GR surfaces and As species requires complementary analysis at high spatial resolution as afforded by (scanning) transmission electron microscopy (S/TEM). Only direct observations of mineral-metal surface interactions by S/TEM (Huang et al., 2018; Ling et al., 2017; Ling et al., 2018; Ling and Zhang, 2017; Thomas et al., 2018; Wang et al., 2011), combined with EXAFS bonding and structural information from pair distribution function

(PDF) analysis (Harrington et al., 2010; Li et al., 2011; van Genuchten and Peña, 2016), will lead to quantitative mechanistic information about As-GR interactions.

In this study, we document just that; we analyzed the interactions between As species [As(III) and As(V)] and synthetic GR sulfate and directly visualized the morphological changes and quantified the differences in elemental As distributions at GR binding sites through energy dispersive X-ray (EDX) mapping and high angle annular dark field (HAADF) imaging in STEM. This direct visualization was complemented by local structure data from high energy X-ray total scattering and PDF analysis and As oxidation state and local bonding environment data from As K-edge X-ray absorption spectroscopic (XAS). Based on these complementary datasets, we documented the differences and similarities in As(III) and As(V) adsorption in GR.

4.2 Experimental Section

GR sulfate was synthesized anoxically using well-documented methods (Géhin et al., 2002; Perez et al., 2019a; Perez et al., 2018). Freshly-precipitated GR slurries (~27 mM Fe_{tot}) were reacted with either As(III) or As(V) ($[As]_{initial} \approx 6.7$ mM) at pH ~7 for 5 days. The resulting solids were characterized by STEM imaging and spectral analyses using an FEI Titan Themis^3 G2 S/TEM operated at 300 kV and equipped with an FEI Super-X 4-detector silicon drift EDX system and a Gatan OneView 4K CMOS CCD. High energy X-ray total scattering data were collected at beamline 11-ID-B of the Advanced Photon Source (Argonne National Laboratory). Arsenic K-edge XAS data were obtained at beamline BM23 of the European Synchrotron Radiation Facility. Detailed information about anoxic sample preparation, analyses of total adsorbed As, as well as details of all solid-state characterization can be found in the Supporting Information (Section 4.4.1).

4.3 Results and Discussion

4.3.1 Localization of immobilized As and formation of secondary As phase

Freshly-precipitated GR particles form thin hexagonal plates, about 0.1-1 µm in diameter and 20-50 nm thick (Figure S4.1) (Freeman et al., 2019). After 5 days of reaction with As species, GR removed almost all (≥98% removal efficiency) of the initially added As species, consistent with our previous work (Perez et al., 2019a).

HAADF-STEM images of As(III)-reacted GR platelets revealed a bright rim (~10 nm wide, see arrows in Figure 4.1a) around the crystals, which was separated from the remaining GR particle by a darker band (ca. 20 to 30 nm wide, indicated by dashed lines). HAADF contrast correlates with particle thickness and atomic number (typical $Z^{\sim 1.7}$),(Bach et al., 2014) and thus STEM-EDX analysis was used to confirm whether or not the dark bands and bright rims were simply a different thickness compared to the rest of the GR particle or indeed compositionally different. The EDX maps (Figure 4.1b-d) and integrated intensity line profiles (Figure S4.2) across the darker bands confirmed that the absolute Fe, O and S signal intensities decreased significantly within the band compared to the bulk GR crystal, while the relative intensities remained constant. This suggests that the GR platelets were thinner in the darker bands, which is best explained by crystal dissolution. The

integrated intensities (Figure S4.2) were ~2.5-fold higher at the very rim, confirming that As was preferentially adsorbed at GR crystal edges (Figure 4.1e,f) (Jönsson and Sherman, 2008; Perez et al., 2019a; Wang et al., 2010). We suggest that the GR crystal can partially dissolve and form the dark bands because the amount of adsorbed As(III) does not fully cover all adsorption sites at the crystal edges. Noteworthy also that the dark dissolution bands are not continuous because some crystal edge areas exhibited substantially more As than other areas (green arrows in Figure 4.1a; red/yellow hotspots in Figure 4.1g), meaning the adsorbed As protected the underlying crystal from further dissolution.

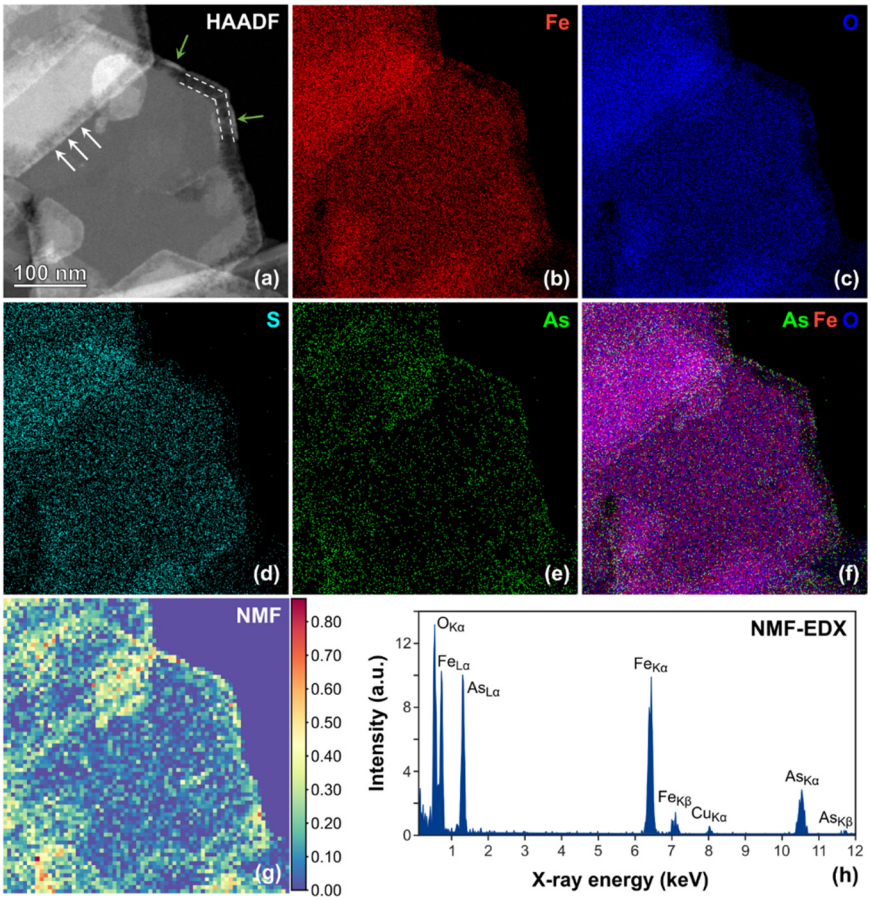

Figure 4.1. (a) HAADF-STEM image of As(III)-reacted GR and the corresponding EDX elemental maps: (b) Fe (red); (c) O (blue); (d) S (cyan); (e) As (green); and (f) combined As, Fe and O. (g) Non-negative matrix factorization (NMF) loading revealing As-rich areas and (h) the corresponding NMF factors related to the EDX spectra with high As Kα- and Lα-edges signal intensities (ca. 10.5 and 1.3 eV, respectively).

In contrary, the As(V)-reacted GR plates did not exhibit any dark bands/bright rims, but instead they were characterized by small dissolution cracks (Figure S4.3) and secondary thread-like structures (Figure 4.2a, S4.3) that were closely associated with the GR plates. EDX maps revealed no change in the bulk As(V)-reacted GR composition as evidenced by the near-homogeneous distribution of Fe, O and S across the GR plates (Figure 4.2f and S4.4). The thread-like structures were enriched in As (Figure 4.2e,f), suggesting that the secondary phase was As-bearing. Similar to As(III), the As EDX map of the As(V)-reacted GR also showed higher signals at particle edges, suggesting that these are the preferred adsorption sites for As(V) on GR (Sherman and Randall, 2003; Wang et al., 2010).

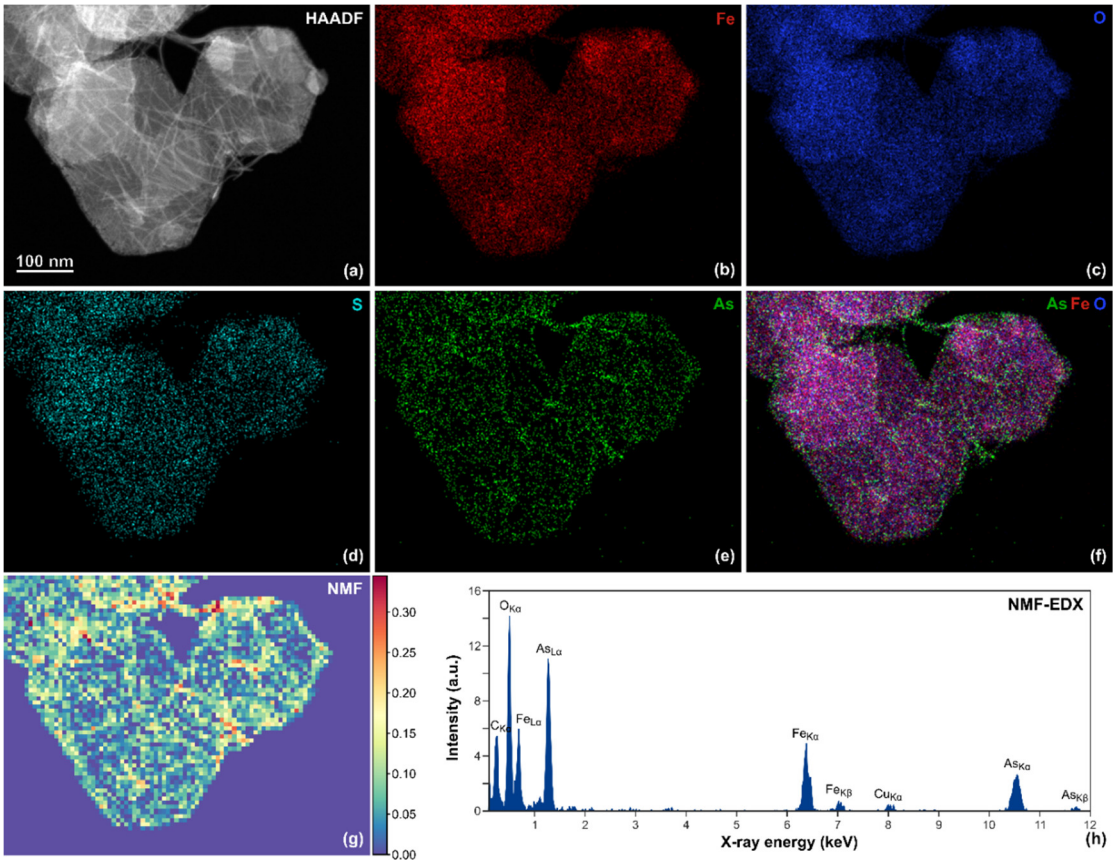

Figure 4.2. (a) HAADF-STEM image of As(V)-reacted GR and the corresponding EDX elemental maps: (b) Fe (red); (c) O (blue); (d) S (cyan); (e) As (green); and (f) combined As, Fe and O. (g) NMF loading revealing As-rich areas in the GR particles and (h) the corresponding NMF factors related to the EDX spectra with high As Kα- and Lα-edges signal intensities (ca. 10.5 and 1.3 eV, respectively).

Principal component analysis (PCA) and non-negative matrix factorization (NMF) of the EDX data (Cacovich et al., 2016) helped to identify differences in the signals within the elemental maps (see Figure 4.1g and 4.2g; Section 4.4.1). In the As(III)-reacted GR data, we identified 4 NMF components (i.e., different phases): (i) bulk GR crystal without As signal (Figure S5a), (ii) substrate carbon film (Figure S4.5b), (iii) GR crystal edges with high As peak intensity (Figure 4.1g,h) and (iv) bulk GR crystal with relatively small As peak intensity (Figure S4.5d). The As peak intensity at the GR edges (3rd component) was up to ~7-fold higher compared to that in the GR bulk crystal (4th component), confirming that As(III) is preferentially bound at the GR edges. For the As(V)-reacted GR, 3 NMF components were extracted: (i) bulk GR crystal without As contributions (Figure S4.6a), (ii) GR particle edges and thread-like structures with high relative As peak intensity (Figure 4.2g,h) and (iii) bulk GR crystal with a relatively low As peak intensity (Figure S4.6c). The high As signal in the thread-like structures clearly indicated that, besides the As adsorbed at the GR edges, a secondary As-bearing precipitate formed.

4.3.2 Structure of As-reacted green rust and formed secondary As phase

To determine what this secondary As-rich phase was, we employed high energy X-ray diffraction (XRD) analyses. The I(Q) patterns of the As(V)-reacted GR samples confirmed

the STEM observations and revealed that the secondary As-bearing phase was parasymplesite (Ito et al., 1954; Runčevski et al., 2015) (arrows in Figure 4.3a, middle pattern). To confirm the structure of this new phase, we prepared synthetic parasymplesite using a co-precipitation method (Johnston and Singer, 2007), and characterized it using S/TEM and conventional XRD analyses (Figure S4.7). The morphology of the synthetic parasymplesite is also thread/needle-like (Fig S4.7a,b), and equivalent to the secondary phase associated with the As(V)-reacted GR plates (Figure 4.2). This implies that the parasymplesite associated with our As(V)-reacted GR must have formed through the partial dissolution (Figure S4.3) of the initial As(V)-GR, releasing As(V) and Fe^{2+} (Jia et al., 2006; Wang et al., 2018). This released Fe^{2+} then formed a ternary complex with the As(V) surface complexes leading to surface precipitation of parasymplesite (Carlson et al., 2002; Tian et al., 2017), a similar process previously reported in experiments when As species were reacted with ferrihydrite (Jia et al., 2006), schwertmannite (Carlson et al., 2002) and siderite (Tian et al., 2017).

These observations were cross-confirmed by PDF analyses of the high energy X-ray total scattering data, where the G(r) of the pure and As-reacted GR samples exhibited similar structural coherence domains of 80 Å (Figure 4.3b), with the decay in peak oscillation mainly reflecting instrumental dampening (Figure S4.8). In all GR patterns, the peak at ~1.49 Å corresponds to the S-O bond of the SO_4^{2-} anions in the GR interlayer, while the peak at 1.69 Å in the As(V)-GR was attributed to the As^{V}-O pair of $As^{V}O_4^{3-}$. Meanwhile, the peaks at r-values between 2 and 4 Å (Figure 4.3b) correspond to atomic correlations within the Fe hydroxide sheet of GR. For example, the intense peaks at ~2.08 and ~3.18 Å match the first neighbor octahedrally-coordinated Fe-O and edge-sharing Fe-Fe pairs, respectively. The positions of these peaks are similar for the pure and As-reacted GR samples, confirming that the local coordination environment of Fe within the GR sheets did not change significantly during the reaction.

In the PDFs, slight peak broadening and some asymmetry is visible in the Fe-Fe peak at ~3.18 Å of the As-reacted GRs (Figure 4.3b). This may be attributed to atomic correlations from adsorbed As, and from parasymplesite in the case of As(V)-reacted GR. We calculated the differential PDFs, which has proven a very useful approach for identifying surface complexes on minerals (Harrington et al., 2010; Li et al., 2011; van Genuchten and Peña, 2016) or surface coatings on nanoparticles (Mangayayam et al., 2019) The first clear peak in our d-PDF of As(III)-GR (red pattern, Figure 4.3c) matches the As-O atomic pair (r ≈ 1.80 Å) of the $As^{III}O_3$ pyramid, while peaks at 3.10 and 3.45 Å fit with As^{III}-Fe atomic correlations for mononuclear edge-sharing ^2E and bidentate binuclear ^2C inner-sphere surface complexes, respectively (Jönsson and Sherman, 2008; van Genuchten et al., 2012b). The d-PDF of As(V)-GR (blue pattern, Figure 4.3c), instead, shows a peak (r ≈ 1.69 Å) that matches the atomic distance of As-O in tetrahedral $As^{V}O_4$. In addition, a second asymmetric peak (r ≈ 3.39 Å; arrow in Figure 4.3c) indicated the presence of multiple As(V)-Fe distances. We know from the complementary analyses that this sample contains parasymplesite, and thus this peak was fitted with three sub-peaks (based on the crystal structure from Runčevski et al. (2015), Figure S4.8b), yielding r-values of ~3.30, 3.39 and 3.52 Å. Noteworthy that the peak at ~3.4 Å also matches the As^{V}-Fe pair distance

for ^{2}C surface complexes (~3.4 Å) (Jönsson and Sherman, 2008; Randall et al., 2001; Wang et al., 2010).

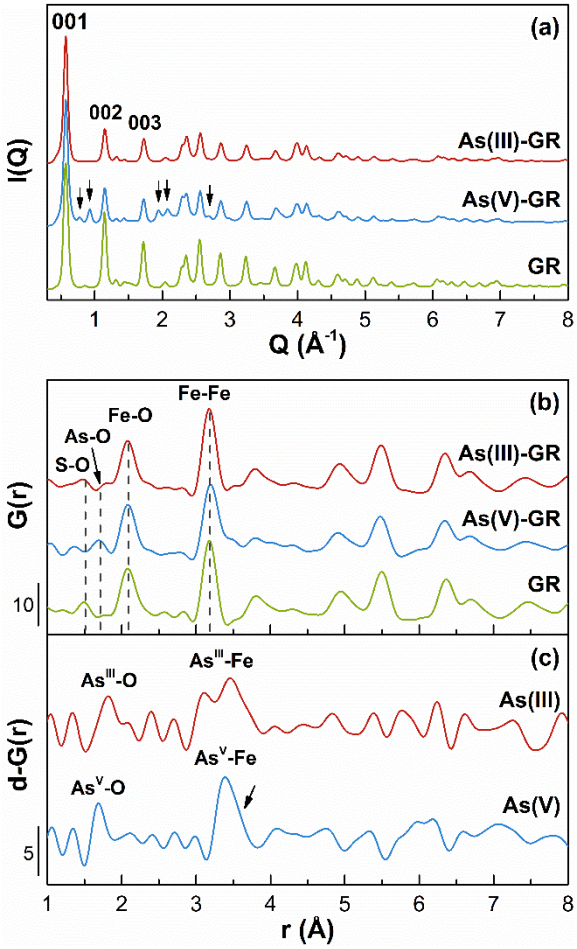

Figure 4.3. (a) High energy XRD patterns [I(Q)] of pure and As-reacted GR. All peaks represent GR, except those marked with arrows which correspond to parasymplesite [$Fe^{II}_3(As^{V}O_4)_2{\cdot}8H_2O$]; (b) PDFs [G(r)] of the low r-value region showing the short-range structure of the solids. The full PDFs are shown in Figure S4.8a. (c) The differential PDFs (d-PDFs) [d-G(r)] were obtained by subtracting the PDF of pure GR from the As-reacted samples to isolate atomic correlations arising from adsorbed species and/or surface precipitates. Prior to subtraction, the individual PDFs were normalized to have identical intensities of the first neighbor Fe-O pairs (~2 Å).

4.3.3 Bonding environment of immobilized As species

Although STEM and PDF analyses gave us highly quantitative information about the structure and adsorbed species of the As(III)- and As(V)-reacted GR, we combined these results with As K-edge XAS data (XANES and EXAFS) to determine if any changes in the As oxidation state occurred during the 5-day reaction with GR and confirm the As adsorption geometry using shell-by-shell fits (Figure S4.9). Our XANES observations (Figure S4.9a) support previous studies that have shown that GR cannot oxidize As(III) or reduce As(V) (Jönsson and Sherman, 2008; Randall et al., 2001; van Genuchten et al., 2019b; Wang et al., 2010). It is noteworthy, however, that As(III) oxidation to As(V) under anoxic conditions has been reported for other iron-bearing minerals such as siderite (Tian

et al., 2017), Fe(II)-bearing nontronite (Ilgen et al., 2012; Ilgen et al., 2017), lepidocrocite (Wang and Giammar, 2015) and goethite (Amstaetter et al., 2010). Furthermore, As(V) reduction has been observed during Fe^{2+}-catalyzed transformations of Fe-bearing minerals wherein GR has been found as an intermediate phase (Karimian et al., 2017; Perez et al., 2019b; van Genuchten et al., 2019a).

Table 4.1 Summary of shell-by-shell fitting results for As-reacted GR samples.

Sample	Atomic Pairs	CN	R (Å)	σ^2 (Å^2)	ΔE_0 (eV)	R-factor
As(III)	As-O	2.9 (0.2)	1.77 (0.002)	0.002 (0.0005)	9.8 (0.1)	15.1
	As-O-O	6	1.82(R_{As-O}) = 3.23	σ^2 (As-O)		
	As-Fe	3.2 (0.4)	3.40 (0.01)	0.008		
As(V)	As-O	4.2 (0.3)	1.69 (0.01)	0.002	5.7 (2.1)	509.5
	As-O-O	12	1.82(R_{As-O}) = 3.07	σ^2 (As-O)		
	As-Fe	4.1 (1.7)	3.34 (0.03)	0.008		
	As-Fe	2.0 (3.0)	3.51 (0.08)	0.008		

Note: CN - coordination number, R - interatomic distance, σ^2 - mean-squared atomic displacement and ΔE_0 - change in threshold energy. The passive electron reduction factor (S_0^2) was fixed at 1.0. The multiple scattering As-O-O path was constrained geometrically to the single scattering As-O path (R_{As-O-O} = 1.82 R_{As-O}). All fits were carried out from 1 to 4 Å in R+ΔR-space. The number of independent points (N_{IDP}) in the fits was 19.8 and the number of variables (N_{Var}) was 6.

The first-neighbor contribution to the EXAFS fit for As(III)-GR spectra is consistent with As-O atomic correlation in an $As^{III}O_3$ pyramid (Shannon, 1976) with a coordination number (CN) of ~3 and an interatomic distance (R) of 1.77 ± 0.01 Å (Figure S4.9c). For the second-neighbor contribution, three possible geometries were considered in the fit corresponding to inner-sphere surface complexes of As(III) at the GR particle edges (see also Figure S4.10): (1) monodentate mononuclear ^1V geometry (R_{As-Fe} ≈ 3.5 Å); (2) bidentate binuclear ^2C geometry (R_{As-Fe} ≈ 3.4 Å); and (3) mononuclear edge-sharing ^2E geometry (R_{As-Fe} ≈ 3.0 Å) (Ona-Nguema et al., 2005). The As-Fe path corresponding to a monodentate ^1V geometry was not supported by the fit, which yielded unrealistically high R_{As-Fe} values (see Table S4.1). The predicted dominant second-neighbor contribution was the bidentate ^2C geometry (R_{As-Fe} = 3.40 ± 0.01 Å, CN_{As-Fe} = 3.2 ± 0.4), which also complements our d-PDF data for As(III)-GR (Figure 4.3c). This fit yielded physically reasonable parameters with low fit-derived standard errors (reduced chi-square χ^2) and a low R-factor (≤ 0.05, see Table 4.1) (Kelly et al., 2008a). A second As-Fe path corresponding to the edge-sharing ^2E geometry was also added but did not result in a statistically improved fit (i.e., the decrease in reduced χ^2 with two As-Fe paths did not pass the test of statistical significance (Kelly et al., 2008a)) although an atomic pair at 3.1 Å was observed in the d-PDF (Figure 4.3c). Because As(III) dimers have been previously reported to form on GR surfaces, we attempted to fit an As-As path consistent with an As(III) dimer (R_{As-As} ≈ 3.3 Å, CN_{As-As} = 2). This fit, however, yielded an overlap of the two atomic correlations (i.e., As-Fe and As-As) near ~3.4 Å, indicating that the fit did not support the presence of both As-Fe atomic pairs and As-As dimers. When the second-neighbor contribution was first fitted with the edge sharing ^2E geometry instead of the ^2C geometry and an As(III) dimer was added in a second fitting step, the resulting fit yielded

reasonable fitting parameters. However, based on previous work (Ona-Nguema et al., 2009; Wang et al., 2010), an As-As dimer requires two adjacent As(III) pyramids bound in the ^1V geometry. Since the ^1V geometry was not accepted by our fits, and considering the geometrical constraints imposed on As(III), when bound in the ^2E geometry, we argue against the presence of both As-Fe and As-As bonds in our data. Therefore, we suggest that the dominant surface complex in the As(III)-reacted GR was present in the ^2C geometry, with As(III) dimers and edge-sharing ^2E surface complexes constituting a very minor species, if at all present.

For As(V)-GR, the first-neighbor contribution to the EXAFS fit corresponds to the As-O atomic correlation for tetrahedral $As^{V}O_4^{3-}$ ($R_{As\text{-}O} = 1.69 \pm 0.01$ Å, $CN_{As\text{-}O} = 4.2 \pm 0.3$). Again, there are two possible bonding geometries (see Figure S4.10) for the second-neighbor contribution: (1) ^1V geometry ($R_{As\text{-}Fe} \approx 3.5$ Å) and (2) ^2C geometry ($R_{As\text{-}Fe} \approx 3.4$ Å). In addition to these, atomic correlations from the As-Fe pairs of parasymplesite ($R_{As\text{-}Fe} \approx 3.30$, 3.34, 3.45 Å, each with $CN_{As\text{-}Fe} = 2$) have to also be considered (Runčevski et al., 2015). Similar to As(III), the fits revealed that ^2C surface complexes ($R_{As\text{-}Fe} = 3.35 \pm 0.02$ Å, $CN_{As\text{-}Fe} = 2.9 \pm 1.0$) were the dominant bonding geometry for As(V), which confirms our d-PDF observations (Figure 4.3c). The calculated $CN_{As\text{-}Fe}$ is higher than the expected value for a ^2C geometry. This can be attributed to the additional As-Fe pair of parasymplesite, and therefore, a second As-Fe path was added to account for the precipitated parasymplesite ($R_{As\text{-}Fe} \approx 3.3$ Å, $CN_{As\text{-}Fe} \approx 5$). This resulted in a good R-factor, yet not statistically significantly better fit compared to the initial sole ^2C geometry fitting parameter values: (i) $R_{As\text{-}Fe1} = 3.34 \pm 0.03$ Å, $CN_{As\text{-}Fe1} = 4.1 \pm 1.7$ and (ii) $R_{As\text{-}Fe2} = 3.51 \pm 0.08$ Å, $CN_{As\text{-}Fe2} = 2.0 \pm 2.0$). Hence, we employed a linear combination fitting (LCF) approach of the EXAFS data using As(V)-adsorbed GR (van Genuchten et al., 2019b) and parasymplesite references and this revealed that ~87% of As(V) in the solids were present as parasymplesite, while the remaining ~13% accounts for the adsorbed As(V) species (see LCF results and statistics in Table S4.2 and Figure S4.11).

Our EXAFS results cross-correlate and confirm the STEM-EDX and d-PDF observations that the thread-like phase (Figure 4.2) was indeed the secondary As-rich precipitate parasymplesite. This secondary phased formed through a so far not described mechanism. Upon reaction of the GR with the As(V) solution, GR was partially dissolved and released some Fe^{2+}, which then combined with the largest proportion of the initial aqueous As(V) and precipitated as the thread-like secondary parasymplesite.

4.3.4 Implications on fate of arsenic in the environment

Our high-resolution STEM images and elemental maps combined with the PDF and XAS data documented new, nano-scale information about the mechanisms of As binding onto GR particle edges (Figure 4.1 and 4.2). Both As(III) and As(V) adsorbed to GR particle edges primarily as bidentate binuclear ^2C inner-sphere surface complexes (Figure 4.3 and S4.9). Although not unequivocal, our data also does not suggest the formation of multi-nuclear As(III) oligomers on GR_{SO4} edges, which is contrary to findings on GRs intercalated with other anions (e.g., chloride or carbonate) (Ona-Nguema et al., 2009; Wang et al., 2010). We also showed that parasymplesite (a ferrous arsenate nanophase), formed through

the dissolution of the GR particles in the As(V)-reacted sample. Although the GR_{SO4} used in this study clearly can efficiently adsorb As, changes in pH and redox conditions can cause potential re-release of As back into the environment. However, the re-sequestration of As through the precipitation of secondary As-bearing mineral phases such as parasymplesite, which themselves have a high As content, are highly stable and poorly soluble, can thus further decrease the mobility of As in anoxic, Fe^{2+}-rich groundwaters and sediments (Johnston and Singer, 2007; Raghav et al., 2013). Overall, our results provide new crucial mechanistic insights into how redox-active minerals, such as GR phases, interact with As species and their potentially critical role in controlling the toxicity and mobility of As in contaminated subsurface environments.

4.4 Supporting Information

4.4.1 Material synthesis and batch experiments

GR_{SO4} was synthesized at room temperature inside an anaerobic chamber (97% N_2, 3% H_2, Coy Laboratory Products, Inc.) using a co-precipitation method (Géhin et al., 2002; Perez et al., 2019a) In brief, a mixture of 0.3 M $(NH_4)_2Fe^{II}(SO_4)_2{\cdot}6H_2O$ and 0.1 M $Fe^{III}_2(SO_4)_3$ solutions (~pH 2) was slowly titrated with 0.3 M NaOH until pH 8. The resulting dark-blue green suspension was stirred and aged further for 1 h. The synthetic GR suspension was washed with deoxygenated ultrapure water (Milli-Q) by centrifugation and re-suspension. The washed GR suspension was used for batch experiments within the day of synthesis. The washed GR_{SO4} suspension (~27 mM Fe_{total}) was mixed with either As(III) or As(V) solutions (~6.7 mM $[As]_{initial}$), prepared from ACS reagent grade $NaAsO_2$ and $Na_2HAsO_4{\cdot}7H_2O$, in headspace crimp vials. The pH of the GR suspension and As stock solutions were adjusted to pH 7 with either HCl or NaOH prior to batch experiments. The vials were shaken on an orbital shaker at 250 rpm, at room temperature for 120 h. Separation of the solid and the liquid phases was done by centrifugation and filtration through 0.22-µm polycarbonate (PC) membrane filters. The obtained liquid phases were acidified (pH ~2 with VWR ARISTAR® grade HNO_3) and stored at 4°C until analysis. The elemental composition of the liquid phases was determined using inductive coupled optical emission spectrometry (ICP-OES Varian 720ES), as previously described in Perez et al. (2019a) The solids were dried in a desiccator inside the anaerobic chamber, and ground and stored until used for solid-state characterization.

Parasymplesite was also synthesized inside the anaerobic chamber using the co-precipitation method described by Johnston and Singer (2007). Briefly, a mixture of 5 mM $(NH_4)_2Fe^{II}(SO_4)_2{\cdot}6H_2O$ and 3 mM $Na_2HAsO_4{\cdot}7H_2O$ was titrated with 1 M NaOH to pH ~7.5. The mixture was aged for 1 h, and then filtered using 0.22-µm PC membrane filters. The collected solid was dried in a desiccator inside the anaerobic chamber, and ground and stored until used for solid-state (see Figure S4.7).

(Scanning) transmission electron microscopy (S/TEM)

Samples for S/TEM were prepared in an anaerobic chamber by diluting the GR_{SO4} suspension with O_2-free Milli-Q water, and drop-casting ~10 µL aliquots onto holey amorphous carbon Cu grids (Agar Scientific Ltd.). The samples were dehydrated with a drop of ethanol, and allowed to further dry inside the anaerobic chamber. Samples were transferred to the TEM laboratory in a grid box inside an anaerobic jar (AnaeroJar™ Oxoid™, Thermo Fisher Scientific), and the Cu grids were immediately loaded into a double tilt FEI TEM holder and inserted into the TEM.

High angle annular dark field scanning electron microscopy (HAADF-STEM) images and energy dispersive X-ray (EDX) spectra and maps were recorded in an FEI Titan^3 Themis G2 S/TEM operating at 300 kV with an FEI Super-X 4-detector EDX system, a Gatan One-View CCD and a Gatan Quantum 965 ER imaging filter. The specimens were stable under the electron beam and no significant changes in morphology or crystal

structure were observed during data acquisition (< 15 min per region of interest) (Freeman et al., 2019).

Principal component analysis (PCA) and non-negative matrix factorization (NMF) were carried out on the acquired EDX maps to separate different phases present in the spectral image. The analyses was carried out using the Python library HyperSpy (dela Peña et al., 2019) by loading the spectral image into HyperSpy and then cropping the energy signal between 0.1 and 12 keV to remove the large EDX peak found at 0 keV and to reduce the size of the dataset. The As(III) data contained information from 198 frames while the As(V) data contained information for 108 frames. To provide sufficient EDX signal for each data point, the data was binned in x and y spatial dimensions by a factor of 8 and 6 respectively, and by a factor of 4 in the energy dimension. After binning the data, PCA was performed by finding the highest variability within the data and ordering it so that the first principal component explains the largest amount of variance, the second component the second largest, etc. Each principal component can then be plotted to show the decomposed EDX signal and an image that shows the position that the decomposed signal arises. One difficulty with using just PCA is in assigning physical meaning to the results due to negative EDX signals. NMF is one method that can be applied to the PCA results allowing a physical interpretation to be applied to the results. In this case, NMF forces the decomposed signals into having positive values. The first 4 NMF components for the As(III) dataset and first 3 NMF components for As(V) are shown in Figure S4.5 and S4.6, respectively.

High energy X-ray total scattering

The local structure of the solids was investigated using pair distribution function (PDF) analysis, following X-ray total scattering analyses. Dry powders of each sample were loaded inside the anaerobic chamber into glass capillaries and sealed with paraffin to prevent oxidation during sample transport and data collection. This procedure prevents oxidation of highly reactive amorphous iron carbonates for at least one week (Dideriksen et al., 2015). X-ray total scattering data were collected at beamline 11-ID-B at the Advanced Photon Source (Argonne National Laboratory, USA) using an X-ray wavelength of 0.2128 Å and a PerkinElmer amorphous Si 2D detector (40 x 40 cm, placed ~18 cm away from the sample). Calibration of the geometry of the setup was conducted from measurement of CeO_2 standard powder with the software Fit-2D (Hammersley et al., 1996; Hammersley et al., 1994), which was also used to correct for polarization and to transform the data to 1D. PDFs were obtained with PDFgetX2 (Qiu et al., 2004) using standard corrections such as subtraction of background (from measurement of empty glass capillary tubes) and incoherent scattering as well as corrections for nonlinearity in the detector response. The Fourier transformation of the reduced total scattering structure function, $F(Q)$, was conducted using Q_{max} of 24 $Å^{-1}$. Differential PDFs (d-PDFs) were obtained by subtracting the PDF of pure GR from the As-reacted samples to isolate atomic correlations arising from adsorbed species and/or surface precipitates. Prior to subtraction, the individual PDFs were normalized to have identical intensities at the first neighbor Fe-O pairs (~2 Å).

X-ray absorption spectroscopy (XAS)

Dry powders of each solid samples were transported to the XAS beamline inside air-tight headspace crimp vials stored inside an anaerobic jar to prevent oxidation during sample transport. Prior to data collection, pellets were prepared inside a station glovebox (MBRAUN, Ar atmosphere) by mixing ~25 mg of dry sample with ~45 mg cellulose using an agate mortar and pestle. Mixture calculations were done using XAFSmass software (Klementiev). The pellets were sealed inside sample holders made of 2 layers of single-sided 70-µm thick Kapton® polyimide tape. The Kapton-sealed samples were fixed onto a beamline custom-specific sample holder and transferred to the station using the anaerobic jar.

Arsenic K-edge XAS data were collected at BM23 of the European Synchrotron Radiation Facility (ESRF, Grenoble, France) (Mathon et al., 2015). Spectra were recorded at liquid nitrogen temperatures (77 K) both in transmission and fluorescence mode out to a reciprocal space value of 14 $Å^{-1}$. For this, a cryostat was used with helium convection. Fluorescence data were collected using a 13-element Ge solid-state detector. The vertical dimension of the X-ray beam during data collection was 1 mm and the horizontal dimension was 2 mm. To prevent second-order harmonics, rejection mirrors were used. A Si(111) crystal pair with a fixed beam exit was used as a monochromator and the maximum in the first derivative of an Au foil was used to calibrate the beam at 11919 eV (Au L_3 edge). The XANES region was measured with 0.35 eV steps. About 4 to 6 scans were collected for each sample depending on data quality. During data collection, changes in line shape and peak position indicative of beam-induced redox reactions were examined and no beam damage was observed. Spectra were aligned, averaged, and background-subtracted using the SIXpack software.(Webb, 2005)

Shell-by-shell fits (Table S4.1) were performed from 1 to 4 Å in R+ΔR-space using SIXPack software (Webb, 2005) based on algorithms derived from IFEFFIT (Newville, 2001). The fits typically included the interatomic distance (R), the coordination number (CN), the mean squared atomic displacement parameter (σ^2), and the change in threshold energy (ΔE_0) for one sample. Phase and amplitude functions for single and multiple scattering paths were calculated using FEFF6 (Rehr et al., 1992) and included As-O, As-O-O and As-Fe paths derived from the structure of scorodite (Kitahama et al., 1975). In preliminary fits, the CN and σ^2 were found to be highly correlated, which produced high fit-derived standard errors in these fitting parameters. Therefore, following previous work (Mikutta et al., 2010; van Genuchten et al., 2012a), we constrained σ^2 to 0.008 in the second shell fits (As-Fe path) to reduce the high correlations. Consistent with previous work (Mikutta et al., 2010; Paktunc et al., 2008), the passive electron reduction parameter, S_0^2, in each fit was set to 1.0. The goodness-of-fit was assessed based on the R-factor, which is defined as the mean square difference between the fit and the data on a point-by-point basis: $R = \sum_i (data_i - fit_i)^2 / \sum_i (data_i)^2$. An R-factor <0.05 is considered to reflect a reasonable fit (Kelly et al., 2008b).

Linear combination fits (LCFs) (Figure S4.10) were performed with SIXPack software using the *k*-range of 2 to 12.5 $Å^{-1}$. Two references were used in the LCFs. The first was a previously published As(V)-adsorbed GR standard prepared by adsorbing As(V) to GR

sulfate (As/Fe ratio = 0.03) (van Genuchten et al., 2019b). Shell-by-shell fits of this reference revealed fitting parameters consistent with As(V) adsorbed in the ^{2}C geometry ($CN_{As\text{-}Fe} = 3.1 \pm 0.9$ and $R_{As\text{-}Fe} = 3.38 \pm 0.02$ Å). The other reference was the As K-edge EXAFS spectrum of the parasymplesite mineral synthesized as part of this work.

4.4.2 Supplementary figures

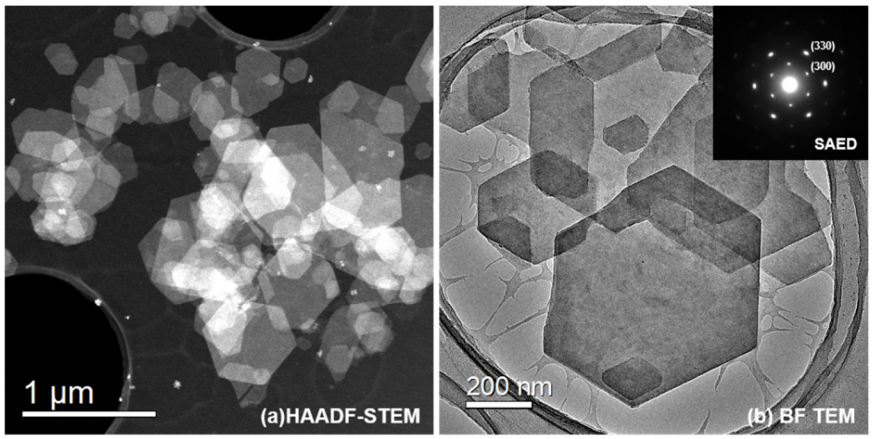

Figure S4.1 (a) HAADF-STEM and (b) bright field (BF) TEM images of freshly-precipitated, pure GR sulfate, with an SAED pattern of a single crystal from (b) in the inset.

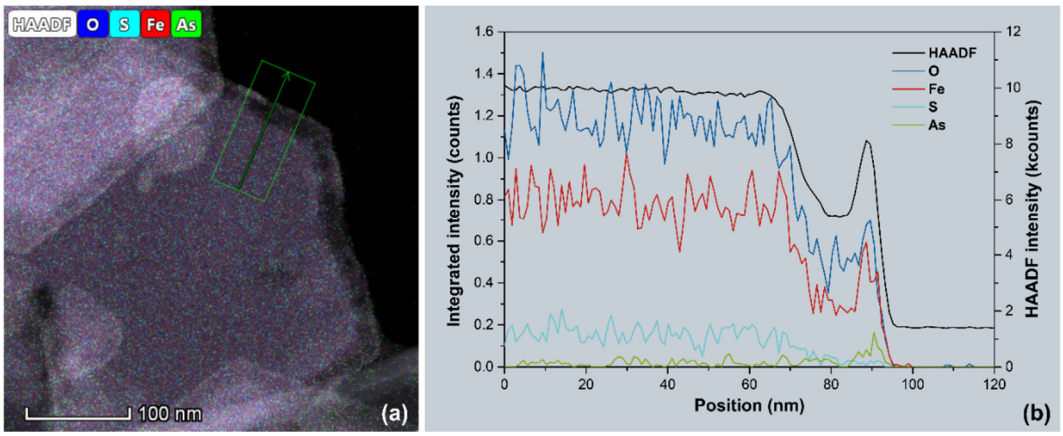

Figure S4.2 (a) Combined HAADF image and EDX elemental maps of As(III)-GR. (b) The integrated EDX signal intensity profiles show the change in elemental concentrations along the line drawn across the marked area in green (a).

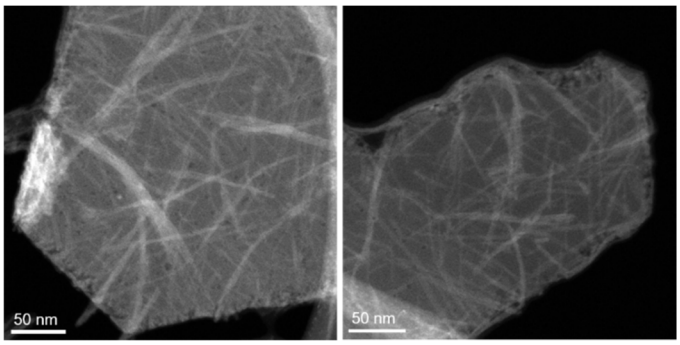

Figure S4.3 HAADF-STEM images of As(V)-reacted GR samples showing the dissolution features at the particle edges and the newly-formed thread-like structures.

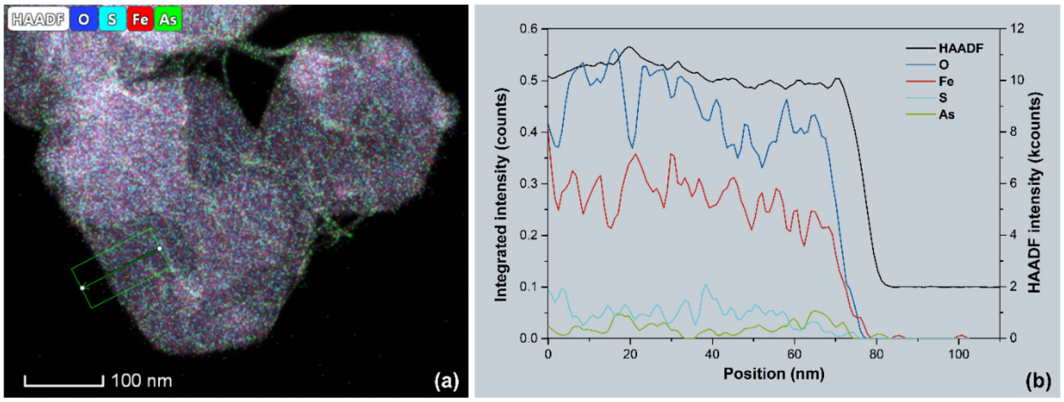

Figure S4.4 (a) Combined HAADF image and EDX elemental maps of As(V)-GR. (b) The integrated EDX signal intensity profiles show the change in elemental concentrations along the line drawn across the marked area in green (a) revealing no sharp change across the edge of the GR particle.

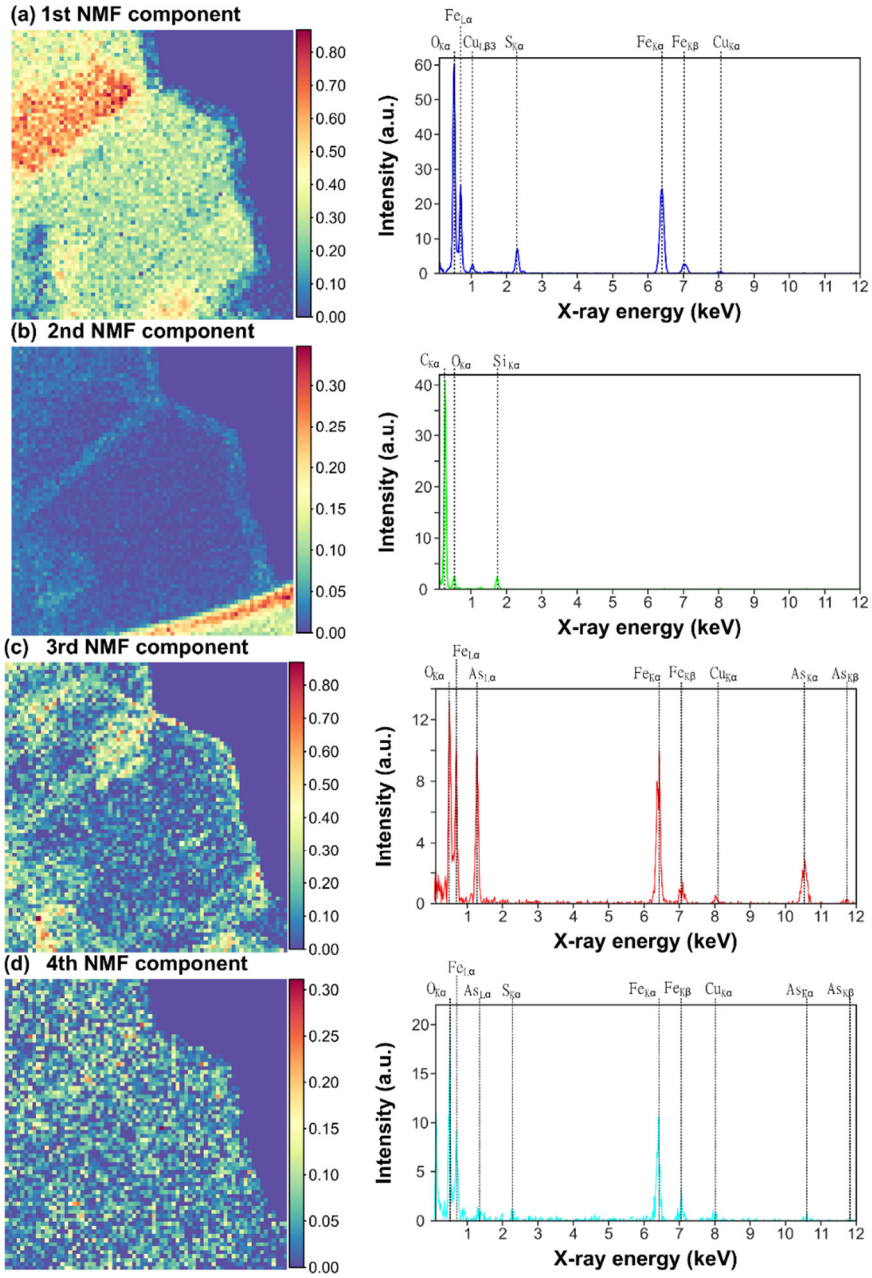

Figure S4.5 NMF results from As(III)-reacted GR: (a) first component shows the spectra for the bulk GR crystal with no As signal and the dissolution edge; (b) the second component shows the carbon film; (c) the third component shows a larger relative As peak in the spectra around the edges of the particle dissolution edge where there is an As rich signal (ca. 1.3 eV); and (d) the fourth component shows the bulk GR crystal, similar to (i) but with a relatively small As peak.

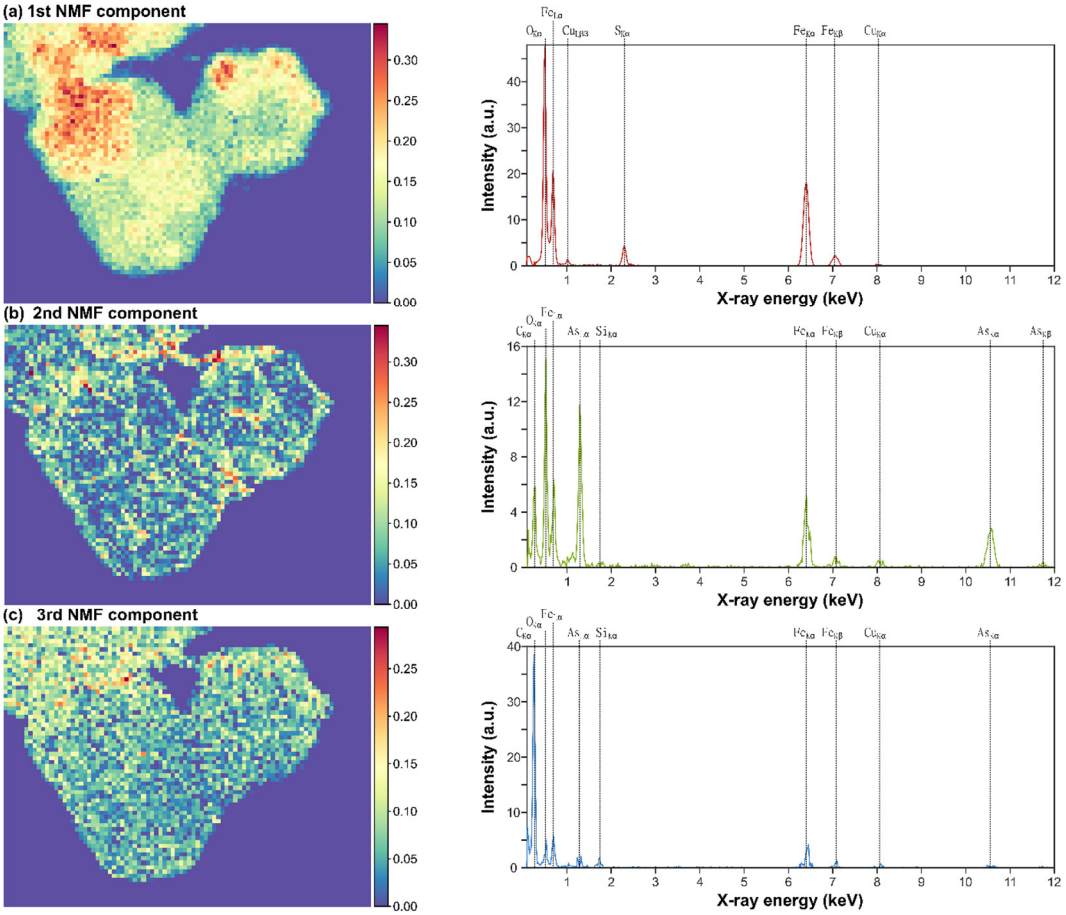

Figure S4.6 NMF results from As(V)-reacted GR: (a) the first component shows the spectra for the bulk GR crystal with no As signal; (b) the second component shows areas with high As content – at the particle edges and the thread-like phases; and (c) the third component shows the bulk GR crystal with a relatively small As peak compared to Fe peak.

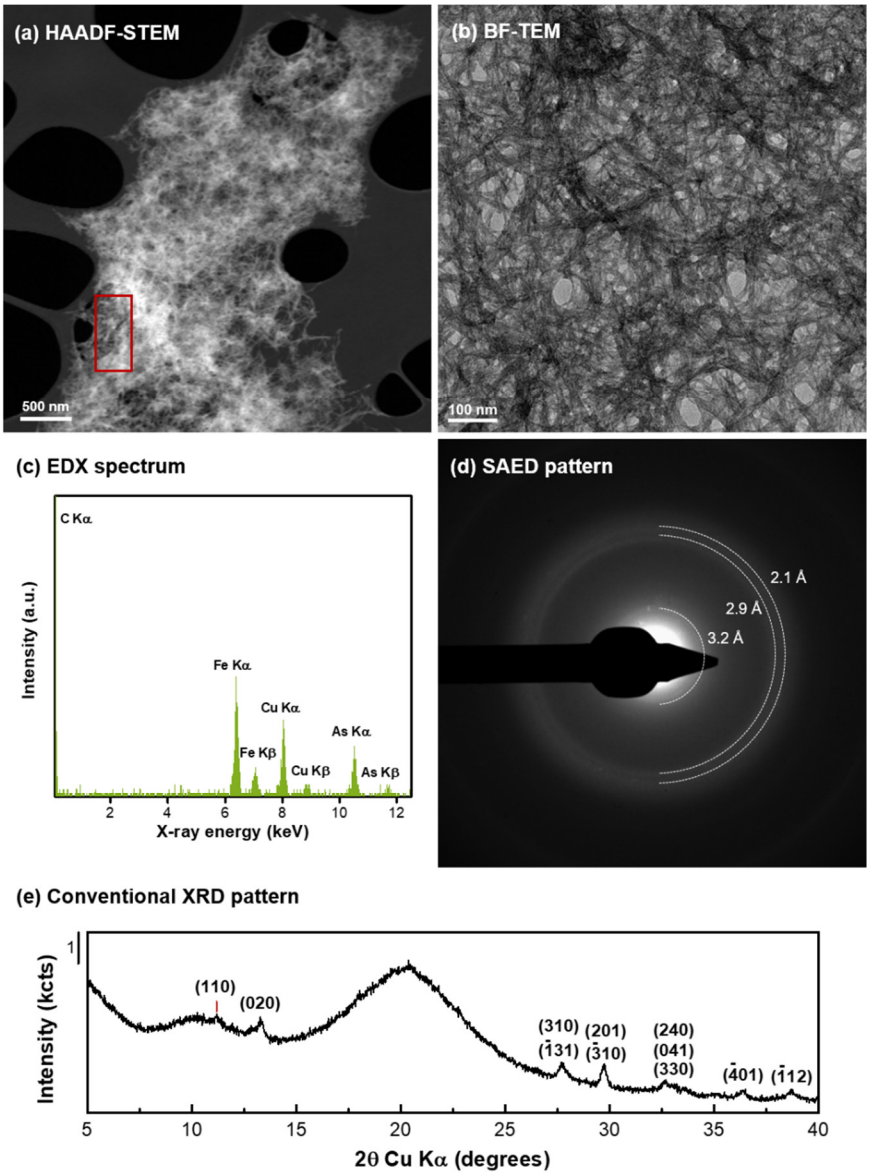

Figure S4.7 Material characterization data for the synthesized parasymplesite ($Fe^{II}_3(As^{V}O_4)_2{\cdot}8H_2O$) used as a reference material for the XAS fitting. The (a) HAADF-STEM and (b) BF-TEM images both show thin, thread-like structures. (c) EDX analysis, collected from the red marked area in (a), confirmed that these structures are composed of Fe and As. The (d) SAED pattern of the marked area in (b), and the (e) XRD pattern of the sample both correspond to the structure of parasymplesite indexed by Mori and Ito (1950).

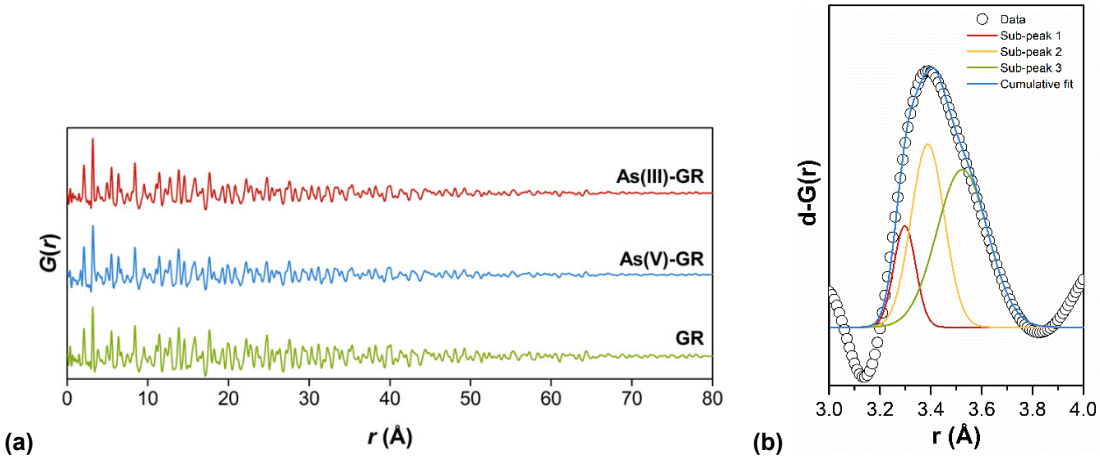

Figure S4.8 (a) PDFs [$G(r)$] of the pure GR_{SO4} and As-reacted GR_{SO4} samples showing the short- and medium-range structure of the solids. (b) Components of the d-PDF peak at ~3.4 Å of the As(V)-reacted GR.

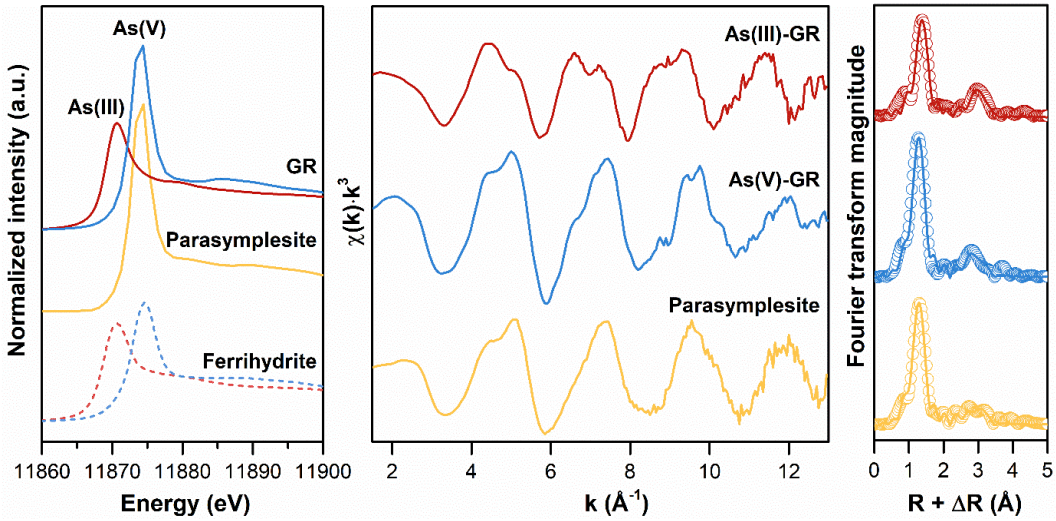

Figure S4.9 Arsenic K-edge XAS of As-reacted GR samples recorded at ~77 K. (a) XANES spectra of the reacted solids and the reference materials (i.e., parasymplesite, As(III) and As(V) adsorbed onto ferrihydrite); (b) k^3-weighted $\chi(k)$ EXAFS spectra; and (c) Fourier-transformed EXAFS spectra. The shell-by-shell fitting output (solid line) is superimposed on the experimental data (open circles) and the shell-by-shell fitting results are given in Table S4.1.

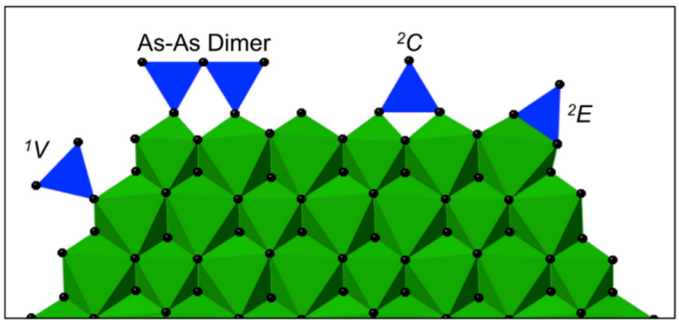

Figure S4.10 Possible coordination geometries for inner-sphere surface complexes of As(III) and As(V) at the GR particle edges: (i) monodentate mononuclear (^1V) geometry; (2) bidentate binuclear (^2C) geometry; (iii) mononuclear edge sharing (^2E) geometry; and (iv) $As^{III}_2O_5$ dimers.

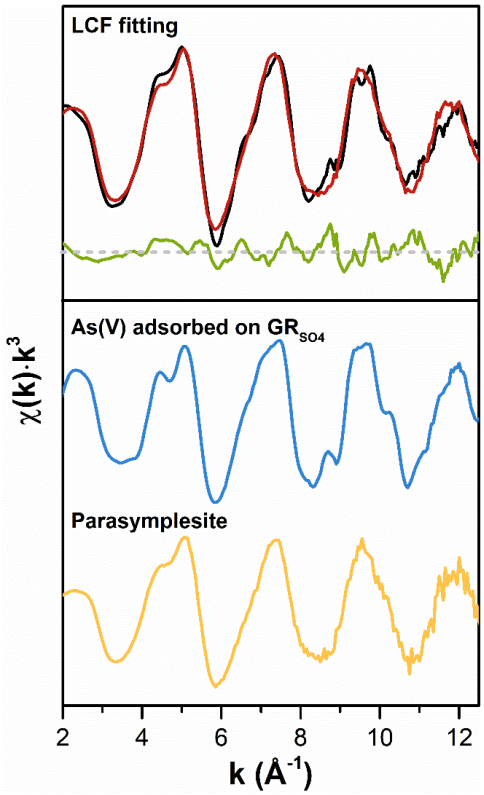

Figure S4.11 k^3-weighted χ(k) As K-edge EXAFS spectra of As(V)-reacted GR (black). Fits (red) are least-squares linear combinations of the reference materials (2 patterns at the bottom): As(V) adsorbed on GR_{SO4} (blue; ^{2}C geometry) and parasymplesite (yellow). Fit boundaries are within the k-value of 2 and 12.5 Å^{-1}. The residuals (green) refers to the difference between the experimental data and the fitted spectra.

4.4.3 Supplementary tables

Table S4.1 Summary of shell-by-shell fitting results for As(III)- and As(V)-reacted GR and synthetic parasymplesite. Entries in color blue denote the dominant bonding geometry for inner-sphere surface complexes of As(III) and As(V). Fitting parameters allowed to float are accompanied by fit-determined standard errors in parenthesis while constrained parameters appear without a parenthesis.

Bonding geometry	Atomic Pairs	CN	R (Å)	σ^2 (Å^2)	ΔE_0 (eV)	Red. χ^2	R-factor
As(III)-GR							
^1V	As-O	2.9 (0.5)	1.78 (0.01)	0.002 (0.001)	9.5 (2.4)	84.0	0.094
	As-O-O	6	1.82(R_{As-O}) = 3.23	σ^2 (As-O)			
	As-Fe	1.5 (1.2)	3.78 (0.05)	0.008			
^2C	As-O	2.9 (0.2)	1.77 (0.002)	0.002 (0.0005)	9.8 (0.1)	15.1	0.017
	As-O-O	6	1.82(R_{As-O}) = 3.23	σ^2 (As-O)			
	As-Fe	3.2 (0.4)	3.40 (0.01)	0.008			
^2E	As-O	2.9 (0.5)	1.78 (0.01)	0.002 (0.001)	10.7 (2.3)	83.3	0.093
	As-O-O	6	1.82(R_{As-O}) = 3.23	σ^2 (As-O)			
	As-Fe	0.9 (0.6)	2.99 (0.05)	0.008			
^2C + ^2E	As-O	2.9 (0.2)	1.77 (0.01)	0.002 (0.001)	9.7 (1.0)	16.4	0.016
	As-O-O	6	1.82(R_{As-O}) = 3.23	σ^2 (As-O)			
	As-Fe	0.2 (0.3)	2.89 (0.06)	0.008			
	As-Fe	3.2 (0.4)	3.40 (0.01)	0.008			
^2C + As dimer	As-O	2.9 (0.2)	1.77 (0.01)	0.002 (0.001)	9.7 (0.1)	17.4	0.017
	As-O-O	6	1.82(R_{As-O}) = 3.23	σ^2 (As-O)			
	As-Fe	2.7 (1.5)	3.39 (0.05)	0.008			
	As-As	0.6 (1.9)	3.37 (0.15)	0.008			
^2E + As dimer	As-O	3.0 (0.2)	1.77 (0.01)	0.002 (0.001)	9.8 (0.1)	16.6	0.016
	As-O-O	6	1.82(R_{As-O}) = 3.23	σ^2 (As-O)			
	As-Fe	0.6 (0.3)	2.90 (0.03)	0.008			
	As-As	3.1 (0.4)	3.35 (0.01)	0.008			
As(V)-GR							
^2C	As-O	4.2 (0.3)	1.69 (0.01)	0.002	5.3 (2.0)	475.31	0.058
	As-O-O	12	1.82(R_{As-O}) = 3.08	σ^2 (As-O)			
	As-Fe	2.9 (1.0)	3.35 (0.02)	0.008			
^2C + ^1V	As-O	4.2 (0.3)	1.69 (0.01)	0.002	5.4 (2.1)	532.3	0.057
	As-O-O	12	1.82(R_{As-O}) = 3.07	σ^2 (As-O)			
	As-Fe	3.1 (1.2)	3.34 (0.03)	0.008			
	As-Fe	-1.0 (1.5)	3.67 (0.11)	0.008			
^2C + parasymplesite	As-O	4.2 (0.3)	1.69 (0.01)	0.002	5.7 (2.1)	509.5	0.054
	As-O-O	12	1.82(R_{As-O}) = 3.07	σ^2 (As-O)			
	As-Fe	4.1 (1.7)	3.34 (0.03)	0.008			
	As-Fe	2.0 (3.0)	3.51 (0.08)	0.008			

Note: ^2C - bidentate, binuclear, ^1V - monodentate mononuclear, ^2E - edge-sharing, CN - coordination number, R - interatomic distance, σ^2 - mean-squared atomic displacement and ΔE_0 - change in threshold energy. The passive electron reduction factor (S_0^2) was fixed at 1.0. The multiple scattering As-O-O path was constrained geometrically to the single scattering As-O path (R_{As-O-O} = 1.82 R_{As-O}). All fits were carried out from 1 to 4 Å in R+ΔR-space. The number of independent points (N_{IDP}) in the fits was 19.8 and the number of variables (N_{Var}) was 6.

Table S4.2 Linear combination fit (LCF) results and statistics of As K-edge k^3-weighted $\chi(k)$ EXAFS spectra of the As(V)-reacted GR using a k-range between 2 and 12.5 $Å^{-1}$.

Component	*Weights (mole fraction)*
Adsorbed As(V) as ^2C	0.129
As(V) as parasymplesite	0.877
Total	1.006
Fitting parameter	
Reduced χ^2	1.300
R-factor	0.042

Chapter 5

Formation of green rust sulfate from the Fe^{2+}-catalyzed transformation of As(V)-bearing ferrihydrite

This chapter is adapted from:

Perez, J.P.H.; Tobler, D.J.; Thomas, A.N.; Freeman, H.M.; Dideriksen, K.; Radnik, J.; Benning, L.G. (2019). Adsorption and reduction of arsenate during the Fe^{2+}-induced transformation of ferrihydrite. *ACS Earth and Space Chemistry*, 3, 884-894.

Available at: https://doi.org/10.1021/acsearthspacechem.9b00031

Abstract

Iron (oxyhydr)oxides play an important role in controlling the mobility and toxicity of arsenic (As) in contaminated soils and groundwaters. Dynamic changes in subsurface geochemical conditions can impact As sequestration and remobilization since the fate of As is highly dependent on the dominant iron mineral phases present and, specifically, the pathways through which these form or transform. To assess the fate of arsenate [As(V)] in subsurface settings, we have investigated the Fe^{2+}-induced transformation of As(V)-bearing ferrihydrite (As(V)-FH) to more crystalline phases under environmentally relevant anoxic subsurface conditions. Specifically, we examined the influence of varying $Fe^{2+}_{(aq)}/Fe(III)_{solid}$ ratios (0.5, 1, 2) on the behavior and speciation of mineral-bound As species during the transformation of As(V)-FH to crystalline iron-bearing phases at circum-neutral pH conditions. At all $Fe^{2+}_{(aq)}/Fe(III)_{solid}$ ratios, goethite (GT), green rust sulfate (GR_{SO4}) and lepidocrocite (LP) formed within the first 2 h of reaction. At low ratios (0.5 to 1), initially formed GR_{SO4} and/or LP dissolved as the reaction progressed, and only GT and some unreacted FH remained after 24 h. At $Fe^{2+}_{(aq)}/Fe(III)_{solid}$ ratio of 2, GR_{SO4} remained stable throughout the 24 h of reaction, alongside GT and unreacted As(V)-FH. Despite the fact that majority of the starting As(V)-FH transformed to other phases, the initially adsorbed As was not released into solution during the transformation reactions and ~99.9% of it remained mineral-bound. Nevertheless, the initial As(V) became partially reduced to As(III), most likely because of the surface-associated Fe^{2+}-GT redox couple. The extent of As(V) reduction increased from ca. 34% to 44%, as the $Fe^{2+}_{(aq)}/Fe(III)_{solid}$ ratio increased from 0.5 to 2. Overall, our results provide important insights into transformation pathways of iron (oxyhydr)oxide minerals in As contaminated, anoxic soils and sediments, and demonstrate the impact that such transformations can have on As mobility and also importantly oxidation state and, hence, toxicity in these environments.

5.1 Introduction

Ferrihydrite (FH) is a nanoparticulate ferric oxyhydroxide mineral commonly found in natural and engineered environments (e.g., soils, groundwater, acid mine drainage and acid sulfate soils) (Cornell and Schwertmann, 2003; Karimian et al., 2018b). FH can sequester considerable amounts of trace or toxic elements via adsorption or co-precipitation due to its high specific surface area (from 120 to 850 m^2 g^{-1}) and reactivity (Brinza et al., 2019; Brinza et al., 2015; Cornell, 1988; Jambor and Dutrizac, 1998; Vu et al., 2010; Vu et al., 2013). However, FH is thermodynamically metastable and usually transforms to more crystalline iron (oxyhydr)oxides (e.g., goethite, hematite, lepidocrocite, green rust or magnetite) (Cornell and Schwertmann, 2003), whereby any adsorbed or incorporated compounds can be remobilized and re-distributed. FH transformation in oxic, ambient conditions and at circum-neutral pH is very slow (months to years) (Schwertmann et al., 2004), and the rates, mechanisms and pathways of transformation strongly depend on physico-chemical factors including pH (Das et al., 2011; Schwertmann and Murad, 1983; Shaw et al., 2005), temperature (Das et al., 2011; Shaw et al., 2005), and the presence of inorganic ions (Cornell, 1988; Jang et al., 2003; Shaw et al., 2005; Vempati and Loeppert, 1989) and organic ligands (Cornell, 1987; Cornell and Schneider, 1989).

In anoxic and non-sulfidic environments, FH transformations can occur more rapidly (within hours or days) due to the presence of aqueous ferrous iron ($Fe^{2+}_{(aq)}$) (Hansel et al., 2005; Liu et al., 2007; Tronc et al., 1992; Yang et al., 2010), generated by dissimilatory iron-reducing bacteria (Fortin and Langley, 2005; Kappler and Straub, 2005). FH transformation usually starts by an initial adsorption of aqueous Fe^{2+} onto FH surface sites and the oxidation of this surface-bound Fe(II) to surface Fe(III) species by loss of an electron to the FH solid. This electron is then conducted through the FH and eventually leads to a release of $Fe^{2+}_{(aq)}$ (Gorski and Scherer, 2011; Hiemstra and van Riemsdijk, 2007; Katz et al., 2012; Williams and Scherer, 2004). This electron conduction process creates "reactive" surface sites, which in turn initiates the dissolution of FH and recrystallization to goethite (GT) and/or lepidocrocite (LP) (Boland et al., 2014; Hansel et al., 2005). If the aqueous Fe^{2+} is in excess compared to the solid Fe(III) (oxyhydr)oxide (e.g., FH, GT and LP), they can transform to mixed-valent Fe minerals such as green rust (GR) and magnetite (MGT) (Ahmed et al., 2010; Sumoondur et al., 2008; Wang et al., 2014). Hence, FH transformations can lead to a variety of Fe mineral phases, and each of these phases has different sorption and redox properties. In turn, this will affect biogeochemical cycling of iron and nutrients (Kappler and Straub, 2005), and importantly also the sequestration of FH-bound toxic elements.

Arsenic is a persistent contaminant affecting groundwater resources worldwide due to its wide-spread occurrence and distribution.(Smedley and Kinniburgh, 2002; Vaughan, 2006) Its mobility in the environment can be greatly influenced by its interaction with mineral phases such as iron (oxhydr)oxides, which have been shown to be highly effective substrates for the sequestration of As in contaminated groundwater. However, the adsorption capacity of iron (oxyhydr)oxides vary dramatically and is also strongly affected by the As oxidation state, which can quickly change during Fe redox transformations. Among the various iron (oxyhydr)oxides, FH, which is often the first Fe phase forming in

subsurface near-neutral environments, exhibits one of the highest adsorption affinity for both As(III) and As(V) while most crystalline Fe phases have far lower As adsorption affinities (Feng et al., 2012; Lin et al., 2012; Mamindy-Pajany et al., 2009; Perez et al., 2019a; Raven et al., 1998; Tang et al., 2011). Under anoxic conditions and in the presence of $Fe^{2+}_{(aq)}$, FH readily transforms to crystalline Fe phases and this can be accompanied by the release and remobilization of As back into the aqueous phase or the As can become associated with the newly-formed Fe phases. However, the mechanisms and pathways of these processes during the inter-transformation of the various iron (oxyhydr)oxides is, however, so far poorly understood or quantified.

To the best of our knowledge, only a few studies examined the Fe^{2+}-induced transformation of As-bearing FH under anoxic conditions. Pedersen et al. (2006) used ^{55}Fe and ^{73}As radiotracers to monitor the transformation of As(V)-co-precipitated FH at pH 6.5 and at varying $Fe^{2+}_{(aq)}$ concentrations (0 to 1 mM), an $Fe(III)_{FH}$ loading of 0.5 mM, and As/Fe_{solid} ratios between 0.001 to 0.005. They showed that after 5 days, LP and GT formed at low $[Fe^{2+}_{(aq)}]$, while GT and MGT formed at higher $[Fe^{2+}_{(aq)}]$. They also inferred that the co-precipitated As had little to no effect on the FH transformation rates and that most of the As remained associated with the solids. More recently, Masue-Slowey et al. (2011) investigated the Fe^{2+}-induced transformation of As(V)-adsorbed FH. They used higher As/Fe_{solid} ratios (0.013 to 0.05), higher $Fe(III)_{FH}$ loadings (20 mM), and also up to 2 mM of $Fe^{2+}_{(aq)}$ concentration. They showed that LP and MGT formed instead of GT, and that the pre-adsorbed As retarded FH transformation. These studies have provided insights into the mineralogical changes that occur when As-bearing FH is reacted with varying $[Fe^{2+}_{(aq)}]$ and revealed how the transformation rates can be affected by the presence of As. However, the fate, bonding environment, or redox state of the co-precipitated or adsorbed As during the crystallizations remains elusive. The question whether transformation reactions in systems where higher amounts of As are associated with the initial FH will cause As release, and what happens if As is only adsorbed to FH rather than co-precipitated are still open. Moreover, As oxidation state could be affected by these redox reactions, and this would affect the toxicity of As in the subsurface. Lastly, the previously tested conditions do not favor GR formation; however, GR phases may be a key substrate for As sequestration in Fe-rich and oxygen-poor subsurface environments (e.g., gley soils or contaminated aquifers), particularly as they can adsorb large amounts of As (Jönsson and Sherman, 2008; Perez et al., 2019a). Thus, GR formation, stability and behavior with respect to As has to be evaluated.

Herein, we aim to fill a part of this knowledge gap by describing a study in which we performed batch experiments under anoxic conditions and examined the Fe^{2+}-induced transformation of As(V)-bearing FH. Experiments were carried out at pH 6.5 with FH onto which As(V) was adsorbed, and was subsequently reacted at varying $Fe^{2+}_{(aq)}/Fe(III)_{solid}$ ratios for up to 24 h. In particular, we tested $Fe^{2+}_{(aq)}/Fe(III)_{solid}$ concentrations and ratios that were higher than in the above mentioned studies but that have been shown to favor the formation of GR (Sumoondur et al., 2008). The mineralogical transformations of As(V)-FH and the fate of As in these processes were assessed using conventional laboratory and synchrotron-based X-ray scattering and spectroscopic techniques and the resulting products were imaged using electron microscopy. Our results provide new insights on the influence

of iron (oxyhydr)oxide mineral transformations on the speciation and hence mobility and toxicity of As in contaminated subsurface environments.

5.2 Experimental Section

5.2.1 General methods

All glass- and plastic-wares were cleaned in 5 M HCl for 24 h, followed by thorough rinsing with Milli-Q water (ca. 18.2 MΩ·cm). All chemicals were ACS reagent grade from Sigma-Aldrich and Acros Organics and were used as received. Stock solutions were prepared inside the anaerobic chamber (97% N_2, 3% H_2, Coy Laboratory Products, Inc.) using O_2-free water, which was obtained by purging Milli-Q water with O_2-free nitrogen for at least 4 h.

5.2.2 Synthesis of 2-line ferrihydrite

Two-line FH was synthesized using the method described by Schwertmann and Cornell (2000) by slowly titrating 0.1 M $Fe_2(SO_4)_3{\cdot}5H_2O$ with 1 M NaOH to pH ~7. The resulting suspension was washed using 6 cycles of centrifugation (9,000 rpm, 5 minutes) and re-dispersion in Milli-Q water to remove excess solutes. Afterwards, the FH slurry was purged with O_2-free N_2 for at least 4 h to remove O_2 and then immediately transferred into the anaerobic chamber. The amount of synthesized FH was determined based on the total iron concentration of an aliquot of the suspension dissolved in 0.3 M HNO_3. The total Fe concentration was analyzed by flame atomic absorption spectrometry (AAS, Perkin Elmer AAS Analyst 800). Each batch of FH (ca. 88.3 mM $Fe(III)_{solid}$) was prepared fresh and used on the day of synthesis.

5.2.3 Batch transformation experiments

All batch experiments were performed in triplicate at room temperature inside the anaerobic chamber. To prepare As(V)-bearing FH, an aliquot of the washed FH was re-suspended in a 0.1 M NaCl solution buffered at pH 6.5 using 0.05 M morpholinoethanesulfonic acid (MOPS). After pH equilibration, the resulting FH suspension was then spiked with an aliquot from an As(V) stock solution prepared from $Na_2HAsO_4{\cdot}7H_2O$. The resulting suspensions [41.6 mM $Fe(III)_{solid}$, 1.33 mM As(V)] were stirred at 350 rpm for 24 h to ensure As(V) adsorption onto FH (Figure S5.1). Afterwards, aliquots of 0.5 M $FeSO_4$ were added to the As(V)-bearing FH suspension to achieve $Fe^{2+}{}_{(aq)}/Fe(III)_{solid}$ ratios of 0.5, 1 or 2 (denoted as R0.5, R1 and R2 from here on). A control experiment without $FeSO_4$ addition (no aqueous Fe^{2+}, R0) was also conducted. The resulting mixtures were stirred at 350 rpm for 24 h, with aliquots of the suspension being removed after 0.5, 1, 2, 4, 8 and 24 h. Parts of the collected suspensions were filtered through 0.22-μm syringe filters, and the resulting solutions were acidified with HNO_3 and stored at 4°C until the concentrations of aqueous As were analyzed by inductively coupled plasma optical emission spectrometry (ICP-OES, Varian 720ES), following the method described by Perez et al. (2019a). Further analytical details can be found in the Supporting Information (see Section 5.5.1 and Table S5.1). The remainder of the collected suspensions

was used to characterize the solid phase. For this, the suspension was filtered using 0.22-μm polycarbonate membrane filters and the obtained solids were dried in a desiccator inside the chamber, ground and stored until use in crimped headspace vials inside the anaerobic chamber.

5.2.4 Mineral characterization and thermodynamic modelling

The solids were analyzed by a suite of laboratory- and synchrotron-based characterization techniques to determine their structure and composition, particle sizes and morphologies, surface properties, as well as As and Fe redox states. Detailed information on sample preparation to minimize oxidation and on solid characterization can be found in the Supporting Information (see Section 5.5.2). Mineralogical changes in the solid phase during the reaction were monitored by X-ray powder diffraction (XRD) using a Bruker D8 powder diffractometer (Cu Kα radiation, λ = 1.5406 Å). The morphology, size, structure and chemical composition of the final solids (collected after 24 h) were characterized by transmission electron microscopy (TEM) and scanning electron microscopy (SEM). TEM micrographs and selected area electron diffraction (SAED) patterns were recorded using a FEI Tecnai G2 F20 X-Twin FEG TEM, operated at 200 keV and equipped with a Gatan Imaging Filter (GIF) Tridiem™. SEM images were acquired using a ZEISS Ultra Plus FE-SEM operated in high vacuum mode at an acceleration voltage of 3 kV with 10 μm aperture size using an InLens secondary electron detector. The local structure was investigated using pair distribution function (PDF) analysis. The high energy X-ray scattering data used for PDF analysis were collected at the 11-ID-B beamline of the Advanced Photon Source (Argonne National Laboratory, USA). X-ray absorption spectroscopic (XAS) analyses were carried out to monitor the changes in As oxidation state and to quantify the Fe phases in the final solids. Fe K-edge extended X-ray absorption fine structure (EXAFS) spectra were collected at the SUL-X beamline of Angströmquelle Karlsruhe (ANKA, Karlsruhe, Germany), and the As K-edge X-ray absorption near-edge structure (XANES) data were collected at the BM23 beamline of the European Synchrotron Radiation Facility (ESRF, Grenoble, France). The Fe K-edge EXAFS spectra of synthetic iron (oxyhydr)oxide mineral samples [i.e., FH (Schwertmann and Cornell, 2000), GT (Atkinson et al., 1967; Schwertmann and Cornell, 2000), LP (Schwertmann and Cornell, 2000), GR sulfate (GR_{SO4}) (Perez et al., 2019a)] were also collected as reference standards for Fe phase quantification. As K-edge XANES spectra of As(III)- and As(V)-interacted GT samples were also collected and were used as reference standards for the determination of As oxidation state. X-ray photoelectron spectroscopy (XPS) measurements were performed using a KRATOS Axis Ultra DLD to determine the surface chemistry of the solids. To predict Fe and As speciation and Fe phase stability in the studied system, thermodynamic modelling was carried out using Geochemist's Workbench® (Bethke, 2010) with the MINTEQ thermodynamic database (see Section 5.5.2 for details). Missing thermodynamic data of mineral phases in the Fe-S-H_2O system (e.g., GR_{SO4}) were manually added to the MINTEQ database (Karimian et al., 2017; 2018a).

5.3 Results and Discussion

5.3.1 Aqueous behavior and speciation of mineral-bound As species

The aqueous concentrations of As revealed that barely any As was released (<0.15 %, Figure S5.1) during the Fe^{2+}-induced transformation of As(V)-bearing FH to GT ± GR. This is consistent with the high uptake capacity of synthetic iron (oxyhydr)oxides for As species determined in the adsorption experiments (Figure S5.2). Similar minimal As release (<1%) were also reported in previous Fe^{2+}-catalyzed transformation experiments of As(V)-bearing ferrhydrite (Gomez et al., 2013; Pedersen et al., 2006) and As(V)/Sb(V)-bearing jarosite (Karimian et al., 2017; 2018a). Moreover, it has also been shown that As removal efficiencies were even higher in experiments wherein As were co-precipitated with iron (oxyhydr)oxides compared to those adsorbed onto pre-synthesized iron (oxyhydr)oxides (Asta et al., 2009; Park et al., 2016; Pedersen et al., 2006).

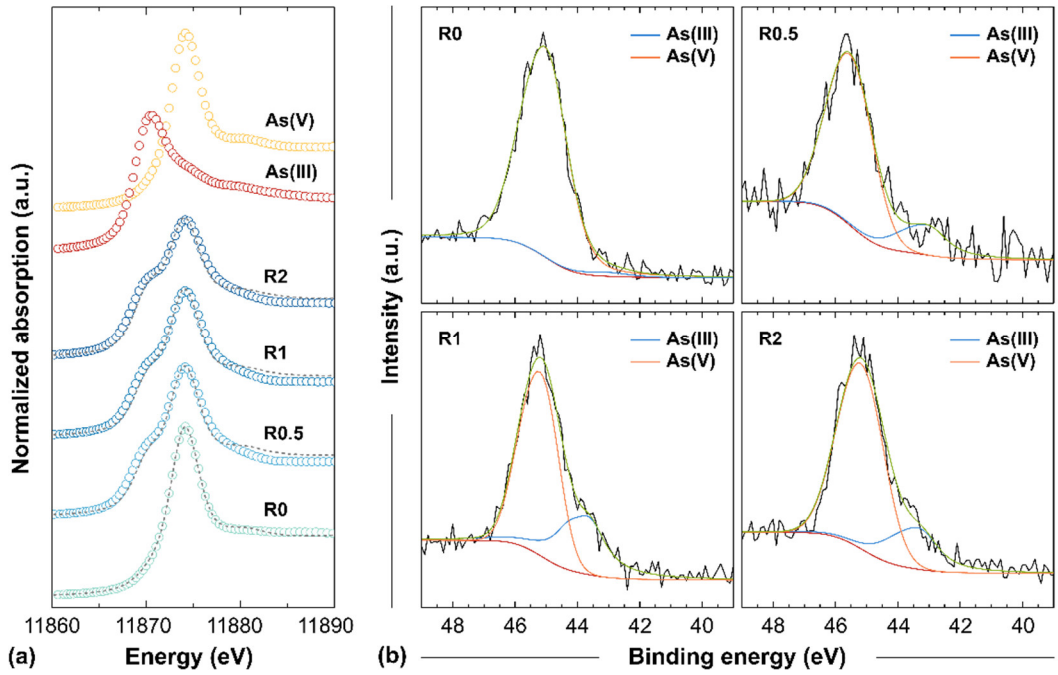

Figure 5.1 (a) Normalized As K-edge XANES spectra of the end-products. Fits (grey dashed lines) are linear combinations of the As reference standards (i.e., As(III) and As(V) adsorbed on GT). (b) Deconvoluted high-resolution As *3d* XPS spectra of the end-products (calibrated to yield adventitious C 1s peak at 285.0 eV). Details of the fitting parameters and statistics for the quantification of As speciation based from the As K-edge XANES and XPS data can be found in the Tables S4.2 and S4.4, respectively.

The oxidation state of As associated with the solids after 24 h of reaction as probed by As K-edge XANES (Figure 5.1a) showed that the initial FH-bound As(V) was partially reduced to As(III) when the initial As(V)-FH was reacted with aqueous Fe^{2+} under anoxic conditions. The degree of As(V) reduction slightly increased from 33.6 ± 1.8% to 42.4 ± 1.8% as the $Fe^{2+}{}_{(aq)}/Fe(III)_{solid}$ ratio increased from 0.5 to 2 (see Table 5.1). This trend was also confirmed by high resolution XPS of the final solids (Figure 5.1b), that showed the presence of a shoulder at a binding energy of ca. 44 eV, indicative of As(III) (see Table S5.3 for As reference binding energies). Due to the uncertainty of the XPS measurements

(see Table S5.4), a fully quantitative determination of the As(III) contents was difficult, but XPS confirmed its presence. Furthermore, XPS analyses showed that the initial As (V) was still the primary valence state in the near surface region (top 10 nm of the samples). A possible reduction of As(V) due to X-ray beam damage is negligible as shown by analysis of the control (R0).

Table 5.1. Arsenic oxidation state and mineralogical composition of the end-products of As(V)-bearing FH transformation with varying $Fe^{2+}_{(aq)}/Fe(III)_{solid}$ ratios (R).

Ratio	As oxidation state			Fe phase composition							
	As K-edge XANES			Fe-K edge EXAFS				PDF			
	As(III)	As(V)	Red. χ^2	FH	GT	GR	Red. χ^2	FH	GT	GR	Goodness of fit (R_w)
0	4.1 ± 0.1	95.9 ± 0.1	0.001	100	-	-	-	100	-	-	0.208
0.5	33.6 ± 1.8	66.4 ± 1.7	0.014	17 ± 4	83 ± 3	-	0.221	70 ± 3	30 ± 1	-	0.205
1	34.3 ± 1.8	65.7 ± 1.8	0.015	15 ± 1	85 ± 1	-	2.663	22 ± 5	78 ± 3	-	0.150
2	42.4 ± 1.8	57.6 ± 1.7	0.013	11 ± 2	84 ± 2	5 ± 1	0.226	-	92 ± 3	8 ± 1	0.175

Thermodynamic calculations based on the Eh-pH conditions used in our experiments (Figure S5.3) suggest that, at equilibrium, all initially adsorbed As(V) species should have been reduced to As(III) during the transformation. The partial reduction of As(V) to As(III) after 24 h observed in our data is likely a result of kinetic limitations since it might take longer time scales for full reduction.

5.3.2 Mineralogical transformation of As(V)-bearing FH

In the absence of aqueous Fe^{2+}, the As(V)-bearing FH did not transform to other iron (oxyhydr)oxides (R0, Figure 5.2a). While barely any As was released during the reactions, exposure of the initial As(V)-bearing FH to varying aqueous Fe^{2+} concentrations led to its rapid transformation into more crystalline iron (oxyhydr)oxides. At $Fe^{2+}_{(aq)}/Fe(III)_{solid}$ ratios of 0.5 and 1 (R0.5 and R1, Figure 5.2b, c, respectively), goethite (GT) formed within the first hour and dominated the pattern over the remaining 24 h. Small amounts of green rust sulfate (GR_{SO4}) and lepidocrocite (LP, only in R0.5) also formed in the R0.5 and R1 experiments. However, both phases dissolved, as supported by aqueous Fe^{2+} release (Figure S5.1), which then precipitated as goethite after 2 h. At an $Fe^{2+}_{(aq)}/Fe(III)_{solid}$ ratio of 2 (R2, Figure 5.2d), both GT and GR_{SO4} formed rapidly within the first 30 min but both also remained present throughout the 24 h of reaction.

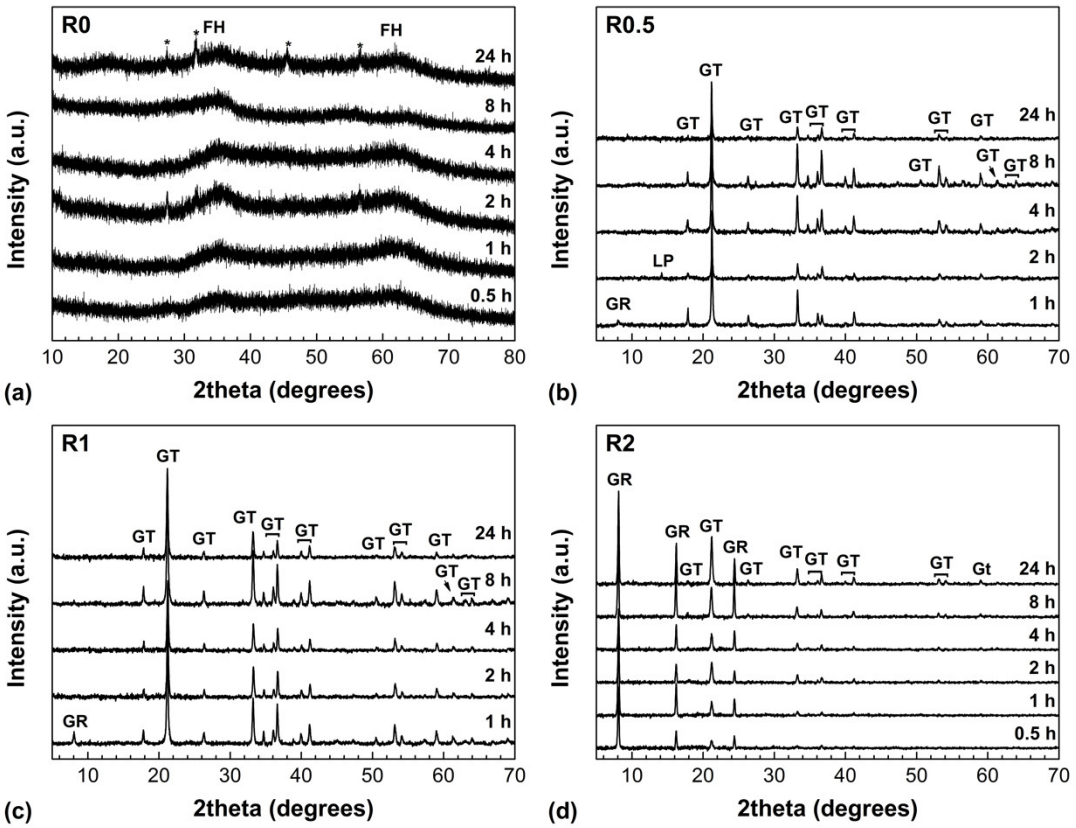

Figure 5.2 XRD patterns showing the change in mineralogical composition in the solid samples during the 24-h transformation of As(V)-FH at varying $Fe^{2+}_{(aq)}/Fe(III)_{solid}$ ratios (R): (a) control (0), (b) 0.5, (c) 1 and (d) 2. The '*' denotes peaks for halite from the background electrolyte. XRD patterns for R0.5 and R1 at 0.5 h are not shown because no crystalline mineral phases were detected. Note that the increased peak intensity of GR_{SO4} (001) comes from preferential orientation of GR_{SO4} plate-like particles along the [001] zone axis during XRD sample preparation.

The high energy XRD pattern [$I(Q)$] of the mineral end-products (Figure 5.3a) corroborated the laboratory-based XRD data (Figure 5.2), with the main end-product being GT and with some GR_{SO4} forming at the highest tested $Fe^{2+}_{(aq)}/Fe(III)_{solid}$ ratio of 2. The broad humps at Q-values of ca. 2.4 and 4.2 Å^{-1} for R0.5 and, in part, R1 stem from unreacted FH, the presence of which was not unexpected in the end-product material because previous studies (Rancourt et al., 2001; Richmond et al., 2004; Waychunas et al., 1993) have shown that As can slow down the transformation of FH to crystalline iron (oxyhydr)oxides. The PDF analyses (Figure 5.3b, S6.4) were used to derive the characteristic interatomic distances in the mineral-end products. The atomic pair correlations at r-values < 4 Å (Figure 5.3b) correspond to the atomic arrangements in the Fe-O polyhedra in iron (oxyhydr)oxides. The first peak at ca. 2.0 Å matches first neighbor Fe-O pairs, while peaks at ca. 3.0 and 3.4 Å represent edge- and corner-sharing Fe-Fe pairs ($Fe\text{-}Fe_E$, $Fe\text{-}Fe_C$), respectively. Changes in peak positions and intensities for these Fe-Fe pairs are a consequence of the presence of mixed iron (oxyhydr)oxides (i.e., GT, FH ± GR_{SO4}) in these solids, when compared with the standard materials (spectra labeled GT, FH, GR in Figure 5.3a and 3b).

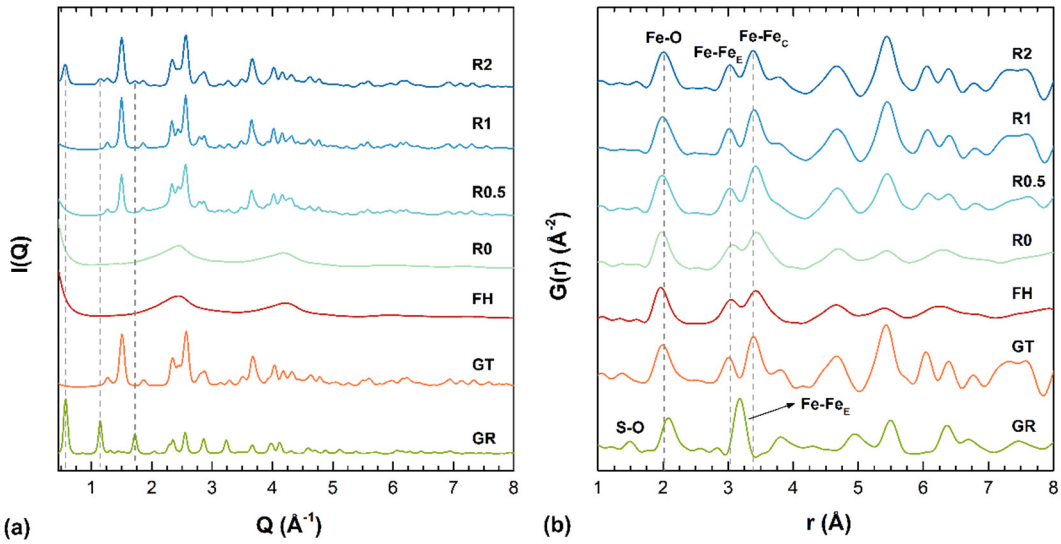

Figure 5.3 High energy X-ray scattering data of the end-products after 24 h Fe^{2+}-induced As(V)-FH transformation at varying $Fe^{2+}_{(aq)}/Fe(III)_{solid}$ ratios (R): (a) HEXRD patterns [*I*(*Q*)]. GR (00*l*) reflections in the R2 end-product are indicated by grey dashed lines while all the other peaks in the transformation end-products can be assigned to GT (except for the R0 end-product, which is naturally still pure As(V)-FH). The patterns of the reference materials (i.e., FH, GT and GR) are shown for comparison; and (b) PDFs [G(r)] of the low *r*-value region showing the short-range structure of the solids. The full PDFs are shown in Figure S-4. Fe-Fe_E and Fe-Fe_c refer to edge- and corner-sharing pairs, respectively.

TEM and SEM analyses of the transformation end-products confirmed that GT was the main product with FH still present in all experiments after 24 h. As shown before with XRD and PDF, GR_{SO4} was only present in reactions with $Fe^{2+}_{(aq)}/Fe(III)_{solid} = 2$ (Figure 5.4a, S6.5, S6.6). GR_{SO4} was identified by its thin hexagonal plate-like particles (Figure 5.4b) (Freeman et al., 2019; Perez et al., 2019a; Perez et al., 2018) GT by its distinctive crystalline nanorod (Figure 5.4d) and FH by its ca. 3 nm-sized particle aggregates (Figure 5.4f, S6.5). SEM images of the end-products also revealed that particle lengths of the GT nanorods gradually decreased with increasing $Fe^{2+}_{(aq)}/Fe(III)_{solid}$ ratios (Figure S5.6, S6.7). Both TEM and SEM images confirmed that GT was the dominant mineral phase in all experiments (Figure 5.4a, S6.5, S6.6) and that FH was closely associated with GT and GR_{SO4} (Figure 5.4a,b). It is important to note that, often, FH was observed to seemingly "fill" voids in GR_{SO4} particles (Figure 5.4a,b and S6.5c). Such features could indicate that the GR_{SO4} particles were still forming from the As(V)-bearing FH precursor after 24 h, or that the formed GR_{SO4} crystals are dissolving from the center, as previously suggested by Skovbjerg et al. (2006). However, dissolution of the GR_{SO4} from the exposed crystal edges (Figure 5.4c) cannot be excluded.

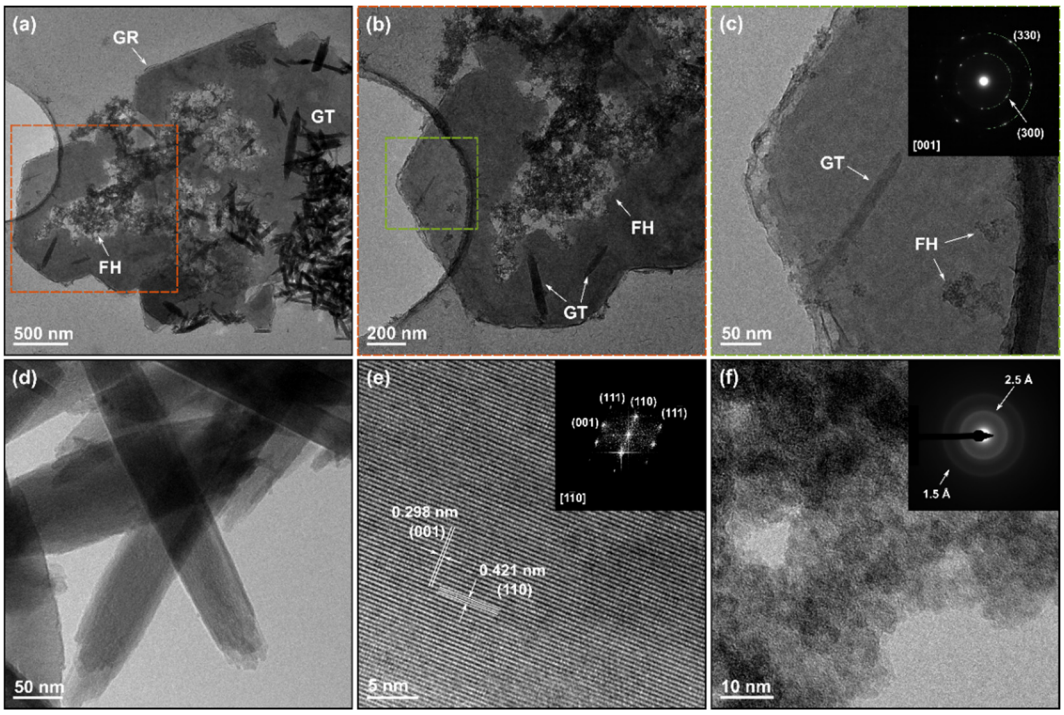

Figure 5.4 TEM images of Fe phases following the 24-h transformation of As(V)-FH at $Fe^{2+}_{(aq)}/Fe(III)_{solid}$ ratio of 2: (a) overview showing the close association between GR_{SO4} (dark grey, >300 nm wide hexagonal platelets), GT (ca. 50 nm wide black rods), and unreacted FH (aggregates of ca. 3 nm sized particles); (b) blow-up of the orange marked area in (a); (c) GR_{SO4} particle seen in green marked area in (b) with the SAED pattern in inset; (d) GT nanorods and the corresponding (e) HRTEM image with the fast Fourier transformation (FFT) pattern in the inset showing the lattice fringes for (001) and (110) planes of GT (in *Pbnm* spacegroup); (f) As(V)-bearing FH nanoparticles with the SAED pattern in inset. The SAED pattern of GR_{SO4} was indexed according to the proposed structure of Christiansen et al. (2009b).

From the evaluation of the Fe K-edge EXAFS and PDF data (Figure 5.5, Table 5.1), we determined the relative amounts (% mol Fe) of the reaction transformation end-products. The Fe K-edge EXAFS data (Figure 5.5a) confirmed GT (≥84%) as the main mineral phase in all Fe^{2+}-spiked experiments, with GR only accounting for ca. 5% in the system with $Fe^{2+}_{(aq)}/Fe(III)_{solid} = 2$. The EXAFS fitting revealed that the amount of remnant As(V)-FH after 24 h was inversely proportional to the Fe^{2+} concentration added to the As(V)-bearing FH. Interestingly, the amount of As(V)-FH derived from the PDF data (Figure 5.5b) followed a similar trend to the EXAFS data, but unreacted FH could not be identified in the R2 end-product PDF pattern. This was most likely due to its low relative amount in the sample (from EXAFS ca. 11%). However, the biggest difference in the relative phase amounts between PDF and EXAFS fitting was seen in the R0.5 end-product. PDF indicates ~70% FH compared to ~16% from the EXAFS evaluation, which naturally also impacted the proportion of GT in this sample. Upon closer inspection, PDF of the R0.5 end-product (Figure 5.3b) seems to lack the characteristic GT features observed in R1 and R2 samples. For example, the small but sharp peak at r ≈ 3.8 Å is missing, and both the peak at 5.5 Å and the double peaks at 6-6.5 Å are also poorly developed. Thus, the bonding environment at ca. 3.8 to 7 Å does not exactly resemble GT. From this, we suspect that there is a short-range distortion in the Fe octahedra that is uncharacteristic of GT. This results in the large discrepancy between the PDF and EXAFS Fe phase

quantification. Despite the variation between the calculated proportions of Fe phases from EXAFS and PDF data, and considering both experimental, analytical and fitting uncertainties the results show that both the extent of FH transformation to GT and/or GR increases as the $Fe^{2+}_{(aq)}/Fe(III)_{solid}$ ratios increase (Boland et al., 2014).

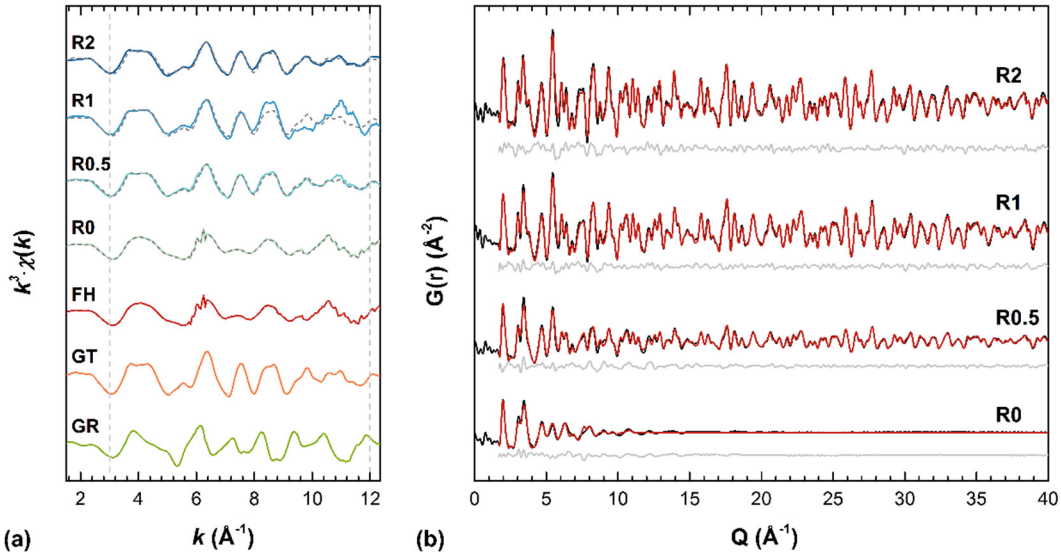

Figure 5.5 (a) k^3-weighted $\chi(k)$ Fe K-edge EXAFS spectra of transformation end-products following the 24 h reaction of As(V)-FH with varying $Fe^{2+}_{(aq)}$ concentrations ($Fe^{2+}_{(aq)}/Fe(III)_{solid}$ ratios from 0 to 2). Fits (grey dashed lines) are least square linear combinations of the reference materials (i.e., lower 3 patterns FH, GT, GR_{SO4}). Fit boundaries are indicated by the vertical dashed lines (k-range = 3-12 Å^{-1}). (b) Fits of PDFs of same end-products ($Fe^{2+}_{(aq)}/Fe(III)_{solid}$ ratio from 0 to 2). The black curves represent the experimental data, whereas red and light grey curves represent the calculated pattern and the residuals. Details of the fitting method for Fe K-edge EXAFS and PDF conducted in Athena (Ravel and Newville, 2005) and PDFgui (Farrow et al., 2007) can be found in Supplementary Information (see Section 4.5.9).

Overall, the composition of the mineral end-products as determined with XRD, PDF, TEM, SEM and EXAFS at the end of the 24 h Fe^{2+}-induced As(V)-bearing FH transformation are consistent with each other, and also match the predicted phases from thermodynamic calculations for the Fe-S-H_2O system (Figure S5.8).

5.3.3 Mechanism of As(V)-ferrihydrite transformation and As redox transformation

Iron redox cycling in subsurface environments highly impacts the mobility and toxicity of As in contaminated sediments and groundwaters. Specifically, mineral transformations involving iron (oxyhydr)oxides are important since specially under reducing conditions such transformation reactions can change the oxidation state of mineral-associated As, which in turn controls As toxicity as well as the extent to which As will be sorbed by minerals. Thus, such reactions may not only release As back into the environment, but these processes could render As to be present in the more toxic form.

Our results demonstrated that the initial As(V)-bearing FH rapidly transforms to GT and to a lesser extent to GR_{SO4} and lepidocrocite upon the addition of Fe^{2+} (Figure 5.2). We also showed that the transformation rate of FH increased with increasing

$Fe^{2+}_{(aq)}/Fe(III)_{solid}$ ratios. This is seen, for example, by the appearance of crystalline Fe phases already after 30 min in experiments with an $Fe^{2+}_{(aq)}/Fe(III)_{solid}$ ratio of 2 (Figure 5.2d), compared to 1 h at lower ratios, or in the lower relative abundance of FH in the end-products at higher $Fe^{2+}_{(aq)}/Fe(III)_{solid}$ ratios (Figure 5.5). Furthermore, the absence of LP at $Fe^{2+}_{(aq)}/Fe(III)_{solid}$ ratios > 0.5 indicates that the transformation was very fast because LP formation requires low levels of FH-surface-adsorbed Fe^{2+} (Hansel et al., 2005; Karimian et al., 2017; Pedersen et al., 2006). Moreover, the smaller GT nanorods obtained at higher $Fe^{2+}_{(aq)}/Fe(III)_{solid}$ ratios (Figure S5.6) indicate faster FH transformation rates, because higher nucleation rates lead to smaller crystals.

GR_{SO4} formed under all tested conditions alongside with GT, but disappeared already after 2 h at lower $Fe^{2+}_{(aq)}/Fe(III)_{solid}$ ratios (<2) and it transformed into the thermodynamically more stable GT (Figure 5.2b, 2c). At $Fe^{2+}_{(aq)}/Fe(III)_{solid} = 2$, GR_{SO4} remained throughout the reaction, which was expected based on previous Fe^{2+}-induced FH transformation experiments where a similar $Fe^{2+}_{(aq)}/Fe(III)_{solid}$ ratio was employed without the addition of As (Ahmed et al., 2010; Sumoondur et al., 2008; Usman et al., 2012). However, in contrast to the As-free FH experiments, which only formed GR, the R2 end-products in the current study also contained FH and GT. Arsenic species have been shown to hinder iron (oxyhydr)oxide transformations (Karimian et al., 2017; Su and Puls, 2004; Wang et al., 2014). Thus, the incomplete conversion of As(V)-bearing FH into GT and/or GR_{SO4} (Figure 5.4 and 4.5) is likely a consequence of crystallite poisoning by the surface-bound As species. Specifically, As species have been shown to inhibit Fe-O-Fe polymerization, thereby inducing distortions in the Fe bonding environment and inhibiting crystal nucleation and growth (Rancourt et al., 2001; Richmond et al., 2004; Waychunas et al., 1993).

The solid-state characterization results and electron microscopy images further suggest that GR_{SO4} formed independently of GT during the Fe^{2+}-induced transformation of As(V)-bearing FH. The XRD data (Figure 5.2) document the rapid and simultaneous occurrence of GT and GR_{SO4} in the early stages of transformation and, thus, suggest that both Fe phases formed directly from FH. This is also supported by the calculated Gibbs free energies (ΔG_{rxn}°), which showed that the formation of GR_{SO4} is more thermodynamically favored from a FH precursor (Table 5.2, Eq. 2) compared to GT (Table 5.2, Eq. 3). Moreover, the added Fe^{2+} rapidly hydrolyzed, as evidenced by the quick decrease in aqueous Fe^{2+} concentration (Figure S5.1a), and thus the simultaneous formation of GT and GR_{SO4} from FH is likely. The formation of GT from FH is well documented (Boland et al., 2014; Gorski and Scherer, 2011; Yee et al., 2006) while the formation pathways and mechanisms of GR phases from other iron (oxyhydr)oxides are far less studied (Ahmed et al., 2010; Usman et al., 2012). Sumoondur et al. (2008) however reported a similar observation wherein GR_{SO4} formed directly from pure FH (no As added, $Fe^{2+}_{(aq)}/Fe(III)_{solid}$ ratios of 0.5 to 2) within the first 10 min of the Fe^{2+}-catalyzed transformation reaction as monitored by synchrotron-based *in situ* time-resolved energy dispersive X-ray diffraction.

Table 5.2 Calculated Gibbs free energies (ΔG_r°) at 25 °C.

	Chemical reaction	ΔG_{rxn}° (kJ mol^{-1})[a]
	Mineral formation	
1	$Fe^{III}(OH)_3 \rightarrow \alpha\text{-}Fe^{III}OOH + H_2O$	-20.4
2	$4Fe^{2+} + 2Fe^{III}(OH)_3 + SO_4^{2-} + 6H_2O \rightarrow Fe^{II}_4Fe^{III}_2(OH)_{12}SO_4 + 6H^+$	124.2
3	$4Fe^{2+} + 2\alpha\text{-}Fe^{III}OOH + SO_4^{2-} + 8H_2O \rightarrow Fe^{II}_4Fe^{III}_2(OH)_{12}SO_4 + 6H^+$	598.4
	Redox reactions	
4	$Fe^{II}_4Fe^{III}_2(OH)_{12}SO_4 + 2H_2As^{V}O_4^- \rightleftharpoons 6\alpha\text{-}Fe^{III}OOH + 2As^{III}(OH)_3 + SO_4^{2-} + 2H_2O$	-122.2
5	$Fe^{II}_4Fe^{III}_2(OH)_{12}SO_4 + 2HAs^{V}O_4^{2-} + 2H^+ \rightleftharpoons 6\alpha\text{-}Fe^{III}OOH + 2As^{III}(OH)_3 + SO_4^{2-} + 2H_2O$	-202.0
6	$Fe^{II}_4Fe^{III}_2(OH)_{12}SO_4 + 2H_2As^{V}O_4^- + 4H_2O \rightleftharpoons 6Fe^{III}(OH)_3 + 2As^{III}(OH)_3 + SO_4^{2-}$	0.2
7	$Fe^{II}_4Fe^{III}_2(OH)_{12}SO_4 + 2HAs^{V}O_4^{2-} + 4H_2O + 2H^+ \rightleftharpoons 6Fe^{III}(OH)_3 + 2As^{III}(OH)_3 + SO_4^{2-}$	-79.6
8	$2Fe^{2+} + H_2As^{V}O_4^- + 3H_2O \rightleftharpoons 2\alpha\text{-}Fe^{III}OOH + As^{III}(OH)_3 + 3H^+$	21.4
9	$2Fe^{2+} + HAs^{V}O_4^{2-} + 3H_2O \rightleftharpoons 2\alpha\text{-}Fe^{III}OOH + As^{III}(OH)_3 + 2H^+$	-18.5
10	$2Fe^{2+} + H_2As^{V}O_4^- + 5H_2O \rightleftharpoons 2Fe^{III}(OH)_3 + As^{III}(OH)_3 + 3H^+$	62.2
11	$2Fe^{2+} + HAs^{V}O_4^{2-} + 3H_2O \rightleftharpoons 2Fe^{III}(OH)_3 + As^{III}(OH)_3 + 2H^+$	22.3
12	$2Fe^{2+} + H_2As^{V}O_4^- + 3H^+ \rightleftharpoons 2Fe^{3+} + As^{III}(OH)_3 + H_2O$	23.2
13	$2Fe^{2+} + HAs^{V}O_4^{2-} + 4H^+ \rightleftharpoons 2Fe^{3+} + As^{III}(OH)_3 + H_2O$	-16.7

[a] Values calculated from the standard Gibbs free energies (ΔG_f°) of minerals and aqueous species (Table S5.6).

During the transformation reaction of the As(V)-bearing FH a minor initial release of As (<0.15%, Figure S5.1b) from its surface was observed. The initial As release is a result of the dissolution of FH, which can have surface areas up to 850 m^2 g^{-1} (Jambor and Dutrizac, 1998), and the formation of GT and GR phases which both have lower surface areas. This released As was quickly adsorbed by the newly-formed GT and/or GR particles (Figure S5.1b). However, the possibility of incorporation of As into the structure of GT cannot be ruled out, especially since the ionic radius of As(V) is similar to tetrahedally-coordinated Fe (Cornell and Schwertmann, 2003), although such phenomenon has not been documented yet (Pedersen et al., 2006).

A more relevant finding of this study is that the initial As(V) was partially reduced to As(III) during the Fe^{2+}-induced transformation of As(V)-bearing FH, and this reduction (i.e., As(III)/As(V) ratio) increased with increasing $Fe^{2+}{}_{(aq)}/Fe(III)_{solid}$ ratio. Based on the calculated ΔG_{rxn}° values (Table 5.2, Eq. 4-7), the most thermodynamically feasible reductant in the Fe-As-S-H_2O system is GR_{SO4}, yet no study to date has been able to document such reduction of As(V) to As(III) by GR (Jönsson and Sherman, 2008; Randall et al., 2001; Wang et al., 2010). Moreover, the formation and stability of the GR in the experiments R0.5 and R1 were substantially lower compared to the R2 experiment (Figure 5.2). This suggests that another redox couple may have induced As(V) reduction. The most likely candidate is the surface-associated Fe^{2+} and GT redox couple (Table 5.2, Eq. 8-9), which has been shown to reduce other groundwater contaminants such as carbon tetrachloride (Amonette et al., 2000), nitrobenzene (Gorski et al., 2016; Stewart et al., 2018) and chromate (Buerge and Hug, 1999). The surface-associated Fe^{2+}-GT redox couple might also explain why As(V) reduction was only observed at high Fe^{2+} concentrations during the Fe^{2+}-catalyzed transformation of As(V)/Sb(V)-jarosite ($[Fe(III)_{jarosite}$ = 21.8 mM, $[Fe^{2+}{}_{(aq)}]$ = 0 to 20 mM, As/Fe_{solid} = 0.003) (Karimian et al., 2017). These authors noted that in their experiments, LP was the dominant mineral phase at low Fe^{2+} concentrations while GT was the primary end-product (with minor GR_{SO4}, <10%) at higher Fe^{2+} concentrations.

It must be noted, however, that As(V) reduction has not been observed previously upon interaction with Fe^{2+}-activated synthetic GT (Amstaetter et al., 2010), which examined the interactions at a $Fe^{2+}_{(aq)}/Fe(III)_{solid}$ ratio of 0.03, which is approximately 15 to 55 times lower than the ratios used in this study. Since the reduction reaction is driven by Fe^{2+} concentration, the low Fe^{2+} concentration used in their study could explain why they did not observe any As(V) reduction to As(III) in their system. However, a question arises whether As(V) could be reduced to As(III) at lower $Fe^{2+}_{(aq)}/Fe(III)_{solid}$ ratios and $Fe(III)_{FH}$ loadings similar to those reported by Pedersen et al. (2006) and Masue-Slowey et al. (2011), especially since the mineralogical composition of the end-products is different from what we observed in our study.

Overall, these redox transformations have important implications for the mobility and toxicity of As. The partial reduction of As(V) to As(III), as documented in this study, is an unexpected and also detrimental consequence as such reduction results in the generation of far more toxic and mobile As species (Roberts et al., 2004). On the positive side, the sorption capacities of these Fe mineral phases towards As species is very high, and therefore we observed no significant As release. Noteworthy, however, is the fact that invariably real subsurface environments are significantly more complex. The presence of many different mineral substrates and the variation in mineral sorption capacities will be affected by Eh/pH conditions (Root et al., 2007), the presence of other inorganic ions (e.g., silicate and phosphate anions) (Perez et al., 2019a; Roberts et al., 2004) or organic ligands (Chen et al., 2015; Chen and Sparks, 2018; Hu et al., 2018; Zhou et al., 2018) all competing with As for active surface sites and influencing the mechanisms and pathways Fe (oxyhydr)oxide transformation.

5.4 Conclusion

In subsurface environments, iron-bearing mineral transformations can massively impact the mobility and toxicity of contaminants, since these mineral phases serve as toxic element sinks that can control and even prevent release and further transport of contaminants in soils and groundwaters. In this study, we followed the transformation of As(V)-bearing ferrihydrite, catalyzed by aqueous Fe^{2+}, under anoxic conditions as it converts to more crystalline iron (oxyhydr)oxides. Higher Fe^{2+} concentrations resulted in the formation of both GT and GR phases, while lower Fe^{2+} concentrations led to a GT end-product. However, at all the tested conditions, the conversion of ferrihydrite was incomplete, and our data indicate that this was a consequence of As surface complexation. Analyses of the mineral-bound As species also revealed partial reduction of initial As(V) to As(III), although no significant release of As was observed during the transformation. Overall, our results highlight the need to understand such inter-transformations among iron (oxyhydr)oxide in subsurface environments where aqueous Fe^{2+} is present as it will impact As sequestration, mobilization and transport.

5.5 Supporting Information

5.5.1 Elemental concentration analysis by AAS and ICP-OES

Flame atomic absorption spectrometry (AAS)

The acidified liquid samples were gravimetrically diluted using 0.3 M HNO_3 (Honeywell TRaceSELECT^{TM} Ultra) to ensure that the analyte solutions were within the concentration range of the calibration standards. The quantification of iron concentration was done using a linearity criteria of $R^2 > 0.9990$.

Inductively coupled plasma optical emission spectrometry (ICP-OES)

Prior to ICP-OES analyses, acidified liquid samples (pH ~2) were diluted gravimetrically in acid-cleaned polypropylene (PP) tubes. Sample dilutions were done using 0.3 M HNO_3 (Merck Suprapure grade) containing 1 mg g^{-1} Cs as an ionization buffer to achieve matrix matching with calibration standards prepared from a mixture of single ICP element standards (Merck certipur, traceable to NIST reference materials). Scandium (1 µg g^{-1}) was added as an internal standard. The dilution factor was adapted to ensure that the analyte solutions were within the concentration range of the matrix-matched calibration standards (linearity criteria $R^2 > 0.9990$) and with final HNO_3 and Cs concentrations of 0.3 M and 1 mg g^{-1}, respectively. For each analytical session, instrumental stability and drift were monitored using Ar, Cs and Sc at emission wavelengths of 420.067, 459.311 and 335.372 nm for each sample analysis, respectively, as well as regular measurements of a quality control (QC) solution, similar to sample compositions. Instrumental statistical LoD (3SD above background) or limits of quantification (LoQ = 10SD above background) were determined in each analytical session based on nine repeat analysis of 0.3 M HNO_3 (+ 1 mg g^{-1} Cs) used for sample dilution.

Concentrations of As, Fe and S in the samples were evaluated using the emission wavelengths of 193.696, 261.382 and 180.669 nm, respectively. The determined LoD and LoQ for As were 0.016 and 0.053 µg g^{-1}, respectively. Detection limits translate to maximum detectable removal efficiency of > 99.9%. Analytical uncertainties at a 95% confidence level for concentrations quantified (above LoQ) during this study are ~5% relative, verified by repeat analyses of a QC solution, which was similar to the sample compositions (Table S1).

Table S5.1 ICP-OES analytical results of quality control solutions (QC) analyzed during this study.

	As (µg g^{-1})	Fe (µg g^{-1})	S (µg g^{-1})
QC verify (n = 5)			
SD	0.693	6.41	6.57
RSD	0.00678	0.0140	0.0599
2RSD	0.98%	0.22%	0.91%
Reference value	0.660	6.40	6.45
Uncertainty of reference value	0.003	0.06	0.01
Measured deviation from reference value	**4.95%**	**0.11%**	**1.93%**
QC verify (n = 5)			
SD	0.601	6.31	6.40
RSD	0.00615	0.0451	0.310
2RSD	1.02%	0.72%	4.84%
Reference value	0.595	6.11	5.89
Uncertainty of reference value	0.003	0.06	0.01
Measured deviation from reference value	**1.01%**	**3.31%**	**8.71%**

5.5.2 Mineral characterization and thermodynamic modelling

X-ray diffraction (XRD)

XRD patterns were recorded on a Bruker D8 powder diffractometer equipped with a BSI Si(Li) solid detector operating at 40 kV and 40 mA using Cu Kα radiation (λ = 1.5406 Å) with a 0.017° step in the range of Bragg angles 2ϑ of 5° to 70°. Samples for XRD analysis were loaded on a silicon wafer and the sample holder was sealed using an X-ray transparent dome (Bruker Dome, Polytron) with a low oxygen diffusion rate to minimize oxidation/transformation of air-sensitive Fe phases (e.g. green rust, magnetite).

High energy X-ray scattering

The local structure of the solids was investigated using pair distribution function (PDF) analysis. The dry powder samples were placed inside a glass capillary and sealed with paraffin to prevent oxidation during sample transport and data collection. This procedure prevents oxidation of highly reactive amorphous iron carbonate for at least one week.(Dideriksen et al., 2015) X-ray scattering data were collected at the 11-ID-B beamline of the Advanced Photon Source (Argonne National Laboratory, USA) using an X-ray wavelength of 0.2128 Å and a PerkinElmer amorphous Si 2D detector (40 x 40 cm, placed ~18 cm away from the sample). The geometry of the set-up was calibrated with Fit-2D using a CeO_2 standard powder (Hammersley et al., 1996; Hammersley et al., 1994) This software was also employed for polarization corrections and transformation of the data to the 1D. PDFs were obtained with PDFgetX2 (Qiu et al., 2004) using standard corrections such as subtraction of background (from measurement of empty glass capillary tubes) and incoherent scattering as well as corrections for nonlinearity in the detector response. The Fourier transformation of the reduced total scattering structure function, $F(Q)$, was conducted using Q_{max} of 24 $Å^{-1}$.

Transmission electron microscopy (TEM)

Samples for TEM were prepared in an anaerobic chamber by suspending the solid samples in isopropyl alcohol and dropcasting the suspension onto a holey amorphous coated carbon copper grid. The grid was loaded into a single tilt TEM holder which was sealed during a rapid transfer (< 30 s) into the TEM. Micrographs (TEM) were recorded using an FEI Tecnai G2 F20 X-Twin FEG TEM operated at 200 kV and equipped with a Gatan Imaging Filter (GIF) Tridiem™. Selected area electron diffraction (SAED) patterns were obtained using an aperture with an effective diameter of 250 nm at the image plane. The specimens were stable under the electron beam where no significant changes in morphology or crystal structure were observed during data acquisition (10 min per region of interest).

Scanning electron microscopy (SEM)

Samples for SEM were prepared inside an anaerobic chamber by fixing the dried powder samples onto a double-sided carbon tape attached to SEM stubs. The stubs were put inside an anaerobic jar (AnaeroJar™ Oxoid™, Thermo Fisher Scientific) to minimize oxidation during rapid transfer to the SEM. The stubs were quickly loaded into vacuum sputter coater (BAL-TEC MED 020 Leica Microsystems) and were coated with carbon to avoid charging effects during imaging. SEM images were acquired using a ZEISS Ultra Plus FE-SEM operated in high vacuum mode at an acceleration voltage of 3 kV with 10 µm aperture size using an InLens secondary electron detector.

X-ray absorption spectroscopy (XAS)

The dry solid samples were placed inside air-tight headspace crimp vials and placed inside an anaerobic jar to prevent oxidation during sample transport to the XAS beamline. Prior to data collection, pellets were prepared inside the glovebox (Ar atmosphere) by mixing up to 25 mg of dry sample with 45 mg cellulose using a mortar and pestle, calculated using XAFSmass software (Klementiev). The pellets were fixed onto custom sample holders and transferred to the station using the anaerobic jar.

As K-edge XAS data were collected at BM23 (bending magnet beamline) of the European Synchrotron Radiation Facility (ESRF, Grenoble, France) (Mathon et al., 2015). Spectra were recorded at liquid nitrogen temperatures (77 K) in fluorescence mode out to a reciprocal space value of 14 $Å^{-1}$. For this, a cryostat was used with helium convection. Fluorescence data were collected using a 13-element Ge solid-state detector. The vertical dimension of the X-ray beam during data collection was 1 mm and the horizontal dimension was 2 mm. To prevent second-order harmonics, rejection mirrors were used. A Si(111) crystal pair with a fixed beam exit was used as monochromator and Au foil was used to calibrate the beam (Au L_3 11919 eV). The XANES region was measured with 0.35 eV steps. About 4 to 6 scans were collected for each sample and reference compound, depending on data quality. During data collection, changes in line shape and peak position indicative of beam-induced redox reactions were examined and no beam damage was observed. Spectra were aligned, averaged, and background-subtracted using the Athena software package (Ravel and Newville, 2005). In order to quantify the As oxidation states in the samples,

least squares linear combination fitting (LCF) of the XANES spectra with reference As standards, namely As(III) and As(V) adsorbed onto synthetic goethite.

Meanwhile, Fe K-edge XAS data were collected at the SUL-X beamline of Angströmquelle Kalrsruhe (ANKA, Karlsruhe, Germany) (Stefan et al., 2013). Spectra were collected in transmission mode out to 14 $Å^{-1}$ under ultra-high vacuum, calibrated to a Fe(0) foil (7112 eV), using a Si (111) crystal pair with a fixed beam exit as monochromator. Data reduction and analysis of the EXAFS spectra were performed using the Athena software package. The transmission spectra were normalized using a third-order spline function to represent the background atomic absorption, and replicate scans of each reference material and sample were merged. EXAFS LCFs were performed on the k^3-weighted $\chi(k)$ Fe spectra of each sample between 3 and 12 $Å^{-1}$ using a Kaiser-Bessel window with dk of 3 $Å^{-1}$.

X-ray photoelectron spectroscopy (XPS)

The surface composition of the solids was examined using X-ray photoelectron spectroscopy (XPS). Analysis was performed using a KRATOS Axis Ultra X-ray photoelectron spectrophotometer with a monochromated Al Kα X-ray (1486.6 eV) operated at 150 W with a charge neutralizer. Analytical chamber base pressure was maintained at about. 10^{-9} mbar throughout data collection. Survey and high-resolution scans were recorded with pass energies of 80 and 20 eV, respectively. Accurate binding energies were calibrated with respect to the adventitious C 1s peak at 285.0 eV. The spectra were fitted by a least-squares fitting routine using Unifit software after subtraction with a Shirley background.

Thermodynamic modelling

Thermodynamic calculations for Fe and As were carried out using The Geochemist's Workbench® (GWB) (Bethke, 2010) with the MINTEQ database. Since the thermodynamic data of GR_{SO4} were missing, the data reported by Karimian et al. (2017; 2018a) were added in the MINTEQ database. Thermodynamically stable iron (oxyhydr)oxides (e.g., hematite, magnetite, goethite, lepidocrocite) were suppressed successively for calculations involving thermodynamically metastable Fe phases. The reaction of HS^- and SO_4^{2-} was decoupled for speciation and solubility calculations for Fe and As.

5.5.3 Aqueous geochemical data

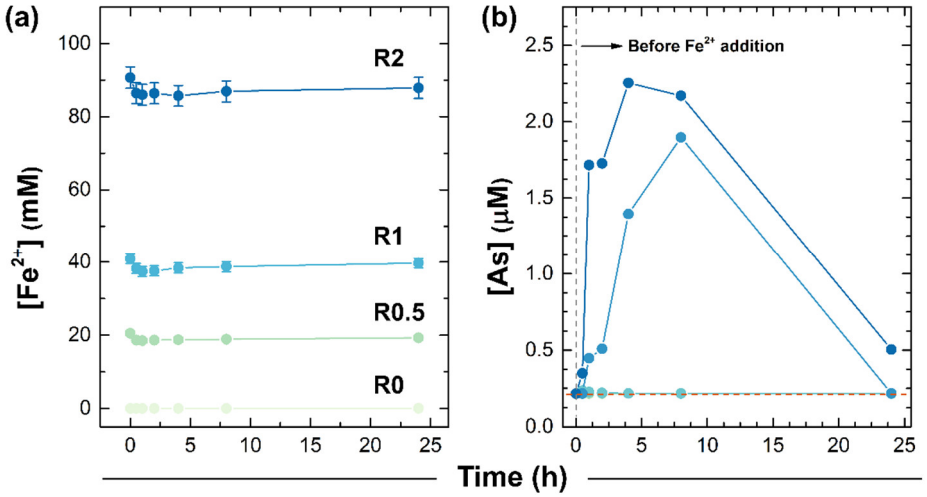

Figure S5.1 Concentrations of aqueous (a) Fe^{2+} and (b) As in the supernatant of the As(V)-bearing FH samples transformed at varying $Fe^{2+}_{(aq)}/Fe(III)_{solid}$ ratios (R). Error bars represent standard deviations of triplicate experiments (< 5% relative). The vertical gray line in (b) represents the As concentration in the supernatant after the adsorption of As(V) onto FH for 24 h and prior to the addition of aqueous Fe^{2+}. The horizontal orange line in (b) refers to the limit of detection (LoD).

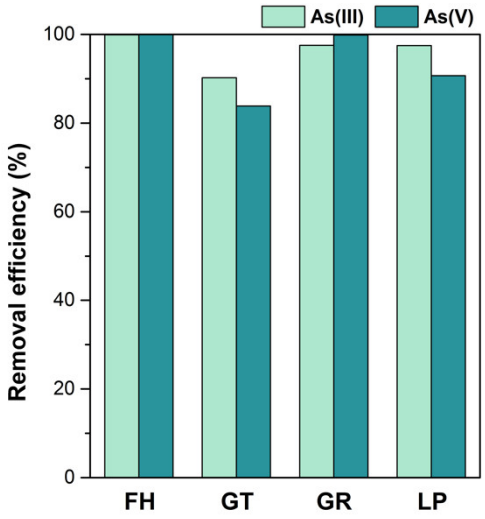

Figure S5.2 Removal of As(III) and As(V) upon interaction with different iron (oxyhydr)oxides after 24 h. Batch adsorption experiments were performed by adding the pre-formed synthetic iron (oxyhydr)oxides, prepared according to previously described methods,(Atkinson et al., 1967; Perez et al., 2019a; Schwertmann and Cornell, 2000) to As(III) or As(V) solutions (1.33 mM) at an adsorbent loading of 4 g L^{-1} at pH 6.5 (0.05 M MOPS) in 0.1 M NaCl. Phase separation and arsenic concentration analysis were done based on the method described by Perez et al. (2019a).

5.5.4 Oxidation state of As based on XANES and XPS

Table S5.2 As K-edge XANES linear combination fit results and statistics.

$Fe^{2+}_{(aq)}/Fe(III)_{solid}$ ratio	Weights[a]		Sum	*R*-factor	Red $\chi 2$	Bulk composition (%)	
	As(III)	As(V)				As(III)	As(V)
0 (control)	0.040 (0.005)	0.0946 (0.005)	0.987	0.001	0.001	4.1 ± 0.1	95.9 ± 0.1
0.5	0.348 (0.019)	0.688 (0.018)	1.035	0.019	0.014	33.6 ± 1.8	66.4 ± 1.7
1	0.353 (0.019)	0.675 (0.020)	1.028	0.022	0.015	34.3 ± 1.8	65.7 ± 1.8
2	0.432 (0.018)	0.587 (0.017)	1.019	0.020	0.013	42.4 ± 1.8	57.6 ± 1.7

[a] Values in parenthesis denote uncertainty values.

Table S5.3 XPS As reference binding energies.

Entry no.	Speciation	Binding energy (eV)	Reference
1	As(III) (As_2O_3)	44.5	Vadahanambi et al. (2013))
	As(V) (As_2O_5)	45.4	
2	As(III) (As_2O_3)	44.0	Chowdhury et al. (2011))
	As(V) (As_2O_5)	45.2	
3	As(III)	44.5	Zouboulis and Katsoyiannis (2005))
	As(V)	46.5	
4	As(III) ($NaAsO_2$)	44.2	Wagner and Muilenberg (1979))
	As(V) (Na_2HAsO_4)	45.5	
5	As(V) (AsO_4^{3-})	44.9	Bang et al. (2005))
	As(V) ($HAsO_4^{2-}$)	45.5	
	As(V) ($H_2AsO_4^-$)	46.7	

Table S5.4 As speciation data derived from the deconvoluted high-resolution As 3d spectra.

$Fe^{2+}_{(aq)}/Fe(III)_{solid}$ ratio	Binding energy[a] (eV)	FWHM[b] (eV)	Relative area (%)	Peak assignment	Surface composition[c] (%)
0 (control)	42.8	1.5	1.2	As (III)	1.9 ± 1.2
	43.5	1.5	0.7		
	44.8	1.5	62.0	As(V)	98.2 ± 12.3
	45.5	1.5	36.2		
0.5	42.9	1.5	12.2	As(III)	18.1 ± 6.9
	43.6	1.5	5.9		
	45.3	1.5	49.2	As(V)	81.9 ± 22.1
	46.0	1.5	32.7		
1	43.6	1.2	19.6	As(III)	32.6 ± 13.3
	44.3	1.2	13.0		
	45.0	1.2	40.4	As(V)	67.4 ± 18.3
	45.7	1.2	27.0		
2	43.2	1.5	14.8	As(III)	21.9± 3.9
	43.9	1.5	7.1		
	44.9	1.5	46.9	As(V)	78.1 ± 10.1
	45.6	1.5	31.2		

[a] Uncertainty of the binding energy is ± 0.3 eV. [b] full width at half-maximum. [c] Determination of the uncertainty is based on the peak area determination (Hesse et al., 2004). Values above 100 can be explained with a higher amount of As.

5.5.5 Thermodynamic modelling of As speciation and oxidation state

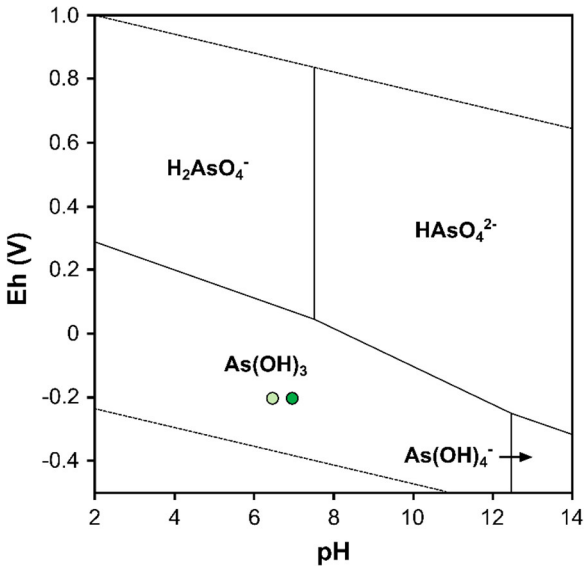

Figure S5.3 Eh-pH diagram of As at 25 °C and 1.013 bars using an activity of 10^{-9} for As. Thermodynamic calculations were performed with The Geochemist Workbench® using the MINTEQ database. Circles represent pH conditions: light green – pH 6.5; dark green – 7.

5.5.6 Pair distribution function analysis

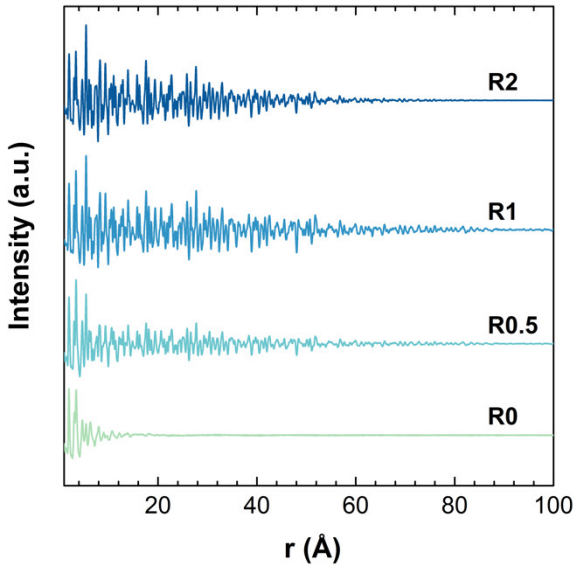

Figure S5.4 PDFs [$G(r)$] of the As(V)-bearing ferrihydrite samples transformed at varying $Fe^{2+}_{(aq)}/Fe(III)_{solid}$ ratios (R) which shows the short- and medium-range structure of the solids.

5.5.7 Transmission electron microscopy

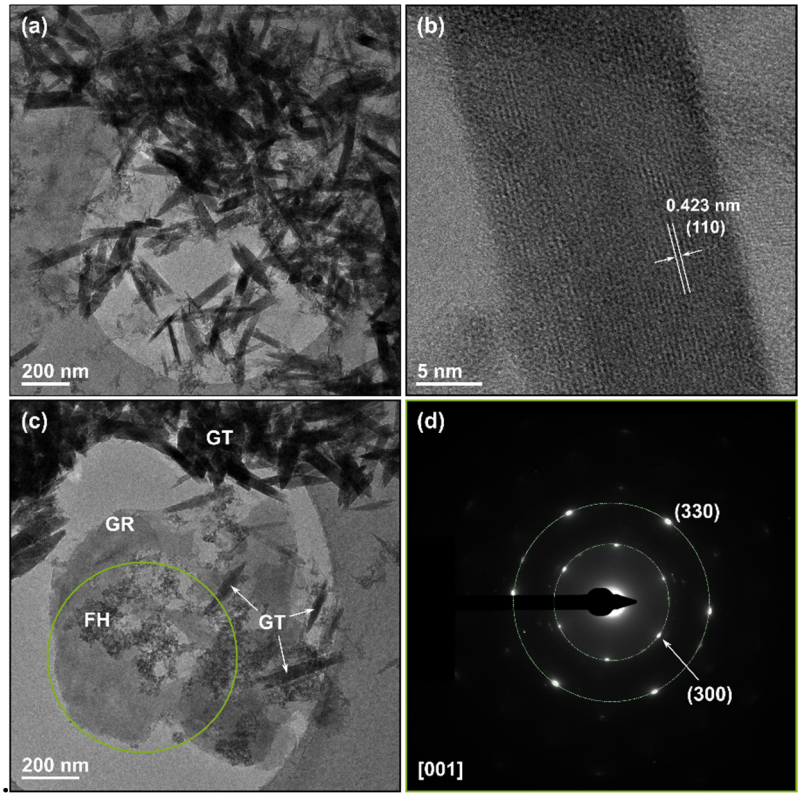

Figure S5.5 TEM images of the As(V)-bearing ferrihydrite samples transformed at an $Fe^{2+}_{(aq)}/Fe(III)_{solid}$ ratio of 2 showing the presence of (a-c) goethite (GT, dominant mineral phase), (c) green rust sulfate (GR_{SO4}) as confirmed by the SAED pattern in (d), and (c) ferrihydrite (FH). The green circle in (c) show the collected area for SAED in (d).

5.5.8 Scanning electron microscopy

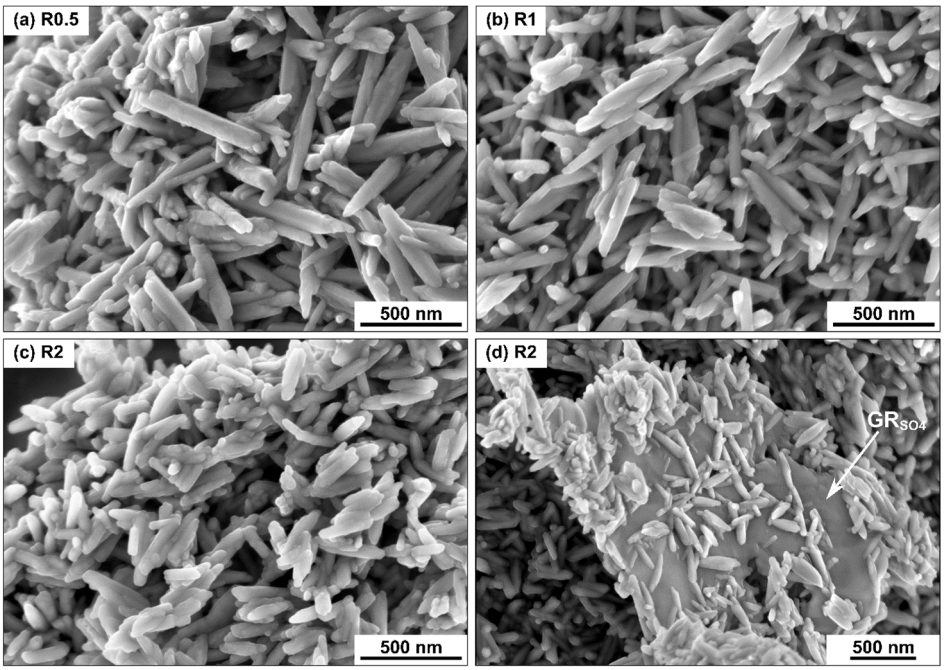

Figure S5.6 SEM images of the end-products of As(V)-bearing ferrihydrite transformed under varying $Fe^{2+}_{(aq)}/Fe(III)_{solid}$ ratios (R): (a) 0.5, (b) 1 and (c,d) 2.

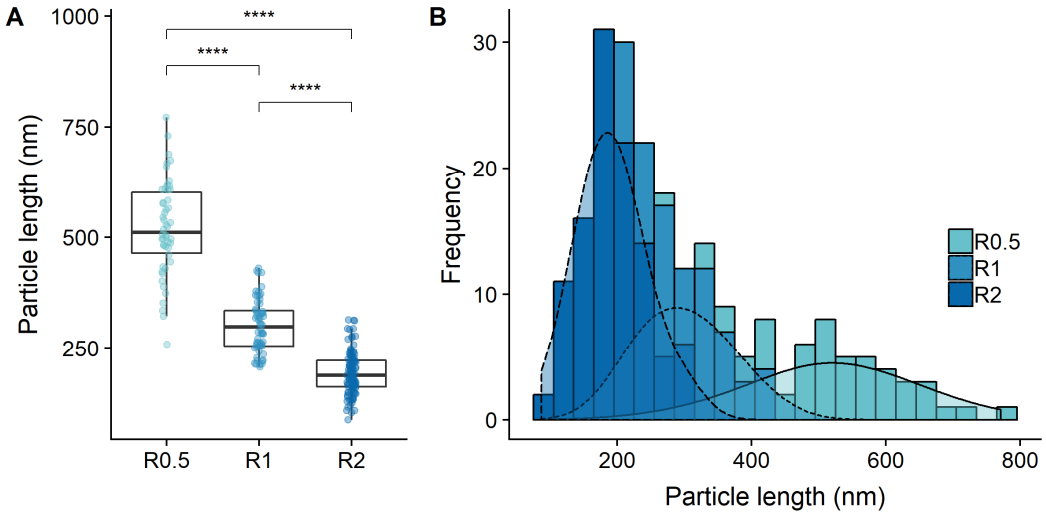

Figure S5.7 Analysis of the particle lengths (measured from SEM images) of the GT end-products of the As(V)-bearing FH transformed under varying $Fe^{2+}_{(aq)}/Fe(III)_{solid}$ ratios (R). A minimum of 50 particles were counted for each sample. (a) Box and whisker plots: The data points are plotted as circles, the 25th and 75th percentiles are bound by the boxes and the 10th and 90th percentiles are denoted by the whiskers. The particle lengths of goethite end-products under varying $Fe^{2+}_{(aq)}/Fe(III)_{solid}$ ratios are significantly different from each other (**** denotes p-value < 0.00001, Wilcoxon rank-sum test). (b) Distribution of the particle lengths of the GT end-products.

5.5.9 Phase quantification based on Fe K-edge EXAFS and PDF

Fe K-edge EXAFS

Data reduction and analysis of the EXAFS spectra were performed using the Athena software (Ravel and Newville, 2005), as previously reported by Thomas et al. (2018). The transmission spectra were normalized using a third-order spline function to represent the background atomic absorption or fluorescence, and replicate scans of each reference compound and sample were merged. LCFs were performed on the Fe k^3-weighted $\chi(k)$ EXAFS spectra of each sample between 3 and 12 Å.

Table S5.5 Linear combination fit results and statistics of Fe k^3-weighted $\chi(k)$ EXAFS spectra of transformation end-products during the 24 h reaction of As(V)-Fhy with varying $Fe^{2+}_{(aq)}$ concentrations ($Fe^{2+}_{(aq)}/Fe(III)_{solid}$ ratio from 0 to 2).

$Fe^{2+}_{(aq)}/Fe(III)_{solid}$ ratio	Weights			Sum	R-factor	Red. $\chi 2$
	FH	GT	GR			
0 (control)	1.0	-	-	1.0	-	-
0.5	0.135 (0.032)	0.666 (0.021)	-	0.801	0.042	0.221
1	0.140 (0.111)	0.768 (0.073)	-	0.908	0.288	2.663
2	0.096 (0.020)	0.718 (0.013)	0.042 (0.010)	0.856	0.043	0.226

PDF analysis

Fitting of PDFs was performed in PDFgui (Farrow et al., 2007) using the structures from Michel et al. (2007) (ferrihydrite), Hoppe (1941) (goethite) and Christiansen et al. (2009b) (green rust sulfate). An instrumental dampening of 0.033 was derived from fitting a synthetic, well crystalline goethite. Fitting of multiple structures to the data can easily result in unrealistic crystallographic parameters, in particular for phases present in trace amounts. To minimize this, we used starting values for the crystallographic parameters that had previously been derived from fitting of the structures to pure, synthetic ferrihydrite, goethite and green rust. Moreover, crystallographic parameters were only fitted for phases where a preliminary fit indicated >75% abundance (ferrihydrite for R0; goethite in R1 and R2). During the fitting, parameters were set free in the order: (1) scale; (2) SP diameter (describing the size of spherical coherently scattering domains); (3) δ^2 (describing the effect on peak broadening from correlated atomic motion); (4) unit cell axes dimension; (4) atomic displacement parameters (ADPs); and (5) atomic positions under the symmetry constrains of the structures' space group. If the scaling factor for a phase was (slightly) negative at the end of the fit sequence, the fitting was redone without the phase.

Table S5.6 Structural parameters obtained from PDF fitting of end-products after the 24 h reaction of As(V)-Fhy with varying $Fe^{2+}_{(aq)}$ concentrations ($Fe^{2+}_{(aq)}/Fe(III)_{solid}$ ratio from 0 to 2).

	$Fe^{2+}_{(aq)}/Fe(III)_{solid}$ ratio (R)						
	0	0.5		1		2	
Phase	FH	FH	GT	FH	GT	GT	GR
Scale	1.50	1.03	0.43	0.26	0.93	1.21	0.13
SP diameter (Å)	12.8				247	120	
δ^2	3.40				3.13	2.95	
a (Å)	5.99				4.62	4.60	9.54
b (Å)	5.99				9.95	9.94	9.54
c (Å)	8.98				3.02	3.02	10.95
Fe ADP	0.014				0.005	0.005	0.007
O ADP	0.008				0.009	0.009	0.016
S ADP							0.039
Na ADP							0.040
Interlayer water O ADP							0.059
Fe1 (occ.)	0.812				1.24	1.19	
Fe2 (occ.)	0.604						
Fe3 (occ.)	0.985						
Goodness of fit (*Rw*)	0.208		0.205		0.150	0.175	
Fraction of unit cell	1.00	0.594	0.406	0.146	0.854	0.9580	0.042
Number of Fe in unit cell	8.05	8.05	4.96	8.05	4.96	4.74	9.00
Fe in phase (moles)	8.05	4.78	2.01	1.17	4.24	4.54	0.375
Mole fraction of Fe	1.00	0.704	0.296	0.217	0.783	0.924	0.076
Mass fraction of phase	1.00	0.686	0.314	0.203	0.797	0.884	0.116

Note: *a*, *b* and *c* - unit cell parameters; ADP - atomic displacement parameter; Fe1, Fe2 and Fe3 occ. - Fe occupancy; δ_2 - vibrational correlation; *Rw* values were calculated between r_{min} = 1.69 Å and r_{max} = 40.0 Å.

5.5.10 Thermodynamic modelling of Fe mineral phases

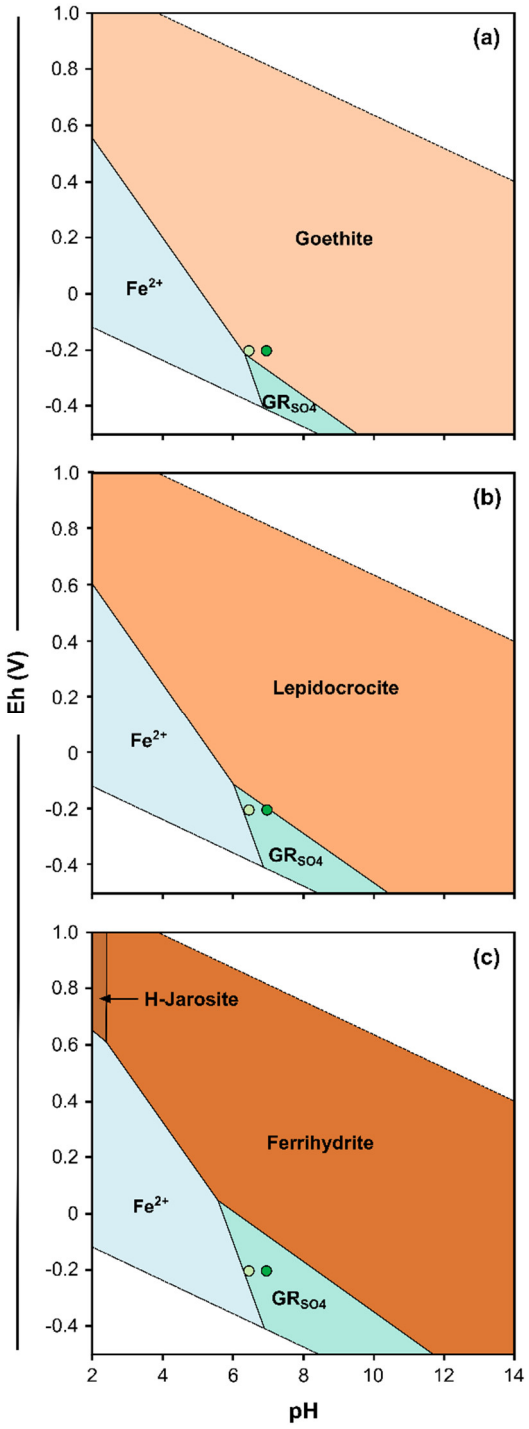

Figure S5.8 Eh-pH diagram for Fe-SO_4-H_2O system at 25 °C and 1.013 bars, assuming an activity of 10^{-2} for $Fe^{2+}_{(aq)}$ and 10^{-2} for $SO_4^{2-}{}_{(aq)}$. Thermodynamic calculations were performed with The Geochemist Workbench® using the MINTEQ database. The sequential distribution of metastable phases and precursors as more thermodynamically stable phases are suppressed are shown from (a) to (c). Circles represent pH conditions: light green – pH 6.5; dark green – 7). The sequential distribution of Fe phases at pH 6.5 and $0.5 \leq Fe^{2+}_{(aq)}/Fe(III)_{solid} \leq 2$: GT > LP > GR_{SO4} > FH.

5.5.11 Reference data for the calculation of Gibbs free energies

Table S5.7 Standard Gibbs free energy of formation (ΔG_f°) at 25 °C.

	ΔG_f° (kJ mol^{-1})	Reference
Mineral		
Green rust sulfate [$Fe^{II}_4Fe^{III}_2(OH)_{12}SO_4$]	-3819.4	Ayala-Luis et al. (2008))
Goethite [α-FeOOH]	-491.8	Robie and Hemingway (1995))
Lepidocrocite [γ-FeOOH]	-480.1	Majzlan et al. (2003))
Magnetite [Fe_3O_4]	-1012.7	Robie and Hemingway (1995))
2-line ferrihydrite [$Fe(OH)_3$]	-708.5	Majzlan et al. (2004))
6-line ferrihydrite [$Fe(OH)_3$]	-711.0	Majzlan et al. (2004))
White rust [$Fe^{II}(OH)_3$]	-490.0	Refait et al. (1999))
Aqueous species		
Fe^{2+}	-90.0	Robie and Hemingway (1995))
Fe^{3+}	-16.7	Robie and Hemingway (1995))
OH^-	-157.3	Robie and Hemingway (1995))
SO_4^{2-}	-744.0	Robie and Hemingway (1995))
H_2O	-237.1	Robie and Hemingway (1995))
$As^{III}(OH)_3$	-639.9	Nordstrom et al. (2014))
$H_3As^VO_4$	-766.4	Nordstrom et al. (2014))
$H_2As^VO_4^-$	-753.6	Nordstrom et al. (2014))
$HAs^VO_4^{2-}$	-713.7	Nordstrom et al. (2014))
$As^VO_4^{3-}$	-647.6	Nordstrom et al. (2014))

Chapter 6

Long-term stability and reactivity of green rust in natural groundwater

This chapter is adapted from:

Perez, J.P.H.; Schiefler, A.A.; Navaz Rubio, S.; Reischer, M.; Overheu, N.D.; Benning, L.G.; Tobler, D.J. Arsenic removal from natural groundwater using 'green rust' and its implication on contaminant mobility. *In the final stages of preparation for submission.*

Abstract

Arsenic (As) contamination in soil and groundwater remains a pressing global challenge due to its high toxicity and high mobility. Most As contaminations result from natural geological sources, but anthropogenic sources are also prevalent; for example, industries that used chromated copper arsenate formulations (containing ~30% wt. As) for wood preservation. In this study, we evaluated the potential of green rust (GR), an Fe(II)-Fe(III) layered double hydroxide, that is frequently occurring in suboxic/anoxic soils and groundwaters, for the natural attenuation of As contamination at a former wood preservation site. Based on the water chemistry of collected samples, our thermodynamic calculations indicated that GR phases (e.g., GR_{SO4}, GR_{CO3}) would be stable in the suboxic, circum-neutral deep aquifers at this site. To test the effectiveness of GR phases in reducing As contamination at this site, we performed long-term batch experiments by aging synthetic GR_{SO4} in collected (pristine) and As-spiked natural groundwater at ambient (25 °C) and low (4 °C) temperatures. Arsenic was efficiently removed from the As-spiked groundwater within 120 days at 25 °C, while aging at 4 °C resulted in 2-times slower As uptake rate. The long-term stability of GR_{SO4} in groundwater was strongly influenced by the presence of adsorbed As species and temperature. At 25 °C, GR_{SO4} aged in pristine groundwater (no As added) transformed to GR_{CO3} via ion exchange and was eventually fully converted to magnetite within 120 days. Both the addition of As to groundwater and decrease in temperature enhanced the GR_{SO4} long-term stability by a factor of 4, by inhibiting (i) ion exchange in the GR interlayer (i.e., slower conversion to GR_{CO3}) and (ii) transformation of GR to magnetite. The GR stability was multitudes higher (> 1 year) when both As was present and temperature, showing their synergistic stabilizing effects. We have successfully documented that GR is an important mineral substrate for the immobilization of As in contaminated suboxic subsurface environments and that remediation technologies should take this highly reactive phase into account when designing groundwater treatment approaches.

6.1 Introduction

From 1930s to 1990s, chromated copper arsenate (CCA) was widely used as wood preservative, replacing most oil-based preservatives such as creosote and pentachlorophenol (Humphrey, 2002). The extensive use of CCA in the wood preservation industry resulted in the uncontrolled release of these metal(loids) into underlying soils and groundwater (Nielsen et al., 2016; Nielsen et al., 2011), and nearby surface waters (Bhattacharya et al., 2002). Arsenic (As), which constitutes ~30 % wt. of CCA formulations, is highly mobile compared to copper (Cu) and chromate (Cr), and can penetrate deep into the soil layers (Hingston et al., 2001; Stilwell and Gorny, 1997; Zagury et al., 2003). In CCA-contaminated soils and groundwater, As is commonly present as the inorganic species arsenite [As(III)] and arsenate [As(V)]. Both these species persist in oxic and anoxic conditions due their relatively slow redox transformation kinetics (Masscheleyn et al., 1991; Zagury et al., 2008).

Natural attenuation processes can aid in mitigating As toxicity and mobility in CCA-impacted soils and groundwater (Reisinger et al., 2005). This primarily involves As sorption to naturally-occurring metal (oxyhydr)oxide phases (i.e., Fe, Al, Mn) (Wang and Mulligan, 2006), or precipitation of secondary As-bearing phases (Raghav et al., 2013). Specifically, iron (oxyhydr)oxides, which are ubiquitous in nature, can effectively remove As either by adsorption or co-precipitation and reduce the contamination level to background concentrations (Asta et al., 2010; Carlson et al., 2002; Fukushi et al., 2003; Maillot et al., 2013).

In suboxic to anoxic, circum-neutral subsurface environments, redox-active iron phases could be particularly important substrates for As sequestration. Green rust (GR) is a mixed-valent iron layered double hydroxide consisting of positively charged Fe(II)-Fe(III) hydroxide sheets alternating with negatively charged hydrated interlayers with anions (e.g., Cl^-, CO_3^-, SO_4^{2-}) (Usman et al., 2018), and occasional monovalent cations (Christiansen et al., 2009b; Christiansen et al., 2014). The thermodynamic and redox properties of GR suggest that it should be a common Fe-bearing phase in suboxic and anoxic environments (Ayala-Luis et al., 2008; Drissi et al., 1995; Linke and Gislason, 2018). GR phases are increasingly observed in natural settings, despite the fact that sampling and handling this highly reactive GR is difficult due to its high oxygen sensitivity. For example, GR has been identified in suboxic/anoxic environments such as gley soils (Abdelmoula et al., 1998; Trolard et al., 1997), groundwater (Christiansen et al., 2009a), ferruginous (Fe^{2+}-rich) lakes (Koeksoy et al., 2019; Vuillemin et al., 2019; Zegeye et al., 2012), mofette sites (Rennert et al., 2012) or mine drainage sites (Bearcock et al., 2006; Johnson et al., 2014). Importantly, naturally occurring GR particles have been reported to sequester arsenic (Root et al., 2007) and other trace elements (e.g., Zn, Cu, Ni) (Johnson et al., 2014; Johnson et al., 2015) in contaminated environments. Although these studies have successfully shown that GR can immobilize these contaminants, much less is known about the fate of these As-bearing GR upon aging in subsurface environments. This is an important consideration because GR, like many other Fe phases that have high As sorption capacities (e.g., ferrihydrite, schwertmannite, jarosite), are metastable, and they will eventually transform, which could result in the re-release of immobilized As.

In this study, we evaluated the potential of GR phases as substrates for the natural attenuation of As in a former CCA treatment site in Denmark. This site is well characterized and it is well documented that the majority of the contamination is located within the top 0.5 m soil layer, consisting of Cu, Cr (each ~100 mg kg^{-1}) and very high As concentrations (~2000 mg kg^{-1}) (Aktor and Nielsen, 2011; Nielsen et al., 2011). Due to its high mobility, As is however also present in the underlying shallow aquifer (ca. 100-600 µg L^{-1}) and to some extent in the deeper aquifer (0.1 to 0.5 µg L^{-1}). According to a previous technical report by the Danish Environmental Protection Agency (EPA) (Aktor and Nielsen, 2011), significant As leakage into the deep aquifer is prohibited by the presence of Fe (oxyhydr)oxides in the upper soil layers, but no further information is given. Based on initial thermodynamic modelling of existing data, we predicted that GR sulfate (GR_{SO4}) is a dominant iron-bearing phase in the deeper, suboxic zone at this site. Because it is highly reactive, GR could therefore play a key role in prohibiting As from leaking into the deeper aquifer. However, how stable is any As-bearing GR phase upon prolonged aging in the groundwater is unknown, and the question about the ultimate fate of As in the environment in case that GR transformations occurs is also unsolved

To investigate this, we collected groundwater samples from different soil depths at this former CCA treatment site, characterized their water chemistry and performed thermodynamic modelling to reaffirm the hypothesized presence of GR in the deeper, suboxic zones. Next, we set-up aging experiments where synthetic GR sulfate (GR_{SO4}) was exposed to the collected, suboxic groundwater at two different temperatures. In addition, we also spiked the collected groundwater with higher As concentrations (~6 mg L^{-1}) and reacted it with GR_{SO4} at two temperatures, to determine the stability of As-bearing GR. Our results provide new insights into the potential role of GR for controlling the mobility and toxicity of As in contaminated subsurface environments while also highlighting the geochemical parameters that control GR long-term stability in subsurface environments.

6.2 Materials and Methods

6.2.1 Site description

The investigated CCA treatment site was run by Collstrop from 1936 to 1976 in the town of Hillerød in Denmark (55°57' N, 12°21' E) (Figure S6.1). The top soil at this site became heavily contaminated with Cu, Cr (each ~100 mg kg^{-1}) and As (~2000 mg kg^{-1}) by CCA spills from tanks and by drippings from treated timber (Aktor and Nielsen, 2011; Nielsen et al., 2011). The top soil at the site consists of 1-5 meters of alternating sand and clay layers interpreted as meltwater deposits, and contains a shallow groundwater aquifer (ternary aquifer). The water table is about 3 m below surface. Underneath the shallow aquifer is a clay till layer of varied thickness (4-19 m thick). This is followed by the deeper groundwater aquifer (secondary aquifer), which is composed of a layer of relatively homogenous alluvial sand (20-40 m thick). A lower clay till layer (13-40 m) separates the secondary aquifer from the primary aquifer. The primary aquifer is composed of alluvial sands and the limestone below the sand. The groundwater flow direction in the shallow aquifer is primarily towards the east to a network of ditches while the flow direction in the deeper aquifer is north-northeast.

6.2.2 Groundwater sampling and analyses

Water samples were collected from Eks.P1 (surface ditch, oxic), well 129 (shallow aquifer, oxic) and well MD2 (secondary aquifer, suboxic) on February 2018 using an electric submersible pump. For groundwater extraction from wells 129 and MD2, the wells were first pumped until field parameters, i.e., pH, oxygen reduction potential (ORP), electrical conductivity (EC), dissolved oxygen (DO), temperature stabilized. ORP, EC, DO and pH were measured (Table S6.1) using a WTW Multi 3420 and WTW Multi 3430 handheld meter. The groundwater samples were collected in acid-cleaned (0.3 M HNO_3) airtight 1-L glass bottles (Duran®) and quickly transported to the laboratory for sample processing. In the laboratory, the collected groundwater samples were rapidly transferred inside the anaerobic chamber (97% N_2, 3% H_2, Coy Laboratory Products, Inc.) and immediately filtered through 0.2-µm polyethersulfone (PES) membrane filters to avoid equilibration with the chamber atmosphere. An aliquot of the filtrate was acidified with concentrated HNO_3 (Honeywell TRaceSELECT™ Ultra) in acid-cleaned 13-mL polypropylene (PP) tubes for inductively coupled plasma mass spectrometry (ICP-MS) analyses. Another aliquot was directly filled into acid-cleaned 20-mL glass vials (leaving no headspace), crimp capped and wrapped in aluminum foil for ion chromatography (IC) analyses. All samples were stored at 4 °C until analysis.

6.2.3 Synthesis of green rust sulfate

All used laboratory glass- and plasticwares were cleaned by soaking them in 0.3 M HNO_3 for at least 24 h, followed by thorough rinsing with deionized water (~18.2 MΩ·cm). All reagents used were analytical grade from Sigma-Aldrich and Acros Organics. Stock solutions used inside the anaerobic chamber were prepared using deoxygenated deionized water obtained by bubbling it with O_2- and CO_2 free nitrogen for at least 4 h.

Green rust sulfate (GR_{SO4}) was synthesized by aqueous Fe(II) oxidation at constant pH inside the anaerobic chamber (Mangayayam et al., 2018). In a PFA vessel, 50 mM $FeSO_4{\cdot}7H_2O$ was oxidized by bubbling CO_2-free air at a constant rate of ~5.0 mL min^{-1} using a peristaltic pump while maintaining the pH at ~7 by titration of 1 M NaOH. Oxidation and titration were stopped immediately after reaching an $[Fe]_{total}/[OH^-]$ ratio of ~4.55. The supernatant of the freshly-precipitated GR_{SO4} was removed and the remaining slurry was washed with O_2-free Milli-Q water to remove excess solutes. After washing, the supernatant was removed to obtain a thick slurry of GR_{SO4}. The density of the slurry was determined based on the difference between the $[Fe_{tot}]$ of an aliquot of the slurry dissolved in 0.3 M HNO_3 and the dissolved $[Fe_{tot}]$ in the supernatant after filtration through a 0.2-µm syringe filter. Dissolved $[Fe_{tot}]$ concentrations were analyzed by atomic absorption spectroscopy (AAS). The GR_{SO4} slurry (~152 mM $[Fe_{tot}]$) was used for the aging experiments on the day of synthesis.

6.2.4 Aging experiments

In 100-mL crimp cap glass bottles, an aliquot of the GR_{SO4} slurry was diluted to 90 mL using the collected groundwater from well MD2 (deep aquifer) to achieve an $[Fe_{tot}]$ of ~12.5

mM. In another set-up, the groundwater was spiked with 6 mg L^{-1} As (~80 µM), consisting of equimolar amounts of As(III) and As(V), to simulate their frequent co-occurrence in suboxic environments (Masscheleyn et al., 1991; Zagury et al., 2008). The effect of water depth was also examined by aging the samples at different temperatures of 25 °C inside the anaerobic chamber and at 4 °C (i.e., subsurface temperature) inside a refrigerator. The initial groundwater pH was ~7.5 and only marginally varied during aging (± 0.3 pH units). All experiments were done in triplicates. Aliquots of the GR suspension were collected after 1, 7, 15, 30, 60, 120 or 365 days. A portion of the collected sample was filtered (0.22-µm syringe filters), and the filtrate was acidified with HNO_3 and stored in acid-cleaned tubes at 4 °C. Major aqueous elemental concentrations were determined by inductively coupled plasma optical emission spectroscopy (ICP-OES Varian 720ES) as described in our previous work (Perez et al., 2019a) (see Table S6.2 for limits of detection (LoD) and uncertainty analysis of the method). The rest of the collected samples at specific time intervals were used to characterize the solid phase. For this, aliquots of the suspension were transferred into glass vials, crimp capped and centrifuged outside of the anaerobic chamber. Afterwards, the solids were separated inside the chamber and prepared for X-ray powder diffraction (XRD) and scanning electron microscopy (SEM) imaging.

6.2.5 Analytical methods, mineral characterization and thermodynamic modelling

Major, minor and trace elements in the groundwater samples were measured by ICP-MS on a Thermo Fisher iCAPQc ICP-MS. Dissolved Fe^{2+} concentrations were estimated using the ferrozine method (Viollier et al., 2000). Dissolved inorganic and organic anions in the groundwater samples were analyzed by suppressed IC system (Sykam Chromatographie) using a SeQuant SAMS anion IC suppressor (EMD Millipore), an S5200 sample injector, a 3.0 × 250 mm lithocholic acid 14 column and an S3115 conductivity detector. The eluent was 5 mM Na_2CO_3 with 20 mg L^{-1} 4-hydroxybenzonitrile and 0.2% methanol. The flow rate was set to 1 mL min^{-1} and the column oven temperature to 50°C.

XRD patterns were recorded on a Bruker D-8 Discover powder diffractometer equipped with a Lynxeye 1-D detector operating at 40 kV and 40 mA using Cu Kα radiation (λ = 1.5406 Å) with a 0.017° step, a 2.5 s per step scan length, and 2ϑ from 5° to 70°. Samples for XRD analysis were loaded onto a silicon wafer and the sample holder was sealed using an X-ray transparent dome (Bruker Dome, Polytron) with a low diffusion rate to minimize sample oxidation. Phase quantification was done via Rietveld refinement of the XRD patterns using the software GSASII (Toby and Von Dreele, 2013). The high background produced by the dome was corrected by subtracting the XRD pattern of the empty sample holder from the sample XRD, and by applying a Savitzky-Golay smoothing filter. In addition, the background was determined separately from the Rietveld refinement using a Chebyshev polynomial. The instrumental parameters were refined from a corundum standard.

Particle morphologies and sizes of aged solids were characterized by SEM (Quanta 3D, 10 kV, high vacuum). Samples for SEM imaging were prepared inside the anaerobic

chamber by suspending an aliquot of a solid sample in ethanol and drop-casting the suspension onto SEM stubs.

Thermodynamic calculations were carried out using The Geochemist's Workbench® (Bethke, 2010) with the MINTEQ database and the chemical compositions of the analyzed groundwater. Thermodynamic data of GR_{SO4} and GR_{CO3} (Karimian et al., 2017) were added to the MINTEQ database. Thermodynamically stable iron (oxyhydr)oxides (e.g., hematite, magnetite, goethite, lepidocrocite) were suppressed successively for calculations involving thermodynamically metastable Fe phases (Linke and Gislason, 2018). The reaction of HS^- and SO_4^{2-} was decoupled for speciation and solubility calculations for Fe and As species.

6.3 Results and Discussion

6.3.1 Groundwater chemistry and predicted iron phases in Collstrop

The geochemical compositions of the three groundwaters collected at the CCA site are shown in Table S6.1. The As concentration was highest in the surface ditch water (~5,000 µg L^{-1}, Eks.P1), and then clearly decreased with soil depth, as shown by As concentrations of ~134 µg L^{-1} in the shallow aquifer (129) and <0.48 µg L^{-1} in the deep aquifer (MD2). These values fit well with measurements performed in 2009 (Aktor and Nielsen, 2011), and demonstrate that the highest degree of CCA contamination is still contained within the topmost soil layer, while As concentrations in the deep aquifer are below the threshold value of 5 µg L^{-1} set for water quality in Denmark (Ministry of Environment and Food of Denmark, 2017). These new geochemical data (Table S6.1) were then used to calculate Eh-pH profiles (Figure S6.2) to reaffirm the stability of GR phases in the suboxic zones and to discern potential GR transformation pathways.

The thermodynamic calculations revealed that, under suboxic conditions, GR phases (i.e., GR_{CO3}, GR_{SO4}) are expected to form first based on the Eh-pH diagram (Figure S6.2a). Specifically, under the circum-neutral, suboxic conditions characterizing well MD2, GR_{SO4} was predicted to be the stable GR phase. Interestingly however, so far, only GR_{CO3} has been observed in suboxic groundwater. For example, Christiansen et al. (2009a) documented the presence of GR_{CO3} in suboxic groundwater wells with similar groundwater chemistry (i.e., circum-neutral pH, high concentrations of HCO_3^- and SO_4^{2-}). The dominance of GR_{CO3} over GR_{SO4} may be due to the abundance of CO_3^{2-}. The calculations also confirmed that GR is thermodynamically metastable at near-neutral pH and reduced conditions, and will eventually transform to more stable Fe (oxyhydr)oxides, in this case likely magnetite, as shown by the Eh-pH diagram after aging (Figure S6.2b) Such transformations have been documented previously in laboratory experiments (Sumoondur et al., 2008).

6.3.2 GR stability in suboxic groundwater

Our thermodynamic calculations show that GR_{SO4} phases can potentially form in the deep aquifer and soil layers where suboxic, circum-neutral pH conditions dominate. To test the

long-term stability of GR under these conditions, we first performed GR_{SO4} aging experiments in As-free suboxic groundwaters (well MD2) at 25 and 4 °C.

GR_{SO4} aging at 25°C

For GR_{SO4} aged at 25 °C, the mineralogy of the solids changed from GR_{SO4} to GR_{CO3} (peak at ~11.8°, Figure S6.3a) over the first 7 days of aging, with GR_{CO3} making up ~80% of the solids after 7 days. Upon longer aging (i.e., day 15), trace amounts of magnetite could be detected (XRD peak at ~35.6°, Figure S6.3a) and with further aging, the magnetite fraction increased, particularly after 30 days aging, at the expense of both GR_{SO4} and GR_{CO3} phases. After 120 days, magnetite was the dominant mineral phase (>99%), with only traces of GR left (Figure 6.1a). In addition to GR and magnetite, trace amounts of another carbonate-intercalated layered double hydroxide (LDH) phase were detected in samples collected between day 7 and day 30 (Figure S6.3a). The GR to magnetite transformation documented by the XRD results was corroborated by SEM imaging of the resulting solids. The images revealed thin hexagonal GR plates (Figure 6.1d), which were replaced by small isometric magnetite crystals in the 120-day sample(Figure 6.1e).

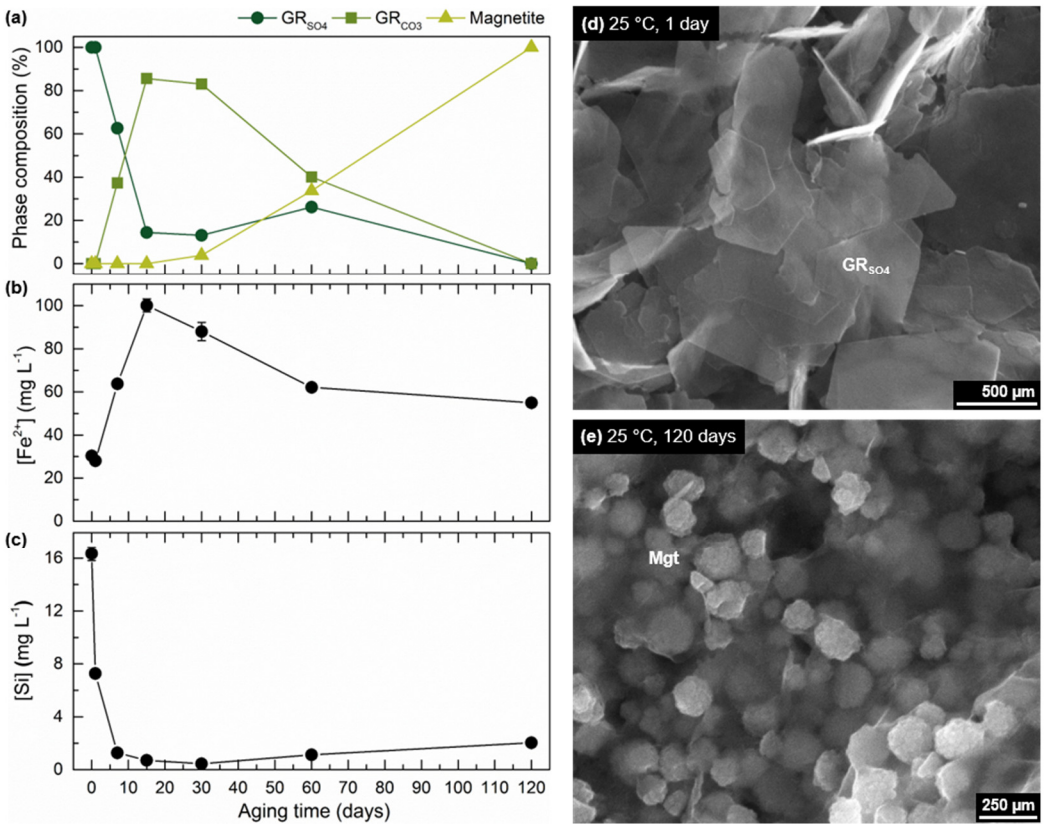

Figure 6.1 The time evolution of (a) solid phase mineralogy, (b) dissolved [Fe^{2+}] and (c) dissolved Si during aging of GR_{SO4} in suboxic groundwater at 25 °C over a period of 120 days. SEM image of solids collected after aging GR_{SO4} for (d) 1 day (thin hexagonal µm-sized GR_{SO4} platelets) and (e) 120 days (aggregates of magnetite nanoparticles). Dissolved [Fe^{2+}] was approximated by total dissolved Fe, because aqueous Fe^{3+} has a very low solubility (calculated maximum dissolved [Fe^{3+}] at circum-neutral pH = 10^{-12} mg L^{-1}), thus can be assumed negligible (Perez et al., 2019b).

These mineral transformations are also reflected in the changes in solution chemistry. Specifically, a rapid increase in aqueous [Fe^{2+}] (Figure 6.1b) coincided with the transformation of GR_{SO4} to GR_{CO3} between day 1 and day 15 (Figure 6.1a). This suggests that GR_{SO4} partially dissolves and transforms to GR_{CO3} by interlayer anion exchange. After 15 days, aqueous [Fe^{2+}] starts to decrease, in conjunction with the gradual formation of magnetite and disappearance of GR_{CO3}.

Interestingly among the other aqueous ions analyzed as a function of aging time, dissolved silica also clearly changed during GR transformation. Specifically, all initial dissolved silica ($[Si]_{initial}$ = ~16 mg L^{-1}) was removed from solution during the first 30 days (Figure 6.1c), when GR phases dominated. It has been demonstrated previously that Si binds strongly to GR (Yin et al., 2018), and adsorbed Si can also inhibit GR transformation to other Fe (oxyhydr)oxides (Kwon et al., 2007). However, once GR started to transform to magnetite, partial Si release was observed.

GR_{SO4} aging at 4°C

Similar mineralogical changes were observed when GR was aged at 4 °C, compared to 25 °C, but they occurred at much slower rates. For example, significant transformation of GR_{SO4} to GR_{CO3} (>10%) was only observed on day 60, and magnetite only appeared on day 120 at 4 °C. Meanwhile, at 25 °C, these processes occurred on days 7 and 15, respectively. At the end of 120 days of aging at 4 °C, GR_{CO3} (~65%) and GR_{SO4} (~34%) were still the dominant phases (Figure 6.2a), with magnetite constituting <1% (mainly spotted in SEM images, Figure 6.2e). Similar to reactions at 25 °C, the dissolved [Fe^{2+}] increased simultaneously with the formation of GR_{CO3} in the system (Figure 6.2c), confirming that sulfate interlayer exchange must co-occur with GR_{SO4} dissolution. Similarly, all dissolved Si was removed from solution by the present GR phases. No Si release occurred here over 120 days because magnetite formation was insignificant over this time frame.

Overall, these results show that GR_{SO4} is indeed metastable and will change into GR_{CO3}, and eventually magnetite as projected in calculated Eh-pH diagrams. However, temperature has a strong impact on the time-scale of these transformations, indicating at least a 4-fold increase in GR_{SO4} long-term stability by lowering the temperature from 25 to 4 °C. Noteworthy, it has been shown that adsorbed Si inhibits GR transformation to other Fe (oxyhydr)oxides (Kwon et al., 2007), thus here, GR stability may have also been positively affected by the adsorbed silica.

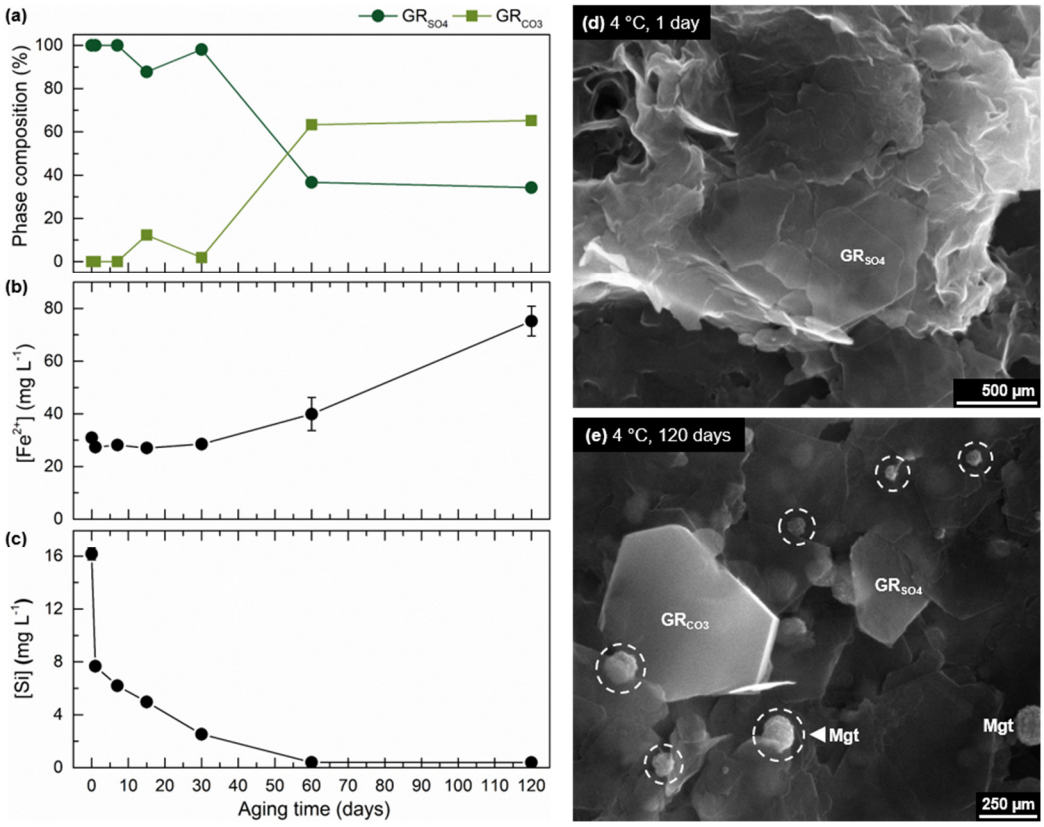

Figure 6.2 The time evolution of (a) solid phase mineralogy, (b) dissolved [Fe^{2+}] and (c) dissolved Si during aging of GR_{SO4} in suboxic groundwater at 4 °C over a period of 120 days. SEM image of solids collected after aging GR_{SO4} for (d) 1 day (thin hexagonal µm-sized GR_{SO4} platelets) and (e) 120 days (mostly GR_{SO4} and thick hexagonal µm-sized GR_{CO3}, with small amounts of magnetite).

6.3.3 GR aging in As-spiked suboxic groundwater

To assess the fate of potential leaked As in these deeper, suboxic layers, and its impact on GR long-term stability, we set-up similar GR_{SO4} aging experiments as above (both at 25 and 4 °C) and then spiked the reactors with a mixture of equivalent concentrations of As(III) and As(V) (initial [As_{total}] = 6 mg L^{-1}).

GR_{SO4} aging at 25 °C with As

At 25 °C and in the presence of As, GR_{SO4} showed prolonged stability, with significant GR_{CO3} only forming between day 60 and 120 (Figure 6.3a), and trace amounts of magnetite (<1%) appearing after 120 days (as seen from SEM images, Figure 6.3b). Noteworthy that, similar to sample aged at 25 °C without As, a clear peak splitting can also be observed in the GR_{CO3} peak at ~11.8° (Figure S6.3c and S6.4), indicating the presence of minor amounts of either pyroaurite (Ingram and Taylor, 1967) or a partially Mg-substituted GR_{CO3} (Refait et al., 2002). Dissolved [Fe^{2+}] and dissolved [Si] mirror these trends as observed and discussed before (Section 3.2). In terms of dissolved As, ~36% is removed within the first day of aging, while after, adsorption is slower but steady, with almost all As removed after 120 days aging. When comparing these trends (Figure 6.3) to As-free aging of GR_{SO4} (Figure 6.1), it is clear that the added As species temporarily stabilizes GR_{SO4}, delaying its transformation to GR_{CO3} and ultimately magnetite. Such stabilization is best explained by

fast adsorption of As species onto GR particle surfaces as supported by the removal of dissolved As and the fact that all other parameters were identical between As-spiked and As-free systems.

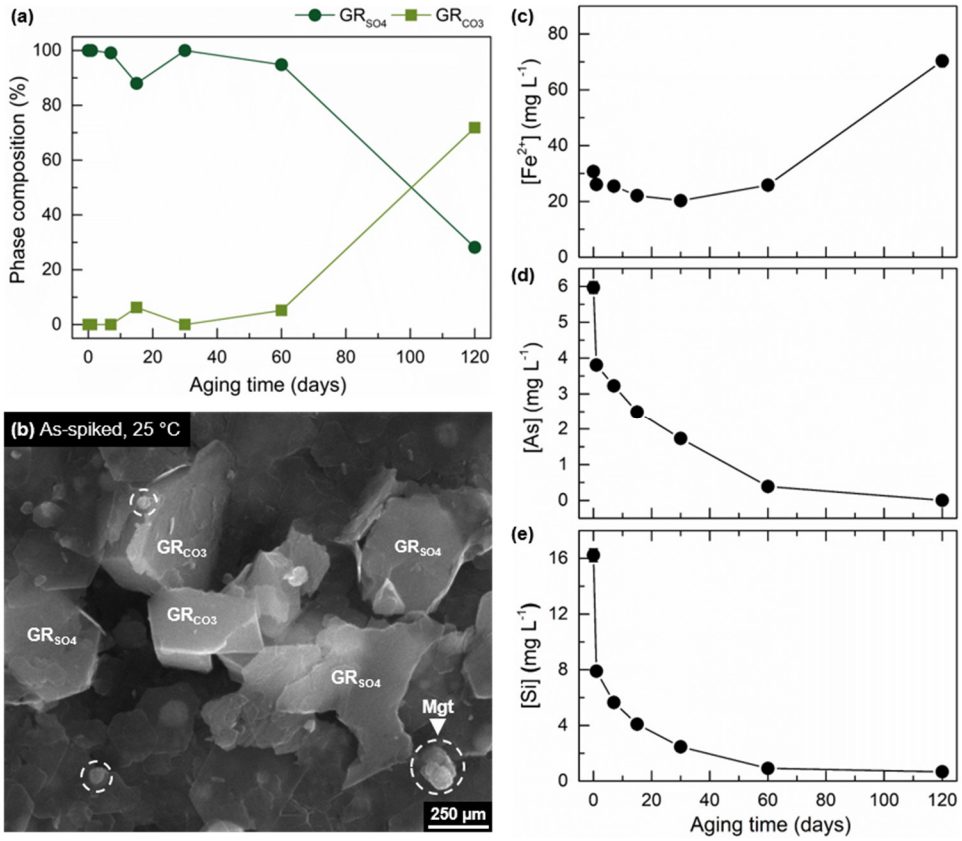

Figure 6.3 The time evolution of (a) solid phase mineralogy, (b) SEM image of the aged GR_{SO4} solids (showing partial transformation to GR_{CO3} and minor amounts of magnetite after 120 days), (c) dissolved [Fe^{2+}], (d) dissolved As and (e) dissolved Si during aging of GR_{SO4} in suboxic groundwater at 4 °C over a period of 120 days.

If such an As stabilization mechanisms is acting on GR_{SO4}, it is surprising however, that it took 120 days for all As to become adsorbed. For example, As adsorption by GR_{SO4} in ultrapure water systems at 25 °C and at similar As/Fe loadings is completed within 4 hours (Perez et al., 2019a). The slower adsorption kinetics in groundwater observed here compared to the pure system probed by Perez et al. can partly be explained by the presence of other solutes with similarly high sorption affinities for GR. A primary sorption competitor in the water here is dissolved silica, seeing that it is abundant and structurally analogous to As, meaning it competes for the same GR surface sites as As (Kwon et al., 2007). In a previous study, it was shown that As sorption capacity by Fe (oxyhydr)oxides was reduced by up to ~70% in the presence of 10 mg L^{-1} dissolved Si (Meng et al., 2000). Here, we see signs for this site competition as well. Specifically, we observed that the rate of Si removal is much slower in the As-spiked system (Figure 6.3e) compared to the pure system (no As added, Figure 6.1c), indicating that Si is indeed competing with As for adsorption sites when they co-exist. Other sorption competitors include magnesium (Mg^{2+})

and phosphate (PO_4^{3-}) however, their abundances were too low (Table S2) to have an impact on As removal here (Perez et al., 2019a).

GR_{SO4} aging at 4 °C with As

No significant changes in mineralogy were observed when GR_{SO4} was aged in As-spiked groundwater at 4 °C. GR_{SO4} was still the dominant mineral phase (~92%) after 120 days and only a small amount of GR_{CO3} (~8%) formed (Figure 6.4a and 4b). The As removal rate was also much slower, with only ~66% of the initial As immobilized after 120 days (Figure 6.4d). This is also demonstrated by the calculated adsorption rate (Table S3), which is about 2 times lower at 4 °C than 25 °C. Consequently, the trend of silicate adsorption was very similar to As, with slower and incomplete removal (~86%, Figure 6.4e). These results indicate that < 10 °C subsurface temperatures and the presence of adsorbed species significantly increase the long-term stability of GR_{SO4} in suboxic groundwater environments.

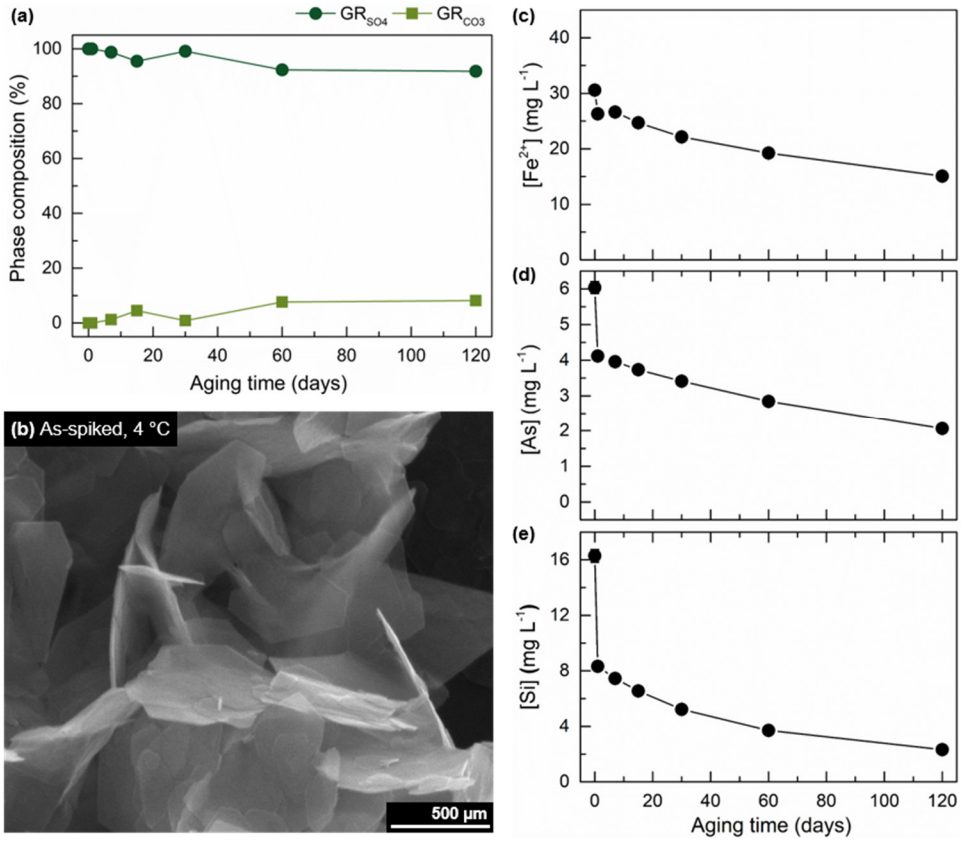

Figure 6.4 The time evolution of (a) solid phase mineralogy, (b) SEM image of the aged GR_{SO4} solids, (c) dissolved [Fe^{2+}], (d) dissolved As and (e) dissolved Si during aging of GR_{SO4} in suboxic groundwater at 4 °C over a period of 120 days.

6.3.4 GR transformation and implications on As mobility

The mobility and toxicity of arsenic in contaminated soils and groundwaters are often controlled by their sorption affinity to mineral surfaces present in the subsurface. Specifically, naturally-occurring iron (oxyhydr)oxides are effective sorbents for arsenic immobilization. GR phases are expected to form first in ferruginous subsurface

environments (Christiansen et al., 2009a), and can effectively sequester toxic metals (Bearcock et al., 2011; Johnson et al., 2015) and metalloids (O'Loughlin et al., 2003; Perez et al., 2019a; Thomas et al., 2018). However, GR is a metastable phase in comparison to more thermodynamically stable iron (oxyhydr)oxides such as goethite or magnetite and often transform to these minerals with time (Usman et al., 2018). Arsenic sequestered by GR can therefore be remobilized and redistributed in the environment during such transformations.

When aged in groundwater at 25 °C, our results show that synthetic GR_{SO4} was partially converted to GR_{CO3} through ion exchange within a few days, accompanied by Fe^{2+} release in the supernatant. Magnetite appeared after 30 days, at the expense of GR, and was the main transformation end-product. Some trace Fe(III) oxyhydroxides (e.g., lepidocrocite and goethite) eventually appeared after 1 year, which typically form at low dissolved [Fe^{2+}] (< 2 mM) (Hansel et al., 2005; Pedersen et al., 2005). The formation of magnetite from GR was much slower in the natural groundwater matrix compared to ultrapure water matrix which only took a few hours to several days (Ahmed et al., 2010; Sumoondur et al., 2008). On the other hand, GR transformation rates were much slower at 4 °C compared to ambient conditions. GR_{SO4} only started transforming to GR_{CO3} after 60 days and traces amounts of magnetite only appeared after 120 days. The relative composition of these phases also did not change significantly even after one year of aging (Figure S6.5), indicating that low temperatures increases the longevity of GR in subsurface environments.

Aging GR_{SO4} in As-spiked groundwater at 25 °C also slowed down the ion exchange rate, delaying the formation of GR_{CO3}, and inhibiting the formation of magnetite in the system up until 120 days. However, further aging of the sample up to a year, did ultimately result in magnetite formation (Figure S6.5). As(III) and As(V) has been shown to form inner-sphere surface complexes at the GR particle edges (Jönsson and Sherman, 2008; Wang et al., 2010). These surface complexes are suggested to prevent the transformation of GR by stabilizing the particle edges, thus inhibiting crystal dissolution and precipitation of magnetite. Depending on the As oxidation state and amount of adsorbed As, magnetite formation can be delayed from days to a year (van Genuchten et al., 2019a; Wang et al., 2014). Arsenic was also completely removed despite the complex composition of the natural groundwater and the high concentration of competing ions (i.e., dissolved silica). Most importantly, the transformation of GR to magnetite did not result in any release of adsorbed As species into the supernatant. Magnetite can also effectively remove As because of its high adsorption capacity (van Genuchten et al., 2019b; Yean et al., 2005) and the possibility to incorporate As in its crystal structure (Huhmann et al., 2017; van Genuchten et al., 2019a; Wang et al., 2011).

Upon aging in As-spiked groundwater at 4 °C, the initial GR_{SO4} remained fairly stable (>90%), with a minor fraction transforming to GR_{CO3}. No magnetite was detected in the samples despite aging for up to a year (Figure S6.5). These results are consistent with our thermodynamic calculations which show that GR_{SO4} is indeed the most stable Fe-bearing phase at circum-neutral, suboxic conditions (Figure S6.2). Our results at low temperature are particularly important because the temperature in the subsurface typically reflects the average annual air temperature at the surface with only a minor seasonal variation

(Wisotzky et al., 2018). Previously measured temperatures in the deep wells at the Collstrop site are typically lower than 10 °C (Aktor and Nielsen, 2011) whereas average annual air temperature in Denmark is around 8.7 °C (Cappelen, 2012). The As removal rate is slower at subsurface temperatures (~66% removal after 120 days), but complete removal (>99%) was achieved after one year of aging. Hence, it is likely that GR can efficiently remove As species in case of potential leakage into these subsurface environments, where low temperature significantly increases its long-term stability.

Overall, the increased stability of As-bearing GR_{SO4} at low temperatures (> 1 year) observed in this study gives important insights on how GR phases can limit As mobility in the subsurface. Moreover, even if GR eventually transforms to magnetite (likely at time spans > 1 year), we do not expect any significant As release, given the high As sorption capacity of magnetite (van Genuchten et al., 2019a; van Genuchten et al., 2019b). A point to consider here that the presented experiments to a large extent excluded microbially-driven processes, i.e., groundwaters were filtered (0.2 µm) prior to testing. However, in these suboxic settings, iron reduction and oxidation reactions are in parts also mediated by microbes (Melton et al., 2014), thus would likely also influence GR transformation processes; an aspect to investigate in future studies.

6.4 Conclusion

In this study, we examined the potential of GR for the natural attenuation of arsenic using natural groundwater from a former wood preservation site. Thermodynamic calculations based on the water chemistry of collected samples from the contaminated site show that GR can form in these suboxic subsurface environments. We performed long-term batch experiments by aging synthetic GR_{SO4} in suboxic groundwater, with or without added As, at ambient (25 °C) and low (4 °C) temperatures. Arsenic was completely removed (>99%) from the natural groundwater after 120 days of aging at ambient temperatures, while the As removal rate was slower at lower temperature and complete removal was only achieved after one year of aging. The longevity of GR_{SO4} during aging in natural groundwater was greatly affected by temperature and the presence of adsorbed As species. Under ambient temperature, GR_{SO4} transformed to GR_{CO3} and ultimately to magnetite within one month of aging in pristine groundwater. The addition of As to the groundwater significantly slowed down these mineral transformation rates due to the adsorption of As onto GR_{SO4}. A similar stabilization effect was achieved when GR_{SO4} was aged in pristine groundwater at 4 °C. Remarkably, GR_{SO4} remained stable for even up to one year when aged in As-spiked groundwater at 4 °C. Overall, our results highlight the importance of GR in removing As species from groundwater, and their potential as critical host phases for As in natural attenuation processes in contaminated subsurface environments.

6.5 Supporting Information

Supplementary tables and figures

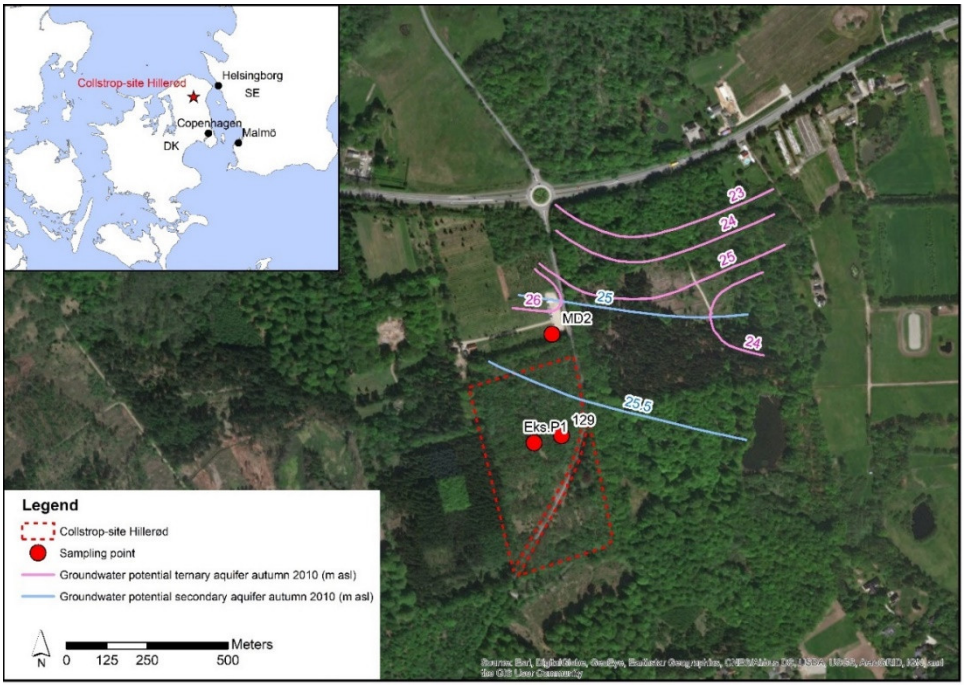

Figure S6.1 Location and distribution of the sampling sites (red dot) at the Collstrop site. The general flow directions of the ternary (magenta lines) and secondary (blue lines) aquifer are also shown (Aktor and Nielsen, 2011).

Table S6.1. Aqueous geochemical composition of collected groundwater samples from Collstrop site.

Parameter	**Sampling sites**		
	Eks.P1	129	MD2
Description	Surface ditch	Shallow well	Deep well
Well depth (m)	n.a.	5.9	20
Chemical parameters			
pH	6.65	6.56	7.53
Temperature (°C)	1.2	7.4	8.1
ORP (mV)	254	277	6.5
EC (µS cm^{-1})	171	407	655
DO (mg L^{-1})	6.6	8.6	0.1
Anions (mg L^{-1})			
Br^-	< 0.16	< 0.16	< 0.16
Cl^-	10.84	26.67	60.76
F^-	15.41	4.24	0.21
HCO_3^-	n.a.	n.a.	276
NO_3^-	< 0.12	0.28	2.59
SO_4^{2-}	2.07	14.31	50.28
PO_4^{3-}	0.48	< 0.02	< 0.02
Major elements (mg L^{-1})			
Al	3.79	0.42	< 0.03
Ba	< 0.15	< 0.15	< 0.15
Ca	5.49	49.72	110.68
Fe_{tot}	0.60	0.02	0.14
Fe(II)	< LoD	< LoD	0.13
K	8.81	2.37	1.43
Mg	1.37	5.08	8.45
Mn	0.30	0.45	0.22
Na	25.63	35.85	29.13
Si	n.a.	n.a.	16.25
Sr	< 0.01	0.13	0.22
Trace elements (µg L^{-1})			
As	5,016.05	134.24	< 0.48
B	26.12	16.73	41.05
Be	0.52	< 0.10	< 0.10
Co	0.45	1.13	0.64
Cr	64.95	3.80	< 0.16
Cs	< 0.02	< 0.02	0.47
Cu	85.88	7.8	1.45
Li	0.86	0.68	5.42
Mo	0.59	0.75	1.01
Ni	3.72	5.22	1.44
Pb	0.54	0.41	0.37
Sb	6.18	4.87	< 0.09
Se	< 1.04	< 1.04	< 1.04
Sn	< 3.20	< 3.20	< 3.20
Ti	14.46	66.80	147.61
V	< 2.33	< 2.33	< 2.33
U	< 0.0002	0.05	0.15
Zn	54.85	< 7.51	11.37

Note: Concentrations denoted by '<' refer to calculated values for the limit of detection (LoD). 'n.a.' - not analyzed.

Table S6.2 ICP-OES analytical results of quality control solutions (QC) analyzed during this study prepared from single elements standard solutions (Merck, CertiPur) to achieve chemical compositions similar to experimental sample solutions. The mean results of *n* replicate analyses are given together with the standard deviation (SD) and the relative standard deviation (RSD) (SD represents 68% of the population, 2SD represents 95% of the population). The measured deviation from reference value is a quantitative estimation of accuracy.

	As (mg L^{-1})	Cr (mg L^{-1})	Cu (mg L^{-1})	Fe (mg L^{-1})	Si (mg L^{-1})
Wavelength	193.696	267.716	324.754	261.382	288.158
Instrumental limits					
Limit of detection (LoD)	0.0165	0.0003	0.0004	0.0314	0.0093
Limit of quantification (LoQ)	0.0551	0.0009	0.0013	0.0744	0.0166
Quality control					
QC verify ($n = 8$)	0.635	0.060	0.058	5.767	0.245
SD	0.003	0.0003	0.0005	0.032	0.001
RSD	0.52%	0.45%	0.79%	0.56%	0.52%
2RSD	1.03%	0.90%	1.58%	1.12%	1.03%
Reference value	0.618	0.057	0.057	5.599	0.238
Measured deviation from reference value	2.76%	4.12%	2.05%	3.01%	2.83%

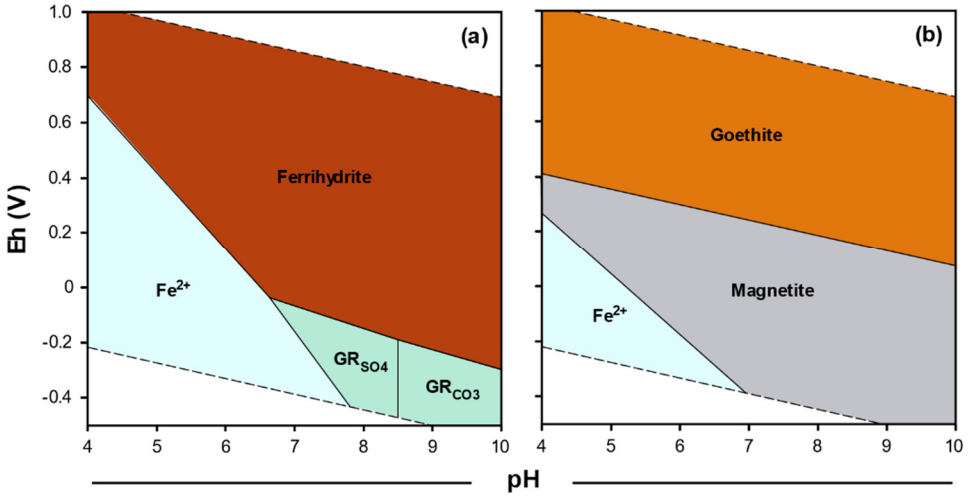

Figure S6.2 Eh-pH diagram of the Fe-bearing mineral phases in MD2 at Collstrop site at 8 °C and 1.013 bars: (a) mineral phases expected to precipitate first in the system; and (b) mineral phases expected to form after aging. Thermodynamic calculations were performed with The Geochemist Workbench® (Bethke, 2010) using the MINTEQ database.

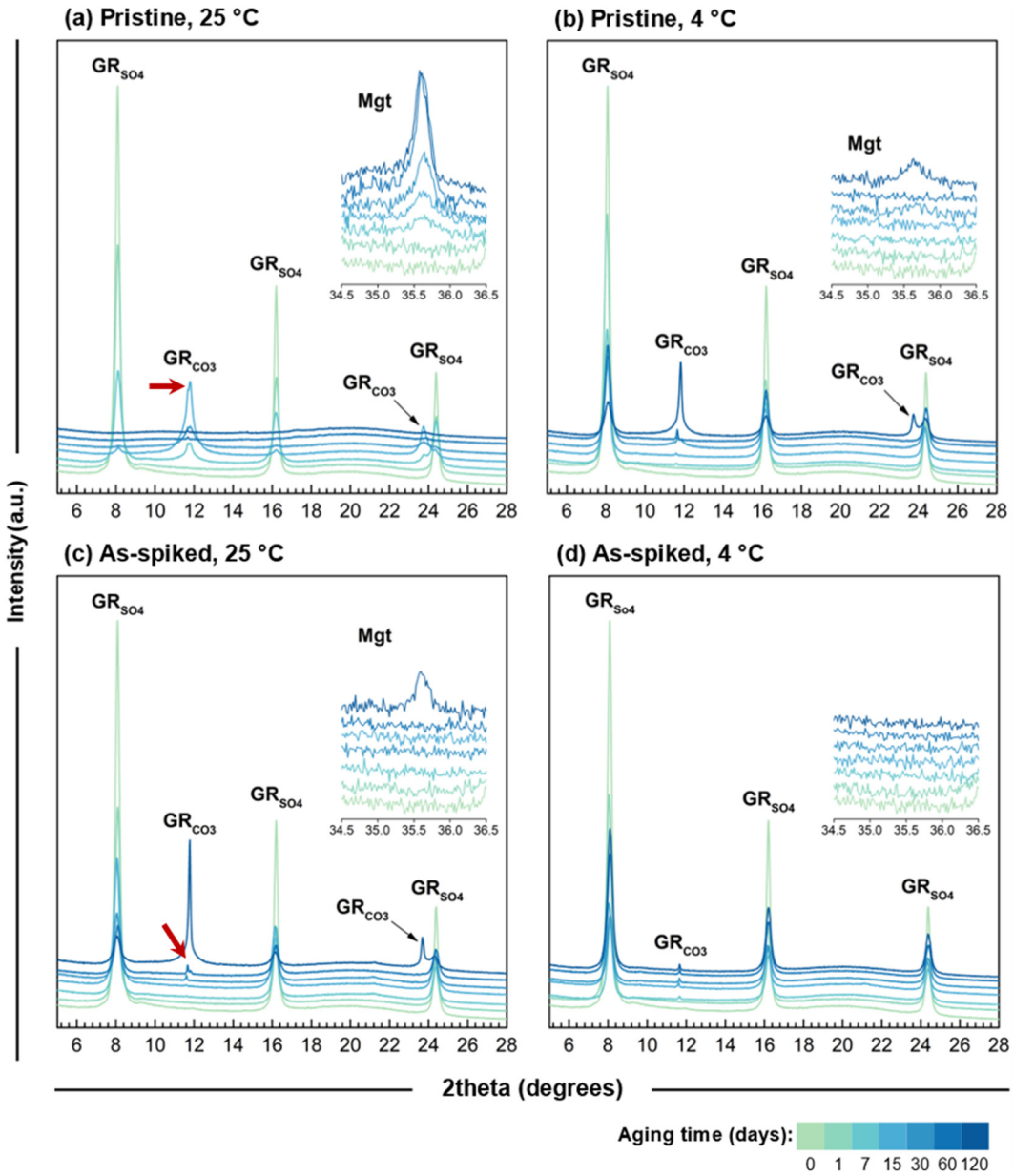

Figure S6.3 XRD patterns of the aged GR_{SO4} samples: (a) pristine, 25°C; (b) pristine, 4°C; (c) As-spiked, 25°C; and (d) As-spiked, 4 °C. The broad amorphous hump at ~20° 2theta comes from the XRD sample holder. The 2theta ranges were clipped from 5 to 28° for clarity. It is noteworthy that there is a noticeable peak splitting for the GR_{CO3} (003) reflection at ~11.8 ° (indicated by the red arrows) in some of the samples, which indicates the presence of either pyroaurite or a partially Mg-substituted GR_{CO3} (see Figure S6.4).

Table S6.3 Adsorption fitting parameters of As for the evaluated kinetic models.

	1st-order model		2nd-order model		Pseudo-2nd order model	
	Rate constant, k_1 (day^{-1})	R^2	Rate constant, k_2 (L mg As^{-1} day^{-1})	R^2	Rate constant, k_1 (day^{-1})	R^2
25 °C	0.047	0.989	0.463	0.797	**0.013**	**0.985**
4 °C	0.007	0.827	0.002	0.936	**0.024**	**0.979**

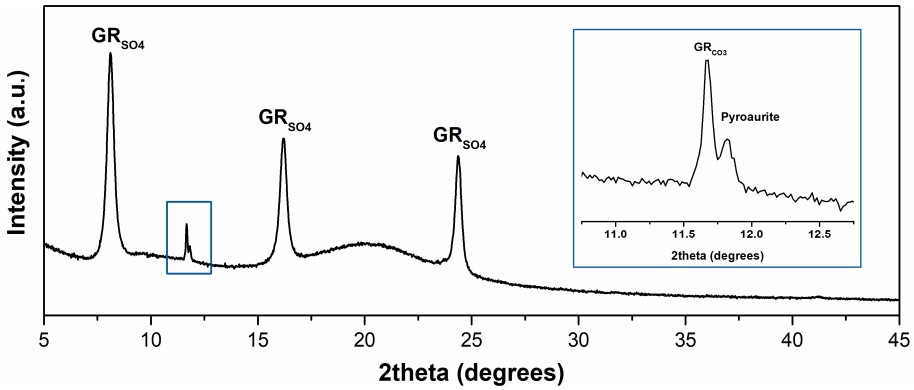

Figure S6.4 Zoomed-in image of the As-spiked sample aged at 25 °C for 60 days. The new peak at ~11.8 ° 2theta (blue rectangle) is shown in the inset which clearly shows the peak splitting due to the presence of GR_{CO3} and pyroaurite-like phases (e.g., Mg-Fe LDH).

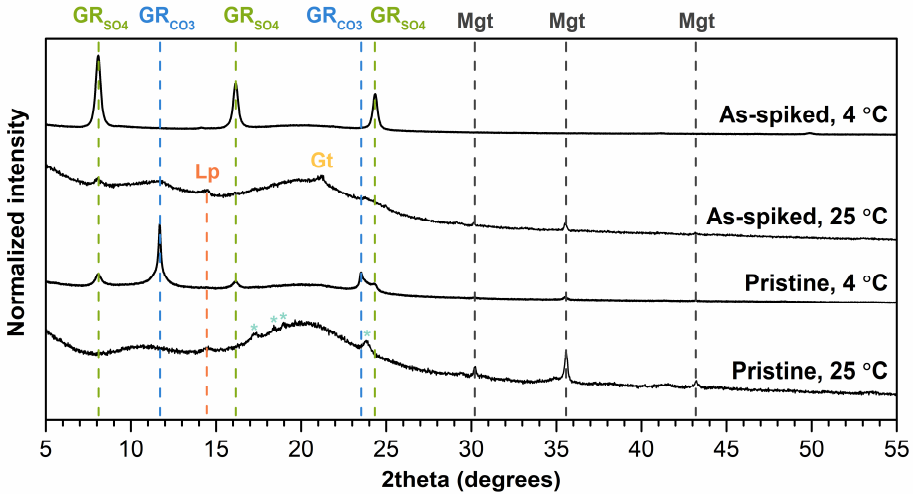

Figure S6.5 Mineralogical composition of GR_{SO4} after aging for 1 year. Mgt, Lp and Gt denote magnetite, lepidocrocite and goethite, respectively. The peaks marked with '*' (light blue) in the pristine sample aged at 25 °C can be assigned to melanterite ($Fe^{II}SO_4$).

Chapter 7

Concluding remarks

7.1 Summary and Conclusions

The work presented in this dissertation contributes to a better fundamental understanding of the complex interaction between GR and As species. Using a series of complementary experimental geochemical approaches combined with various conventional laboratory and synchrotron-based characterization techniques, as well as some field observations, I was able to establish key controlling factors and mechanisms of As removal by GR phases, and reveal the interplay between GR formation and transformation, stability and reactivity and its impact on As cycling in contaminated subsurface environments.

7.1.1 Unravelling reactions at the mineral-water interface using integrated nano-scale characterization tools

GR has been investigated extensively for toxic metals and metalloids due to its redox reactivity, nanoparticulate nature and point of zero charge at near-neutral pH. Regarding the interaction between As and GR phases, earlier studies using As K-edge EXAFS data have helped determine the bonding environment of immobilized As at the GR edges sites (Jönsson and Sherman, 2008; Ona-Nguema et al., 2009; Randall et al., 2001; Wang et al., 2010). However, it also became clear that studies based only on EXAFS data to describe As-GR interactions are not enough and thus, it is not surprising that conflicting results were reported. For example, Ona-Nguema et al. (2009) and Wang et al. (2010) both reported the formation of multi-nuclear As(III) oligomers at the edges of GR_{CO3} and GR_{Cl}, respectively; however, these As(III) oligomers have not been observed in more recent studies on GR_{CO3} and GR_{SO4} (van Genuchten et al., 2019a; van Genuchten et al., 2019b).

I have therefore in my work used a different approach and employed analytical (scanning) transmission electron microscopy (S/TEM) as a useful tool in determining the morphology, crystal structure, chemical composition and oxidation state of the mineralogical end-products of metal-GR interactions. In addition, because previous studies using TEM approaches often assume that GR does not change significantly during analyses, I also tested and determined the potential effects on GR during analyses. Thus, I analyzed freshly-synthesized GR samples in the TEM using two sample preparation methods (i.e., anoxic drop-cast with drying and frozen-hydrated cryogenic) and exposed the GR samples to increasing electron fluence (i.e., amount of electron dose received by the sample) (Chapter 2) to analyze the effects on stability.

Based on the quantitative analyses of the collected Fe $L_{3,2}$-edge electron energy loss spectra (EELS), I demonstrated that electron beam irradiation was the primary reason for GR oxidation during TEM analysis, regardless of the sample preparation technique (Section 2.3). I determined a stoichiometric Fe(II)/Fe(III) ratio (2 for GR_{SO4}) at an electron fluence of 50 e^{-} $Å^{-2}$, and showed that continuous beam irradiation leads to the logarithmic decrease of the Fe(II)/Fe(III) ratio, regardless if the TEM samples were prepared by anoxic drop-cast or frozen-hydrated cryogenic (Figure 2.4, Section 2.3). From these results, I clearly showed the importance of working within low fluences in analytical S/TEM to avoid sample oxidation and to get a quantitative and representative values of Fe(II)/Fe(III) ratios when studying the iron chemistry of highly redox-active phases such as GR. The low electron fluence approach I have established here for EELS analysis of redox-sensitive materials could be a valuable characterization tool for investigating redox reactions at the mineral-water interface. This work is published in *Micron* (2019).

After I established the approach to image and spectrally characterize and analyze GR using S/TEM without compromising sample stability, I also then used STEM imaging coupled with energy dispersive X-ray (EDX) spectroscopy to directly visualize and pinpoint the nano-scale reactions at the GR surfaces. I complemented these spatially-resolved STEM data with a detailed analysis of the local structure based on high energy X-ray total scattering and pair distribution function (PDF) analysis and As bonding data from As K-edge EXAFS and differential PDF (d-PDF). More importantly, I determined the bonding mechanisms for both As(III) and As(V) on GR_{SO4}.

My data revealed that for As(III)-reacted GR_{SO4}, EDX maps showed that As(III) were preferentially adsorbed at the crystal edges, while EXAFS and d-PDF revealed that it is primarily bound as bidentate, binuclear inner-sphere (^2C) surface complexes. Contrary to previous findings, the elusive multi-nuclear As(III) oligomers were not observed in the As-reacted GR_{SO4} samples. This was confirmed from the absence of newly-formed As phases based on the collected STEM and PDF data (cf. Section 4.3; Wang et al. (2011) for magnetite) and corroborated by the robust As K-edge EXAFS fitting approach used in this study. In the case of the As(V)-reacted GR, the As EDX map and PDF data revealed the formation of parasymplesite, a ferrous arsenate phase, that sequestered ~87% of the immobilized As(V). The remaining As fraction (~13%) was adsorbed at the GR particle edges as bidentate ^2C surface complexes. Overall, these results show that only by employing bulk X-ray-based characterization methods and complementing these with highly spatially resolved analytical S/TEM, it is possible to derive molecular-scale reaction mechanisms at the mineral-water interface. This work has been submitted for publication in *Environmental Science & Technology Letters*.

7.1.2 Geochemical factors influencing As removal by GR

One goal of my PhD was to evaluate fundamental pathways that would best characterize how As is removed from solution by GR and how this knowledge can be transferred to subsurface environments. Earlier studies have shown that GR phases can adsorb large amounts of As(III) and As(V) (Jönsson and Sherman, 2008; Su and Wilkin, 2005), although fundamental adsorption parameters (e.g., pH, ionic strength, presence of co-existing ions,

temperature, etc.) were not evaluated in detail. With my work, I aimed to close this research gap through experimental batch reactions under anoxic and near-neutral pH conditions (Chapter 3 and 6).

Based on such batch As adsorption experiments using GR_{SO4} in ultrapure water matrix (Chapter 3) revealed that As removal decreased as the ionic strength increased, wherein the inhibitory effect being more pronounced in As(III) compared to As(V). Co-existing groundwater ions such as Mg^{2+} and PO_4^{3-} also decreased As removal efficiency by blocking and competing for the specific adsorption sites for As species at the GR surface. In the pH values tested, As(III) removal was higher at slightly alkaline conditions (pH 8-9), reaching a maximum uptake of 160 mg As(III) g^{-1} GR_{SO4}. Meanwhile, As(V) was more efficiently removed at circum-neutral conditions (pH 7) with a maximum adsorption of 105 mg As(V) g^{-1} GR_{SO4}. This work is published in *Science of the Total Environment* (2019).

Meanwhile, when GR_{SO4} was reacted in an As-spiked natural groundwater (Chapter 6), it took 120 days to achieve complete As removal. This was much slower compared to rate of As removal observed at ambient temperature (25 °C) under similar As/Fe loadings in the ultrapure water system (Chapter 3) wherein complete removal took only 4 hours. This slow adsorption kinetics resulted from the presence of high concentrations of dissolve silica (~16 mg L^{-1}), which is the primary competitor for As adsorption sites. The adsorption kinetics was even slower by ~2-fold when GR was reacted with the As-spiked groundwater at 4 °C, resulting in 66% removal after 120 days. This work is in the final stages of preparation for submission in *Journal of Hazardous Materials*.

Taken together, these results demonstrate the complex interplay between water chemistry (e.g., pH, ionic strength, co-existing groundwater ions) and physical factors (e.g., temperature) that control As removal by GR phases under relevant anoxic subsurface conditions. In addition, the results show a pathway of how GR could potentially be used for remediation purposes.

7.1.3 GR formation and transformation and its impact on the fate of As

In many Earth subsurface environments, The (bio)geochemical redox cycling of iron in highly impacts the fate of As in contaminated soils and groundwaters. Specifically, iron (oxyhydr)oxide mineral phases are important because of their ability to sequester high amounts of As, either by adsorption or co-precipitation. This makes mineral transformation reactions involving iron (oxyhydr)oxide mineral phases crucial in contaminated systems as this can result to the re-release of immobilized As species back in to the environment. In such natural subsurface settings, upon the development of anoxic conditions, it is likely that GR phases form from the Fe^{2+}-catalyzed transformation of ferrihydrite (see Section 1.3.3). However, the influence of As on GR formation and transformation were still poorly understood prior to my work.

Witht this, I followed the transformation of As(V)-bearing ferrihydrite (see Chpater 5). I initiated the transformation by adding dissolved Fe^{2+} to the As-bearing ferrihydrite slurry in batch reactors. The dissolved Fe^{2+} concentrations were varied, thereby changing the $Fe^{2+}_{(aq)}/Fe(III)_{solid}$ ratios, because I wanted to determine its effect on the fate of mineral-associated As and the mineral transformation pathway. I could show that at low

$Fe^{2+}_{(aq)}/Fe(III)_{solid}$ ratios (<2), GR_{SO4} and/or lepidocrocite initially formed alongside goethite, but eventually both GR_{SO4} and lepidocrocite disappeared and transformed to goethite at later stages of reaction (>2 h). Meanwhile, at $Fe^{2+}_{(aq)}/Fe(III)_{solid} = 2$, GR_{SO4} was formed and remained stable throughout the transformation reaction together with goethite, but goethite (~85%) remained as the dominant mineral end-product. This was unexpected since GR_{SO4} was the sole Fe mineral phase formed at an equivalent $Fe^{2+}_{(aq)}/Fe(III)_{solid}$ ratio in As-free systems (cf. Sumoondur et al. (2008)). At all tested $Fe^{2+}_{(aq)}/Fe(III)_{solid}$ ratios, ferrihydrite was also not fully converted to either GR_{SO4} or goethite. This incomplete conversion of ferrihydrite to GR_{SO4}, in comparison to the As-free system, resulted from the crystallite poisoning by the adsorbed As species (Rancourt et al., 2001; Richmond et al., 2004; Waychunas et al., 1993). Perhaps, the most important finding from this experiment was the partial reduction of As(V) to As(III) during the transformation, wherein the extent of reduction increased from ~34% to 42% as the $Fe^{2+}_{(aq)}/Fe(III)_{FH}$ ratio increased from 0.5 to 2 (see Section 5.3.1). This partial As(V) reduction was induced by the surface-associated Fe^{2+}-GT redox couple, as supported by the thermodynamic calculations in this work. The observed As(V) reduction in this study was unexpected, and also an unfavorable result since this generates the far more toxic and mobile As(III) species. On the positive note, the high As sorption capacities of the resulting Fe (oxyhydr)oxide mineral phases ensured that there was no significant release throughout the transformation reactions. This work is published in *ACS Earth & Space Chemistry* (2019).

7.1.4 Potential of GR for As sequestration in contaminated groundwater

The premise of the work presented in this study is that GR phases, based on their thermodynamic and redox properties, should be a common Fe-bearing phase in suboxic to anoxic environments. This is indeed the case as GR has been increasingly identified in many O_2-limited natural and engineered environments (see Section 1.2). More importantly, naturally occurring GR phases have also been observed in contaminated environments, and they were able to sequester toxic metals and metalloids (Johnson et al., 2014; Johnson et al., 2015; Root et al., 2007). In my work (Chapter 6), I evaluated the stability and reactivity of GR for As sequestration using long-term batch experiments, wherein synthetic GR_{SO4} was aged in suboxic natural groundwater at two different temperatures (4 and 25 °C) for up to 1 year.

My results showed that in As-free, suboxic groundwaters at ambient temperature (25 °C), the initial GR_{SO4} was converted to GR_{CO3} by ion exchange within a few days, while magnetite appeared after 30 days at the expense of GR and was the main transformation end-product after 120 days. It must be noted that while GR transformation to magnetite was expected, the observed conversion rate in the used natural groundwater matrix was much slower compared to previous studies in ultrapure water systems (see Sumoondur et al. (2008)). Meanwhile, at low temperature (4 °C), GR transformation was much slower compared to ambient temperatures (25 °C). GR_{CO3} was only formed after 60 days while there were only trace amounts of magnetite appeared after 120 days. This relative phase composition did not significantly change even after 1 year of aging. Overall, I showed here

that low temperatures can increase GR stability which is important for many subsurface settings where low temperatures prevail.

Interestingly, in the presence of As at ambient temperature, GR transformation also slowed down substantially, delaying ion exchange and only forming significant amounts of GR_{CO3} at the end of 120 days. Trace amounts of magnetite were observed after 120 days, but aging the GR samples ultimately resulted in its full conversion to magnetite after 1 year. Such stabilization effect has been observed in the aging of As-bearing GR phases in ultrapure water systems (see van Genuchten et al. (2019a)). Remarkably, when GR was aged in the As-spiked groundwater at 4 °C, synergistic stabilizing effect was observed wherein the initial GR_{SO4} remained fairly stable (>90%), with a small amount of GR_{CO3} formed in the system. This relative phase composition did not change even after 1 year of aging.

The results I presented here (Chapter 6) are particularly important because it is one of the few studies that report on the long-term stability and reactivity of GR in a more "complex" matrix. I showed in these batch experiments that GR can effectively sequester As, and that in subsurface environments where temperatures are expected to be low (<10 °C), this As-bearing GR can remain stable for a prolonged time period. Even if GR eventually transforms to magnetite and/or other Fe (oxyhydr)oxides (longer than the periods tested in this work), it is unlikely that this will result to a significant As release, as previously documented in both Chapter 5 and 6. This work is in the final stages of preparation for submission in *Journal of Hazardous Materials*.

7.2 Future Directions

The results generated from this study have revealed important and novel findings about the formation and transformation of GR phases and their interaction mechanisms with As species. However, my work also raised many new questions that need to be addressed in order to further improve our understanding of (bio)geochemical redox processes involving GR in natural subsurface settings and to be able to predict how they affect nutrient- or toxic contaminant cycling and dynamics.

For instance, in Chapter 5, I showed that GR_{SO4} formation is inhibited during the Fe^{2+}-induced transformation of As-bearing ferrihydrite. Interestingly, it was goethite that was the main end-product even at stoichiometric $Fe^{2+}{}_{(aq)}/Fe(III)_{solid}$ ratios where GR_{SO4} should have been the sole Fe-bearing phase. Thus, the presence of As species changed the stability of GR. There is still an open question about the effect of As(III) and As(V) on the GR formation kinetics, and about how the stability of As-bearing GR is affected, changed or stabilized against its transformation to magnetite. An earlier study by Wang et al. (2014) showed that GR chloride forms as an intermediate during the Fe^{2+}-induced transformation of As(III)- and As(V)-bearing lepidocrocite to magnetite and that As(III)-bearing GR had a stronger inhibition efficiency against magnetite formation compared to As(V). However, due to their limited temporal resolution and reaction monitoring length (only up to 7 days), it was impossible to assess the long-term stability of the formed As(III)-bearing GR. Moreover, the question also arises whether the stabilization effect observed both in their and my studies changed the GR formation kinetics in the presence of, for

example, co-existing As(III) and As(V) species and/or in the presence of competing inorganic ions such as dissolved Si or PO_4^{3-}.

I also showed in Chapter 5 that GR could form from ferrihydrite, independently of goethite, within the first 30 min of reaction. Based on our current understanding of the iron(oxyhydr)oxide formation and transformation pathways from mixed Fe^{2+}/Fe^{3+} solutions, GR has been shown to form from via schwertmannite and nano-goethite precursors (Ahmed et al., 2010), Nevertheless, the direct formation of GR from ferrihydrite has also been documented in preliminary *in situ* XRD studies (Sumoondur et al. (2008). The difference between these two pathways is striking and it would be interesting to determine the pathway and mechanism of this much less studied pathway of GR formation from ferrihydrite. Specifically considering the changed stability due to the presence of As species, it would be very relevant to assess this in the presence of both As species but to do this while using *in situ* characterization methods such as synchrotron-based X-ray scattering (i.e., SAXS, WAXS) and/or liquid phase and cryogenic S/TEM. With such *in situ* methods, it would be possible to identify all potential intermediates, including iron clusters or amorphous/nano-crystalline precursors/intermediates that are important in the GR_{SO4} formation reaction. Such steps and intermediate stages have been documented in other crucial (bio)geochemical mineral systems such as carbonates (Nielsen et al., 2014; Pouget et al., 2009; Stawski et al., 2018), phosphates (Hövelmann et al., 2019), sulfates (Stawski et al., 2019; Stawski et al., 2016) or sulfides (Matamoros-Veloza et al., 2018a; Matamoros-Veloza et al., 2018b).

While the results I presented in this work mainly address As cycling in modern subsurface environments, the findings are also important in advancing our overall fundamental understanding of (bio)geochemical systems in the past and specifically on Early Earth. This is because, GR phases have recently been suggested to have contributed to Fe cycling in our ancient oceans ~2.5 billion years ago (Ga) (Halevy et al., 2017), a process that was compared to the existence of GR phases in modern non-sulfidic ferruginous lakes (Koeksoy et al., 2019; Vuillemin et al., 2019; Zegeye et al., 2012). The time period in Earth's early history where GR was deemed important, coincides with the first rise in atmospheric oxygen, which triggered the concurrent deposition of large iron formations across the oceans (i.e., banded iron formations; see Bekker et al. (2010); Planavsky et al. (2014)). The formation of highly reactive GR in these anoxic, ferruginous and non-sulfidogenic ancient oceans would have dramatically impacted many other crucial element cycles (i.e., nutrients and toxins), and thus the chemistry and associated microbial life signals preserved in the iron deposits (Chi Fru et al., 2015; Sforna et al., 2014). What is still unknown however, is how these nutrients (e.g., P, Ni) and toxins (e.g., As, Cr) in our ancient oceans were affected by interactions with GR phases. Ultimately what we need to understand is what iron phases and associated As and P signals should have been preserved in banded iron deposits that bear witness to this time period. If we could test this experimentally, then analyses of ancient rocks could help better understand processes on Early Earth.

Thus, although I addressed many aspects related to As-GR interactions through my PhD research, invariably with each answer, new questions continue to arise.

Appendix A

List of Publications and Presentations

A. Scientific publications

Manuscripts under review, submitted or in preparation

1. **Perez, J.P.H.**; Schiefler, A.A.; Navaz Rubio, S.; Reischer, M.; Overheu, N.D.; Benning, L.G.; Tobler, D.J. Arsenic removal from natural groundwater using 'green rust' and its implication on contaminant mobility. In preparation for submission to *Journal of Hazardous Materials*.
2. Mangayayam, M.C.; Dideriksen, K.; Alonso-de Linaje, V.; **Perez, J.P.H.**; Benning, L.G.; Tobler, D.J. Selectivity of sulfidized zerovalent iron towards chlorinated hydrocarbons from groundwater. In preparation for submission to *Journal of Hazardous Materials*.
3. Wang, H.Y.; Byrne, J.M.; Benning, L.G.; Thomas, A.N.; Göttlicher, J.; Höfer H.E.; Mayanna, S.; **Perez, J.P.H.**; Kontny, A.; Kappler, A.; Guo, H.M.; Norra, S. Arsenic sequestration in pyrite and greigite in the buried peat of As-contaminated aquifer. Submitted to *Geochimica et Cosmochimica Acta*.

Publications in peer-reviewed journals

4. **Perez, J.P.H.**; Freeman, H.M.; Brown, A.P.; Van Genuchten, C.M.; Dideriksen, K.; S'ari, M.; Tobler, D.J.; Benning, L.G. (2020). Direct visualization of arsenic binding on green rust sulfate. *Environmental Science & Technology*. DOI: 10.1021/acs.est.9b07092.
5. Mangayayam, M.C.; **Perez, J.P.H.**; Dideriksen, K.; Freeman, H.M.; Bovet, N.; Benning, L.G.; Tobler, D.J. (2019). Structural transformation of sulfidized zero valent iron and its impact on long-term reactivity. *Environmental Science: Nano*, 6, 3422-3430. DOI: 10.1039/C9EN00876D.
6. Hövelmann, J.; Stawski, T.M.; Freeman, H.M.; Besselink, R.B.; Mayanna, S.; **Perez, J.P.H.**; Hondow, N.S.; Benning, L.G. (2019). Struvite crystallization and the effect of Co^{2+} ions. *Minerals*, 9(9), 503. DOI: 10.3390/min9090503.
7. **Perez, J.P.H.**; Tobler, D.J.; Thomas A.N.; Freeman, H.M.; Dideriksen, K.; Radnik, J.; Benning, L.G.B. (2019). Adsorption and reduction of arsenate during the Fe^{2+}-induced transformation of ferrihydrite. *ACS Earth & Space Chemistry*, 3, 884-894. DOI: 10.1021/acsearthspacechem.9b00031.
8. Freeman, H.M.; **Perez, J.P.H.**; Hondow, N.; Benning, L.G.B.; Brown, A.P. (2019). Beam-induced oxidation of green rust monitored by STEM-EELS. *Micron*, 122, 46-52. DOI: 10.1016/j.micron.2019.02.002.
9. **Perez, J.P.H.**; Freeman, H.M.; Schuessler, J.A.; Benning, L.G.B. (2019). The interfacial reactivity of arsenic species with green rust sulfate (GR_{SO4}). *Science of the Total Environment*, 648, 1161-1170. DOI: 10.1016/j.scitotenv.2018.08.163.
10. **Perez, J.P.H.***; Folens, K.*; Leus, K.; Vanhaecke, F.; Van Der Voort; P., Du Laing; G. (2018). Progress in hydrometallurgical technologies to recover critical raw materials and

* Both authors contributed equally to this work

precious metals from low-concentrated streams. *Resources, Conservation and Recycling*, 142, 177-188. DOI: 10.1016/j.resconrec.2018.11.029.

11. **Perez, J.P.H.***; Mangayayam, M.*; Navaz Rubio, S.; Freeman, H.M.; Tobler, D.J., Benning, L.G.B. (2018). Intercalation of aromatic sulfonates in 'green rust' via ion exchange. *Energy Procedia*, 146, 179-187. DOI: 10.1016/j.egypro.2018.07.023.
12. Leus, K.; Folens, K.; Nicomel, N.R.; **Perez, J.P.H.**; Filippousi M.; Meledina, M.; Dîrtu, M.M.; Turner, S.; Van Tendeloo, G.; Garcia, Y.; Du Laing, G.; Van Der Voort; P. (2018). Removal of arsenic and mercury species from water by covalent triazine framework encapsulated γ-Fe_2O_3 nanoparticles. *Journal of Hazardous Materials*, 353, 312-319. DOI: 10.1016/j.jhazmat.2018.04.027.
13. Leus, K.*, **Perez, J.P.H.***, Folens, K., Meledina, M., Van Tendeloo, G., Du Laing, G., Van Der Voort, P. (2017). UiO-66-$(SH)_2$ as stable, selective and regenerable adsorbent for the removal of mercury from water under environmentally-relevant conditions. *Faraday Discussions*, 201, 145-161. DOI: 10.1039/C7FD00012J.
14. Addicoat, M.; Bennett, T.; Chapman, K.; Denysenko, D.; Dincă M.; Doan, H.; ... Perez, J.P.H.; ...Yaghi, O. (2017). New directions in gas sorption and separation with MOFs: General discussion. *Faraday Discussions*, 201, 175-194. DOI: 10.1039/C7FD90044A.
15. Carraro, F.; Chapman, K.; Chen, Z.; Dincă, M.; Easun, T.; Eddaoudi, M.; ... Perez, J.P.H.; ... Yaghi, O. (2017). Catalysis in MOFs: General discussion. *Faraday Discussions*, 201, 369-394. DOI: 10.1039/C7FD90046E.

B. Conference contributions

First author contributions

1. **Perez, J.P.H.**; Freeman, H.M.; Brown, A.P.; Van Genuchten, C.M.; Tobler, D.J., Dideriksen, K.; Benning, L.G. *Mapping arsenic-induced changes on the green rust surface at the nanoscale*. Goldschmidt 2019, August 18-23, 2019, Barcelona (Spain), oral (flash talk) and poster presentation.
2. **Perez, J.P.H.**; Freeman, H.M.; Brown, A.P.; Van Genuchten, C.M.; Tobler, D.J.; Dideriksen, K.; Benning, L.G. *Revealing the interfacial reactions between green rust and arsenic species at the nanoscale*. Clay Minerals Group Research in Progress Meeting, May 17, 2019, Newcastle (UK), poster presentation, *Best Poster Award*.
3. **Perez, J.P.H.**; Freeman, H.M.; Hondow, N.; Brown, A.P.; Benning, L.G. *Interaction between 'green rust' and arsenic revealed by STEM-EDX elemental mapping and mono-EELS*. Microscopy Characterization of Organic-Inorganic Interfaces: Advances in imaging beam sensitive materials in the transmission electron microscope, March 8-9, 2019, Berlin (Germany), poster presentation.
4. **Perez, J.P.H.**; Mangayayam, M.; Navaz Rubio, S.; Freeman, H.M.; Tobler, D.J.; Benning, L.G.B. *Intercalation of aromatic sulfonates in 'green rust' via ion exchange*. International Carbon Conference 2018, September 10-14, 2018, Reykjavik (Iceland), poster presentation.
5. **Perez, J.P.H.**; Tobler, D.J.; Freeman, H.M.; Dideriksen, K.; Cecatto, M.; Benning, L.G. *Fate and role of arsenic during green rust formation via reductive dissolution of ferrihydrite*. Goldschmidt 2018, August 12-17, 2018, Boston (USA), oral presentation.
6. **Perez, J.P.H.**; Freeman, H.M.; Schuessler, J.A.; Benning, L.G.B. *Efficient removal of arsenic species by green rust sulfate (GR_{SO4})*. 7th International Congress on Arsenic in the Environment

- Environmental Arsenic in a Changing World (As2018), July 1-6, 2018, Beijing (China), oral presentation.

7. **Perez, J.P.H.**; Freeman, H.M.; Schuessler, J.A.; Benning, L.G.B. *The role of 'green rust' as a control on arsenic mobility in contaminated groundwaters*. Environmental Sciences: Water (Gordon Research Conference and Seminar), June 23-29, 2018, New Hampshire (USA), poster presentation.
8. **Perez, J.P.H.**; Navaz Rubio, S.; Schuessler, J.A.; Freeman, H.M.; Benning, L.G.B. *Interfacial reactivity of green rust sulfates with metal contaminants*. Goldschmidt 2017, August 13-18, 2017, Paris (France), poster presentation.

Other conference contributions

9. Benning, L.G.; **Perez, J.P.H.**; Navaz Rubio, S.; Stawski, T.M.; Hövelmann, J.; Tobler, D.J.; Thomas, A.N.; Füllenbach, L.; Oelkers, E.H.; Freeman, H.M. How nanominerals form and their role in contaminant cycling. Goldschmidt 2019, August 18-23, 2019, Barcelona (Spain), keynote presentation.
10. Wang, H.; Byrne, J.; **Perez, J.P.H.;** Thomas, A.N.; Benning, L.G.; Mayanna, S.; Hoefer, H.; Kontny, A.; Eiche, E.; Guo, H.; Kappler, A.; Norra, S. *Arsenic speciation and distribution in peat deposits of the Hetao Basin, China*. Goldschmidt 2019, August 18-23, 2019, Barcelona (Spain), oral (flash talk) and poster presentation.
11. Füllenbach, L.; **Perez, J.P.H.**; Freeman, H.M.; Benning, L.G.; Oelkers, E. Using siderite to remove lead from contaminated acidic (sub)surface waste waters. Goldschmidt 2019, August 18-23, 2019, Barcelona (Spain), poster presentation.
12. Freeman, H.M.; **Perez, J.P.H.**; Hondow, N.; Benning, L.G.; Brown, A.P. Using STEM EDX mapping and mono-EELS to understand the reaction kinetics of environmentally relevant iron oxide minerals for water remediation. Microscience Microscopy Congress 2019, July 1-4, 2019, Manchester (UK), poster presentation.
13. Navaz Rubio, S.; **Perez, J.P.H.**; Stawski, T.M.; Freeman, H.; Benning, L.G. *Mechanisms of Ni^{2+} removal by green rust sulfate (GR_{SO4})*. Goldschmidt 2018, August 12-17, 2018, Boston (USA), oral presentation.
14. Freeman, H.M.; **Perez, J.P.H.**; Brown, A.P.; Hondow, N.; Benning, L.G. *Using cryo-mono-EELS to accurately measure the oxidation state of environmentally relevant iron oxide minerals*. EMAG2018: Applications of Electron Microscopy to Beam Sensitive Materials, July 4-6, 2018, Warwick (UK), poster presentation.
15. Freeman, H.M.; Stawski, T.M.; Hoevelman, J.; **Perez, J.P.H.**; Hondow, N.; Benning, L.G. *Liquid cell transmission electron microscopy of geomaterials*. Microscopy and Microspectroscopy of Nanomaterials in Liquids, September 18, 2017, York (UK), poster presentation.

Appendix B

List of Awards and Grants

The following awards and grants were received in association with this doctoral thesis:

2019

Best Poster Award given by the Clay Minerals Group (Mineralogical Society of Great Britain and Ireland) and Environmental Chemistry Group (Royal Society of Chemistry) during the Research in Progress 2019 Joint Meeting

Travel Grant for Outgoing Early Career Scientist (2,500 EUR) awarded by Geo.X Research Network to visit University of Leeds (United Kingdom) for analytical S/TEM measurements

2018

Researcher Mobility Grant (5,000 GBP) awarded by the Royal Society of Chemistry for the research, "Revealing green rust oxidation *in situ* using monochromated scanning transmission electron microscopy electron energy loss spectroscopy (STEM-EELS)", at the University of Leeds (United Kingdom)

Conference Travel Grant (500 EUR) awarded by the Geo.X Research Network to present in As2018 Conference in Beijing, China

2017

Travel Grant to attend the To.Sca.Lake 2.0: Total Scattering for Nanotechnology Summer School in Como, Italy

References

Abdelmoula, M., Trolard, F., Bourrié, G., Génin, J.-M.R. (1998). Evidence for the Fe(II)-Fe(III) green rust "fougerite" mineral occurrence in a hydromorphic soil and its transformation with depth. *Hyperfine Interact.*, 112: 235-238.

Ahmad, A., Bhattacharya, P. (2019). Arsenic in drinking water: Is 10 μg/L a safe limit? *Curr. Pollut. Rep.*, 5: 1-3.

Ahmad, A., Cornelissen, E., van de Wetering, S., van Dijk, T., van Genuchten, C., Bundschuh, J., van der Wal, A., Bhattacharya, P. (2018). Arsenite removal in groundwater treatment plants by sequential Permanganate—Ferric treatment. *J. Water. Process. Eng.*, 26: 221-229.

Ahmed, I.A.M., Benning, L.G., Kakonyi, G., Sumoondur, A.D., Terrill, N.J., Shaw, S. (2010). Formation of green rust sulfate: A combined *in situ* time-resolved X-ray scattering and electrochemical study. *Langmuir*, 26: 6593-6603.

Ahmed, I.A.M., Shaw, S., Benning, L.G. (2008). Formation of hydroxysulphate and hydroxycarbonate green rusts in the presence of zinc using time-resolved *in situ* small and wide angle X-ray scattering. *Mineral. Mag.*, 72: 159-162.

Aissa, R., Francois, M., Ruby, C., Fauth, F., Medjahdi, G., Abdelmoula, M., Génin, J.-M. (2006). Formation and crystallographical structure of hydroxysulphate and hydroxycarbonate green rusts synthetised by coprecipitation. *J. Phys. Chem. Solids*, 67: 1016-1019.

Aktor, H., Nielsen, K.A. (2011). *Investigation and risk assessment of Collstrop site in relation to Esrum Lake (in Danish)*. Danish Environmental Proctection Agency, Copenhagen, Denmark.

Amini, M., Abbaspour, K.C., Berg, M., Winkel, L., Hug, S.J., Hoehn, E., Yang, H., Johnson, C.A. (2008). Statistical modeling of global geogenic arsenic contamination in groundwater. *Environ. Sci. Technol.*, 42: 3669-3675.

Amonette, J.E., Workman, D.J., Kennedy, D.W., Fruchter, J.S., Gorby, Y.A. (2000). Dechlorination of carbon tetrachloride by Fe(II) associated with goethite. *Environ. Sci. Technol.*, 34: 4606-4613.

Amstaetter, K., Borch, T., Larese-Casanova, P., Kappler, A. (2010). Redox transformation of arsenic by Fe(II)-activated goethite (α-FeOOH). *Environ. Sci. Technol.*, 44: 102-108.

Andreeva, D., Mitov, I., Tabakova, T., Mitrov, V., Andreev, A. (1995). Influence of iron (II) on the transformation of ferrihydrite into goethite in acid medium. *Mater. Chem. Phys.*, 41: 146-149.

Antony, H., Legrand, L., Chaussé, A. (2008). Carbonate and sulphate green rusts - Mechanisms of oxidation and reduction. *Electrochim. Acta*, 53: 7146-7156.

Asere, T.G., De Clercq, J., Verbeken, K., Tessema, D.A., Fufa, F., Stevens, C.V., Du Laing, G. (2017). Uptake of arsenate by aluminum (hydr)oxide coated red scoria and pumice. *Appl. Geochem.*, 78: 83-95.

Asta, M.P., Ayora, C., Román-Ross, G., Cama, J., Acero, P., Gault, A.G., Charnock, J.M., Bardelli, F. (2010). Natural attenuation of arsenic in the Tinto Santa Rosa acid stream (Iberian Pyritic Belt, SW Spain): The role of iron precipitates. *Chem. Geol.*, 271: 1-12.

Asta, M.P., Cama, J., Martínez, M., Giménez, J. (2009). Arsenic removal by goethite and jarosite in acidic conditions and its environmental implications. *J. Hazard. Mater.*, 171: 965-972.

Atkinson, R.J., Posner, A.M., Quirk, J.P. (1967). Adsorption of potential-determining ions at the ferric oxide-aqueous electrolyte interface. *J. Phys. Chem.*, 71: 550-558.

Ayala-Luis, K.B., Kaldor, D.K., Koch, C.B., Strobel, B.W., Hansen, H.C.B. (2007). Synthesis of linear alkylbenzene sulphonate intercalated iron(II) iron(III) hydroxide sulphate (green rust) and adsorption of carbon tetrachloride. *Clay Miner.*, 42: 307-317.

Ayala-Luis, K.B., Koch, C.B., Hansen, H.C.B. (2008). The standard Gibbs energy of formation of Fe(II)Fe(III) hydroxide sulfate green rust. *Clays Clay. Miner.*, 56: 633-644.

Ayala-Luis, K.B., Koch, C.B., Hansen, H.C.B. (2010a). Intercalation of linear C9–C16

carboxylates in layered Fe^{II}–Fe^{III}-hydroxides (green rust) *via* ion exchange. *Appl. Clay Sci.*, 48: 334-341.

Ayala-Luis, K.B., Koch, C.B., Hansen, H.C.B. (2010b). One-pot synthesis and characterization of Fe^{II}–Fe^{III} hydroxide (green rust) intercalated with C9–C14 linear alkyl carboxylates. *Appl. Clay Sci.*, 50: 512-519.

Bach, D., Christiansen, B.C., Schild, D., Geckeis, H. (2014). TEM study of green rust sodium sulphate ($GR_{Na,\ SO4}$) interacted with neptunyl ions (NpO_2^+). *Radiochimica Acta*, 102: 279-289.

Bang, S., Johnson, M.D., Korfiatis, G.P., Meng, X. (2005). Chemical reactions between arsenic and zero-valent iron in water. *Water Res.*, 39: 763-770.

Bearcock, J., Perkins, W., Dinelli, E., Wade, S. (2006). Fe(II)/Fe(III) 'green rust'developed within ochreous coal mine drainage sediment in South Wales, UK. *Mineral. Mag.*, 70: 731-741.

Bearcock, J.M., Perkins, W.T., Pearce, N.J.G. (2011). Laboratory studies using naturally occurring "green rust" to aid metal mine water remediation. *J. Hazard. Mater.*, 190: 466-473.

Bekker, A., Slack, J.F., Planavsky, N., Krapež, B., Hofmann, A., Konhauser, K.O., Rouxel, O.J. (2010). Iron Formation: The Sedimentary Product of a Complex Interplay among Mantle, Tectonic, Oceanic, and Biospheric Processes*. *Econ. Geol.*, 105: 467-508.

Bernal, J.D., Dasgupta, D.R., Mackay, A.L. (1959). The oxides and hydroxides of iron and their structural inter-relationships. *Clay Miner. Bull.*, 4: 15-30.

Bethke, C.M. (2010). *Geochemical and Biogeochemical Reaction Modeling*: Cambridge University Press.

Bhattacharya, P., Mukherjee, A.B., Jacks, G., Nordqvist, S. (2002). Metal contamination at a wood preservation site: characterisation and experimental studies on remediation. *Sci. Total Environ.*, 290: 165-180.

Bhave, C., Shejwalkar, S. (2018). A review on the synthesis and applications of green rust for environmental pollutant remediation. *Int. J. Sci. Environ. Sci. Technol.*, 15: 1243-1248.

Bissen, M., Frimmel, F.H. (2003). Arsenic — a Review. Part I: Occurrence, toxicity, speciation, mobility. *Acta Hydroch. Hydrob.*, 31: 9-18.

Bocher, F., Géhin, A., Ruby, C., Ghanbaja, J., Abdelmoula, M., Génin, J.-M.R. (2004). Coprecipitation of Fe(II–III) hydroxycarbonate green rust stabilised by phosphate adsorption. *Solid State Sci.*, 6: 117-124.

Boland, D.D., Collins, R.N., Miller, C.J., Glover, C.J., Waite, T.D. (2014). Effect of solution and solid-phase conditions on the Fe(II)-accelerated transformation of ferrihydrite to lepidocrocite and goethite. *Environ. Sci. Technol.*, 48: 5477-5485.

Bostick, B.C., Fendorf, S. (2003). Arsenite sorption on troilite (FeS) and pyrite (FeS_2). *Geochim. Cosmochim. Acta*, 67: 909-921.

Brinza, L., Vu, H.P., Neamtu, M., Benning, L.G. (2019). Experimental and simulation results of the adsorption of Mo and V onto ferrihydrite. *Sci. Rep.*, 9: 1365.

Brinza, L., Vu, H.P., Shaw, S., Mosselmans, J.F.W., Benning, L.G. (2015). Effect of Mo and V on the hydrothermal crystallization of hematite from ferrihydrite: An *in situ* energy dispersive X-ray diffraction and X-ray absorption spectroscopy study. *Cryst. Growth. Des.*, 15: 4768-4780.

Brown, A.P., Hillier, S., Brydson, R.M.D. (2017). Quantification of Fe-oxidation state in mixed valence minerals: a geochemical application of EELS revisited. *J. Phys. Conf. Ser.*, 902: 012016.

Brown, A.P., Moore, R.G.C., Evans, S.D., Brydson, R.M.D. (2001). Characterisation of iron oxide nanoparticles using EELS. *J. Phys. Conf. Ser.*, 168: 255-258.

Buerge, I.J., Hug, S.J. (1999). Influence of mineral surfaces on chromium(VI) reduction by iron(II). *Environ. Sci. Technol.*, 33: 4285-4291.

Burton, E.D., Bush, R.T., Johnston, S.G., Watling, K.M., Hocking, R.K., Sullivan, L.A., Parker, G.K. (2009). Sorption of arsenic(V) and arsenic(III) to schwertmannite. *Environ. Sci. Technol.*, 43: 9202-9207.

Burton, E.D., Bush, R.T., Sullivan, L.A., Mitchell, D.R.G. (2007). Reductive transformation of iron and sulfur in schwertmannite-rich accumulations associated with acidified coastal lowlands. *Geochim. Cosmochim. Acta*, 71: 4456-4473.

Burton, E.D., Bush, R.T., Sullivan, L.A., Mitchell, D.R.G. (2008). Schwertmannite transformation to goethite via the Fe(II) pathway: Reaction rates and implications for

iron–sulfide formation. *Geochim. Cosmochim. Acta*, 72: 4551-4564.

Cacovich, S., Divitini, G., Ireland, C., Matteocci, F., Di Carlo, A., Ducati, C. (2016). Elemental Mapping of Perovskite Solar Cells by Using Multivariate Analysis: An Insight into Degradation Processes. *ChemSusChem*, 9: 2673-2678.

Cappelen, J. (2012). *Denmark - DMI Historical Climate Data Collection 1768-2011* Technical Report 12-02. Danish Meteorological Institute, pp. 90.

Carlson, L., Bigham, J.M., Schwertmann, U., Kyek, A., Wagner, F. (2002). Scavenging of As from acid mine drainage by schwertmannite and ferrihydrite: A comparison with synthetic analogues. *Environ. Sci. Technol.*, 36: 1712-1719.

Cavé, L., Al, T., Loomer, D., Cogswell, S., Weaver, L. (2006). A STEM/EELS method for mapping iron valence ratios in oxide minerals. *Micron*, 37: 301-309.

Chen, C., Kukkadapu, R., Sparks, D.L. (2015). Influence of coprecipitated organic matter on $Fe^{2+(aq)}$-catalyzed transformation of ferrihydrite: Implications for carbon dynamics. *Environ. Sci. Technol.*, 49: 10927-10936.

Chen, C., Sparks, D.L. (2018). Fe(II)-induced mineral transformation of ferrihydrite–organic matter adsorption and co-precipitation complexes in the absence and presence of As(III). *ACS Earth Space Chem.*, 2: 1095-1101.

Chen, Y., Gao, S., Liu, Z., Shao, S., Yin, W., Fang, Z., Huang, L.-Z. (2018). Prolonged persulfate activation by UV irradiation of green rust for the degradation of organic pollutants. *Environ. Chem. Lett.*, 17: 1017-1021.

Chi Fru, E., Arvestål, E., Callac, N., El Albani, A., Kilias, S., Argyraki, A., Jakobsson, M. (2015). Arsenic stress after the Proterozoic glaciations. *Sci. Rep.*, 5: 17789.

Choi, J., Batchelor, B. (2008). Nitrate reduction by fluoride green rust modified with copper. *Chemosphere*, 70: 1108-1116.

Chowdhury, S.R., Yanful, E.K., Pratt, A.R. (2011). Arsenic removal from aqueous solutions by mixed magnetite–maghemite nanoparticles. *Environmental Earth Sciences*, 64: 411-423.

Christiansen, B.C., Balic-Zunic, T., Dideriksen, K., Stipp, S.L.S. (2009a). Identification of green rust in groundwater. *Environ. Sci. Technol.*, 43: 3436-3441.

Christiansen, B.C., Balic-Zunic, T., Petit, P.O., Frandsen, C., Mørup, S., Geckeis, H., Katerinopoulou, A., Stipp, S.L.S. (2009b). Composition and structure of an iron-bearing, layered double hydroxide (LDH) – Green rust sodium sulphate. *Geochim. Cosmochim. Acta*, 73: 3579-3592.

Christiansen, B.C., Dideriksen, K., Katz, A., Nedel, S., Bovet, N., Sørensen, H.O., Frandsen, C., Gundlach, C., Andersson, M.P., Stipp, S.L.S. (2014). Incorporation of monovalent cations in sulfate green rust. *Inorg. Chem.*, 53: 8887-8894.

Christiansen, B.C., Geckeis, H., Marquardt, C.M., Bauer, A., Römer, J., Wiss, T., Schild, D., Stipp, S.L.S. (2011). Neptunyl (Np) interaction with green rust. *Geochim. Cosmochim. Acta*, 75: 1216-1226.

Cornell, R.M. (1987). Comparison and classification of the effects of simple ions and molecules upon the transformation of ferrihydrite into more crystalline products. *Z. Planz. Bodenkunde*, 150: 304-307.

Cornell, R.M. (1988). The influence of some divalent cations on the transformation of ferrihydrite to more crystalline products. *Clay Miner.*, 23: 329-332.

Cornell, R.M., Schneider, W. (1989). Formation of goethite from ferrihydrite at physiological pH under the influence of cysteine. *Polyhedron*, 8: 149-155.

Cornell, R.M., Schwertmann, U. (2003). *The Iron Oxides: Structure, Properties, Reactions, Occurrences and Uses*. Weinheim, FRG: Wiley-VCH Verlag GmbH & Co. KGaA.

Cundy, A.B., Hopkinson, L., Whitby, R.L.D. (2008). Use of iron-based technologies in contaminated land and groundwater remediation: A review. *Sci. Total Environ.*, 400: 42-51.

Das, S., Hendry, M.J., Essilfie-Dughan, J. (2011). Transformation of two-line ferrihydrite to goethite and hematite as a function of pH and temperature. *Environ. Sci. Technol.*, 45: 268-275.

Davidson, L.E., Shaw, S., Benning, L.G. (2008). The kinetics and mechanisms of schwertmannite transformation to goethite and hematite under alkaline conditions. *Am. Mineral.*, 93: 1326.

de Roy, A., Forano, C., Besse, J.P. (2001). *Layered Double Hydroxides: Synthesis and*

Post-Synthesis Modification. In: Rives, V., editor. Layered Double Hydroxides: Present and Future. Nova Science Publishers, New York, pp. 1-39.

dela Peña, F., Prestat, E., Fauske, V.T., Burdet, P., Jokubauskas, P., Nord, M., Ostasevivius, T., MacArthur, K.E., Sarahan, M., Johnstone, D.N., Taillon, J., Eljarrat, A., Lähnemann, J., Migunov, V., Caron, J., Mazzucco, S., Aarholt, T., Walls, M., Slater, T., Winkler, F., pquinn-dls, Martineau, B., Donval, G., McLeod, R., Hoglund, E.R., Alxneit, I., Lundeby, D., Henninen, T., Zagonel, L.F., A., G. (2019). *Hyperspy/hyperspy: v1.4.2*.

Dey, A., Lenders, J.J.M., Sommerdijk, N.A.J.M. (2015). Bioinspired magnetite formation from a disordered ferrihydrite-derived precursor. *Faraday Discuss.*, 179: 215-225.

Dideriksen, K., Frandsen, C., Bovet, N., Wallace, A.F., Sel, O., Arbour, T., Navrotsky, A., De Yoreo, J.J., Banfield, J.F. (2015). Formation and transformation of a short range ordered iron carbonate precursor. *Geochim. Cosmochim. Acta*, 164: 94-109.

Drissi, S.H., Refait, P., Abdelmoula, M., Génin, J.-M.R. (1995). The preparation and thermodynamic properties of Fe(II)-Fe(III) hydroxide-carbonate (green rust 1); Pourbaix diagram of iron in carbonate-containing aqueous media. *Corros. Sci.*, 37: 2025-2041.

Erbs, M., Bruun Hansen, H.C., Olsen, C.E. (1999). Reductive dechlorination of carbon tetrachloride using iron(II) iron(III) hydroxide sulfate (green rust). *Environ. Sci. Technol.*, 33: 307-311.

Ersbøll, A.K., Monrad, M., Sørensen, M., Baastrup, R., Hansen, B., Bach, F.W., Tjønneland, A., Overvad, K., Raaschou-Nielsen, O. (2018). Low-level exposure to arsenic in drinking water and incidence rate of stroke: A cohort study in Denmark. *Environ. Int.*, 120: 72-80.

Farrow, C.L., Juhas, P., Liu, J.W., Bryndin, D., Božin, E.S., Bloch, J., Th, P., Billinge, S.J.L. (2007). PDFfit2 and PDFgui: Computer programs for studying nanostructure in crystals. *J. Phys. Condens. Matter*, 19: 335219.

Feng, L., Cao, M., Ma, X., Zhu, Y., Hu, C. (2012). Superparamagnetic high-surface-area Fe_3O_4 nanoparticles as adsorbents for arsenic removal. *J. Hazard. Mater.*, 217–218: 439-446.

Ferguson, J.F., Gavis, J. (1972). A review of the arsenic cycle in natural waters. *Water Res.*, 6: 1259-1274.

Filella, M., Belzile, N., Chen, Y.-W. (2002). Antimony in the environment: A review focused on natural waters: I. Occurrence. *Earth-Sci. Rev.*, 57: 125-176.

Folens, K., Leus, K., Nicomel, N.R., Meledina, M., Turner, S., Van Tendeloo, G., Laing, G.D., Van Der Voort, P. (2016). Fe_3O_4@MIL-101 - A selective and regenerable adsorbent for the removal of As species from water. *Eur. J. Inorg. Chem.*: 4395-4401.

Fortin, D., Langley, S. (2005). Formation and occurrence of biogenic iron-rich minerals. *Earth-Sci. Rev.*, 72: 1-19.

Freeman, H.M., Perez, J.P.H., Hondow, N., Benning, L.G., Brown, A.P. (2019). Beam-induced oxidation of mixed-valent Fe (oxyhydr)oxides (green rust) monitored by STEM-EELS. *Micron*, 122: 46-52.

Fukushi, K., Sasaki, M., Sato, T., Yanase, N., Amano, H., Ikeda, H. (2003). A natural attenuation of arsenic in drainage from an abandoned arsenic mine dump. *Appl. Geochem.*, 18: 1267-1278.

Garvie, L.A.J., Zega, T.J., Buseck, P.R., Rez, P. (2004). Nanometer-scale measurements of $Fe^{3+}/\Sigma Fe$ by electron energy-loss spectroscopy: A cautionary note. *Am. Mineral.*, 89: 1610-1616.

Géhin, A., Ruby, C., Abdelmoula, M., Benali, O., Ghanbaja, J., Refait, P., Génin, J.-M.R. (2002). Synthesis of Fe(II-III) hydroxysulphate green rust by coprecipitation. *Solid State Sci.*, 4: 61-66.

Génin, J.-M.R., Aïssa, R., Géhin, A., Abdelmoula, M., Benali, O., Ernstsen, V., Ona-Nguema, G., Upadhyay, C., Ruby, C. (2005). Fougerite and Fe^{II-III} hydroxycarbonate green rust; ordering, deprotonation and/or cation substitution; structure of hydrotalcite-like compounds and mythic ferrosic hydroxide $Fe(OH)_{(2+x)}$. *Solid State Sci.*, 7: 545-572.

Génin, J.-M.R., Olowe, A.A., Refait, P., Simon, L. (1996). On the stoichiometry and pourbaix diagram of Fe(II)-Fe(III) hydroxy-sulphate or sulphate-containing green rust 2: An electrochemical and Mössbauer spectroscopy study. *Corros. Sci.*, 38: 1751-1762.

Génin, J.-M.R., Ruby, C. (2004a). Anion and cation distributions in Fe(II–III) hydroxysalt green rusts from XRD and Mössbauer analysis

(carbonate, chloride, sulphate, ...); the "fougerite" mineral. *Solid State Sci.*, 6: 705-718.

Génin, J.-M.R., Ruby, C. (2004b). Anion and cation distributions in Fe(II–III) hydroxysalt green rusts from XRD and Mössbauer analysis (carbonate, chloride, sulphate, ...); the "fougerite" mineral. *Solid State Sciences*, 6: 705-718.

Génin, J.-M.R., Ruby, C., Upadhyay, C. (2006). Structure and thermodynamics of ferrous, stoichiometric and ferric oxyhydroxycarbonate green rusts; redox flexibility and fougerite mineral. *Solid State Sci.*, 8: 1330-1343.

Génin, J.M.R., Ruby, C. (2008). Structure of some Fe^{II-III} hydroxysalt green rusts (carbonate, oxalate, methanoate) from Mössbauer spectroscopy. *Hyperfine Interact.*, 185: 191-196.

Goh, K.-H., Lim, T.-T., Dong, Z. (2008). Application of layered double hydroxides for removal of oxyanions: A review. *Water Res.*, 42: 1343-1368.

Gomez, M.A., Jim Hendry, M., Hossain, A., Das, S., Elouatik, S. (2013). Abiotic reduction of 2-line ferrihydrite: Effects on adsorbed arsenate, molybdate, and nickel. *RSC Adv.*, 3: 25812-25822.

Gorski, C.A., Edwards, R., Sander, M., Hofstetter, T.B., Stewart, S.M. (2016). Thermodynamic characterization of iron oxide–aqueous Fe^{2+} redox couples. *Environ. Sci. Technol.*, 50: 8538-8547.

Gorski, C.A., Scherer, M.M. (2011). *Fe^{2+} sorption at the Fe oxide-water interface: A revised conceptual framework*. In: Tratnyek, P.G., Grundl, T.J., Haderlein, S.B., editors. Aquatic Redox Chemistry. 1071. American Chemical Society, pp. 315-343.

Gubbens, A., Barfels, M., Trevor, C., Twesten, R., Mooney, P., Thomas, P., Menon, N., Kraus, B., Mao, C., McGinn, B. (2010). The GIF Quantum, a next generation post-column imaging energy filter. *Ultramicroscopy*, 110: 962-970.

Guilbaud, R., White, M.L., Poulton, S.W. (2013). Surface charge and growth of sulphate and carbonate green rust in aqueous media. *Geochim. Cosmochim. Acta*, 108: 141-153.

Guo, X., Chen, F. (2005). Removal of arsenic by bead cellulose loaded with iron oxyhydroxide from groundwater. *Environ. Sci. Technol.*, 39: 6808-6818.

Gupta, A., Chauhan, V.S., Sankararamakrishnan, N. (2009). Preparation and evaluation of iron–chitosan composites for removal of As(III) and As(V) from arsenic contaminated real life groundwater. *Water Res.*, 43: 3862-3870.

Halevy, I., Alesker, M., Schuster, E.M., Popovitz-Biro, R., Feldman, Y. (2017). A key role for green rust in the Precambrian oceans and the genesis of iron formations. *Nat. Geosci.*, 10: 135.

Hammersley, A.P., Svensson, S.O., Hanfland, M., Fitch, A.N., Hausermann, D. (1996). Two-dimensional detector software: From real detector to idealised image or two-theta scan. *High Pressure Res.*, 14: 235-248.

Hammersley, A.P., Svensson, S.O., Thompson, A. (1994). Calibration and correction of spatial distortions in 2D detector systems. *Nucl. Instrum. Methods Phys. Res.*, 346: 312-321.

Handler, R.M., Beard, B.L., Johnson, C.M., Scherer, M.M. (2009). Atom exchange between aqueous Fe(II) and goethite: An Fe isotope tracer study. *Environ. Sci. Technol.*, 43: 1102-1107.

Handler, R.M., Frierdich, A.J., Johnson, C.M., Rosso, K.M., Beard, B.L., Wang, C., Latta, D.E., Neumann, A., Pasakarnis, T., Premaratne, W.A.P.J., Scherer, M.M. (2014). Fe(II)-catalyzed recrystallization of goethite revisited. *Environ. Sci. Technol.*, 48: 11302-11311.

Hansel, C.M., Benner, S.G., Fendorf, S. (2005). Competing Fe(II)-induced mineralization pathways of ferrihydrite. *Environ. Sci. Technol.*, 39: 7147-7153.

Hansen, H.C.B., Borggaard, O.K., Sørensen, J. (1994). Evaluation of the free energy of formation of Fe(II)-Fe(III) hydroxide-sulphate (green rust) and its reduction of nitrite. *Geochim. Cosmochim. Acta*, 58: 2599-2608.

Hansen, H.C.B., Koch, C.B., Nancke-Krogh, H., Borggaard, O.K., Sørensen, J. (1996). Abiotic nitrate reduction to ammonium: Key role of green rust. *Environ. Sci. Technol.*, 30: 2053-2056.

Harrington, R., Hausner, D.B., Bhandari, N., Strongin, D.R., Chapman, K.W., Chupas, P.J., Middlemiss, D.S., Grey, C.P., Parise, J.B. (2010). Investigation of surface structures by powder diffraction: A differential pair distribution function study on arsenate

sorption on ferrihydrite. *Inorg. Chem.*, 49: 325-330.

Hesse, R., Chassé, T., Streubel, P., Szargan, R. (2004). Error estimation in peak-shape analysis of XPS core-level spectra using UNIFIT 2003: how significant are the results of peak fits? *Surf. Interface Anal.*, 36: 1373-1383.

Hiemstra, T., van Riemsdijk, W.H. (2007). Adsorption and surface oxidation of Fe(II) on metal (hydr)oxides. *Geochim. Cosmochim. Acta*, 71: 5913-5933.

Hingston, J.A., Collins, C.D., Murphy, R.J., Lester, J.N. (2001). Leaching of chromated copper arsenate wood preservatives: A review. *Environ. Pollut.*, 111: 53-66.

Ho, Y.-S. (2006). Review of second-order models for adsorption systems. *J. Hazard. Mater.*, 136: 681-689.

Hongshao, Z., Stanforth, R. (2001). Competitive adsorption of phosphate and arsenate on goethite. *Environ. Sci. Technol.*, 35: 4753-4757.

Hoppe, W. (1941). Über die Kristallstruktur von α-AlOOH (Diaspor) und α-FeOOH (Nadeleisenerz). *Z. Kristallogr. Cryst. Mater.*, 103: 73.

Hövelmann, J., Stawski, T.M., Freeman, H.M., Besselink, R., Mayanna, S., Perez, J.P.H., Hondow, N.S., Benning, L.G. (2019). Struvite crystallisation and the effect of Co^{2+} ions. *Minerals*, 9: 503.

Hu, S., Lu, Y., Peng, L., Wang, P., Zhu, M., Dohnalkova, A.C., Chen, H., Lin, Z., Dang, Z., Shi, Z. (2018). Coupled kinetics of ferrihydrite transformation and As(V) sequestration under the effect of humic acids: A mechanistic and quantitative study. *Environ. Sci. Technol.*, 52: 11632-11641.

Huang, L.-Z., Zhu, M., Liu, Z., Wang, Z., Hansen, H.C.B. (2019). Single sheet iron oxide: An efficient heterogeneous electro-Fenton catalyst at neutral pH. *J. Hazard. Mater.*, 364: 39-47.

Huang, X.-y., Ling, L., Zhang, W.-x. (2018). Nanoencapsulation of hexavalent chromium with nanoscale zero-valent iron: High resolution chemical mapping of the passivation layer. *J. Environ. Sci.*, 67: 4-13.

Hughes, M.F. (2002). Arsenic toxicity and potential mechanisms of action. *Toxicology Letters*, 133: 1-16.

Huhmann, Brittany L., Neumann, A., Boyanov, M.I., Kemner, K.M., Scherer, M.M. (2017). Emerging investigator series: As(v) in magnetite: incorporation and redistribution. *Environ. Sci.: Process. Impacts*, 19: 1208-1219.

Huminicki, D.M.C., Hawthorne, F.C. (2003). The crystal structure of nikischerite, $NaFe^{2+6}Al_3(SO_4)_2(OH)_{18}(H_2O)_{12}$,a mineral of the shigaite group. *Can. Mineral.*, 41: 79-82.

Humphrey, D.G. (2002). The chemistry of chromated copper aresenate wood preservatives. *Rev. Inorg. Chem.*, 22: 1-40.

Ilett, M., Brydson, R., Brown, A., Hondow, N. (2019). Cryo-analytical STEM of frozen, aqueous dispersions of nanoparticles. *Micron*, 120: 35-42.

Ilgen, A.G., Foster, A.L., Trainor, T.P. (2012). Role of structural Fe in nontronite NAu-1 and dissolved Fe(II) in redox transformations of arsenic and antimony. *Geochim. Cosmochim. Acta*, 94: 128-145.

Ilgen, A.G., Kruichak, J.N., Artyushkova, K., Newville, M.G., Sun, C. (2017). Redox transformations of As and Se at the surfaces of natural and synthetic ferric nontronites: Role of structural and adsorbed Fe(II). *Environ. Sci. Technol.*, 51: 11105-11114.

Ingram, L., Taylor, H.F.W. (1967). The crystal structures of sjögrenite and pyroaurite. *Mineral. Mag.*, 36: 465-479.

Inskeep, W.P., McDermott, T.R., Fendorf, S. (2002). *Arsenic (V)/(III) recycling in soils and natural waters: Chemical and microbiological processes*. In: Frankenberger, W.T., editor. Environmental Chemistry of Arsenic. Marcel Dekker, New York, pp. 183-215.

Ito, T.-i., Minato, H., Sakurai, K.i. (1954). Parasymplesite, a new mineral polymorphous with symplesite. *P. Jpn. Acad.*, 30: 318-324.

Jain, A., Raven, K.P., Loeppert, R.H. (1999). Arsenite and Arsenate Adsorption on Ferrihydrite: Surface Charge Reduction and Net OH- Release Stoichiometry. *Environ. Sci. Technol.*, 33: 1179-1184.

Jambor, J.L., Dutrizac, J.E. (1998). Occurrence and constitution of natural and synthetic ferrihydrite, a widespread iron oxyhydroxide. *Chem. Rev.*, 98: 2549-2586.

Jang, J.-H., Dempsey, B.A., Catchen, G.L., Burgos, W.D. (2003). Effects of Zn(II), Cu(II), Mn(II), Fe(II), NO_3^-, or SO_4^{2-} at pH 6.5 and 8.5 on transformations of hydrous ferric oxide (HFO) as evidenced by Mössbauer spectroscopy. *Colloid Surf. A Physicochem. Eng. Asp.*, 221: 55-68.

Jia, Y., Xu, L., Fang, Z., Demopoulos, G.P. (2006). Observation of surface precipitation of arsenate on ferrihydrite. *Environ. Sci. Technol.*, 40: 3248-3253.

Johnson, C.A., Freyer, G., Fabisch, M., Caraballo, M.A., Küsel, K., Hochella, M.F. (2014). Observations and assessment of iron oxide and green rust nanoparticles in metal-polluted mine drainage within a steep redox gradient. *Environ. Chem.*, 11: 377-391.

Johnson, C.A., Hochella, M.F., Jr., Murayama, M., Küsel, K. (2015). Polycrystallinity of green rust minerals and their synthetic analogs: Implications for particle formation and reactivity in complex systems. *Am. Mineral.*, 100: 2091-2105.

Johnson, T.M., Bullen, T.D. (2003). Selenium isotope fractionation during reduction by Fe(II)-Fe(III) hydroxide-sulfate (green rust). *Geochim. Cosmochim. Acta*, 67: 413-419.

Johnston, R.B., Singer, P.C. (2007). Solubility of symplesite (ferrous arsenate): Implications for reduced groundwaters and other geochemical environments. *Soil Sci. Soc. Am. J.*, 71: 101-107.

Jolivet, J.-P., Chaneac, C., Tronc, E. (2004). Iron oxide chemistry. From molecular clusters to extended solid networks. *Chem. Commun.*: 481-483.

Jolivet, J.-P., Tronc, E., Chanéac, C. (2006). Iron oxides: From molecular clusters to solid. A nice example of chemical versatility. *CR Geosci.*, 338: 488-497.

Jönsson, J., Sherman, D.M. (2008). Sorption of As(III) and As(V) to siderite, green rust (fougerite) and magnetite: Implications for arsenic release in anoxic groundwaters. *Chem. Geol.*, 255: 173-181.

Kappler, A., Straub, K.L. (2005). Geomicrobiological cycling of iron. *Rev. Mineral. Geochem.*, 59: 85-108.

Karimian, N., Johnston, S.G., Burton, E.D. (2017). Antimony and arsenic behavior during Fe(II)-induced transformation of jarosite. *Environ. Sci. Technol.*, 51: 4259-4268.

Karimian, N., Johnston, S.G., Burton, E.D. (2018a). Antimony and arsenic partitioning during Fe^{2+}-induced transformation of jarosite under acidic conditions. *Chemosphere*, 195: 515-523.

Karimian, N., Johnston, S.G., Burton, E.D. (2018b). Iron and sulfur cycling in acid sulfate soil wetlands under dynamic redox conditions: A review. *Chemosphere*, 197: 803-816.

Katz, J.E., Zhang, X., Attenkofer, K., Chapman, K.W., Frandsen, C., Zarzycki, P., Rosso, K.M., Falcone, R.W., Waychunas, G.A., Gilbert, B. (2012). Electron small polarons and their mobility in iron (oxyhydr)oxide nanoparticles. *Science*, 337: 1200-1203.

Kelly, S.D., Hesterberg, D., Ravel, B. (2008a). *Analysis of soils and minerals using X-ray absorption spectroscopy*. In: Ulery, A.L., Drees, L.R., editors. Methods of Soil Analysis Part 5—Mineralogical methods. Soil Science Society of America, Madison, WI.

Kelly, S.D., Hesterberg, D., Ravel, B. (2008b). *Analysis of soils and minerals using X-ray absorption spectroscopy. In Methods of Soil Analysis. Part 5. Mineralogical Methods. SSA Book Series No.5.*

Kitahama , K., Kiriyama, R., Baba, Y. (1975). Refinement of crystal-structure of scorodite. *Acta Crystallographica Section B-Structural Science*: 322-324.

Klementiev, K.V. *XAFSmass*.

Klencsár, Z., Kuzmann, E., Vértes, A. (1996). User-friendly software for Mössbauer spectrum analysis. *J. Radioanal. Nucl. Chem.*, 210: 105-118.

Koeksoy, E., Sundman, A., Byrne, J.M., Kappler, A., Planer-Friedrich, B., Lohmayer, R., Halevy, I., Konhauser, K.O. (2019). Formation of green rust and elemental sulfur in an analogue for oxygenated ferro-euxinic transition zones of Precambrian oceans. *Geology*, 47: 211-214.

Kwon, S.-K., Kimijima, K.i., Kanie, K., Suzuki, S., Muramatsu, A., Saito, M., Shinoda, K., Waseda, Y. (2007). Influence of silicate ions on the formation of goethite from green rust in aqueous solution. *Corros. Sci.*, 49: 2946-2961.

Latta, D.E., Boyanov, M.I., Kemner, K.M., O'Loughlin, E.J., Scherer, M. (2015). Reaction of uranium(VI) with green rusts: Effect of interlayer anion. *Curr. Inorg. Chem.*, 5: 156-168.

Legrand, L., Abdelmoula, M., Géhin, A., Chaussé, A., Génin, J.M.R. (2001). Electrochemical formation of a new Fe(II)-Fe(III) hydroxy-carbonate green rust: Characterisation and morphology. *Electrochim. Acta*, 46: 1815-1822.

Legrand, L., El Figuigui, A., Mercier, F., Chausse, A. (2004). Reduction of aqueous chromate by Fe(II)/Fe(III) carbonate green

rust: Kinetic and mechanistic studies. *Environ. Sci. Technol.*, 38: 4587-4595.

Lenoble, V., Bouras, O., Deluchat, V., Serpaud, B., Bollinger, J.-C. (2002). Arsenic adsorption onto pillared clays and iron oxides. *J. Colloid Interface Sci.*, 255: 52-58.

Leus, K., Folens, K., Nicomel, N.R., Perez, J.P.H., Filippousi, M., Meledina, M., Dîrtu, M.M., Turner, S., Van Tendeloo, G., Garcia, Y., Du Laing, G., Van Der Voort, P. (2018). Removal of arsenic and mercury species from water by covalent triazine framework encapsulated γ-Fe_2O_3 nanoparticles. *J. Hazard. Mater.*, 353: 312-319.

Leus, K., Perez, J.P.H., Folens, K., Meledina, M., Van Tendeloo, G., Du Laing, G., Van Der Voort, P. (2017). UiO-66-$(SH)_2$ as stable, selective and regenerable adsorbent for the removal of mercury from water under environmentally-relevant conditions. *Faraday Discuss.*, 201: 145-161.

Li, W., Harrington, R., Tang, Y., Kubicki, J.D., Aryanpour, M., Reeder, R.J., Parise, J.B., Phillips, B.L. (2011). Differential pair distribution function study of the structure of arsenate adsorbed on nanocrystalline γ-alumina. *Environ. Sci. Technol.*, 45: 9687-9692.

Lightstone, F.C., Schwegler, E., Hood, R.Q., Gygi, F., Galli, G. (2001). A first principles molecular dynamics simulation of the hydrated magnesium ion. *Chem. Phys. Lett.*, 343: 549-555.

Limousin, G., Gaudet, J.P., Charlet, L., Szenknect, S., Barthès, V., Krimissa, M. (2007). Sorption isotherms: A review on physical bases, modeling and measurement. *Appl. Geochem.*, 22: 249-275.

Lin, S., Lu, D., Liu, Z. (2012). Removal of arsenic contaminants with magnetic γ-Fe_2O_3 nanoparticles. *Chem. Eng. J.*, 211–212: 46-52.

Lin, Z., Puls, R.W. (2003). Potential indicators for the assessment of arsenic natural attenuation in the subsurface. *Adv. Environ. Res.*, 7: 825-834.

Ling, L., Huang, X., Li, M., Zhang, W.-x. (2017). Mapping the reactions in a single zero-valent iron nanoparticle. *Environ. Sci. Technol.*, 51: 14293-14300.

Ling, L., Tang, C., Zhang, W.-x. (2018). Visualization of silver nanoparticle formation on nanoscale zero-valent iron. *Environ. Sci. Technol. Lett.*, 5: 520-525.

Ling, L., Zhang, W.-x. (2017). Visualizing arsenate reactions and encapsulation in a single zero-valent iron nanoparticle. *Environ. Sci. Technol.*, 51: 2288-2294.

Linke, T., Gislason, S.R. (2018). Stability of iron minerals in Icelandic peat areas and transport of heavy metals and nutrients across oxidation and salinity gradients – a modelling approach. *Energy Procedia*, 146: 30-37.

Liu, H., Li, P., Zhu, M., Wei, Y., Sun, Y. (2007). Fe(II)-induced transformation from ferrihydrite to lepidocrocite and goethite. *J. Solid State Chem.*, 180: 2121-2128.

Loyaux-Lawniczak, S., Refait, P., Ehrhardt, J.J., Lecomte, P., Génin, J.-M.R. (2000). Trapping of Cr by formation of ferrihydrite during the reduction of chromate ions by Fe(II)–Fe(III) hydroxysalt green rusts. *Environ. Sci. Technol.*, 34: 438-443.

Loyaux-Lawniczak, S., Refait, P., Lecomte, P., Ehrhardt, J.-J., Génin, J.-M.R. (1999). The reduction of chromate ions by Fe(II) layered hydroxides. *Hydrol. Earth Syst. Sci.*, 3: 593-599.

Maillot, F., Morin, G., Juillot, F., Bruneel, O., Casiot, C., Ona-Nguema, G., Wang, Y., Lebrun, S., Aubry, E., Vlaic, G., Brown, G.E. (2013). Structure and reactivity of As(III)- and As(V)-rich schwertmannites and amorphous ferric arsenate sulfate from the Carnoulès acid mine drainage, France: Comparison with biotic and abiotic model compounds and implications for As remediation. *Geochim. Cosmochim. Acta*, 104: 310-329.

Majzlan, J., Grevel, K.-D., Navrotsky, A. (2003). Thermodynamics of Fe oxides: Part II. Enthalpies of formation and relative stability of goethite (α-FeOOH), lepidocrocite (γ-FeOOH), and maghemite (γ-Fe_2O_3). *Am. Mineral.*, 88: 855-859.

Majzlan, J., Navrotsky, A., Schwertmann, U. (2004). Thermodynamics of iron oxides: Part III. Enthalpies of formation and stability of ferrihydrite ($\sim Fe(OH)_3$), schwertmannite ($\sim FeO(OH)_{3/4}(SO_4)_{1/8}$), and ε-Fe_2O_3. *Geochim. Cosmochim. Acta*, 68: 1049-1059.

Malis, T., Cheng, S.C., Egerton, R.F. (1988). EELS log-ratio technique for specimen-thickness measurement in the TEM. *J. Electron Microsc. Tech.*, 8: 193-200.

Mamindy-Pajany, Y., Hurel, C., Marmier, N., Roméo, M. (2009). Arsenic adsorption onto

hematite and goethite. *CR Chim.*, 12: 876-881.

Mandal, B.K., Suzuki, K.T. (2002). Arsenic round the world: A review. *Talanta*, 58: 201-235.

Mangayayam, M., Dideriksen, K., Ceccato, M., Tobler, D.J. (2019). The structure of sulfidized zero-valent iron by one-pot synthesis: Impact on contaminant selectivity and long-term performance. *Environ. Sci. Technol.*, 53: 4389-4396.

Mangayayam, M.C., Dideriksen, K., Tobler, D.J. (2018). Can or cannot green rust reduce chlorinated ethenes? *Energy Procedia*, 146: 173-178.

Mann, S., Sparks, N.H.C., Couling, S.B., Larcombe, M.C., Frankel, R.B. (1989). Crystallochemical characterization of magnetic spinels prepared from aqueous solution. *J. Chem. Soc. Faraday Trans.*, 85: 3033-3044.

Masscheleyn, P.H., Delaune, R.D., Patrick, W.H. (1991). Arsenic and selenium chemistry as affected by sediment redox potential and pH. *J. Environ. Qual.*, 20: 522-527.

Masue-Slowey, Y., Loeppert, R.H., Fendorf, S. (2011). Alteration of ferrihydrite reductive dissolution and transformation by adsorbed As and structural Al: Implications for As retention. *Geochim. Cosmochim. Acta*, 75: 870-886.

Matamoros-Veloza, A., Cespedes, O., Johnson, B.R.G., Stawski, T.M., Terranova, U., de Leeuw, N.H., Benning, L.G. (2018a). A highly reactive precursor in the iron sulfide system. *Nat. Commun.*, 9: 3125.

Matamoros-Veloza, A., Stawski, T.M., Benning, L.G. (2018b). Nanoparticle assembly leads to mackinawite formation. *Cryst. Growth. Des.*, 18: 6757-6764.

Mathon, O., Beteva, A., Borrel, J., Bugnazet, D., Gatla, S., Hino, R., Kantor, I., Mairs, T., Munoz, M., Pasternak, S., Perrin, F., Pascarelli, S. (2015). The time-resolved and extreme conditions XAS (TEXAS) facility at the European Synchrotron Radiation Facility: the general-purpose EXAFS bending-magnet beamline BM23. *J. Synchr. Radiat.*, 22: 1548-1554.

Matschullat, J. (2000). Arsenic in the geosphere — a review. *Sci. Total Environ.*, 249: 297-312.

Melton, E.D., Swanner, E.D., Behrens, S., Schmidt, C., Kappler, A. (2014). The interplay of microbially mediated and abiotic reactions in the biogeochemical Fe cycle. *Nat. Rev. Microbiol.*, 12: 797.

Meng, X., Bang, S., Korfiatis, G.P. (2000). Effects of silicate, sulfate, and carbonate on arsenic removal by ferric chloride. *Water Res.*, 34: 1255-1261.

Michel, F.M., Barrón, V., Torrent, J., Morales, M.P., Serna, C.J., Boily, J.-F., Liu, Q., Ambrosini, A., Cismasu, A.C., Brown, G.E. (2010). Ordered ferrimagnetic form of ferrihydrite reveals links among structure, composition, and magnetism. *Proc. Natl. Acad. Sci.*, 107: 2787-2792.

Michel, F.M., Ehm, L., Antao, S.M., Lee, P.L., Chupas, P.J., Liu, G., Strongin, D.R., Schoonen, M.A.A., Phillips, B.L., Parise, J.B. (2007). The Structure of Ferrihydrite, a Nanocrystalline Material. *Science*, 316: 1726-1729.

Mikutta, C., Frommer, J., Voegelin, A., Kaegi, R., Kretzschmar, R. (2010). Effect of citrate on the local Fe coordination in ferrihydrite, arsenate binding, and ternary arsenate complex formation. *Geochimica Et Cosmochimica Acta*: 5574-5592.

Ministry of Environment and Food of Denmark (2017). Bekendtgørelse om vandkvalitet og tilsyn med vandforsyningsanlæg. BEK no. 1147 of 24/10/2017.

Misawa, T., Hashimoto, K., Shimodaira, S. (1973). Formation of $Fe(II)_1\boxtimes Fe(III)_1$ intermediate green complex on oxidation of ferrous ion in neutral and slightly alkaline sulphate solutions. *J. Inorg. Nucl. Chem.*, 35: 4167-4174.

Misawa, T., Hashimoto, K., Shimodaira, S. (1974). The mechanism of formation of iron oxide and oxyhydroxides in aqueous solutions at room temperature. *Corros. Sci.*, 14: 131-149.

Mitsunobu, S., Takahashi, Y., Sakai, Y., Inumaru, K. (2009). Interaction of synthetic sulfate green rust with antimony(V). *Environ. Sci. Technol.*, 43: 318-323.

Miyata, S. (1983). Anion-exchange properties of hydrotalcite-like compounds. *Clays Clay. Miner.*, 31: 305-311.

Mori, H., Ito, T. (1950). The structure of vivianite and symplesite. *Acta Crystallogr.*, 3: 1-6.

Mukherjee, A., Sengupta, M.K., Hossain, M.A., Ahamed, S., Das, B., Nayak, B., Lodh, D., Rahman, M.M., Chakraborti, D. (2006). Arsenic contamination in groundwater: A

global perspective with emphasis on the Asian scenario. *J. Health Popul. Nutr.*, 24: 142-163.

Mullet, M., Guillemin, Y., Ruby, C. (2008). Oxidation and deprotonation of synthetic Fe^{II}-Fe^{III} (oxy)hydroxycarbonate Green Rust: An X-ray photoelectron study. *J. Solid State Chem.*, 181: 81-89.

Murad, E., Taylor, R.M. (1984). The Mössbauer spectra of hydroxycarbonate green rust. *Clay Miner.*, 19: 77-83.

Nedel, S., Dideriksen, K., Christiansen, B.C., Bovet, N., Stipp, S.L.S. (2010). Uptake and release of cerium during Fe-oxide formation and transformation in Fe(II) solutions. *Environ. Sci. Technol.*, 44: 4493-4498.

Newman, S.P., Jones, W. (1998). Synthesis, characterization and applications of layered double hydroxides containing organic guests. *New J. Chem.*, 22: 105-115.

Newville, M. (2001). IFEFFIT: interactive XAFS analysis and FEFF fitting. *Journal of Synchrotron Radiation*: 322-324.

Nickson, R.T., McArthur, J.M., Ravenscroft, P., Burgess, W.G., Ahmed, K.M. (2000). Mechanism of arsenic release to groundwater, Bangladesh and West Bengal. *Appl. Geochem.*, 15: 403-413.

Nielsen, M.H., Aloni, S., De Yoreo, J.J. (2014). In situ TEM imaging of $CaCO_3$ nucleation reveals coexistence of direct and indirect pathways. *Science*, 345: 1158.

Nielsen, S.S., Kjeldsen, P., Jakobsen, R. (2016). Full scale amendment of a contaminated wood impregnation site with iron water treatment residues. *Front. Environ, Sci. En.*, 10: 3.

Nielsen, S.S., Petersen, L.R., Kjeldsen, P., Jakobsen, R. (2011). Amendment of arsenic and chromium polluted soil from wood preservation by iron residues from water treatment. *Chemosphere*, 84: 383-389.

Nordstrom, D.K., Majzlan, J., Königsberger, E. (2014). Thermodynamic properties for arsenic minerals and aqueous species. *Rev. Mineral. Geochem.*, 79: 217-255.

O'Loughlin, E.J., Kelly, S.D., Cook, R.E., Csencsits, R., Kemner, K.M. (2003). Reduction of uranium(VI) by mixed iron(II)/iron(III) hydroxide (green rust): Formation of UO_2 nanoparticles. *Environ. Sci. Technol.*, 37: 721-727.

O'Loughlin, E.J., Kelly, S.D., Kemner, K.M., Csencsits, R., Cook, R.E. (2003). Reduction of Ag^{I}, Au^{III}, Cu^{II}, and Hg^{II} by Fe^{II}/Fe^{III} hydroxysulfate green rust. *Chemosphere*, 53: 437-446.

Ona-Nguema, G., Morin, G., Juillot, F., Calas, G., Brown, G.E. (2005). EXAFS analysis of arsenite adsorption onto two-line ferrihydrite, hematite, goethite, and lepidocrocite. *Environ. Sci. Technol.*, 39: 9147-9155.

Ona-Nguema, G., Morin, G., Wang, Y., Menguy, N., Juillot, F., Olivi, L., Aquilanti, G., Abdelmoula, M., Ruby, C., Bargar, J.R., Guyot, F., Calas, G., Brown, G.E. (2009). Arsenite sequestration at the surface of nano-$Fe(OH)_2$, ferrous-carbonate hydroxide, and green-rust after bioreduction of arsenic-sorbed lepidocrocite by *Shewanella putrefaciens*. *Geochim. Cosmochim. Acta*, 73: 1359-1381.

Paktunc, D., Dutrizac, J., Gertsman, V. (2008). Synthesis and phase transformations involving scorodite, ferric arsenate and arsenical ferrihydrite: Implications for arsenic mobility. *Geochimica Et Cosmochimica Acta*: 2649-2672.

Pan, Y.-H., Sader, K., Powell, J.J., Bleloch, A., Gass, M., Trinick, J., Warley, A., Li, A., Brydson, R., Brown, A. (2009). 3D morphology of the human hepatic ferritin mineral core: New evidence for a subunit structure revealed by single particle analysis of HAADF-STEM images. *J. Struct. Biol.*, 166: 22-31.

Pan, Y.-H., Vaughan, G., Brydson, R., Bleloch, A., Gass, M., Sader, K., Brown, A. (2010). Electron-beam-induced reduction of Fe^{3+} in iron phosphate dihydrate, ferrihydrite, haemosiderin and ferritin as revealed by electron energy-loss spectroscopy. *Ultramicroscopy*, 110: 1020-1032.

Pan, Y., Brown, A., Brydson, R., Warley, A., Li, A., Powell, J. (2006). Electron beam damage studies of synthetic 6-line ferrihydrite and ferritin molecule cores within a human liver biopsy. *Micron*, 37: 403-411.

Park, J.H., Han, Y.-S., Ahn, J.S. (2016). Comparison of arsenic co-precipitation and adsorption by iron minerals and the mechanism of arsenic natural attenuation in a mine stream. *Water Res.*, 106: 295-303.

Paterson, J.H., Krivanek, O.L. (1990). ELNES of *3d* transition-metal oxides: II. Variations with oxidation state and crystal structure. *Ultramicroscopy*, 32: 319-325.

Pedersen, H.D., Postma, D., Jakobsen, R. (2006). Release of arsenic associated with the

reduction and transformation of iron oxides. *Geochim. Cosmochim. Acta*, 70: 4116-4129.

Pedersen, H.D., Postma, D., Jakobsen, R., Larsen, O. (2005). Fast transformation of iron oxyhydroxides by the catalytic action of aqueous Fe(II). *Geochim. Cosmochim. Acta*, 69: 3967-3977.

Perez, J.P.H., Freeman, H.M., Schuessler, J.A., Benning, L.G. (2019a). The interfacial reactivity of arsenic species with green rust sulfate (GR_{SO4}). *Sci. Total Environ.*, 648: 1161-1170.

Perez, J.P.H., Mangayayam, M.C., Rubio, S.N., Freeman, H.M., Tobler, D.J., Benning, L.G. (2018). Intercalation of aromatic sulfonates in 'green rust' via ion exchange. *Energy Procedia*, 146: 179-187.

Perez, J.P.H., Tobler, D.J., Thomas, A.N., Freeman, H.M., Dideriksen, K., Radnik, J., Benning, L.G. (2019b). Adsorption and reduction of arsenate during the Fe^{2+}-induced transformation of ferrihydrite. *ACS Earth Space Chem.*, 3: 884-894.

Planavsky, N.J., Asael, D., Hofmann, A., Reinhard, C.T., Lalonde, S.V., Knudsen, A., Wang, X., Ossa Ossa, F., Pecoits, E., Smith, A.J.B., Beukes, N.J., Bekker, A., Johnson, T.M., Konhauser, K.O., Lyons, T.W., Rouxel, O.J. (2014). Evidence for oxygenic photosynthesis half a billion years before the Great Oxidation Event. *Nat. Geosci.*, 7: 283.

Pouget, E.M., Bomans, P.H.H., Goos, J.A.C.M., Frederik, P.M., de With, G., Sommerdijk, N.A.J.M. (2009). The initial stages of template-controlled $CaCO_3$ formation revealed by cryo-TEM. *Science*, 323: 1455.

Qiu, X., Thompson, J.W., Billinge, S.J.L. (2004). PDFgetX2: A GUI-driven program to obtain the pair distribution function from X-ray powder diffraction data. *J. Appl. Crystallogr.*, 37: 678.

Raghav, M., Shan, J., Sáez, A.E., Ela, W.P. (2013). Scoping candidate minerals for stabilization of arsenic-bearing solid residuals. *J. Hazard. Mater.*, 263: 525-532.

Rancourt, D.G., Fortin, D., Pichler, T., Thibault, P.-J., Lamarche, G., Morris, R.V., Mercier, P.H.J. (2001). Mineralogy of a natural As-rich hydrous ferric oxide coprecipitate formed by mixing of hydrothermal fluid and seawater: Implications regarding surface complexation and color banding in ferrihydrite deposits. *Am. Mineral.*, 86: 834-851.

Randall, S.R., Sherman, D.M., Ragnarsdottir, K.V. (2001). Sorption of As(V) on green rust ($Fe_4(II)Fe_2(III)(OH)_{12}SO_4{\cdot}3H_2O$) and lepidocrocite ($\gamma$-FeOOH): Surface complexes from EXAFS spectroscopy. *Geochim. Cosmochim. Acta*, 65: 1015-1023.

Ravel, B., Newville, M. (2005). ATHENA, ARTEMIS, HEPHAESTUS: Data analysis for X-ray absorption spectroscopy using IFEFFIT. *J. Synchr. Radiat.*, 12: 537-541.

Raven, K.P., Jain, A., Loeppert, R.H. (1998). Arsenite and arsenate adsorption on ferrihydrite: Kinetics, equilibrium, and adsorption envelopes. *Environ. Sci. Technol.*, 32: 344-349.

Refait, P., Abdelmoula, M., Génin, J.-M.R. (1998a). Mechanisms of formation and structure of green rust one in aqueous corrosion of iron in the presence of chloride ions. *Corros. Sci.*, 40: 1547-1560.

Refait, P., Abdelmoula, M., Génin, J.-M.R., Jeannin, M. (2007). *Synthesis and characterisation of the Fe(II–III) hydroxy-formate green rust*. ICAME 2005. Springer Berlin Heidelberg, pp. 717-722.

Refait, P., Bauer, P., Olowe, A.A., Genin, J.M.R. (1990). The substitution of Fe^{2+} ions by Ni^{2+} ions in the green rust 2 compound studied by Mössbauer effect. *Hyperfine Interact.*, 57: 2061-2066.

Refait, P., Bon, C., Simon, L., Bourrié, G., Trolard, F., Bessière, J., Gènin, J.M.R. (1999). Chemical composition and Gibbs standard free energy of formation of Fe(II)-Fe(III) hydroxysulphate green rust and Fe(II) hydroxide. *Clay Miner.*, 34: 499-510.

Refait, P., Charton, A., Génin, J.-M.R. (1998b). Identification, composition, thermodynamic and structural properties of a pyroaurite-like iron(II)-iron(III) hydroxy-oxalate green rust. *Eur. J. Solid State Inorg. Chem.*, 35: 655-666.

Refait, P., Drissi, S., Abdelmoula, M., Génin, J.-M.R. (2002). Synthesis and reactivity of Mg(II)–Fe(II)–Fe(III) hydroxycarbonates. *Hyperfine Interact.*, 139: 651-655.

Refait, P., Simon, L., Génin, J.-M.R. (2000). Reduction of SeO_4^{2-} anions and anoxic formation of iron(II)–iron(III) hydroxy-selenate green rust. *Environ. Sci. Technol.*, 34: 819-825.

Rehr, J., Albers, R., Zabinsky, S. (1992). High-order multiple-scattering calculations of X-ray absorption fine structure. *Physical Review Letters*: 3397-3400.

Reisinger, H.J., Burris, D.R., Hering, J.G. (2005). *Remediating subsurface arsenic contamination with monitored natural attenuation*. ACS Publications.

Rennert, T., Eusterhues, K., De Andrade, V., Totsche, K.U. (2012). Iron species in soils on a mofette site studied by Fe *K*-edge X-ray absorption near-edge spectroscopy. *Chem. Geol.*, 332–333: 116-123.

Richmond, W.R., Loan, M., Morton, J., Parkinson, G.M. (2004). Arsenic removal from aqueous solution via ferrihydrite crystallization control. *Environ. Sci. Technol.*, 38: 2368-2372.

Roberts, L.C., Hug, S.J., Ruettimann, T., Billah, M.M., Khan, A.W., Rahman, M.T. (2004). Arsenic removal with iron(II) and iron(III) in waters with high silicate and phosphate concentrations. *Environ. Sci. Technol.*, 38: 307-315.

Robie, R.A., Hemingway, B.S. (1995). *Thermodynamic properties of minerals and related substances at 298.15 K and 1 bar (10^5 pascals) pressure and at higher temperatures*. Bulletin.

Root, R.A., Dixit, S., Campbell, K.M., Jew, A.D., Hering, J.G., O'Day, P.A. (2007). Arsenic sequestration by sorption processes in high-iron sediments. *Geochim. Cosmochim. Acta*, 71: 5782-5803.

Ruby, C., Abdelmoula, M., Aissa, R., Medjahdi, G., Brunelli, M., François, M. (2008). Aluminium substitution in iron(II–III)-layered double hydroxides: Formation and cationic order. *J. Solid State Chem.*, 181: 2285-2291.

Ruby, C., Aïssa, R., Géhin, A., Cortot, J., Abdelmoula, M., Génin, J.-M.R. (2006). Green rusts synthesis by coprecipitation of Fe^{II}–Fe^{III} ions and mass-balance diagram. *CR Geosci.*, 338: 420-432.

Ruby, C., Géhin, A., Abdelmoula, M., Génin, J.-M.R., Jolivet, J.-P. (2003). Coprecipitation of Fe(II) and Fe(III) cations in sulphated aqueous medium and formation of hydroxysulphate green rust. *Solid State Sci.*, 5: 1055-1062.

Runčevski, T., Makreski, P., Dinnebier, R.E., Jovanovski, G. (2015). The crystal structure of symplesite. *Z. Anorg. Allg. Chem.*, 641: 1207-1210.

Sabot, R., Jeannin, M., Gadouleau, M., Guo, Q., Sicre, E., Refait, P. (2007). Influence of lactate ions on the formation of rust. *Corros. Sci.*, 49: 1610-1624.

Sader, K., Schaffer, B., Vaughan, G., Brydson, R., Brown, A., Bleloch, A. (2010). Smart acquisition EELS. *Ultramicroscopy*, 110: 998-1003.

Schuessler, J.A., Kämpf, H., Koch, U., Alawi, M. (2016). Earthquake impact on iron isotope signatures recorded in mineral spring water. *J. Geophys. Res.*, 121: 8548-8568.

Schwertmann, U., Cornell, R.M. (2000). *Iron Oxides in the Laboratory: Preparation and Characterization*. Weinheim, FRG: Wiley-VCH Verlag GmbH & Co. KGaA.

Schwertmann, U., Murad, E. (1983). Effect of pH on the formation of goethite and hematite from ferrihydrite. *Clays Clay. Miner.*, 31: 277-284.

Schwertmann, U., Stanjek, H., Becher, H.H. (2004). Long-term in vitro transformation of 2-line ferrihydrite to goethite/hematite at 4, 10, 15 and 25 °C. *Clay Miner.*, 39: 433-438.

Sforna, M.C., Philippot, P., Somogyi, A., van Zuilen, M.A., Medjoubi, K., Schoepp-Cothenet, B., Nitschke, W., Visscher, P.T. (2014). Evidence for arsenic metabolism and cycling by microorganisms 2.7 billion years ago. *Nat. Geosci.*, 7: 811.

Shannon, R.D. (1976). Revised effective ionic radii and systematic studies of interatomic distances in halides and chalcogenides. *Acta Crystallogr. A*, 32: 751-767.

Sharma, V.K., Sohn, M. (2009). Aquatic arsenic: Toxicity, speciation, transformations, and remediation. *Environ. Int.*, 35: 743-759.

Shaw, S., Pepper, S.E., Bryan, N.D., Livens, F.R. (2005). The kinetics and mechanisms of goethite and hematite crystallization under alkaline conditions, and in the presence of phosphate. *Am. Mineral.*, 90: 1852–1860.

Sherman, D.M., Randall, S.R. (2003). Surface complexation of arsenic(V) to iron(III) (hydr)oxides: structural mechanism from ab initio molecular geometries and EXAFS spectroscopy. *Geochim. Cosmochim. Acta*, 67: 4223-4230.

Shipley, H.J., Yean, S., Kan, A.T., Tomson, M.B. (2009). Adsorption of arsenic to magnetite nanoparticles: Effect of particle concentration, pH, ionic strength, and temperature. *Environ. Toxicol. Chem.*, 28: 509-515.

Simon, L., François, M., Refait, P., Renaudin, G., Lelaurain, M., Génin, J.-M.R. (2003). Structure of the Fe(II-III) layered double

hydroxysulphate green rust two from Rietveld analysis. *Solid State Sci.*, 5: 327-334.

Simon, L., Refait, P., Génin, J.-M.R. (1998). Transformation of Fe(II)-Fe(III) hydroxysulphite into hydroxysulphate green rusts. *Hyperfine Interact.*, 112: 217-222.

Skovbjerg, L.L., Stipp, S.L.S., Utsunomiya, S., Ewing, R.C. (2006). The mechanisms of reduction of hexavalent chromium by green rust sodium sulphate: Formation of Cr-goethite. *Geochim. Cosmochim. Acta*, 70: 3582-3592.

Smedley, P.L., Kinniburgh, D.G. (2002). A review of the source, behaviour and distribution of arsenic in natural waters. *Appl. Geochem.*, 17: 517-568.

Stawski, T.M., Roncal-Herrero, T., Fernandez-Martinez, A., Matamoros-Veloza, A., Kröger, R., Benning, L.G. (2018). "On demand" triggered crystallization of $CaCO_3$ from solute precursor species stabilized by the water-in-oil microemulsion. *Phys. Chem. Chem. Phys.*, 20: 13825-13835.

Stawski, T.M., Van Driessche, A.E.S., Besselink, R., Byrne, E.H., Raiteri, P., Gale, J.D., Benning, L.G. (2019). The structure of $CaSO_4$ nanorods: The precursor of gypsum. *J. Phys. Chem. C*, 123: 23151-23158.

Stawski, T.M., van Driessche, A.E.S., Ossorio, M., Diego Rodriguez-Blanco, J., Besselink, R., Benning, L.G. (2016). Formation of calcium sulfate through the aggregation of sub-3 nanometre primary species. *Nat. Commun.*, 7: 11177.

Stefan, M., Ralph, S., Thomas, S. (2013). High throughput data acquisition at the XAS and SUL-X beamline at ANKA. *J. Phys. Conf. Ser.*, 430: 012022.

Stewart, S.M., Hofstetter, T.B., Joshi, P., Gorski, C.A. (2018). Linking thermodynamics to pollutant reduction kinetics by Fe^{2+} bound to iron oxides. *Environ. Sci. Technol.*, 52: 5600-5609.

Stilwell, D.E., Gorny, K.D. (1997). Contamination of soil with copper, chromium, and arsenic under decks built from pressure treated Wood. *Bull. Environ. Contam. Toxicol.*, 58: 22-29.

Su, C., Puls, R.W. (2004). Significance of iron(II,III) hydroxycarbonate green rust in arsenic remediation using zerovalent iron in laboratory column tests. *Environ. Sci. Technol.*, 38: 5224-5231.

Su, C., Wilkin, R.T. (2005). *Arsenate and arsenite sorption on and arsenite oxidation by iron(II, III) hydroxycarbonate green rust*. Advances in Arsenic Research. 915. American Chemical Society, pp. 25-40.

Sumoondur, A., Shaw, S., Ahmed, I., Benning, L.G. (2008). Green rust as a precursor for magnetite: An *in situ* synchrotron based study. *Mineral. Mag.*, 72: 201-204.

Tang, W., Li, Q., Gao, S., Shang, J.K. (2011). Arsenic (III,V) removal from aqueous solution by ultrafine α-Fe_2O_3 nanoparticles synthesized from solvent thermal method. *J. Hazard. Mater.*, 192: 131-138.

Taylor, R.M. (1980). Formation and properties of Fe (II)Fe(III) hydroxy-carbonate and its possible significance in soil formation. *Clay Miner.*, 15: 369-382.

Thomas, A.N., Eiche, E., Göttlicher, J., Steininger, R., Benning, L.G., Freeman, H.M., Dideriksen, K., Neumann, T. (2018). Products of hexavalent chromium reduction by green rust sodium sulfate and associated reaction mechanisms. *Soil Syst.*, 2: 58.

Tian, Z., Feng, Y., Guan, Y., Shao, B., Zhang, Y., Wu, D. (2017). Opposite effects of dissolved oxygen on the removal of As(III) and As(V) by carbonate structural Fe(II). *Sci. Rep.*, 7: 17015.

Toby, B.H., Von Dreele, R.B. (2013). GSAS-II: the genesis of a modern open-source all purpose crystallography software package. *J. Appl. Crystallogr.*, 46: 544-549.

Trolard, F., Bourrié, G., Abdelmoula, M., Refait, P., Feder, F. (2007). Fougerite, a new mineral of the pyroaurite-iowaite group: description and crystal structure. *Clays Clay. Miner.*, 55: 323-334.

Trolard, F., Génin, J.-M.R., Abdelmoula, M., Bourrié, G., Humbert, B., Herbillon, A. (1997). Identification of a green rust mineral in a reductomorphic soil by Mössbauer and Raman spectroscopies. *Geochim. Cosmochim. Acta*, 61: 1107-1111.

Tronc, E., Belleville, P., Jolivet, J.P., Livage, J. (1992). Transformation of ferric hydroxide into spinel by iron(II) adsorption. *Langmuir*, 8: 313-319.

Usman, M., Byrne, J.M., Chaudhary, A., Orsetti, S., Hanna, K., Ruby, C., Kappler, A., Haderlein, S.B. (2018). Magnetite and green rust: Synthesis, properties, and environmental applications of mixed-valent iron minerals. *Chem. Rev.*, 118: 3251-3304.

Usman, M., Hanna, K., Abdelmoula, M., Zegeye, A., Faure, P., Ruby, C. (2012). Formation of green rust via mineralogical transformation of ferric oxides (ferrihydrite, goethite and hematite). *Appl. Clay Sci.*, 64: 38-43.

Vadahanambi, S., Lee, S.-H., Kim, W.-J., Oh, I.-K. (2013). Arsenic removal from contaminated water using three-dimensional graphene-carbon nanotube-iron oxide nanostructures. *Environ. Sci. Technol.*, 47: 10510-10517.

van Aken, P.A., Liebscher, B. (2002). Quantification of ferrous/ferric ratios in minerals: new evaluation schemes of Fe L23electron energy-loss near-edge spectra. *Phys. Chem. Miner.*, 29: 188-200.

van Genuchten, C., Addy, S., Pena, J., Gadgil, A. (2012a). Removing arsenic from synthetic groundwater with iron electrocoagulation: An Fe and As K-edge EXAFS study. *Environmental Science & Technology*, 46: 986-994.

van Genuchten, C.M., Addy, S.E.A., Peña, J., Gadgil, A.J. (2012b). Removing arsenic from synthetic groundwater with iron electrocoagulation: An Fe and As K-edge EXAFS study. *Environ. Sci. Technol.*, 46: 986-994.

van Genuchten, C.M., Behrends, T., Dideriksen, K. (2019a). Emerging investigator series: Interdependency of green rust transformation and the partitioning and binding mode of arsenic. *Environ. Sci.: Process. Impacts*.

van Genuchten, C.M., Behrends, T., Stipp, S.L.S., Dideriksen, K. (2019b). Achieving arsenic concentrations of <1 µg/L by Fe(0) electrolysis: The exceptional performance of magnetite. *Water Res.*: 115170.

van Genuchten, C.M., Peña, J. (2016). Antimonate and arsenate speciation on reactive soil minerals studied by differential pair distribution function analysis. *Chem. Geol.*, 429: 1-9.

Vaughan, D.J. (2006). Arsenic. *Elements*, 2: 71-75.

Vempati, R., Loeppert, R.H. (1989). Influence of structural and adsorbed Si on the transformation of synthetic ferrihydrite. *Clays Clay. Miner.*, 37: 273-279.

Vinš, J., Šubrt, J., Zapletal, V., Hanousek, F. (1987). Preparation and properties of green rust type substances. *Collect. Czech. Chem. Commun.*, 52: 93-102.

Viollier, E., Inglett, P.W., Hunter, K., Roychoudhury, A.N., Van Cappellen, P. (2000). The ferrozine method revisited: Fe(II)/Fe(III) determination in natural waters. *Appl. Geochem.*, 15: 785-790.

Vu, H.P., Shaw, S., Brinza, L., Benning, L.G. (2010). Crystallization of hematite (α-Fe_2O_3) under alkaline condition: The effects of Pb. *Cryst. Growth. Des.*, 10: 1544-1551.

Vu, H.P., Shaw, S., Brinza, L., Benning, L.G. (2013). Partitioning of Pb(II) during goethite and hematite crystallization: Implications for Pb transport in natural systems. *Appl. Geochem.*, 39: 119-128.

Vuillemin, A., Wirth, R., Kemnitz, H., Schleicher, A.M., Friese, A., Bauer, K.W., Simister, R., Nomosatryo, S., Ordoñez, L., Ariztegui, D., Henny, C., Crowe, S.A., Benning, L.G., Kallmeyer, J., Russell, J.M., Bijaksana, S., Vogel, H. (2019). Formation of diagenetic siderite in modern ferruginous sediments. *Geology*, 47: 540-544.

Wagner, C.D., Muilenberg, G.E. (1979). *Handbook of X-ray Photoelectron Spectroscopy: A Reference Book of Standard Data for Use in X-ray Photoelectron Spectroscopy*: Perkin-Elmer.

Wang, L., Giammar, D.E. (2015). Effects of pH, dissolved oxygen, and aqueous ferrous iron on the adsorption of arsenic to lepidocrocite. *J. Colloid Interface Sci.*, 448: 331-338.

Wang, L., Putnis, C.V., Hövelmann, J., Putnis, A. (2018). Interfacial precipitation of phosphate on hematite and goethite. *Minerals*, 8: 207.

Wang, S., Mulligan, C.N. (2006). Natural attenuation processes for remediation of arsenic contaminated soils and groundwater. *J. Hazard. Mater.*, 138: 459-470.

Wang, Y., Morin, G., Ona-Nguema, G., Brown, G.E. (2014). Arsenic(III) and arsenic(V) speciation during transformation of lepidocrocite to magnetite. *Environ. Sci. Technol.*, 48: 14282-14290.

Wang, Y., Morin, G., Ona-Nguema, G., Juillot, F., Calas, G., Brown, G.E. (2011). Distinctive arsenic(V) trapping modes by magnetite nanoparticles induced by different sorption processes. *Environ. Sci. Technol.*, 45: 7258-7266.

Wang, Y., Morin, G., Ona-Nguema, G., Juillot, F., Guyot, F., Calas, G., Brown, G.E. (2010). Evidence for different surface speciation of arsenite and arsenate on green rust: An

EXAFS and XANES Study. *Environ. Sci. Technol.*, 44: 109-115.

Waychunas, G.A., Rea, B.A., Fuller, C.C., Davis, J.A. (1993). Surface chemistry of ferrihydrite: Part 1. EXAFS studies of the geometry of coprecipitated and adsorbed arsenate. *Geochim. Cosmochim. Acta*, 57: 2251-2269.

Webb, S.M. (2005). SIXpack: a graphical user interface for XAS analysis using IFEFFIT. *Phys. Scr.*, 2005: 1011.

Williams, A.G.B., Scherer, M.M. (2001). Kinetics of Cr(VI) reduction by carbonate green rust. *Environ. Sci. Technol.*, 35: 3488-3494.

Williams, A.G.B., Scherer, M.M. (2004). Spectroscopic evidence for Fe(II)–Fe(III) electron transfer at the iron oxide–water interface. *Environ. Sci. Technol.*, 38: 4782-4790.

Williams, M., Fordyce, F., Paijitprapapon, A., Charoenchaisri, P. (1996). Arsenic contamination in surface drainage and groundwater in part of the southeast Asian tin belt, Nakhon Si Thammarat Province, southern Thailand. *Environ. Geol.*, 27: 16-33.

Wisotzky, F., Cremer, N., Lenk, S. (2018). *Angewandte Grundwasserchemie, Hydrogeologie und hydrogeochemische Modellierung: Grundlagen, Anwendungen und Problemlösungen*: Springer Berlin Heidelberg.

Wolthers, M., Charlet, L., van Der Weijden, C.H., van der Linde, P.R., Rickard, D. (2005). Arsenic mobility in the ambient sulfidic environment: Sorption of arsenic(V) and arsenic(III) onto disordered mackinawite. *Geochim. Cosmochim. Acta*, 69: 3483-3492.

World Health Organization (2017). Guidelines for drinking-water quality: Fourth edition incorporating the first addendum.

Yang, L., Steefel, C.I., Marcus, M.A., Bargar, J.R. (2010). Kinetics of Fe(II)-catalyzed transformation of 6-line ferrihydrite under anaerobic flow conditions. *Environ. Sci. Technol.*, 44: 5469-5475.

Yean, S., Cong, L., Yavuz, C.T., Mayo, J.T., Yu, W.W., Kan, A.T., Colvin, V.L., Tomson, M.B. (2005). Effect of magnetite particle size on adsorption and desorption of arsenite and arsenate. *J. Mater. Res.*, 20: 3255-3264.

Yee, N., Shaw, S., Benning, L.G., Nguyen, T.H. (2006). The rate of ferrihydrite transformation to goethite via the Fe(II) pathway. *Am. Mineral.*, 91: 92-96.

Yin, W., Ai, J., Huang, L.-Z., Tobler, D.J., B. Hansen, H.C. (2018). A silicate/glycine switch to control the reactivity of layered iron(II)–iron(III) hydroxides for dechlorination of carbon tetrachloride. *Environ. Sci. Technol.*, 52: 7876-7883.

Yin, W., Strobel, B.W., B. Hansen, H.C. (2017). Amino acid-assisted dehalogenation of carbon tetrachloride by green rust: Inhibition of chloroform production. *Environ. Sci. Technol.*, 51: 3445-3452.

Zagury, G.J., Dobran, S., Estrela, S., Deschênes, L. (2008). Inorganic arsenic speciation in soil and groundwater near in-service chromated copper arsenate-treated wood poles. *Environ. Toxicol. Chem.*, 27: 799-807.

Zagury, G.J., Samson, R., Deschênes, L. (2003). Occurrence of metals in soil and ground water near chromated copper arsenate–treated utility poles. *J. Environ. Qual.*, 32: 507-514.

Zahid, A., Hassan, M.Q., Balke, K.D., Flegr, M., Clark, D.W. (2008). Groundwater chemistry and occurrence of arsenic in the Meghna floodplain aquifer, southeastern Bangladesh. *Environ. Geol.*, 54: 1247-1260.

Zarzycki, P., Kerisit, S., Rosso, K.M. (2015). Molecular dynamics study of Fe(II) adsorption, electron exchange, and mobility at goethite (α-FeOOH) surfaces. *J. Phys. Chem. C*, 119: 3111-3123.

Zegeye, A., Bonneville, S., Benning, L.G., Sturm, A., Fowle, D.A., Jones, C., Canfield, D.E., Ruby, C., MacLean, L.C., Nomosatryo, S., Crowe, S.A., Poulton, S.W. (2012). Green rust formation controls nutrient availability in a ferruginous water column. *Geology*, 40: 599-602.

Zhang, Y., Wei, S., Lin, Y., Fan, G., Li, F. (2018). Dispersing metallic platinum on green rust enables effective and selective hydrogenation of carbonyl group in cinnamaldehyde. *ACS Omega*, 3: 12778-12787.

Zhou, Z., Latta, D.E., Noor, N., Thompson, A., Borch, T., Scherer, M.M. (2018). Fe(II)-catalyzed transformation of organic matter–ferrihydrite coprecipitates: A closer look using e isotopes. *Environ. Sci. Technol.*, 52: 11142-11150.

Zouboulis, A.I., Katsoyiannis, I.A. (2005). Recent advances in the bioremediation of arsenic-contaminated groundwaters. *Environ. Int.*, 31: 213-219.